REGIONALLY EXTENSIVE DROUGHTS AND CLIMATE CHANGE IN SOUTHERN AFRICA: MECHANISMS, MODEL RELIABILITY AND PROJECTIONS

Report to the
Water Research Commission

by

**BH Abiodun, EL Ujeneza, A Meque, M Naik, SA Omar, S Lawal, M Nguvava,
M Gore, K Molepo, M Maoyi and P Mukwenha**
Department of Environmental and Geographical Science, University of Cape Town

M New
African Climate & Development Initiative, University of Cape Town

M Rouault
Department of Oceanography, University of Cape Town

F Engelbrecht
Climate Studies, Modelling and Environmental Health, Council for Scientific and Industrial Research
Natural Resources and the Environment

AA Abatan
Department of Oceanography, Department of Geography and Atmospheric Science,
Iowa State University

May 2018

Obtainable from

Water Research Commission
Private Bag X03
Gezina, 0031

Printed in the Republic of South Africa

EXECUTIVE SUMMARY

This report details various accomplishments and findings of the project entitled "Regionally Extensive Droughts and Climate Change in Southern Africa: Mechanisms, Reliability and Projections", which was funded by the South African Water Research Commission from 2013 to 2017. The project had the following major objectives: to better characterise droughts over southern Africa; to identify the mechanisms that induce regionally extensive droughts (REDs) over southern Africa; to examine the capability of climate model in simulating southern African droughts; to project future characteristics of REDs under climate change; and to investigate reforestation impacts on the droughts. In addition, the project developed a drought monitoring system over southern Africa.

Incorporating potential evapotranspiration into drought indices to obtain a better characterisation of droughts over southern Africa

Southern African droughts are usually quantified with precipitation anomalies or the Standardised Precipitation Index (SPI), thereby neglecting the important roles of evapotranspiration in drought quantification. Furthermore, most drought studies over the subcontinent have been on local-scale droughts, with little attention on REDs that usually cause more devastating impacts. This project overcomes these shortcomings by using the Standardised Precipitation Evapotranspiration Index (SPEI) to identify droughts and using two techniques to characterise REDs over southern Africa. The first technique identified dominant drought modes and the second technique obtained major drought patterns.

The results of first technique showed that about 50% of southern African droughts can be represented with four major drought modes (called DM1, DM2, DM3 and DM4). The core of DM1 is over the south-western part of southern Africa; DM2 over Zimbabwe; DM3 over Tanzania; and DM4 over Angola. The results of the second technique revealed that southern African drought patterns can be generally classified into three groups: All-dry pattern (showing dry conditions over the entire southern Africa); all-wet pattern (showing wet conditions over the whole region); and dipole pattern (showing wet conditions over a part of the subcontinent and dry conditions elsewhere).

Comparing the results from the two techniques indicates that the second technique (i.e. drought patterns) gives a more robust description of RED characteristics than the first technique (i.e. drought mode), because the characteristics of all the drought modes fall under that of dipole drought patterns. We also found that while each drought pattern can occur in any season, some drought patterns have preference for seasons. Furthermore, some droughts patterns can persist from season to season, while others easily transit to another pattern in the following season.

There are distinctions between SPEI and SPI results. SPEI results suggest a general shift in southern African droughts from all-wet patterns in the 1950s to 1970s to all-dry patterns in 1990 (possibly due to the climate change). However, this shift does not feature in the SPI results, suggesting that SPI may underestimate the influence global warming on southern African drought.

Understanding the mechanisms by which remote and local forcing of drought are translated into climate moisture deficits

Previous studies have identified some atmospheric teleconnections as the main drivers (remote and local) of southern African droughts. However, those studies quantified drought using only precipitation – meaning that their results may not account for the contribution of potential evapotranspiration (or temperature) to the link between atmospheric teleconnections and the droughts. Also, there is a dearth of information on the coupling between atmospheric teleconnections and REDs. Hence, to fill these gaps, this project examined the relationship between atmospheric teleconnections and REDs over southern Africa using SPEI to quantify the droughts.

The results showed a strong dipole correlation between the El Niño Southern Oscillation (ENSO) and southern African droughts (SPEI). The correlation is up to +0.6 over the tropical area and about −0.6 over the subtropical area. While the strong link is due to the influence of ENSO on both precipitation

and temperature fields, the influence is stronger on temperature than on precipitation. Although ENSO influences the four drought modes in southern Africa, the influence of the Indian Ocean Dipole (IOD) on DM2 is as strong as that of ENSO, and the influence of the Tropical North Atlantic Ocean (TNA) on DM3 is stronger than that of ENSO. Moreover, we found that only 20% of droughts patterns (all-dry and all-wet patterns) are solely induced by ENSO; other drought patterns are caused by complex interactions among the atmospheric teleconnections. However, all-dry drought patterns usually occur during El Niño events, while all-wet patterns occur during the La Niña events.

Evaluating the capabilities of climate models to represent REDs and the driving mechanisms

Climate models are fascinating tools for understanding the complexity of climate systems. They can be applied to study the past and future characteristics of droughts. However, for climate model results to be useful, the model should realistically simulate the past climate. Hence, this project examined the performance of some global climate models (GCMs) and regional climate models (RCMs) in simulating the characteristics of the REDs (and the influences of the drought drivers) over southern Africa.

We found that contemporary GCMs give remarkable simulations of the observed characteristics of the drought modes (e.g. the spatial structure). However, they reproduce the characteristics better at a three-month drought scale than at a 12-month drought scale. While about 70% of the GCMs simulate the characteristics of four drought modes well at three-month scale, only 60% of the models capture the characteristics of three drought models well at 12-month scale. Existing RCMs also simulate the spatial structure of the drought modes better at three-month scale than at the 12-month scales, but they capture the temporal variability of the drought modes better at 12-month scale than at three-month scale. They also simulate well the frequency of the drought patterns over southern Africa but perform poorly in reproducing the temporal variability of the drought patterns.

Some RCMs simulate the ENSO influence on the southern African droughts well. In this regard, a variable-resolution global model shows the best simulation, possibly because the model does not have lateral boundary condition problem as other RCMs. However, we found that the simulated link between ENSO and southern African droughts is sensitive to the global data set used for the lateral boundary forcing. In some cases, the RCM downscaling of GCM simulations adds values to the simulated link, but in other cases it does not add values. The added value of RCM to the simulated link decreases as the capability of the GCM to simulate the link increases. This study suggests that downscaling GCM simulations with RCMs over southern Africa may either improve or depreciate the simulated ENSO-drought link over the region.

Understanding the potential impacts of climate change on REDs in southern Africa

There is a concern that the anthropogenic warming may increase the severity of southern African droughts. However, most future projections over the subcontinent usually consider future changes in precipitation and temperature separately, without linking the changes to climate moisture balance to give a better indication of climate change impacts on droughts. The present study investigated the impacts of the anthropogenic warming change droughts over Africa, using SPEI (a climate moisture balance indicator) to characterise droughts. It focused on future changes in drought intensity, area coverage, frequency, modes, and patterns. The future projections are based on series of regional climate model simulations of two future climate scenarios (called RCP4.5 and RCP8.5).

The models projected an increase in droughts intensity, area coverage, and frequency over southern Africa in the future under both RCP4.5 and RCP8.5 scenarios. However, the increase is more pronounced under the RCP8.5 than under RCP4.5. There are substantial differences in future projections of SPEI and SPI droughts. SPEI droughts are more intense, more frequent, and wider than SPI droughts. The model projections show no significant changes in spatial structure of the four drought modes, but more severe droughts are projected over the core areas of the drought modes, and the magnitude of the severity is higher for DM3 and DM4 modes than for DM1 and DM2 modes. The projections also show that all-dry drought patterns would become more frequent in the future, while all-

wet drought patterns would become less frequent, but the frequency of dipole drought patterns would remain unchanged.

Potential impacts of forestation on southern African droughts

Some studies have suggested forestation as a viable climate change mitigation option (because of its biochemical benefits) without investigating the biophysical impacts of forestation. Despite its biochemical benefits, forestation may induce negative impacts on the regional climate, especially over southern Africa. To improve knowledge in this aspect, the project used a series of climate model simulations to investigate impacts of realistic land-use changes (i.e. forestation) over southern Africa on the regional climate in the future.

The results showed that forestation increases the projected future warming over the forested area but reduces the warming elsewhere. In addition, it enhances rainfall over the forested area and lowers rainfall elsewhere. These changes are largely due to the albedo effect and dynamic effect of forestation on the atmosphere. The darker forest (relative to pre-existing vegetation cover) decreases the surface albedo and increases the amount of solar radiation absorbed at the surface. This produces extra energy in the system, which increases the amount of sensible and latent heat over the forested area, thereby increasing the temperature and rainfall, respectively. Hence, the study concluded that forestation would alleviate droughts over some areas and aggravate drought over other areas.

Drought monitoring systems over southern Africa

The Drought Atlas, a collection of past drought maps, is very useful for drought monitoring and forecasting. We can learn from past drought events and compare real-time droughts with similar past conditions. A previous study developed a Drought Atlas over South Africa in 2007 using SPI to define drought. The atlas is now almost a decade old, meaning that it does not include recent droughts patterns. It might also underestimate drought intensity because it does not include the influence of evapotranspiration in characterising the droughts. In addition, since the focus of the atlas is over South Africa, it may be unsuitable for representing REDs over southern Africa. Hence, as part of the project, we developed a drought monitoring system (http://hail.csag.uct.ac.za/droughtmonitor/home.php), which includes a new Drought Atlas over the entire southern Africa from 1951 to 2015. The system also provides the composites of drought patterns during the active phases of important atmospheric teleconnection (e.g. ENSO and IOD) and provides future projections of droughts over southern African countries (and any other area of interest) under two possible future climate change scenarios (RCP4.5 and RCP8.5).

Capacity building and publications

Part of this project comprised a PhD thesis (Arlindo Meque; graduated) and two master's theses (Evaline Ujeneza and Myra Naik; both graduated) submitted to the University of Cape Town. Some of the findings from the project are now published in three peer-reviewed papers (Meque and Abiodun 2015; Naik and Abiodun 2016; Ujeneza and Abiodun 2015), while others are awaiting publication.

The project outputs (i.e. computer codes and data) have been used in other three peer-review papers (Abbar and Abiodun 2016; Abiodun et al. 2016; Browne-Klutse et al. 2015) and in two PhD theses (Mariam Nguvava and Shakirudeen Lawal; both ongoing) at University of Cape Town and a PhD thesis (Abayomi Abatan; ongoing) at Iowa State University in the United States of America.

The new Drought Atlas also provides teaching resources for two postgraduate courses (EGS4023F: Research Methods for Natural Science; EGS4024S: Climate Modelling) at the University of Cape Town.

Recommendation

Results of this project can be improved or applied in several ways. For instance, it can be improved by using more observational, reanalysis and simulation data sets that cover a longer time period. Using data sets with a longer time period (i.e. paleo-climate data sets) would give better information on whether the disappearance of the all-wet drought since the last few decades is due to the impact of

climate change or it is a part of natural climate variability. Performing the analysis with more data sets will help in quantifying the uncertainties in the results, hence making them more robust for policymaking.

There is need for additional studies to investigate why the stretched-grid global climate model (SGCM) performed better than the limited-area climate models (i.e. RCMs) in simulating a link between ENSO and southern African droughts. The most plausible reason is that the lateral boundary condition problem may be a major bottleneck in simulating the link in RCMs, whereas there is no boundary condition problem in the SGCM. However, to establish this postulation, a climate model that can function as GCM, SGCM and RCM is required to study the influence of boundary condition problem on simulating the link between atmospheric teleconnection and southern African droughts. The results of such a study will assist the climate model development community (especially in southern Africa) to focus their efforts and resources on areas that will improve the simulations of southern African droughts.

Although, the analysis of the project has focused on characteristics of REDs in past climate and in future climate projection, the analysis can be easily extended to forecasting of REDs at subseasonal to seasonal scales. The emphases of conventional seasonal forecasting systems in southern Africa have been on rainfall and temperature anomalies. Incorporating the methodology and results of this project into the current seasonal forecasting systems will make the systems provide more relevant and useful information for minimising drought impacts over the subcontinent. Lastly, the results of the project can also be applied in studying impacts of REDs on southern African river basins and in investigating how land-use management (e.g. land-cover changes) can be used to mitigate the impacts.

ACKNOWLEDGEMENTS

Page left blank intentionally

TABLE OF CONTENTS

LIST OF FIGURES

LIST OF TABLES

LIST OF ABBREVIATIONS

AAO	Antarctic Oscillation
CMIP5	Coupled Model Intercomparison Project Phase 5
CORDEX	Coordinated Regional Climate Downscaling Experiment
CRU	Climate Research Unit
DJF	December-January-February
DM1	Drought Mode 1
DM2	Drought Mode 2
DM3	Drought Mode 3
DM4	Drought Mode 4
DRC	Democratic Republic of Congo
ECMWF	European Centre for Medium-Range Weather Forecasts
EN3	El Niño Type 3
EN4	El Niño Type 4
ENSO	El Niño Southern Oscillation
ERA-Int	ERA-Interim Reanalysis
GCM	Global Climate Model
GWS	Global Wavelet Spectrum
HAD	Met Office Hadley Centre Model (HADGEM2-ES)
ICTP	International Centre for Theoretical Physics
IOD	Indian Ocean Dipole
IPCC	Intergovernmental Panel on Climate Change
JJA	June-July-August
LN1	La Niña Type 1
LN4	La Niña Type 4
LP	Limpopo
MAM	March-April-May
MEI	Multivariate ENSO Index
MPI	Max Planck Institute for Meteorology Model (MPI-ESM-LR)
NS	North-Eastern South Africa
NZ	North-Eastern Tanzania
PCA	Principal Component Analysis
PDSI	Palmer Drought Severity Index
PET	Potential Evapotranspiration
PF1	Principal Factor 1
PF2	Principal Factor 2

PF3	Principal Factor 3
PF4	Principal Factor 4
RCA	Rossby Centre Regional Atmospheric Model
RCM	Regional Climate Model
RCP	Representative Concentration Pathway
RED	Regionally Extensive Drought
RegCM	Regional Climate Model Version 4.3
SADC	South African Development Community
SGCM	Stretched-Grid Global Climate Model
SIOD	Subtropical Indian Ocean Dipole
SOM	Self-Organising Map
SON	September-October-November
SPEI	Standardised Precipitation Evapotranspiration Index
SPI	Standardised Precipitation Index
SST	Sea Surface Temperature
TNA	Tropical Northern Atlantic Ocean
TTT	Tropical Temperate Troughs
UDEL	University of Delaware
UK	United Kingdom
USA	United States of America
WPS	Wavelet Power Spectrum
WRF	Weather Research Forecasting Model Version 3.1.1

1   INTRODUCTION

1.1   Motivation

Drought is a natural hazard with severe socio-economic impacts in many southern African countries. It is a threat to water management, water-dependent activities and livelihoods in southern Africa. Impacts of drought are usually severe in communities where the socio-economic activities of the people depend on the of availability of water in surface and subsurface sources. Of particular concern are regionally extensive droughts (REDs), which produce widespread impacts that cannot be compensated by the redistribution of water, food and energy production from other parts of a resource system.

Drought can have transnational and multifaceted impacts. In 1991 and 1992, drought-depleted groundwater reservoirs reduced the fresh water availability and forced people to use water from unprotected sources. As a result, many people suffered from cholera, diarrhoea and dysentery (Calow et al. 2010), and more than 90% of small inland dams in the eastern part of southern Africa dried up (Jury and Mwalifurwa 2002). The drought was also associated with widespread food shortages across the affected region.

With more than 60% of southern Africa vulnerable to drought, changes in characteristics (such as frequency, intensity, duration and spatial extent) of large drought events would have serious consequences for regional water, food and energy security. The focus of previous studies on droughts has largely been within South Africa (e.g. Rouault and Richard 2003) with a minimal exploration of the coherence of REDs in southern Africa. Meanwhile, the devastating impacts of REDs in 1991 and 1992 call for better understanding of the spatial and temporal characteristics of REDs. This project squarely addresses this need.

Few studies have investigated the characteristics of droughts in southern Africa. Richard et al. (2001) showed that countries in southern Africa experienced more intense and more widespread droughts from 1979 to 1988. Rouault and Richard (2003) established the existence of decadal variability in the spatial extension and intensity of droughts in South Africa and found that wet years had enhanced since the 1970s. Rouault and Richard (2003) also found that the number of dry districts in South Africa had increased, but there was still a substantial decadal variability. However, all these previous studies used either rainfall anomalies or the Standardised Precipitation Index (SPI) to characterise the droughts. Since they did not include evapotranspiration in characterising the droughts, they might have under-estimated the intensity and spatial coverage of the droughts. For instance, suppose a given area receives the same amount of rainfall during two different seasons under different temperatures, it is likely that the region will be drier during the warmer season due to a higher evapotranspiration. Vicente-Serrano et al. (2011) introduced a new a multiscale drought index, namely, the Standardised Precipitation Evapotranspiration Index (SPEI), which accounts for the influence of potential evapo-transpiration in characterising droughts at various scales. However, no study has used SPEI to investigate characteristics of southern African droughts. The present project fills that gap.

The mechanisms that induce droughts in southern Africa remain unclear. Rouault and Richard (2005) suggested that the El Niño Southern Oscillation (ENSO) might play a crucial role on South African droughts because most of the severe droughts that occurred in South African during the period 1901–2004 were associated with ENSO events. Richard et al. (2001) found that some ENSO events (e.g. in 1997–1998) were not accompanied by droughts over southern Africa. Many studies argued that other general circulations may have a strong influence on southern Africa droughts as well (Fauchereau et al. 2003; Jury and Mwafulirwa 2002; Manatsa et al. 2008, Manatsa and Matarira 2009; Manatsa et al. 2012). Nevertheless, no studies have investigated the mechanisms that induce REDs in southern Africa or considered whether the models associate REDs with the correct regional or global forcing. The present project examines the regional and global atmospheric features that induce the REDs in observations and climate models.

As many studies continue to show that drought severity can increase with temperature (Dai et al. 2004; Dai 2011; Sheffield and Wood 2008; Vicente-Serrano et al. 2010a; Washington and Preston 2006), there is a concern that the ongoing global warming may increase the severity of droughts in southern Africa. Climate change projections suggest a decrease in mean rainfall and an increase in evapotranspiration across much of subtropical southern Africa (e.g. Christensen et al. 2007; Engelbrecht et al. 2009; 2011). A better understanding on how this may influence future characteristics of REDs over the regional will foster stronger collaborations among the Southern African Development Community (SADC) countries on how to mitigate impacts of REDs on socio-economic activities in the future. The present project is in that line.

Hence, the aim of the project was to study the characteristics of REDs over southern Africa (using SPEI to identify the droughts), mechanisms that control REDs, and impacts of future climate change on REDs. We analysed observation and climate simulation data sets to achieve the aim. Overall, the project has five main objectives as listed in Table 1.

Table 1: List of the project objectives

No.	Description	Chapter(s)
1	Obtain a better characterisation of droughts over southern Africa by using a drought index that is based on climate moisture balance and identify REDs	2, 7
2	Understand the mechanisms by which remote and local forcing of drought are translated into climate moisture deficits	3
3	Evaluate abilities of climate models to represent REDs and the associated mechanisms	4, 5
4	Understand the potential impacts of climate change on REDs in southern Africa	5
5	Examine the potential impacts of droughts in southern Africa	6

1.2 Basis

One of the major obstacles in drought monitoring is the lack of a unique and universal definition for drought. This has led to a variety of drought indices in the past century. Droughts are generally classified into four types, namely, meteorological, agricultural, hydrological and socio-economic droughts (Mishra and Singh 2010). The drought indices are used specifically to assess one or two drought types. For instance, the Standardised Run-off Index, Palmer Reclamation Drought Index, Hydrological Drought Index, Surface Water Supply Index and Palmer Drought Severity Index (PDSI) are mainly used to monitor hydrological drought. The Vegetation Condition Index, Crop Moisture Index, and Drought Monitor are mainly used to monitor agriculture drought. The Percentage of Normal, SPI, Deciles and, more recently, the SPEI are used for meteorological drought. The socio-economic drought is a more complex concept to quantify; hence, no index has been defined to monitor it yet.

The most used drought index is the PDSI (Palmer 1965). It employs precipitation, evapotranspiration, soil moisture and temperature in determining moisture supply and demand (Mishra and Singh 2010). Modified versions of the PDSI have been introduced and adapted to monitor different types of drought (i.e. Palmer Hydrological Drought Index in Karl 1986; modified PDSI in Heddinghaus and Sabol 1991; the self-calibrated PDSI in Wells et al. 2004; and the Crop Moisture Index in Palmer 1968). However, the major weakness of the PDSI is that its temporal scale is limited from nine to 12 months (Sivakumar et al. 2011; Vicente-Serrano et al. 2010a; Vicente-Serrano et al. 2011).

SPI, a multiscale drought index developed by Mckee et al. (1993), is another popular drought index for detecting meteorological and agricultural drought at the three- and six-month scales, as well as hydrological drought at the six-, 12-, 24- and 48-month scales (Hayes et al. 1999; Vicente-Serrano and López-Moreno 2005; Vicente-Serrano et al. 2010a; 2010b). SPI can detect wet and dry events occurring simultaneously at different time scales. However, the main shortcoming of SPI is that it uses only one climate variable, namely, rainfall for monitoring droughts (Sivakumar et al. 2011; Vicente-Serrano et al. 2011). It assumes rainfall has a stronger influence on droughts than other climate variables such as temperature, wind speed, wind direction and potential evapotranspiration; hence, these variables are neglected. Meanwhile, other climate variables such as temperature, wind, and humidity have been shown to have equal, if not more important, influence on drought (Dai 2011).

However, to overcome the shortcomings of SPI, Vicente-Serrano et al. (2010a) proposed a new drought index, namely, the SPEI, which depends on the potential evapotranspiration (PET). SPEI is a modification of the SPI. SPEI accounts for the effect of temperature variability in monitoring droughts at different time scales. As a result, SPEI has the capability to detect the temporal and geographical extent of droughts. This makes it a very good tool for drought monitoring and for accessing the future impact of global warming on droughts. The present project adopted SPEI in characterising southern African droughts.

1.3   Outline

This report first presents the spatial and temporal characteristics of REDs as observed over southern Africa (Chapter 2), then analyses relationships between the REDs and various large-scale atmospheric teleconnections (Chapter 3). It switches to the results of the climate models with Chapter 4 evaluating the capability of the models to simulate the characteristics of the droughts and the relationship between the droughts and the large-scale global climate indices. Chapter 5 projects the degree to which anthropogenic emissions may alter the characteristics of the droughts in the future climate, while Chapter 6 shows the potential impacts of land-use changes on droughts over the subcontinent in the future. Chapter 7 presents the new drought monitoring system over southern Africa. Concluding remarks and further discussions of possible implications of the results are given in Chapter 8. The lists of project outputs are included in the Bibliography.

2 CHARACTERISTICS OF REDs OVER SOUTHERN AFRICA

2.1 Introduction

Drought is a recurring extreme climate event characterised by below-normal moisture availability over a period of months to years. However, most previous studies on southern African droughts (e.g. Richard et al. 2001; Rouault and Richard 2003) have used either rainfall anomalies or the SPI to characterise droughts. Since they did not include evapotranspiration in characterising droughts, these studies might have underestimated the intensity and spatial coverage thereof. In addition, the emphases of the previous studies have been on droughts within South Africa, despite the devastating impacts of REDs, especially in 1991 and 1992. Hence, to fill these gaps, this study presents the characteristics of droughts over the entire southern Africa using the SPEI, a multiscale drought index based on the climate water balance (i.e. precipitation minus potential evaporation).

All the results presented in this chapter are based on analysis of the observation data sets. The descriptions of the data sets and the methods used in analysing the data sets are given in Section 2.2. The results of the analyses are discussed in Section 2.3 and Section 2.4. Section 2.3 focuses on drought modes, while Section 2.4 concentrates on drought patterns. A concluding remark is given in Section 2.5. For a more comprehensive and technical discussion of the results, readers are referred to Ujeneza and Abiodun (2014), Meque (2015), and Meque and Abiodun (2017).

2.2 Data and Methods

2.2.1 Data

Two gridded climate observation data sets (consisting of monthly precipitation and temperature data) were analysed over the southern African region (0°E–45°E, 2°S–37°S; Figure 1). The first data set was obtained from the Climate Research Unit (CRU) version 3.0 (Mitchell and Jones 2005). The CRU data set is based on station data regridded to a 0.5° × 0.5° spatial resolution. The second data set was obtained from the University of Delaware (UDEL) (Legates and Willmott 1990). However, most of our analyses used the CRU data set. We only used the UDEL data set to examine the sensitivity of the results in some cases.
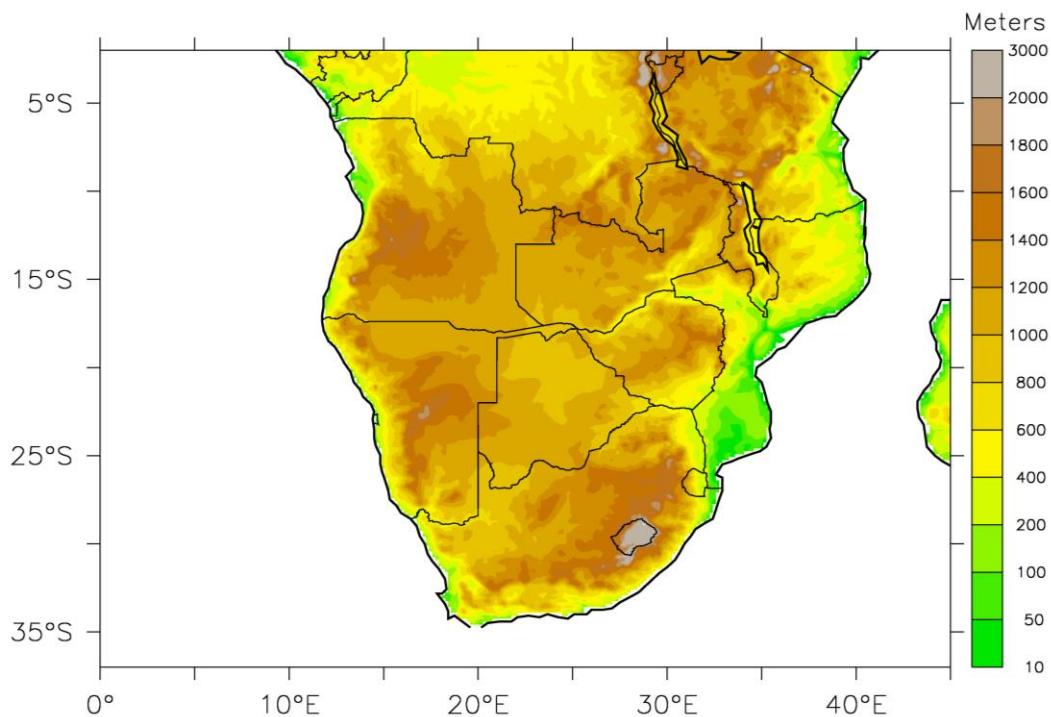
Figure 1: The study domain showing the topography of southern Africa

2.2.2 Characterising droughts using the SPEI

We employed the SPEI developed by Vicente-Serrano et al. (2010a; 2010b) to characterise droughts over southern Africa. The SPEI is similar to the SPI (McKee et al. 1993), which is one of the most common drought indices currently in use worldwide. However, while the SPI requires only monthly rainfall totals for computation, the SPEI requires potential evapotranspiration in addition to rainfall. The inclusion of potential evapotranspiration in the SPEI computation is believed to take the global warming effect into account, which yields better results in terms of drought identification.

The SPEI been being used to study drought over different regions around the world (e.g. Abiodun et al. 2013; McEvoy et al. 2012; Tao et al. 2014), including our study area (e.g. Araujo and Abiodun 2014). The index is usually obtained by fitting a log-logistic (Gamma or Pearson III) distribution to climatic water balance (*D*), which is the relationship between precipitation and PET. The value of SPEI typically ranges from −3 to 3 in depicting the intensity of dryness (drought; negative values) to wetness (positive values). For more details on how to calculate SPEI, readers are referred to Vicente-Serrano et al. (2010). For our study, the SPEI library (Beguería and Vicente-Serrano 2013) in the R software was used to compute the SPEI over each grid point in southern Africa at three- and 12-month scales using the Thornthwaite (1948) method, which uses monthly mean temperature for calculating PET. A more physically based method to calculate the PET (such as the Penman–Monteith) may be preferable, but the Penman–Monteith equation requires more data (e.g., wind speed and solar radiation) for its computation; unfortunately, these data sets are not available over our study area.

2.2.3 Identification of REDs

To identify the REDs, we used two approaches to analyse the spatial coherence of the southern African droughts. The approaches are the Principal Component Analysis (PCA) and Self-Organising Maps (SOMs). Using two approaches helped us establish the robustness of the RED characteristics. However, for clarity sake, the REDs identified using PCA will be called drought modes while those obtained with SOMs technique will be designated as drought patterns.

The PCA, which reduces the dimensionality of a data set and uncovers hidden structures in the data set, has been used in many studies to extract useful information from huge or confusing data sets (i.e. Giannini et al. 2008; Manatsa et al. 2012; Richard et al. 2001). PCA first computes the co-variance matrix of a standardised normalised variable (e.g. SPEI) and then computes the eigenvectors and eigenvalues of the co-variance matrix. The eigenvectors are therefore ordered according to the magnitudes of their associated eigenvalues. The first principal factor is the eigenvector that has the highest magnitude, and hence, represents the mode with the highest variance in the data set. Since PCA is a non-parametric method, it can be used on data with any distribution. In our study, we used PCA with the varimax rotated option to identify the spatial coherence (modes) in temporal variability of the SPEI. Previous studies (Jolliffe 1995; Jolliffe et al. 2003; Richman 1986) have been shown that rotated PCA increases physical relevance and interpretation of PCA. The rotated PCA was applied separately on the SPEI data, and the first four principal factors of the PCA (hereafter, PF1, PF2, PF3 and PF4) were retained and discussed as the most significant drought modes (hereafter, DM1, DM2, DM3 and DM4, respectively).

The SOM algorithm, a class of unsupervised neural networks, objectively clusters objects according to their similarity and, therefore, reduces the dimensionality of a given data set (Agarwal and Skupin 2008; Oettli et al. 2014). It is similar to the k-means clustering method (Everitt et al. 2011), but unlike in the k-means, the SOM algorithm creates an order between the units. For instance, Node 2 in a 3 × 4 SOM array is close to Node 1 and Node 3, showing a clear transition between them; but the same notion is not valid in the k-means clustering where the relationship between different clusters is not indicated (Agarwal and Skupin 2008; Wehrens 2011). Using the SPEI values as the input data, the SOM analysis was performed with the SOM_PAK 3.2 software (Kohonen et al. 1995). The SOM_PAK software was freely obtained from the Helsinki University of Technology (http://www.cis.hut.fi/research/som_pak/). Although the choice of the number of SOM nodes is subjective (Brown et al. 2010; Cavos 1999), we

reasoned that 12 SOM archetypes (3 × 4) were adequate to describe the main drought patterns in southern Africa and, moreover, the same array was previously used for the same area of study by Tadross et al. (2005), Mackellar et al. (2010) and Maure (2013).

2.2.4   Wavelet analysis

We applied wavelet analysis to study the temporal characteristic of the drought modes. The wavelet analysis and spectral analysis are two widely used methods for studying the time series of climate variable in frequency domain (Farge 1992; Labat 2005). Here, we used wavelet analysis instead of spectral analysis because wavelet analysis has various advantages over the spectral analysis in preserving local, non-periodic, multiscaled features. For instance, wavelet analysis can be used to study variability at different scales and does not need a stationary series (Ideião and Santos 2005). It has been used to uncover periodic cycles in rainfall data (Jury and Enfield 2002; Jury and Mwafulirwa 2002), to compare different drought indices (Ntale and Gan 2003), to study interannual variability of sea surface temperatures (i.e. Rao et al. 2002), to examine the link between the variances of ENSO and monsoon (Torrence and Webster 1999), and to investigate the influence of ENSO and the Indian Ocean Dipole (IOD) on summer rainfall in Zimbabwe (Manatsa and Matarira 2009). In the present study, we used the wavelet analysis to uncover periodic cycles in the principal factor scores (i.e. time series) and used the wavelet coherence to study the link between each score and climate indices.

2.3   Characteristics of Drought Modes Over Southern Africa

2.3.1   The spatial characteristics

The PCA results for the three- and 24-month SPEI, respectively, are presented in Figure 2 and Figure 3. The loadings of the first four principal factors (i.e. PF1, PF2, PF3 and PF4) are presented to show the most dominant drought modes (i.e. DM1, DM2, DM3, and DM4). The principal factors jointly explain 46% and 50% of the total variance in the three- and 12-month SPEI, respectively. However, the drought modes have different spatial-temporal structures.

DM1, which explains 13.9% in the three-month SPEI and 19.1% in the 12-month SPEI, shows its core (highest positive loading: 0.8) over south-west southern Africa (i.e. over the border of South Africa, Botswana and Namibia) (Figure 2). This is the driest area in southern Africa with an annual rainfall of less than 400 mm (Richard and Poccard 1998). Various studies have reported drought occurrence over this area (Nash and Endfield 2002; Nicholson et al. 2001; Thomson et al. 2003; Usman and Reason 2004). The correlation between DM1 (i.e. PF1 score) and the SPEI series over the area is high (r > 0.9).

DM2 explains 12.2% and 9.5% variance in three- and 24-month SPEIs, respectively, and shows its core (highest positive loading: 0.8) over Zimbabwe but negative loadings (about −0.8) over the Western Cape. The correlation coefficient between DM2 and SPEI series over Zimbabwe is high (r > 0.8).

DM3 explains about 11% variance in three- and 12-month SPEIs and shows its core (highest positive loadings: 0.8) over Tanzania but negative loadings (about −0.3) over the south-eastern part of southern Africa. The correlation between the DM3 and SPEI series over Tanzania is high (r = 0.88).

DM4 explains about 9% and 10% variance in three- and 12-month SPEIs, respectively, and shows positive loadings (about 0.7) over Angola but negative loadings (about −0.3) over the south-eastern part of southern Africa. There is a strong correlation (r > 0.8) between the DM4 score and the SPEI over Angola.

Since the principal factors are orthogonal, the temporal characteristics of the four drought modes differ, meaning that each drought mode is unique. This suggests that the drought modes may be driven by different sets of atmospheric processes. These processes are discussed in Chapter 3.
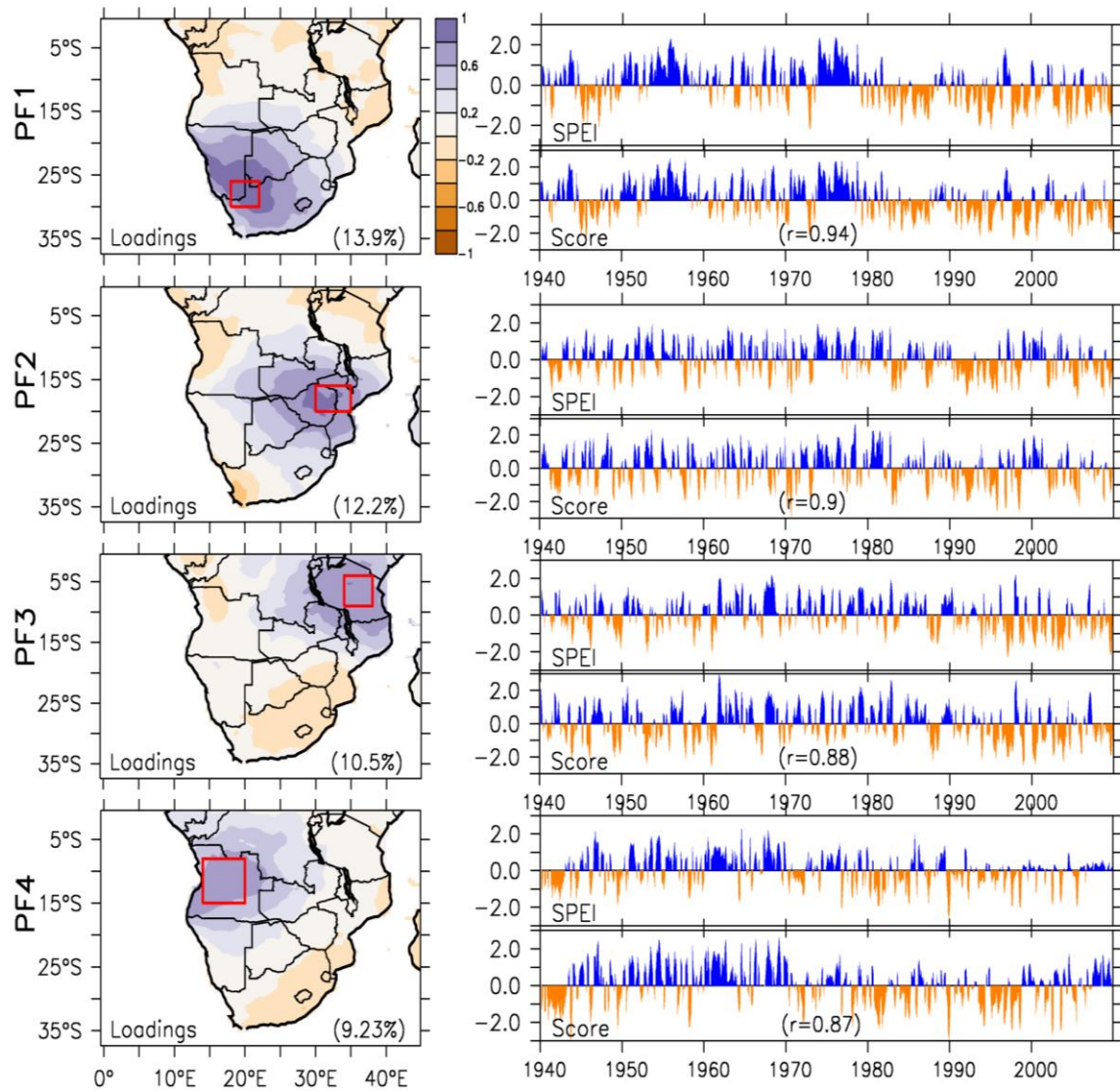
Figure 2: The spatial-temporal variability of SPEI (at three-month scale) over southern Africa. The left panels show the rotated PCA loadings for the SPEI (i.e. the spatial structure of the drought modes); the percentage of variance explained by each principal factor is indicated. The right panels show the corresponding principal factor score (i.e. the temporal structure of the drought mode) and the regional SPEI series averaged over the red box (principal factor region) in the left panel; the correlation (r) between the principal factor score and the SPEI series are indicated
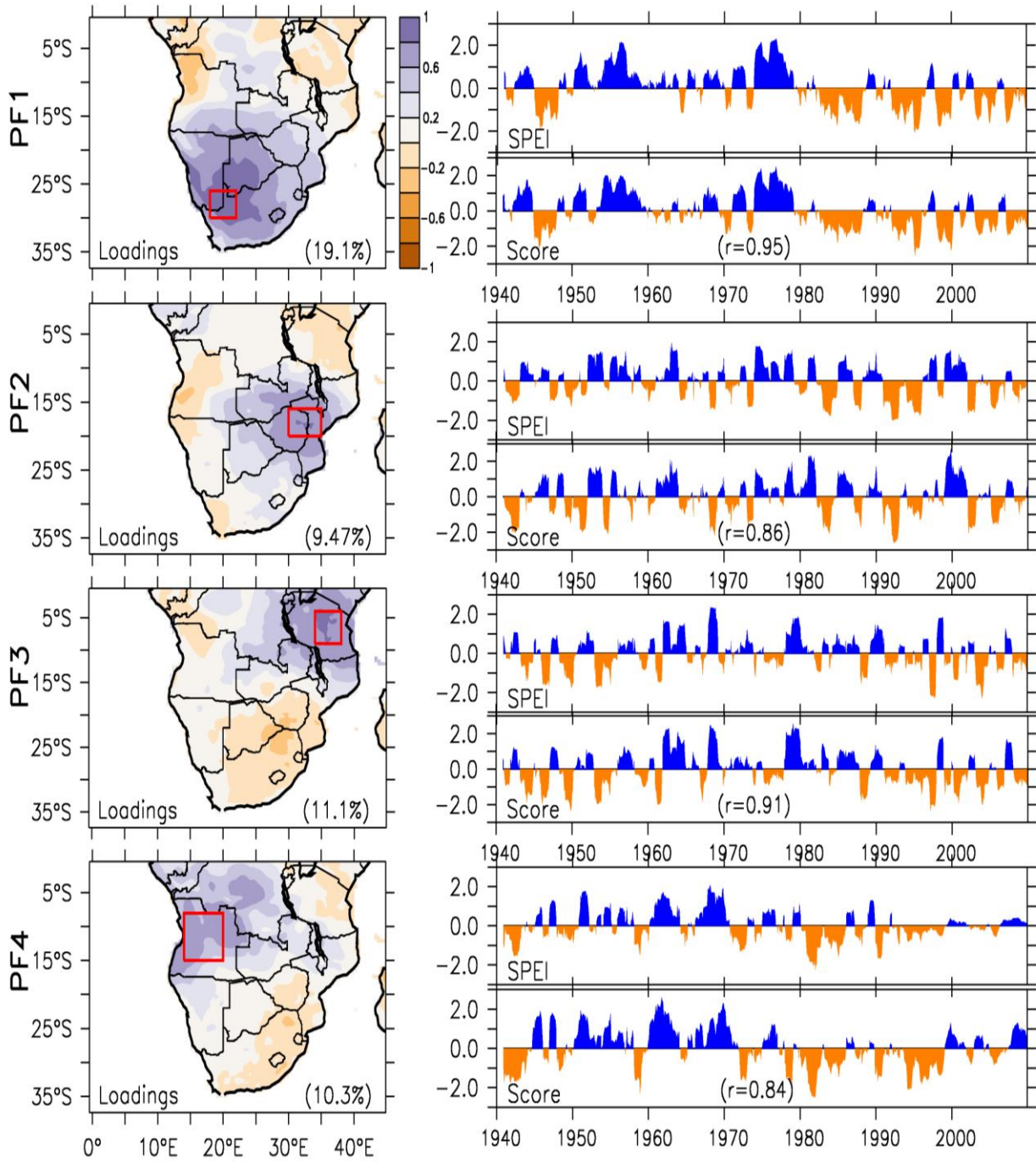
Figure 3: The spatial-temporal variability of SPEI (at 12-month scale) over southern Africa. The left panels show the rotated PCA loadings for the SPEI (i.e. the spatial structure of the drought modes); the percentage of variance explained by each principal factor is indicated. The right panels show the corresponding principal factor score (i.e. the temporal structure of the drought mode) and the regional SPEI series averaged over the red box (principal factor region) in the left panel; the correlation (r) between the principal factor score and the SPEI series are indicated

To test the robustness of drought modes, we compare the SPEI drought modes with the PDSI drought modes in Figure 4. The figure shows a good agreement between drought modes obtained with the two drought indices (SPEI and PDSI). For example, the percentage of total variance of the four principal factors is almost the same in both cases and the structures of the drought modes are similar. The major difference is in DM4. While the peak of DM4 is located over Angola in the SPEI results, it is located over the Democratic Republic of Congo (DRC) in the PDSI results (Figure 4).
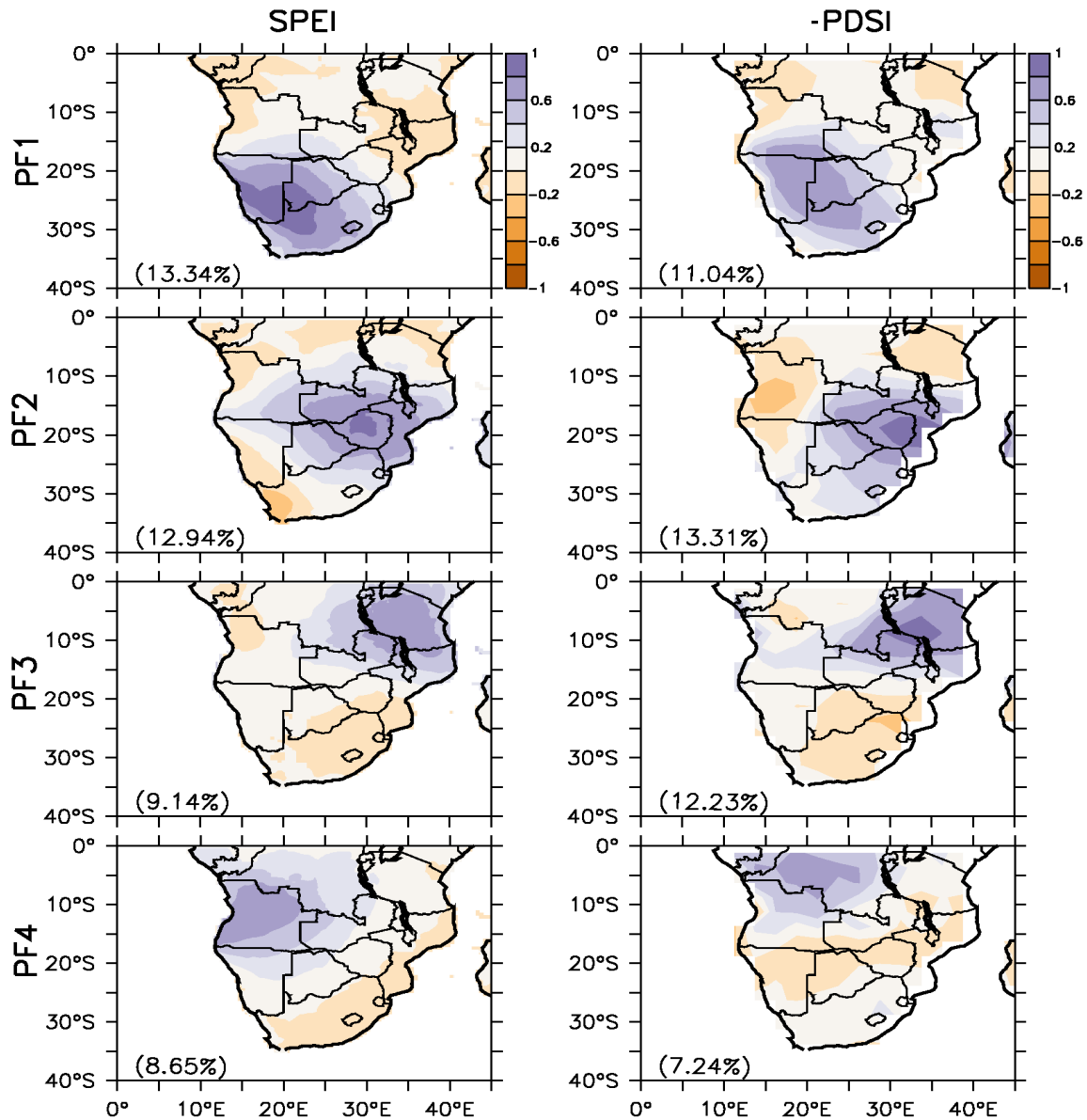
Figure 4: A comparison between the drought modes (i.e. principal factors) obtained using SPEI (left panels) and PDSI (right panels) at a one-month scale

2.3.2 Temporal variability and structure of the drought modes

Each drought mode features decades of continuous dry and wet conditions (Figure 3). DM1 features wet conditions in most of the first three decades (1940–1979) of the study period and dry conditions in most of the last three decades (1980–2009). However, the peaks of the dry conditions (droughts) are in the 1940s, 1980s, 1990s and 2000s.

Unlike DM1, DM2 frequently and uniformly alternates the wet and dry conditions over the study period (1940–2009). Hence, DM2 features short drought episodes in each decade.

With DM3, the main droughts (centred over Tanzania) occurred in the decades of the 1940s, 1950s, 1960s, 1990s and 2000s. The wet and dry conditions over Tanzania are evenly distributed within the study period, but the droughts showed the highest intensities and longest durations in the first and last two decades (i.e. 1940–1960 and 1980–2000).

Finally, with DM4 (centred over Angola), the main droughts occurred in the decades of the 1940s, 1970s and 1980s, with a near normal condition in the period from 2000 to 2009.

Figure 5 presents the decadal drought frequency of the drought modes (i.e. the number of months per decade in which the core area of the drought mode experienced at least a moderate drought; SPEI < −1.0). The decadal drought frequency generally decreases from the 1950s to the 1970s and increases from the 1970s through the 2000s. However, there are some notable differences among the drought modes on the drought frequencies. For instance, with the three-month scale (Figure 5a), the drought modes featured their minimum drought frequency in different decades. While the minimum drought frequency of DM1 occurred in the 1950s, that of DM2 and DM3 occurred in 1960s and 1970s, respectively. The decade for the maximum drought frequency also differs. DM1 featured the maximum drought frequency in the 1990s, but DM3 and DM4 featured it in the 1980s and 2000s, respectively. The differences among the drought modes are more pronounced at 12-month scale than at three-month scale. Nevertheless, the general increase in decadal drought frequency since 1970 (at both three-month and 12-month scale) is consistent with the Intergovernmental Panel on Climate Change (IPCC) (2007) report, which attributed the increase to global warming.
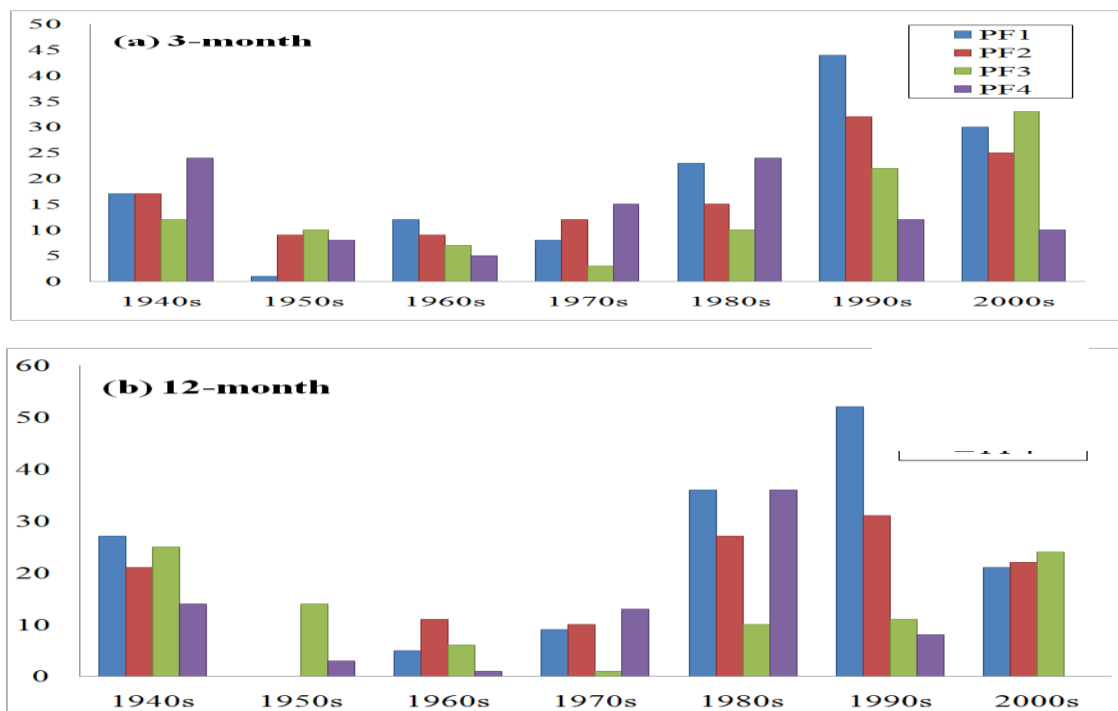
Figure 5: Decadal variation of the three- and 12-month drought frequency over the drought modes core area (indicated with red boxes in Figure 2 and Figure 3, respectively)

Figure 6 presents the wavelet power spectra (WPS) and the global wavelet spectrum (GWS) of the principal factors scores (for three-month SPEI) to reveal temporal cycles in the temporal variability of the drought modes. The scores are characterised by different cycles with different power. In general, the most significant power is in the two- to eight-year cycles. There is also significant power in the less than one-year cycles; but, since these cycles represent the subseasonal to seasonal scale variations, they will not receive our attention in this study.

In DM1 (Figure 6a), the GWS shows the highest variance for the 16-year cycle. This cycle continuously features high power (> 0.5 GWS) from 1940 to 1990 but has small power (< 0.5 GWS) after 1990,

suggesting that the cycle may play a weak role in the post-1990 DM1 droughts (Figure 4a). On the other hand, the two- to eight-year and 35-year cycles show significant power during the post-1990 droughts. The 35-year cycle shows significant power since 1975, while the two- to eight-year cycles show significant power in the 1940s, 1970s, 1990s and 2000s. Although, in GWS, these cycles have lower power than the 16-year cycle period, they may contribute significantly to the intensification of DM1 droughts after 1990.

The GWS and WPS of DM2 show similar structures to that of DM1, but with some notable differences (Figure 6b), especially in the structure two- to eight-year cycles. For instance, the DM2 GWS shows a local peak for the two- to eight-year cycles, and the DM2 WPS two- to eight-year cycles show significant power in the 1950s and 1980s, instead of the 1940s and 1970s in DM1 WPS. Nevertheless, the post-1990 structure of the two- to eight-year cycles is the same in DM1 and DM2.

The GWS and WPS of DM3 differ from those of DM1 and DM2. First, the GPS shows two peaks: a higher peak for the 32-year cycle and a lower peak for the two- to eight-year cycle. The two- to eight-year cycle shows its most significant powers (> 2 GWS) before 1970 and its least power (< 0.5 GWS) after 1990.

The GWS of DM4 shows a peak for the eight-year cycle, which exhibits continuous power anomalies between 1940 and 1990, and significant power for the two- to four-year cycles in 1940s and 1980s.
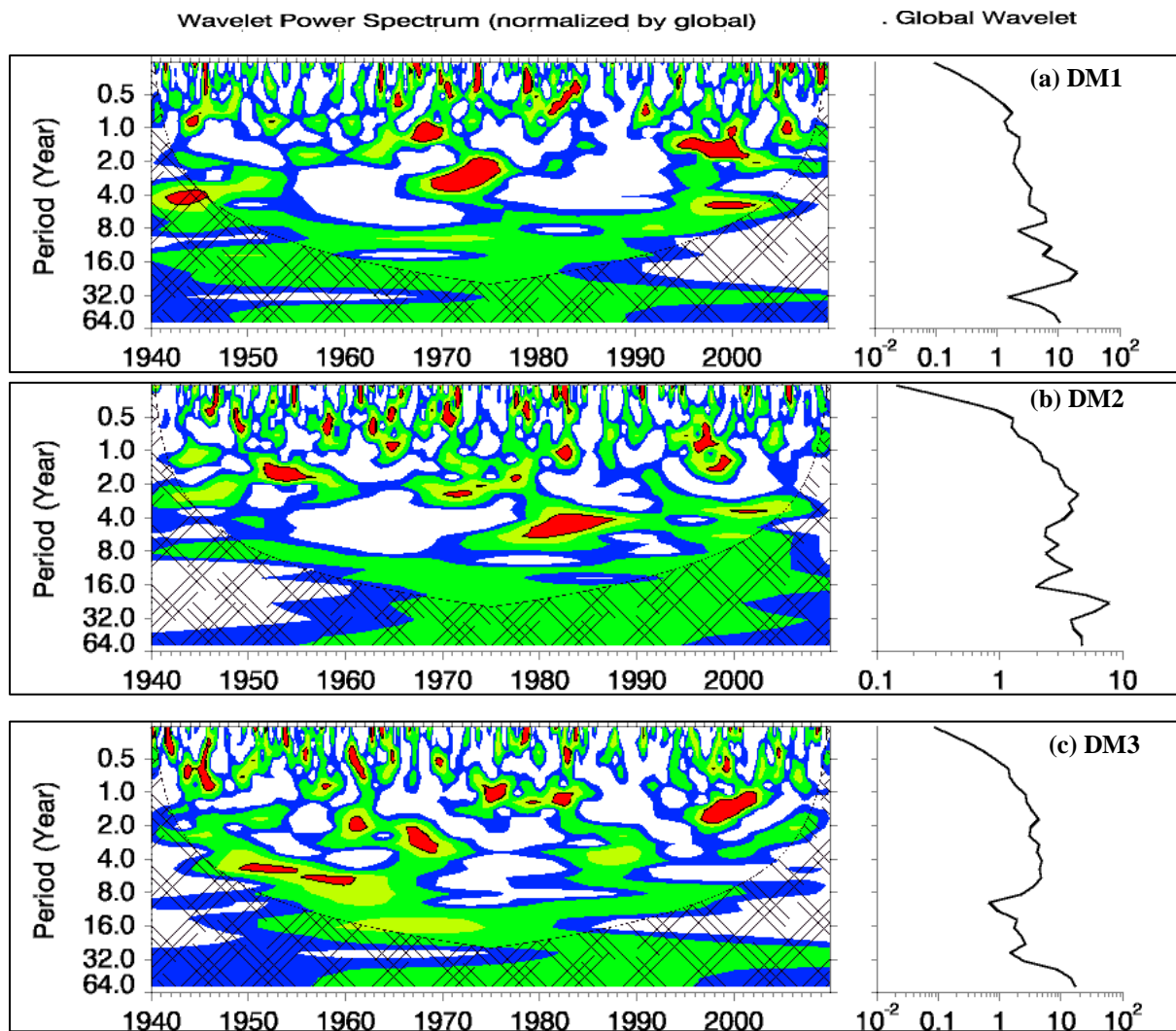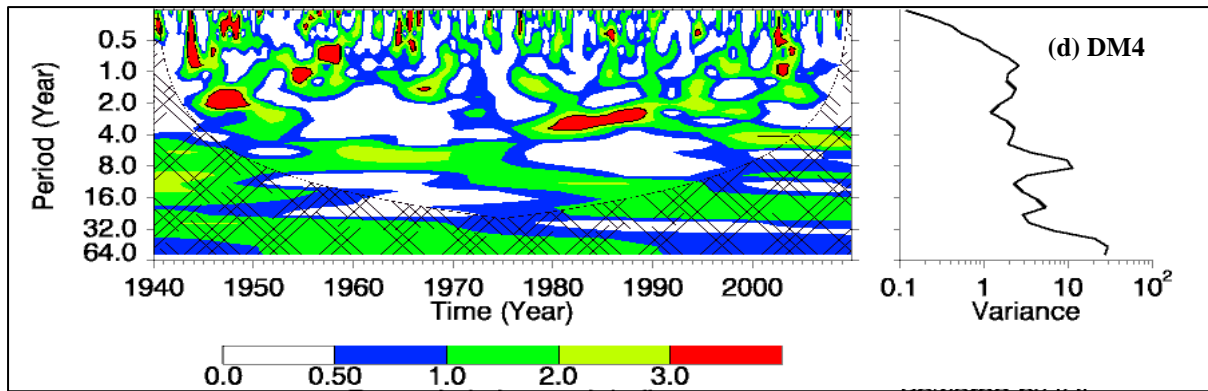
Figure 6: WPS (using the Morlet wavelet) of (a) DM1, (b) DM2, (c) DM3 and (d) DM4. Cross-hatched with line indicate the cone-of-influence. The thick black line contour is the 5% significant level

2.4   Characteristics of Drought Patterns Over Southern Africa

2.4.1   Spatial distribution

Figure 7 presents the SOM classification (3 × 4 nodes array) of SPEI over southern Africa to depict the major drought patterns over the subcontinent. As expected of any SOM result, the nodes at the four edges of the array (i.e. Nodes 1, 4, 9 and 12) show the most extreme patterns, while other nodes feature patterns that provide a continuous transition among the four extreme patterns. Node 1 shows a widespread dry condition (negative SPEI) over the entire southern Africa, except along the tropical eastern coast (north-eastern Mozambique and eastern Tanzania) and south-western tip of South Africa. However, the core of the dry conditions (SPEI < −1.0) is over the Caprivi Strip (northern Botswana, north-eastern Namibia, south-eastern Angola and south-western Zimbabwe).

In contrast to Node 1, Node 12 shows a wet condition (positive SPEI) over the entire southern Africa, and the core of the wet condition (SPEI > 1.0) is located over northern Botswana. Node 9 shows a dipole pattern, with dry conditions located north of 20°S and the wet condition located south of 20°S. The core of the dry condition extends from northern Mozambique to southern DRC, while the core of the wet condition is over the Drakensberg mountain ranges (in Lesotho).

Node 4 is a mirror image of Node 9, except that the core of the wet condition extends from Mozambique to Tanzania while the core of the dry condition is over the northern part of South Africa. The most frequent drought patterns are Node 3 and Node 12, each accounting for about 11% of the data set. The driest drought pattern is Node 1 (i.e. the mean SPEI = −0.53) while the wettest drought pattern is Node 12 (i.e. mean SPEI = +0.53).

In general, the drought patterns may also be broadly classified into three conditions: the all-dry patterns (Nodes 1, 2, 5, and 6), the all-wet patterns (Nodes 7, 8, 11 and 12) and the dipole patterns (Nodes 3, 4, 9 and 10). To check the robustness of the RED patterns, we repeated the SOM analysis separately for each season, i.e., December-January-February (DJF), March-April-May (MAM), June-July-August (JJA) and September-October-November (SON). The classification of the drought patterns for each season (not shown) roughly remains the same as in Figure 7, especially the nodes at the four edges of the array (i.e. Nodes 1, 4, 9 and 12).

We found a good agreement between the SOM drought patterns (Figure 7) and the PCA drought modes (Figure 2). All four drought modes (DM1, DM2, DM3 and DM4) in Figure 1 appear in the 12 drought patterns shown in Figure 6. For instance, the DM1 roughly corresponds to Node 2 and Node 11, the DM2 to Node 5 and Node 8, the DM3 to Node 4 and Node 9, and the DM4 to Node 6 and Node 7. Nevertheless, some of the drought patterns are missing in the drought modes. For instance, the patterns of Node 1 and Node 12, which depict dry and wet conditions (respectively) over the entire southern Africa, are not in the drought modes. In addition, Node 7 that features a wet/neutral condition is also missing in the drought modes. This may be because the PCA classification only accounts for 50% of

the SPEI variations over southern Africa. Hence, the drought patterns classification may provide more robust and more extensive characteristics of the REDs than what the drought modes provide.
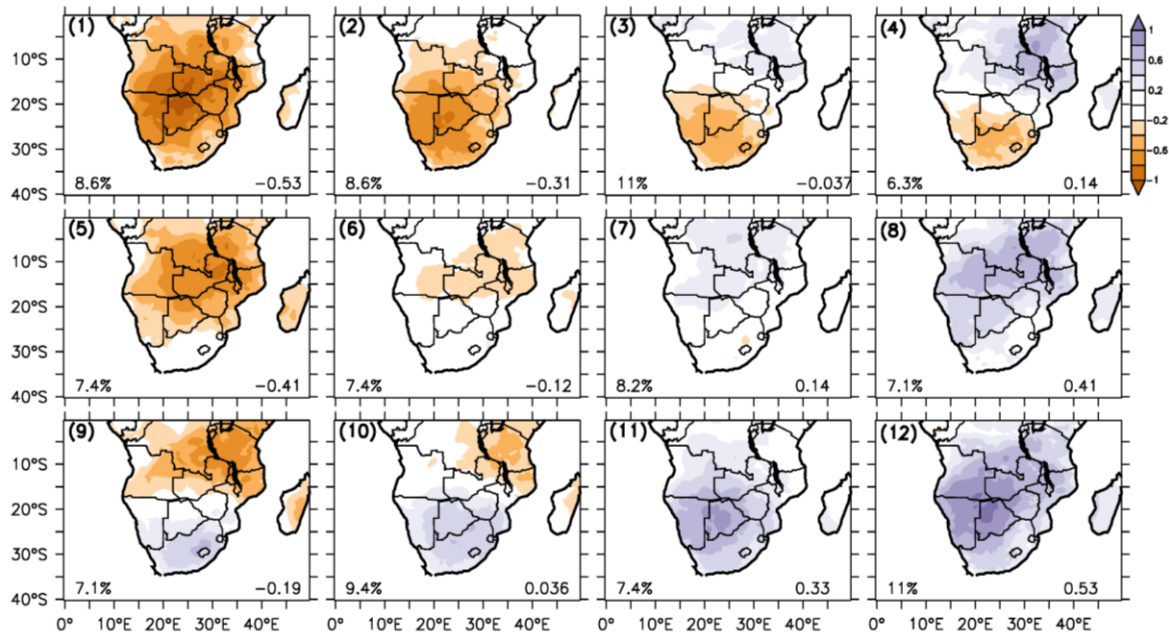
Figure 7: The SOM array (3 × 4 nodes) of the seasonal SPEI (three-month scale). Each node represents a drought pattern over southern Africa in 1950–2013. Negative SPEI corresponds to a dry condition while positive values correspond to a wet condition. In each panel, the node tag is on the upper left corner of the panel, the frequency of occurrence (%) of the node is on the lower left corner, and the mean SPEI (over southern Africa) is on the lower right corner

2.4.2   Temporal variations of the SOM drought patterns

Figure 8 shows the seasonal variation of the drought patterns (presented in Figure 7) and reveals that the drought patterns (except Node 5) can feature in any season. However, each drought pattern has preference for a season. Node 1 has preference for austral autumn (MAM; eight events), while Node 12 has preference for austral winter (JJA; 12 events). Node 10 has its highest frequency in austral spring (SON; ten events), while Node 4 and Node 9 mostly occur in summer (DJF; six and eight events, respectively). Conversely, Node 5 does not occur in summer (DJF), Node 6 rarely occurs in autumn MAM (one event), while Node 10 and Node 11 hardly feature in austral winter (JJA; one event each).

The decadal frequency of the drought patterns (Figure 9) suggests a general shift in drought patterns: from all-wet patterns (in the earlier three decades, i.e. 1950–1970) to all-dry patterns (in the last three decades, 1990–2010). For instance, there has been a positive trend (increase) in the decadal frequency of Nodes 2, 5 and 6 since 1960, but a negative trend (decrease) in the decadal frequency of Nodes 2, 8 and 12. While Nodes 2 and 6 have been the most dominant drought pattern since 1990, Nodes 8 and 12 have not occurred since 1990. However, there is no trend in the decadal frequency of the dipole patterns. Figure 9 also show that the drought patterns have their maximum decadal frequency in different periods. For example, Nodes 1 and 9 feature their maximum decadal frequency in 1990 (nine and six events, respectively), Node 11 in 1950 (nine events), and Node 3 in 1980 (nine events).
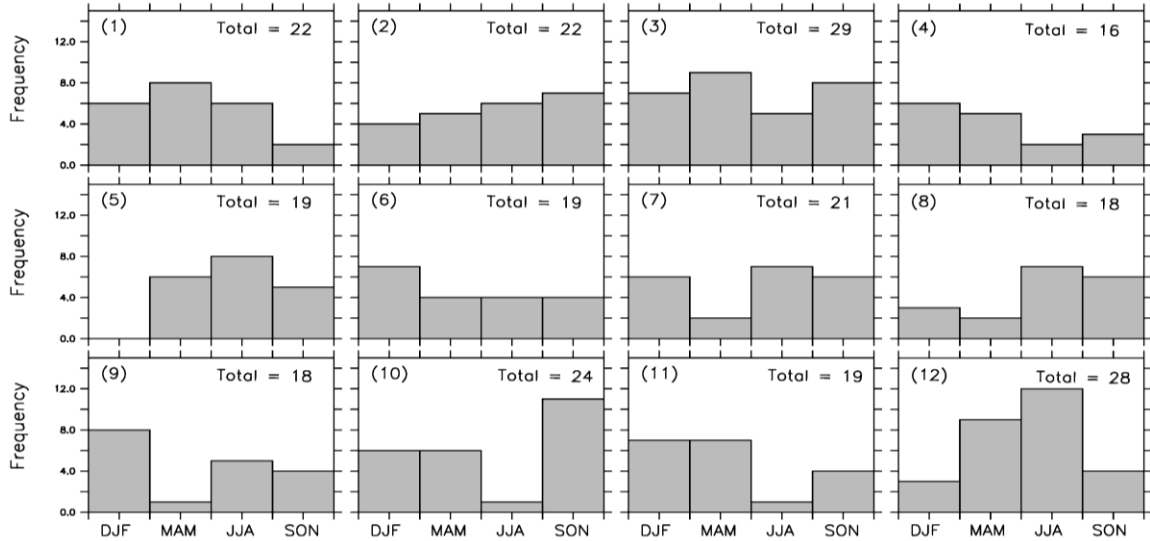
Figure 8: The seasonal variation of the drought patterns (shown in Figure 7). The total number of events for each drought pattern is indicated in the panel
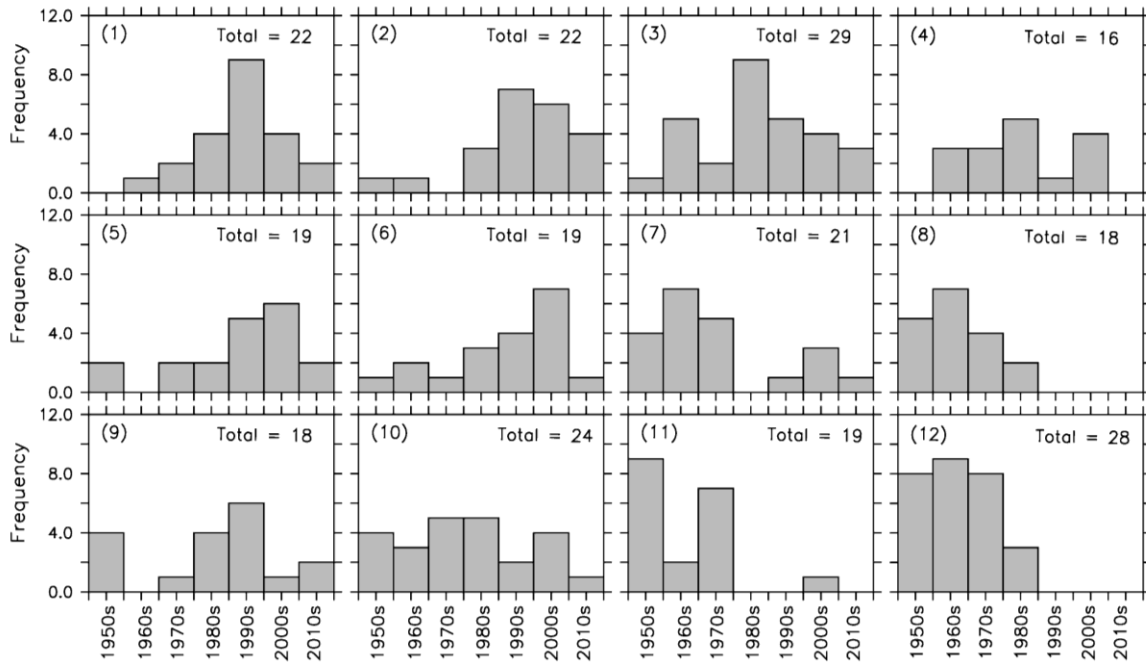
Figure 9: The decadal variation of the drought patterns (shown in Figure 7). The total number of events for each drought pattern is indicated in the panel

2.4.3 Sensitivity to data sets

To investigate the sensitivity of decadal variability results to data sets, we repeated the SOM analysis using another observation data set obtained from the UDEL (Legates and Willmott, 1990). The results for the UDEL data set (shown in Figure 10) are generally the same as for the CRU data set. For instance, the spatial distribution of the extreme drought patterns is the same as for the CRU data set (except for the different arrangement of the patterns), and the percentage frequency of the patterns is comparable with the corresponding patterns of the CRU data set. More importantly, the UDEL data set agrees with CRU data on the shift in southern African drought patterns, from all-wet patterns (in the earlier three decades, i.e. 1950–1970) to all-dry patterns (in the last three decades, 1990–2010). For instance, UDEL data shows that while Node 12 has been dominant since 1990, Node 1 has not featured

14

since 1990. The few differences seen between UDEL and CRU results might be due to the difference in time coverage as UDEL data covers 1950–2010 and CRU data covers 1950–2013.

2.4.4   Sensitivity to drought indices

To examine the influence of evaporation on drought patterns, we repeated the SOM analysis using SPI data (which uses only rainfall to monitor droughts). The SPI was computed according to Mckee et al. (1993) using the CRU rainfall data. The results (Figure 11) show that the drought patterns from SPI are similar those from SPEI (compare Figure 6 and Figure 11). For example, in agreement with SPEI, the SPI indicate that the drought patterns may also be broadly classified into three groups: the all-dry patterns (Nodes 3, 4 and 7), the all-wet patterns (Nodes 6, 9, and 10) and the dipole patterns (Nodes 1, 2, 3, 5, 8, 11 and 12).

In addition, the percentage contribution of each SPI drought pattern in Figure 11 is comparable to its corresponding SPEI drought pattern in Figure 7. However, the decadal variability of the SPI drought patterns differs from that of SPEI, at least in three ways. First, the SPI does not reproduce the general shift in the southern African drought patterns from all-wet patterns to all-dry patterns. Second, in contrast to the SPEI, SPI shows that the all-wet patterns (Node 9 and 10; Figure 11) have occurred more than ten times in the last decades. Third, SPI has not featured the driest drought pattern (Node 4; Figure 11) since 2000, whereas, SPEI has feature it seven times. The comparison of SPEI and SPI results suggests that the general shift in the southern African drought pattern may be due to influence of evapo-transpiration on the drought identification; the shift is consistent with the impact of global warming on the southern African climate (i.e. Tadross et al. 2005). Hence, the comparison further provides compelling evidence that inclusion of temperature in drought monitoring (i.e. in drought index) may give a better understanding of the characteristics and dynamics of southern African droughts.
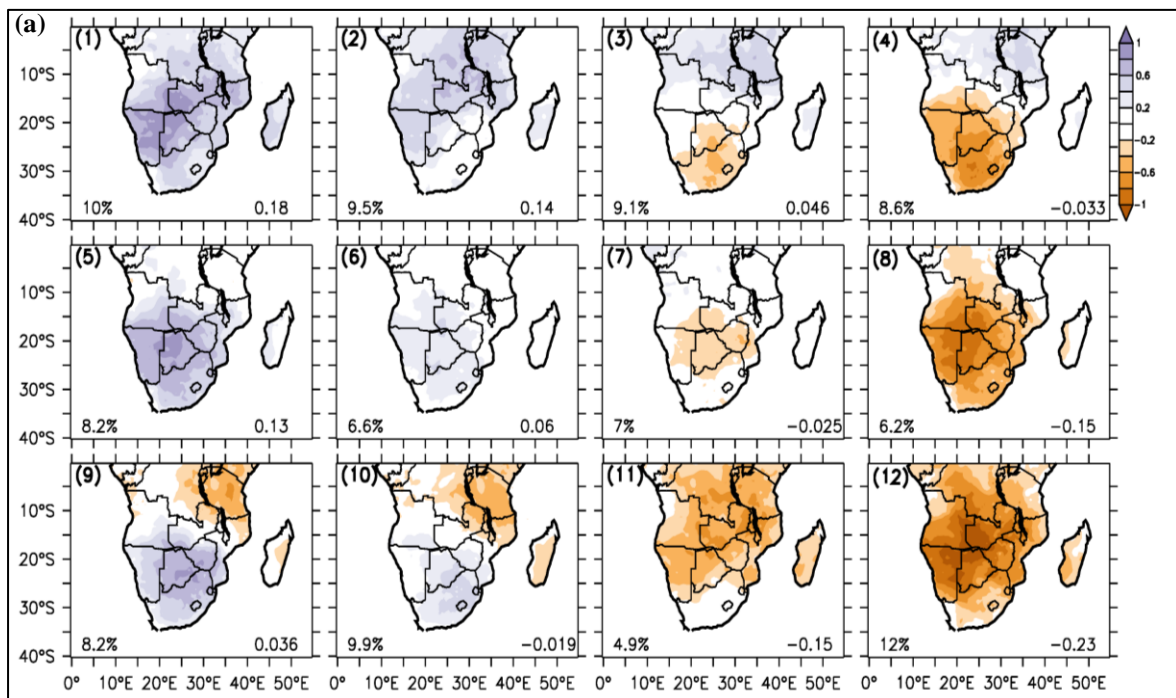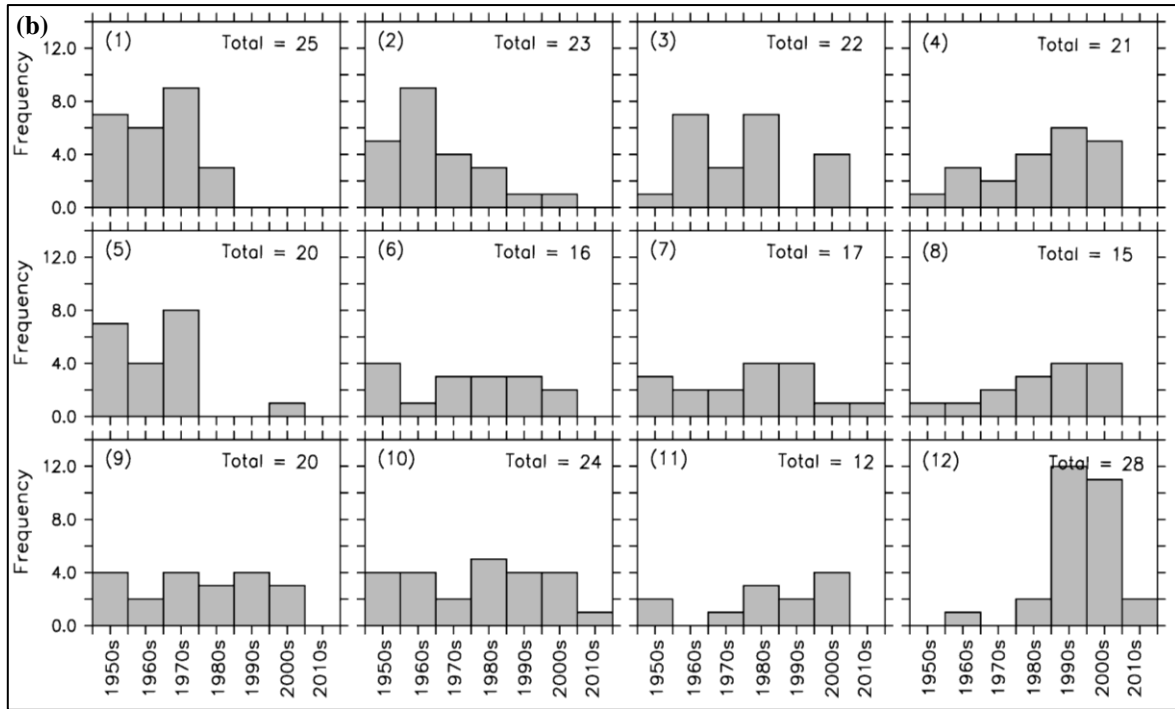
Figure 10: (a) The SOM classification of drought patterns obtained with the UDEL data set (upper panel); and (b) the corresponding decadal frequency of the drought patterns. The labels are as in Figure 7 and Figure 9, respectively
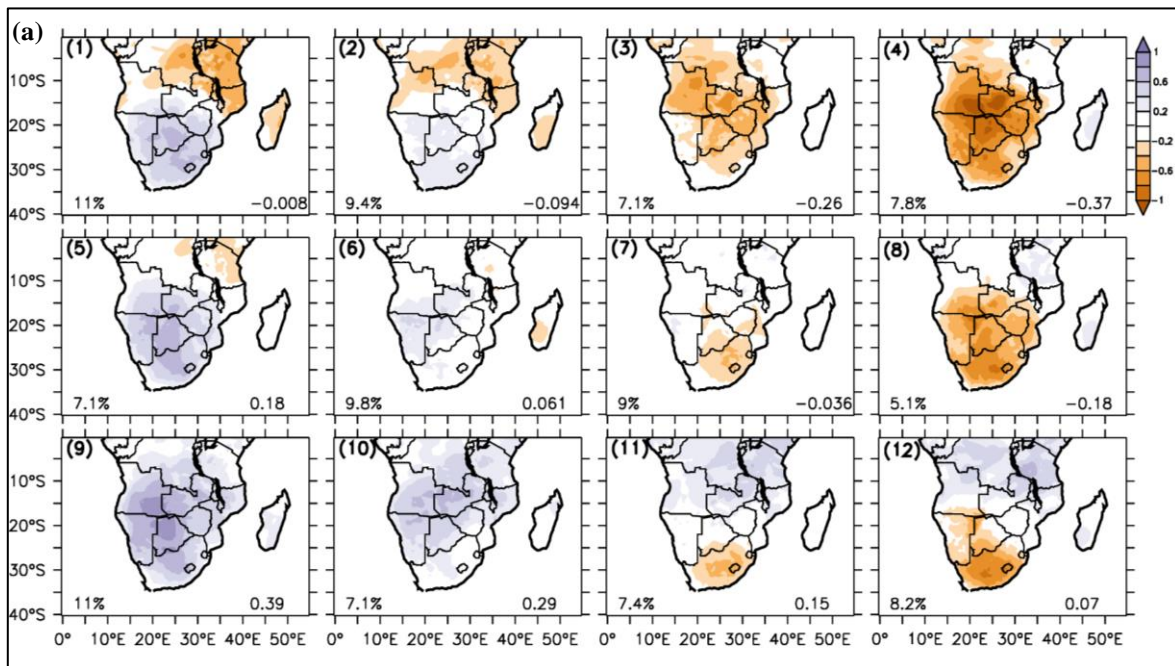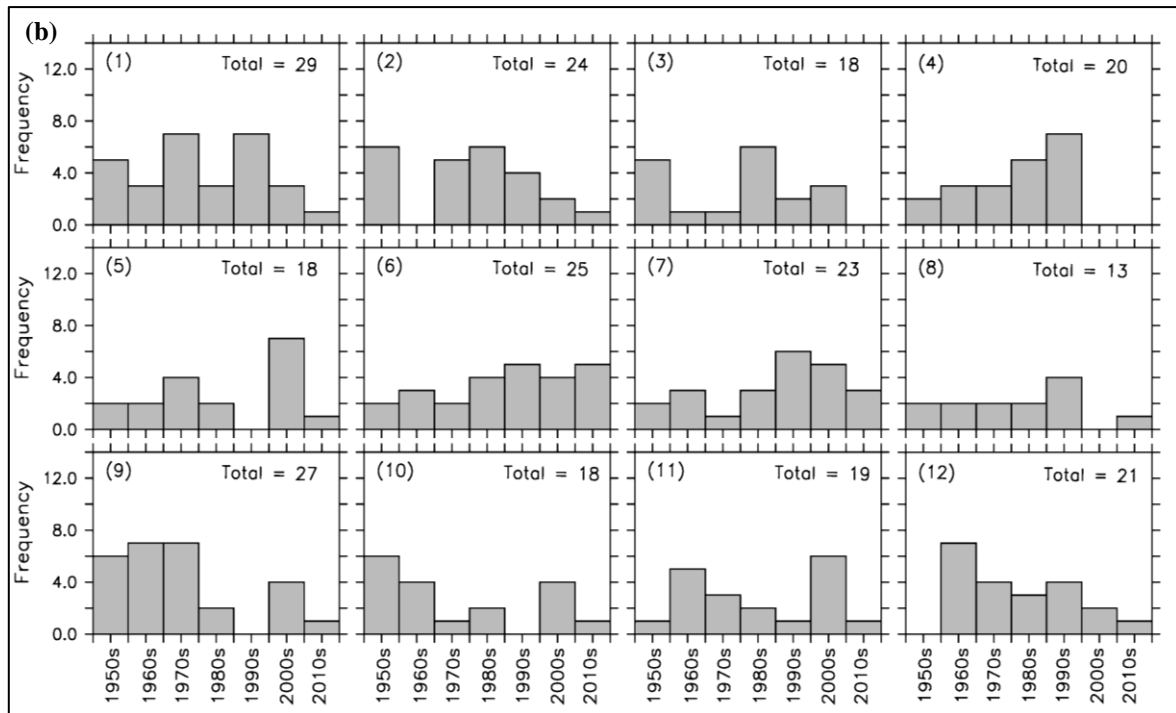
Figure 11: (a) The SOM classification of drought patterns obtained with SPI; and (b) the corresponding decadal frequency of the drought patterns. The labels are as in Figures (1) and (3), respectively

2.4.5   Persistence and transition of the drought patterns

Figure 12 shows that the general shift in the drought patterns (i.e. from all-wet to all-dry patterns) features in all seasons, although it is most remarkable in austral winter (JJA) and least notable in austral summer (DJF). No season has featured an all-wet pattern (e.g. Node 12) in the last three years (2011–2013), meaning that each season has experienced either a persistently dry condition or a dipole condition, or a transition between the two conditions during this period. This suggests that the subcontinent has been experiencing a nett drying condition over the period.

At the interseasonal scale (Figure 12a and Figure 12b), although no drought pattern has persisted for a whole year, some drought patterns have persisted for more than a season (Figure 12a). In this regard, Nodes 7 and 4 have the longest length of persistency. They persisted for three seasons (DJF, MAM and JJA) in 1966 and 1986, respectively. However, Node 12 has the highest number of persistency; it persisted eight times (i.e. about 30% of its total occurrences). On the other hand, Node 10 has the smallest number of persistency (only once), making it is the most transient drought pattern. However, each drought pattern has particular drought patterns it can transit to and those it may not transit to (Figure 12b). The most common transition is from Node 10 to Node 11, and from Node 11 to Node 12. Each of these transitions occurred seven times in the past. Hence, there is a 30% possibility that Node 10 will always transit to Node 11, and about a 40% probability that Node 11 will always transit to Node 12. However, Node 10 has never transited to Node 4 or to Node 8, while Node 11 has never transited to Nodes 1, 2, 4, 6 or 9. In addition, there is a possibility for a two-way transition between two extreme drought patterns. For instance, there is one case of Node 1 transiting to Node 12 and five cases of Node 12 transiting to Node 1.

At an interannual scale (Figure 12a and Figure 12c), Node 12 still has the highest number of persistency (six cases), but four nodes (Nodes 5, 8, 10, 11 and 12) have the longest period of persistency. Node 10 persisted for three austral spring periods (1953–1955), Nodes 12 and 5 persisted for three austral winter periods (1953–1955 and 2001–2003, respectively), while Node 11 lingered for three austral autumn periods (1953–1955).

17

Among the drought patterns, only Node 4 never featured any interannual persistency. However, the interannual transition among the drought patterns is less organised than that of the seasonal transition. The most common interannual transition is from Node 5 to Node 12; it has occurred six times in the past. The dynamics behind the transition and persistence of the drought pattern is not yet clear and is beyond the scope of present study, but a good understanding and application of the persistency and transitioning may help improve the seasonal and interannual forecasts of droughts over southern Africa.

2.5 Conclusion

In the chapter, we have discussed the spatiotemporal characteristics of southern African droughts. We used SPEI to characterise the droughts, rotated PCA to obtain the four dominant drought modes (or modes), and the SOM technique to classify the spatial distribution of the droughts into 12 major patterns. The results can be summarised as follows:

- The PCA results revealed that about 50% of SPEI variance over southern Africa can be represented with four main drought modes. The drought modes (DM1, DM2, DM3 and DM4) feature their maximum variance over the south-western part of southern Africa (i.e. the common border of South Africa, Botswana and Namibia), Zimbabwe, Tanzania, and Angola, respectively.

- The SOM analysis suggests that the drought patterns can be generally classified into three groups. The first group (all-dry patterns) shows a dry condition over the entire southern Africa, the second group (all-wet patterns) shows a wet condition over the whole region, and the third group (dipole patterns) shows both wet and dry conditions over the subcontinent.

- The SOM drought patterns may give a more robust characteristic of the RED than the PCA drought modes; all the PCA drought modes fall within the dipole patterns of the SOM classification.

- Although the drought patterns can occur in any season, some drought patterns have preference for seasons. While some droughts patterns persist from season to season, others easily transit to another pattern in the following season.

- The decadal variability of SPEI drought patterns suggests a general shift in the southern African drought, from an all-wet condition in 1950s–1970s to all-dry condition in 1990 possibly due to the global warming.

- There is a good agreement between the SPEI and SPI drought patterns, but the SPI drought patterns do not feature the general shift in the southern African drought, from all-wet condition all-dry, a general shift in the southern African drought, from all-wet condition in 1950s–1970s to all-dry, suggesting that SPI may underestimate the influence global warming on the droughts.
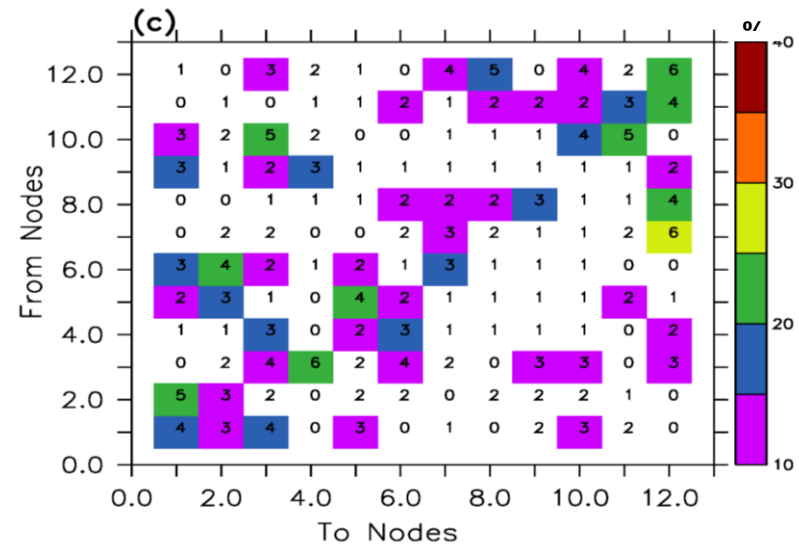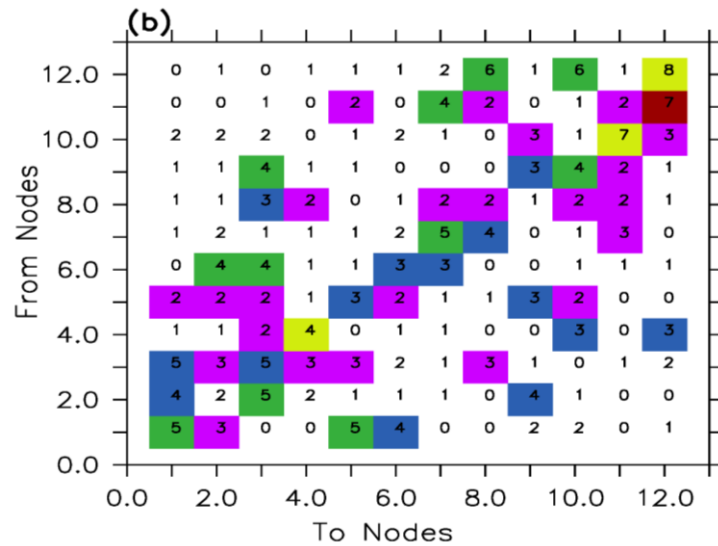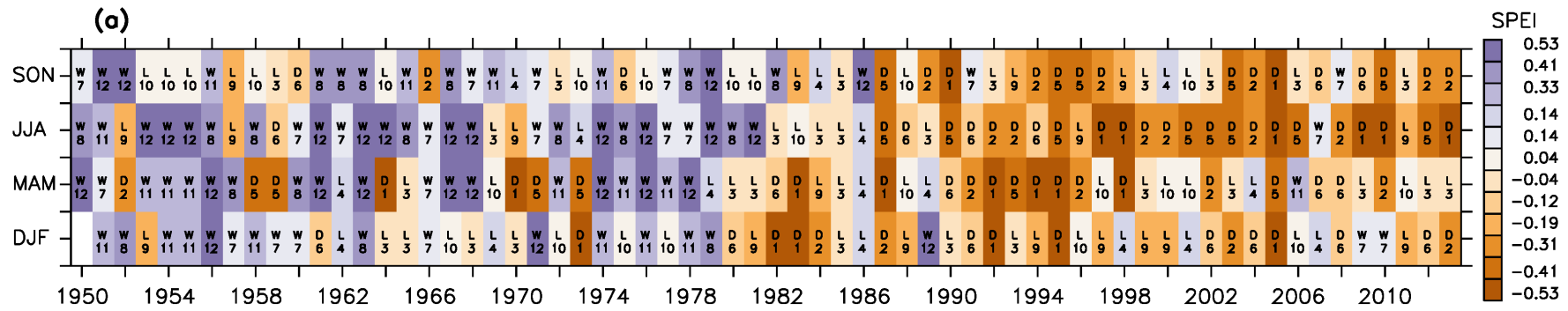
Figure 12: The persistence and transition of the SPEI drought patterns: (a) the seasonal and yearly occurrences of the drought patterns; (b) the interseasonal statistics; and (c) interannual statistics. In panel (a), the numbers (1–12) indicate the tags of the drought patterns; the letters (W, D and L) indicate the general description of the drought patterns (W = all-wet; D = all-dry; L = dipole); and the colours show the spatial mean SPEI for the drought patterns. In panel (b) and (c), the numbers indicate the number of time the drought patterns on y-axis transit to the drought patterns on the x-axis; and the colours indicate the percentage of the transition

3   PHYSICAL MECHANISMS CONTROLLING REDs

3.1   Introduction

The cause of variability in southern African droughts remains controversial. While some studies suggested that the rainfall variability is mainly influenced by the ENSO (Fauchereau et al. 2003; Makarau and Jury 1997; Mason 2001; Misra 2001; Philippon et al. 2011), some studies found no relationship between the southern African winter rainfall and ENSO (Blamey and Reason 2007; Reason and Rouault 2005). Many studies have shown that other general circulations may as well have stronger influences on southern African rainfall. For instance, the IOD is said to have a strong relationship with seasonal rainfall over Zimbabwe (Manatsa et al. 2008) and southern African summer rainfall (Fauchereau et al. 2003; Manatsa and Matarira 2009; Manatsa et al. 2012). Jury and Mwafulirwa (2002) found that the quasi-biennial oscillation influences Malawian summer rainfall. Furthermore, Reason and Rouault (2002) and Reason et al. (2002) found a link between western South African winter rainfall and the Antarctic Oscillation (AAO) and central south Atlantic sea surface temperature (SST). The lack of agreement among previous studies on the causes of southern African droughts calls for more studies on understanding the atmospheric dynamics that modulate drought occurrence and severity over the region. The present study employs a drought index (that incorporates the influence of rainfall and potential evaporation) in investigating the influence of atmospheric teleconnection on the southern African droughts, with an emphasis on the REDs.

In Chapter 2, we identified REDs over southern Africa using SPEI, and described the spatial and temporal characteristics of the REDs (i.e. drought modes and patterns). In this chapter, we discuss the physical mechanism that control REDs over southern Africa. The discussion is in three parts. In the first part (Section 3.2), we investigate the link between ENSO and spatial distribution of summer droughts (SPEI). In the second part (Section 3.3), we present the influence of teleconnections on the drought modes, and in the third part (Section 3.4), we discuss the role of the teleconnection on the drought patterns over southern Africa. The data and methods used to obtain the results are described in each section. A more comprehensive and technical discussion of the materials presented in this chapter can be obtained in Meque and Abiodun (2014), Ujeneza and Abiodun (2014), Meque (2015), and Meque and Abiodun (2016).

3.2   The Link Between ENSO and Summer Drought in Southern Africa

The CRU observation data set and the European Centre for Medium-Range Weather Forecasts (ECMWF) ERA-Interim Reanalysis data set (ERAINT) (Dee et al. 2011) were analysed for the study. We calculated the SPEI separately for each data set over the study period. To assess the impact of ENSO on droughts across southern Africa, we used the Multivariate ENSO index (MEI) (Wolter and Timlin 2011) as a proxy of El Niño and La Niña years. The MEI data for the study period were obtained from the NOAA Earth System Research Laboratory website (http://www.esrl.noaa.gov/psd/enso/mei/table.html). The MEI is a bimonthly ENSO index based on six variables (pressure, zonal and meridional winds, SSTs, surface air temperature and total cloudiness fraction) observed over the tropical Pacific region. Positive MEI values represent El Niño conditions, while negative MEI values indicate La Niña conditions. El Niño and La Niña years were identified as seasons in which the index was +0.5 above and −0.5 below, respectively.

The MEI has been previously applied to study the connection between ENSO and drought in many parts of the world (e.g., Andrews et al. 2004; Hallack-Alegria et al. 2012) including our study region (e.g., Fauchereau et al. 2009; Boulard et al. 2013). Correlation analysis (Wilks 1995) is one of the most common methods used to study the relationship between two variables. We performed the correlation between SPEI values and MEI values. The correlation is performed between DJF MEI and SPEI values over southern Africa (Figure 13). Further analysis was performed over the three selected areas (see Figure 13): Limpopo area (LP: 27°–32°E, 20°–25°S), North-eastern South Africa (NS: 19°–25°E, 30°–26°S) and over north-eastern highlands of Tanzania (TZ: 35°–39°E, 5°–2°S).
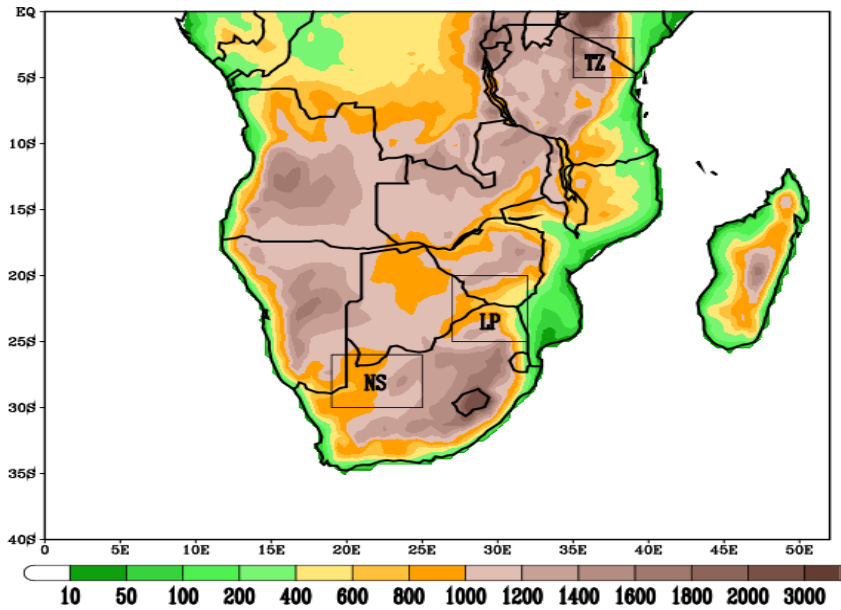
Figure 13: The simulation domain of Coordinated Regional Climate Downscaling Experiment (CORDEX) Africa showing the African topography (metres) and the southern African domain used in this study. The boxes inland (LP: 27°–32°E, 20°–25°S; NS: 19°–25°E, 30°–26°S; and TZ: 35°–39°E, 5°–2°S) indicate the three subregions (i.e. Limpopo area, north-eastern South Africa and north-eastern highlands of Tanzania, respectively) in which time series data is investigated

3.2.1   ENSO and drought coverage over Southern Africa

Figure 14 shows a strong correlation between ENSO and droughts over southern Africa in CRU and ERAINT data sets. In CRU (Figure 14a), the correlation between ENSO and SPEI shows a marked dipole pattern over southern Africa with positive values ($r \geq 0.6$) over the eastern part of the tropical area (north of 15°S) and negative values ($r \leq -0.6$) over the subtropical area (south of 15°S). The correlation is weak ($r = \pm 0.3$) over the western part of the tropical area. It is also weak over the south-western tip of southern Africa, possibly because this area experiences an austral winter mode (Reason et al. 2002; Reason and Jagadhesha 2005; Reason and Rouault 2005; Philippon et al. 2011; Vigaud et al. 2012).
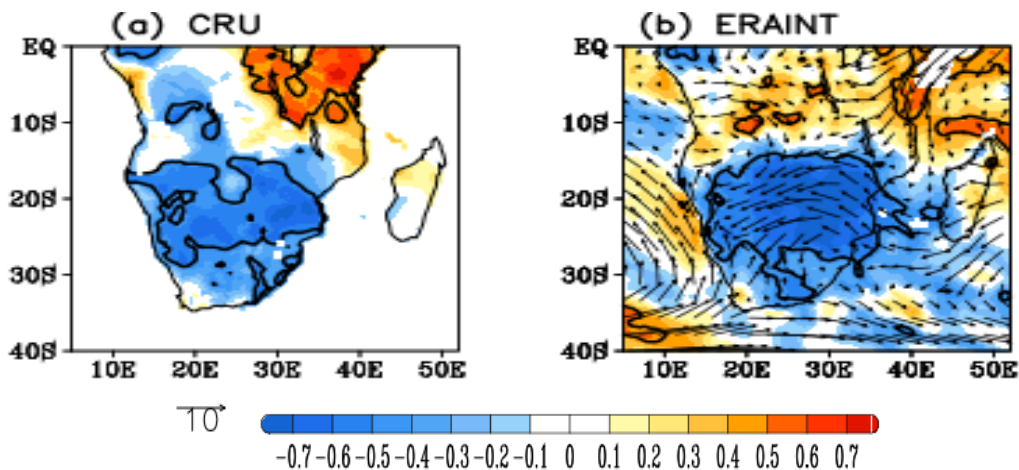
Figure 14: The coefficient of correlation between ENSO and drought (SPEI) over southern Africa in summer (DJF, 1989–2008), as reported by (a) CRU and (b) ERAINT. The contours show areas where the correlation is significant at 95% using the t-test. The corresponding 850 hPa winds are shown in the background; the arrow at lower left corner indicates 10 m/s wind speed

When compared with CRU data, ERAINT (Figure 14b) replicates the dipole pattern very well, except that it shows a weaker positive correlation (r ≈ 0.5) over the eastern part of the tropical area than CRU data, and extends the positive correlation westwards into Angola, making the area of positive correlation wider than in CRU data. The biases in the ERAINT results may be attributed to the low resolution and convective parameterization scheme used in the reanalysis. It is difficult to link the wind pattern with the ENSO-drought correlation pattern, but generally, in the ERAINT, the area of negative correlation experiences easterly winds (from the Indian Ocean), while the area of positive correlation experiences north-easterly or westerly flow.

3.2.2 The influence of ENSO on precipitation and rainfall

Since precipitation and temperature are the two variables used in computing the drought index (SPEI), it is of interest to examine the relationship between ENSO and each of these variables. The correlation between ENSO and precipitation over the study area shows a good resemblance with that of ENSO and drought (compare Figure 14 and Figure 15). The general pattern shows positive correlations (r ≈ 0.5) over the tropical region and negative correlation (r ≈ −0.6) over the subtropical region. The significant negative correlation over central parts of southern Africa suggests that a warm ENSO event will induce lower rainfall over southern Africa, while a cold ENSO event will produce above-normal rainfall conditions, which is consistent with the findings from previous studies over the region. As in CRU data, ERAINT shows negative correlation over central parts of southern Africa.
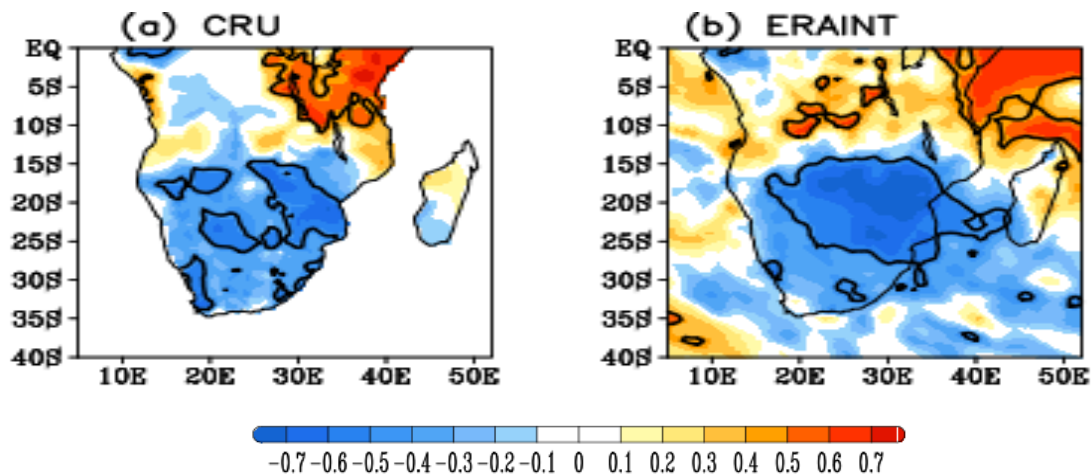
Figure 15: The coefficient of correlation between ENSO and precipitation over southern Africa in summer (DJF), as observed (CRU and ERAINT). The contours show areas where the correlation is significant at 95% using the t-test

The CRU data shows a significant positive correlation between ENSO and temperature in DJF over the bulk of southern Africa (Figure 16). It is also a well-known feature that strong abnormally high temperatures (and sometimes heatwaves) are recorded over most of the southern African subcontinent during El Niño years (Lyon 2009; Richard et al. 2001). During El Niño years, the convergence zone that normally reaches 20°S in January during the austral summer is weakened and shifted to the east and north, resulting in dry conditions over the subcontinent (Mason 2001). The resemblance between the CRU data and ERAINT patterns is noticeable. Both show positive correlation over subtropical areas and negative correlation values over the tropical areas, but they show contrary correlations over a large part of the DRC, where ERAINT shows positive correlation coefficients.
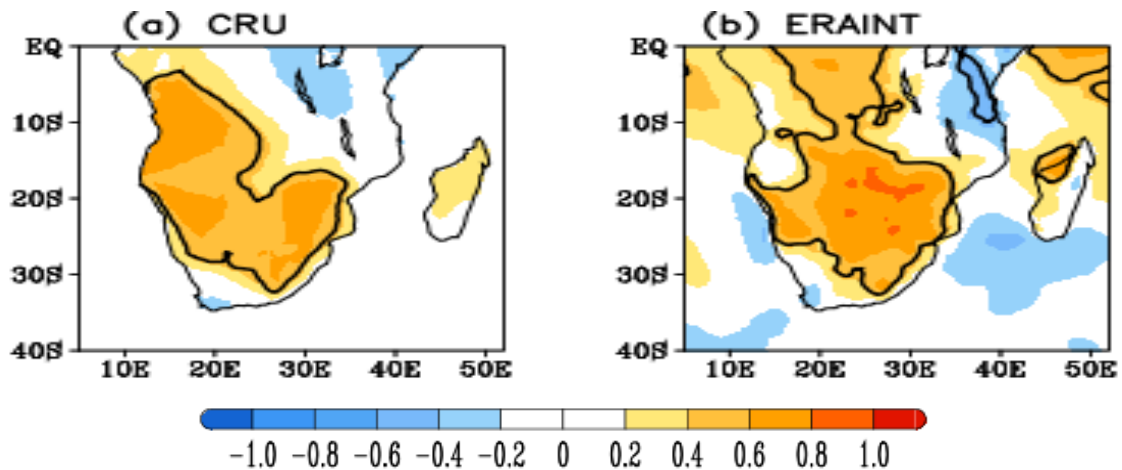
Figure 16: The coefficient of correlation between ENSO and temperature over southern Africa in summer (DJF), as observed (CRU and ERAINT) and simulated [CORDEX regional climate models (RCMs)]. The contours show areas where the correlation is significant at 95% using the t-test

Figure 17 compares the influence of ENSO on rainfall, temperature, and drought over the three selected areas (see Figure 13): Limpopo area (LP: 27°–32°E, 20°–25°S), north-eastern South Africa (NS: 19°–25°E, 30°–26°S) and over north-eastern highlands of Tanzania (TZ: 35°–39°E, 5°–2°S). The Limpopo area is usually considered as the drought corridor in southern Africa (Usman and Reason 2004) because of the high dry-spell frequencies over this area in DJF. Reason et al. (2005) found a good relationship between ENSO and the dry-spell frequencies over this area. However, Figure 17a shows that the correlation between ENSO and temperature ($r \approx 0.7$) over this area is stronger than the correlation between ENSO and rainfall ($r \approx -0.5$). The same is true over north-eastern South Africa (Figure 5b), but the reverse is the case over Tanzania (Figure 17c). This suggests that the influence of ENSO on drought ($r \approx 0.6$) over Limpopo and north-eastern South African areas may be more associated with enhanced evapotranspiration (i.e. warming) than with reduced rainfall; but over Tanzania, the influence is more associated with the reduced rainfall than with enhanced evapo-transpiration. In other words, using only rainfall to quantify, predict, or monitor the influence of ENSO on drought over Limpopo and north-eastern South African areas may underestimate the influence on the drought. ERAINT results also show that the influence of ENSO on temperature (or on SPEI) is stronger than on rainfall over the two areas.
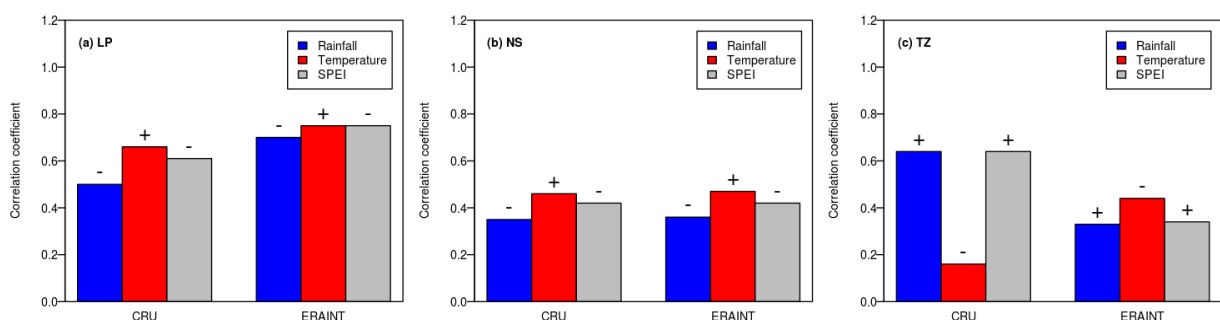
Figure 17: The coefficient of correlation between ENSO and climate variables (rainfall, temperature and SPEI) over (a) Limpopo (LP), (b) north-western South Africa (NS), and (c) north-eastern Tanzania (TZ). The signs of the correlation coefficients are indicated on the bars

3.2.3 Composite of SPEI, Precipitation and Temperature during El Niño and La Niña Events

For a better understanding of the impact of ENSO on southern African droughts, we present the composites of SPEI, precipitation and temperature during El Niño and La Niña conditions. Within our study period (1989–2008), there were six El Niño events (1991/92, 1994/95, 1997/98, 2002/03, 2004/05 and 2006/07) and six La Niña events (1995/96, 1998/99, 1999/2000, 200/01, 2005/06 and 2007/08).

Figure 18 shows the composite of SPEI for the La Niña events. The figure shows that the cold phase of ENSO (La Niña) is associated with positive SPEI (wet conditions) over the subtropical southern Africa and negative SPEI (dry conditions) over the north-eastern tropical area. This is consistent with Figure 14 and agrees with previous studies that explored the composite of rainfall during La Niña events. La Niña events are associated with the occurrence of tropical temperate troughs (TTTs) (Harrison 1984; Todd et al. 2004; Todd and Washington 1999; Washington and Todd 1999), which are NW–SE oriented cloud bands. TTTs form as a result of interaction between tropical and mid-latitude systems and they are responsible for most of the convection and rainfall over southern Africa (Vigaud et al. 2012). They are more common during the November–February period and are associated with an increase in the intensity of the African Walker Cell, which in turn enhances moisture convergence over southern Africa (Ratnam et al. 2012).

The ERAINT simulate that during La Niña years, the anti-cyclonic flow over the Atlantic Ocean is weaker and shifts westward (i.e. off the subcontinent). This will enhance more low convergence and precipitation over the subcontinent. The cold ENSO events are also associated with lower temperature over the bulk of southern Africa and higher temperature over northern Mozambique, Tanzania, north-eastern Zambia and southern DRC (not shown). However, the reverse is the case with the warm phase of the ENSO condition (El Niño, Figure 19). El Niño event favours widespread dry conditions in the region, except over northern Mozambique, southern Tanzania, north-eastern Zambia and eastern DRC, where El Niño events produce wet conditions. The anti-cyclonic flow shifts eastward over the subcontinent, consequently inhibiting precipitation over the region (Figure 19). The warm ENSO produces higher temperatures over most parts of southern Africa and lower temperatures in the subtropical regions.
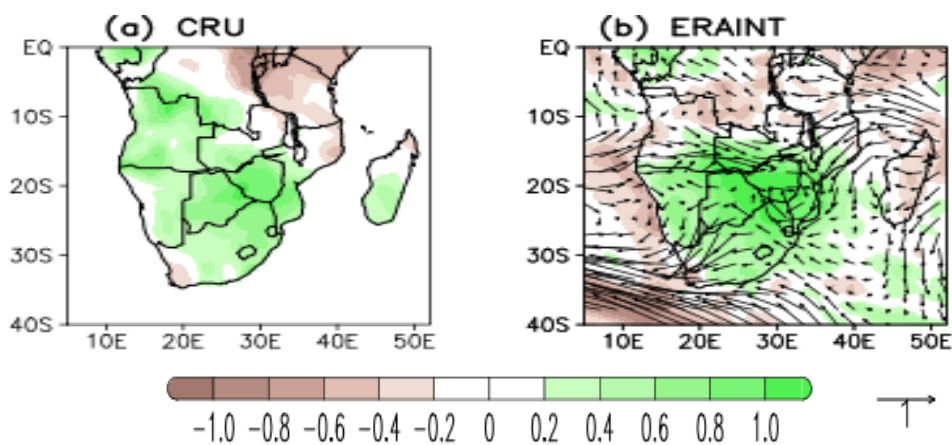
Figure 18: The composite of drought index (SPEI) and wind anomalies at 850 hPa in December–January of La Niña years
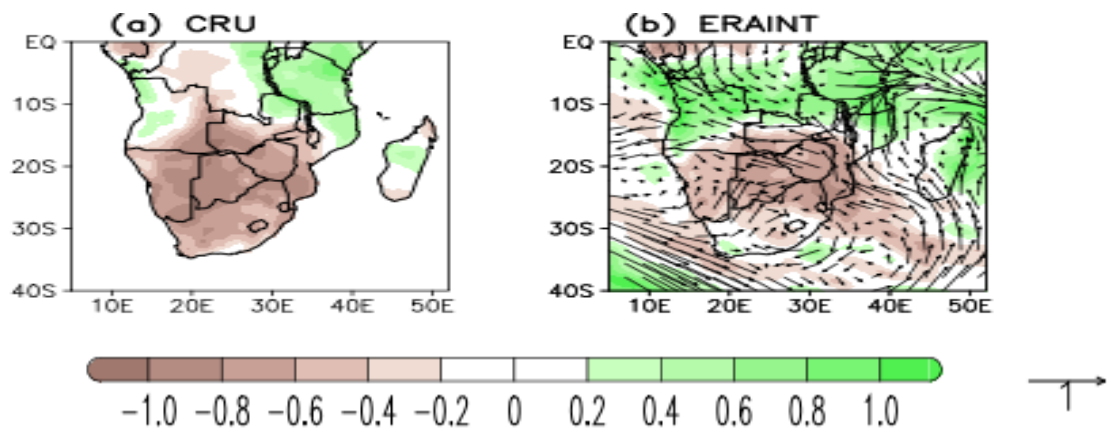
Figure 19: The composite of drought index (SPEI) and wind anomalies at 850 hPa in December–January of El Niño years

3.3 Atmospheric Teleconnections and Drought Modes Over Southern Africa

This section presents the relationship between the six atmospheric teleconnections and the four drought modes (principal factors) described in Chapter 2. As explained in Chapter 2, the drought modes were obtained by performing the PCA on CRU SPEI data. The descriptions of the six atmospheric teleconnections used in the study are given in Table 2.

Table 2: Description of the climate indices used in the study

Abbr.	Index name	Period	Data source
AAO	Antarctic Oscillation	1950–2009	Physical Sciences Division/*NOAA*
IOD	Indian Ocean Dipole	1940–1997	Japan Agency for Marine-Earth Science and Technology
NAO	North Atlantic Oscillation	1940–2000	CRU/University of Anglia
QBO	Quasi-Biennial Oscillation	1948–2009	Physical Sciences Division/*NOAA*
TNA	Tropical Northern Atlantic	1948–2009	Physical Sciences Division/*NOAA*
TSA	Tropical Southern Atlantic	1948–2009	Physical Sciences Division/*NOAA*
ENSO	El Niño Southern Oscillation	1940–2009	CRU/University of Anglia
SSP	Sunspots Count	1940–2009	Solar Influences Data Analysis Center

Figure 20 presents the correlation between each drought mode and the global SST anomalies at three-month scale. In Figure 20, positive correlation values over an ocean area means that a warm (i.e. positive) SST anomaly over the ocean area produces wet conditions (i.e. positive principal factor score) over the region of positive loading in the principal factor pattern (Figure 20), but produce dry conditions (droughts) over the region of negative loadings in the principal factor pattern.

The reverse is the case for an ocean area with negative correlation values. Figure 20 shows that the relationship between principal factors and SST over the global ocean basins is seasonal. The relationship between DM1 and the Pacific Ocean SST exists in all the seasons, but it is most pronounced in summer (DJF, which is the dry season in the DM1 region) and least obvious in the winter (JJA, which is the wet season over the DM1 region).

The same is true for the relationship between DM1 and the Indian Ocean SST, except that the relationship is least distinct in spring (SON). On the other hand, the relation between DM1 and SST is strongest in SON; in this season, the correlation coefficient is high ($r > 0.5$) over the eastern part of the South Atlantic Ocean. Nevertheless, the wavelength coherence analysis shows that the ENSO and Tropical Northern Atlantic (TNA) have the most significant influence on DM1 in the two- to eight-year period (Figure 21). The influence of the teleconnections on DM1 was very strong from 1960 through 2000. Although, AAO also shows some influences in the two- to eight-year period; the influence only started in 2000 (now shown). IOD and TSA also show significant influence on DM1 but at the eight- to 16-year period (not shown). Hence, the most dominant teleconnections influencing DM1 are ENSO and TNA.
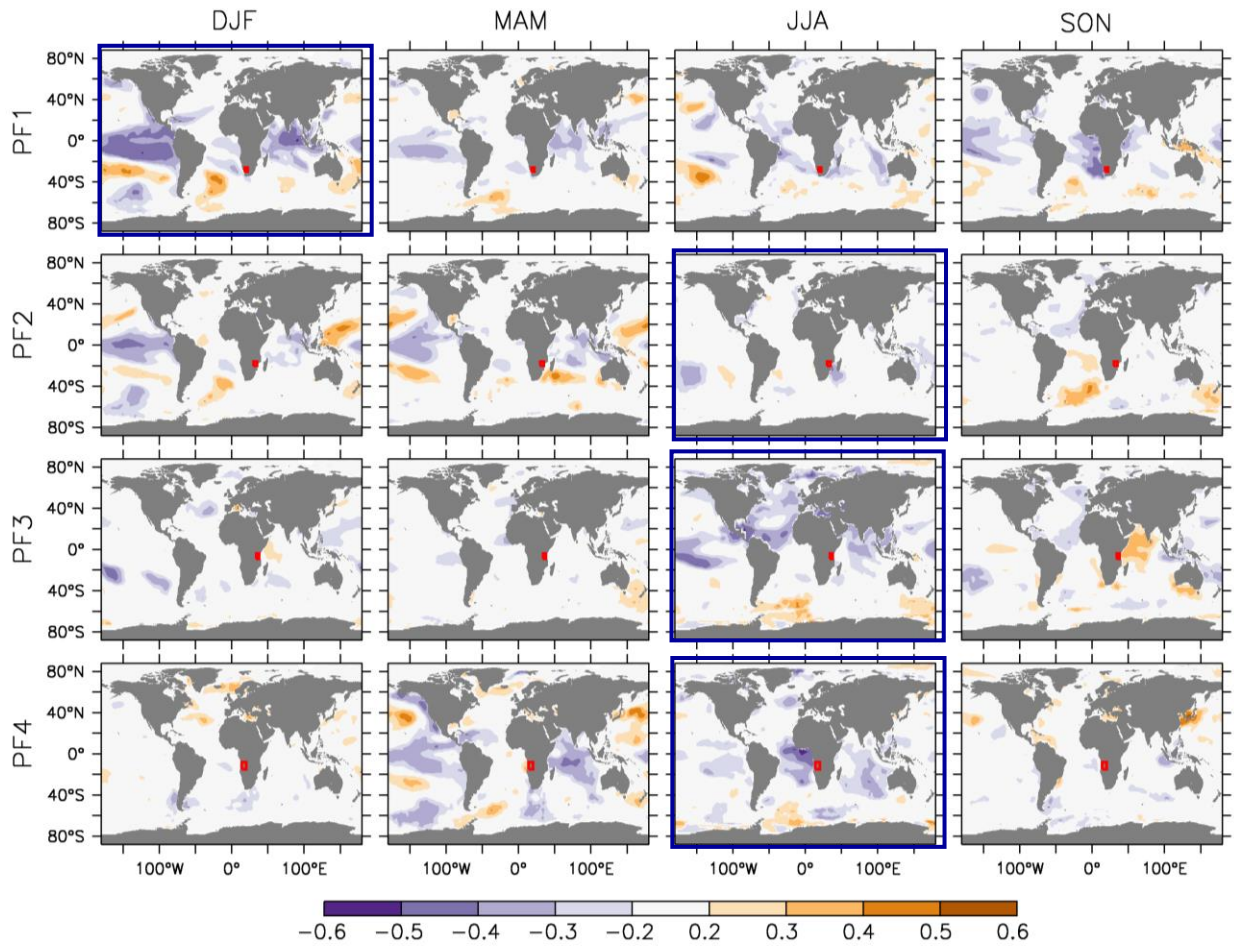
Figure 20: The correlation between the scores of principal factors (PF1, PF2, PF3 and PF4; i.e. drought modes: DM1, DM2, DM3 and DM4, respectively) and global SST in different seasons. The core of each drought mode is indicated with a box, and the dry season panel for each principal factor is indicated with a blue box

(a) ENSO
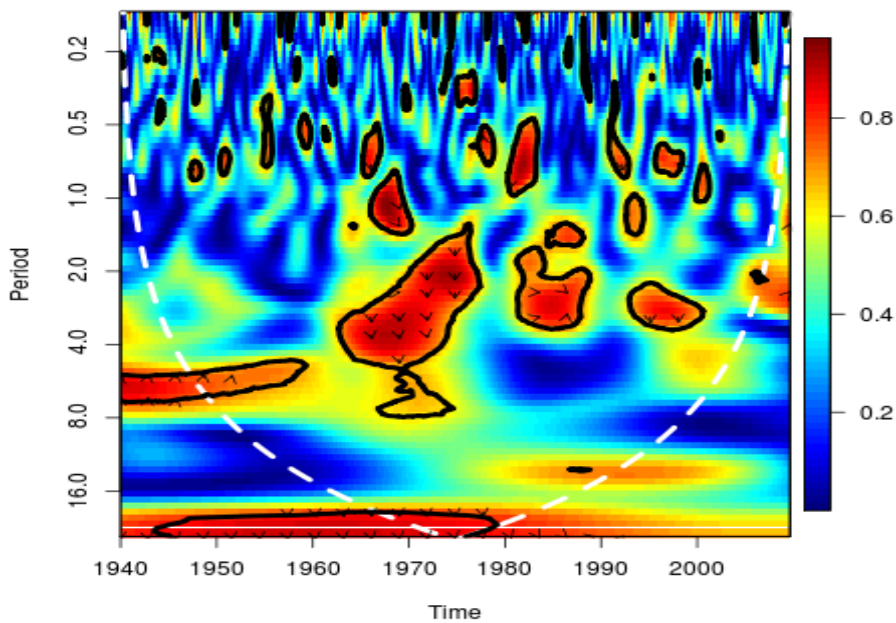
(b) TNA
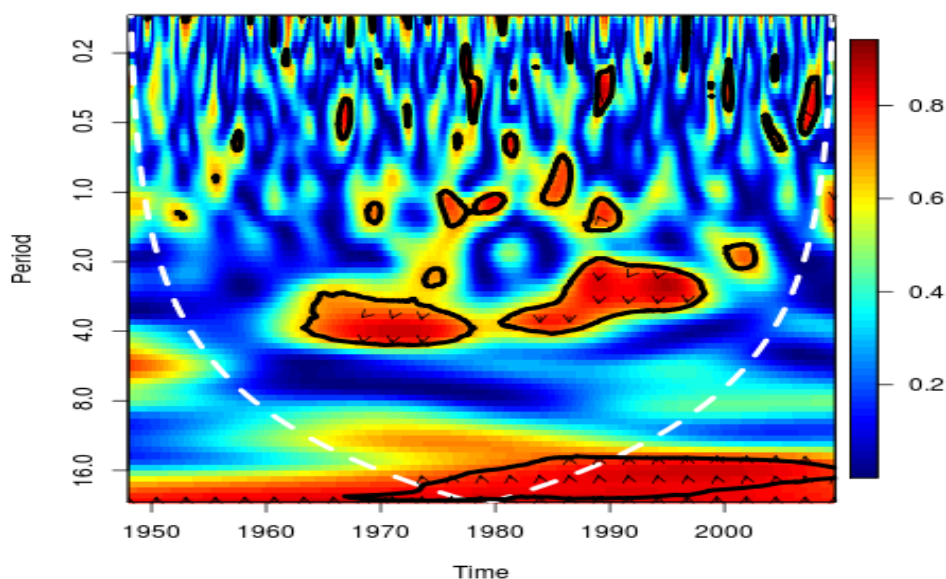
Figure 21: The wavelet coherence (and phase shift) of DM1 drought mode with atmospheric teleconnections: (a) ENSO and (b) TNA. Downward arrows mean the teleconnection leads DM1, and vice versa. Left facing arrow means the teleconnection and DM1 are in phase, and vice versa

The relationship between DM2 and the Pacific Ocean SST only exits in DJF (which is the wet season in the DM2 region) and in MAM, and that between DM2 and Indian Ocean SST also only exist in MAM and JJA (Figure 20). Manatsa and Matarira (2009) found a negative correlation between DJF SPI in Zimbabwe and SST over the Indian and Pacific Oceans. Such correlation does not feature in the present study. The reason for this discrepancy is because Manatsa and Matarira (2009) correlated DJF SPI with SON SST, while we correlated DJF DM2 with DJF SST. When we correlated DJF DM2 with SON SST, we obtained a negative correlation (not shown) as in Manatsa and Matarira (2009). DM2 shows strong correlation with Southern Atlantic Oceans SST in SON but weak or no correlation in other seasons. However, the wavelet coherence analysis shows that IOD and ENSO have the most significant influence on DM2 in the two- to eight-year period (Figure 23). TSA also has significant influence DM2 but in the > eight- to 16-year period (not shown). The influences of other teleconnections (used in study) are not significant.

The relationship between DM3 and the global SST is only distinct in JJA and SON (Figure 20). DM3 has negative correlation with the three-ocean basis in JJA and positive correlation with the Indian Ocean in SON. The wavelet coherence of the drought mode (DM3) with teleconnection indexes shows that TNA and ENSO have the most consistent influence on DM3 in the two- to eight-year period. Other teleconnections (such as IOD, North Atlantic Oscillation and AAO) also show some influence in the period, but the influence is weaker than those of TNA and ENSO.

The influence of the SST on DM4 is mainly in MAM and JJA (Figure 20). While DM4 has a distinct correlation pattern with SST over the Pacific Ocean and Indian Ocean in MAM, its distinct correlation pattern over the Tropical Atlantic Ocean is in JJA. This suggests that while this drought mode may be influenced by the SST over the Pacific Ocean and Indian Oceans in MAM, it may be sensitive to the SST over the Atlantic Ocean in JJA, but not sensitive to SST over any ocean in DJF and SON. Nevertheless, the wavelength coherence analysis shows that this drought mode is poorly coupled with ENSO and other teleconnections. Among the teleconnections, AAO shows the most consistent coherence with DM4 in the one- to two-year period in 1985–1995 (Figure 24). Hence, the influence of global scale teleconnection on drought over DM1 region is weak.

27

Consistent with Section 3.2 above, the results indicate that ENSO influences droughts over most regions in southern Africa except the DM4 region. Nevertheless, the results show that influence of other teleconnection on droughts over drought modes (e.g. DM2 and DM3) may be as important as (or more important than) that of ENSO. For example, IOD is as important as ENSO in influencing the DM2 drought mode while TNA is more important than ENSO influencing drought modes over DM3. However, it seems no teleconnections has significant and persistent influence on DM4 drought mode.

(a) ENSO
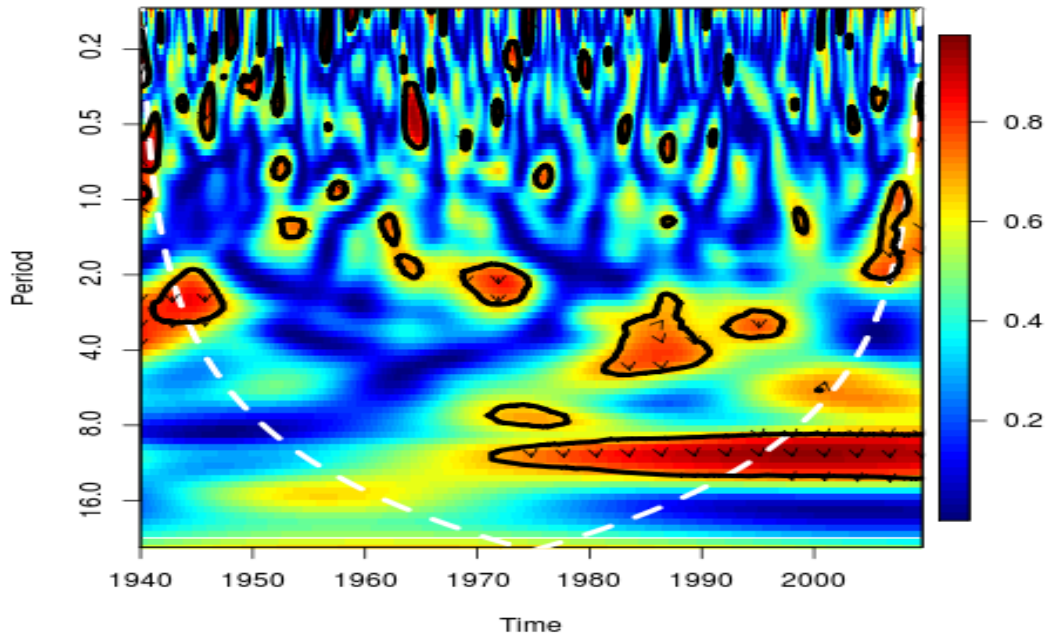
(b) IOD
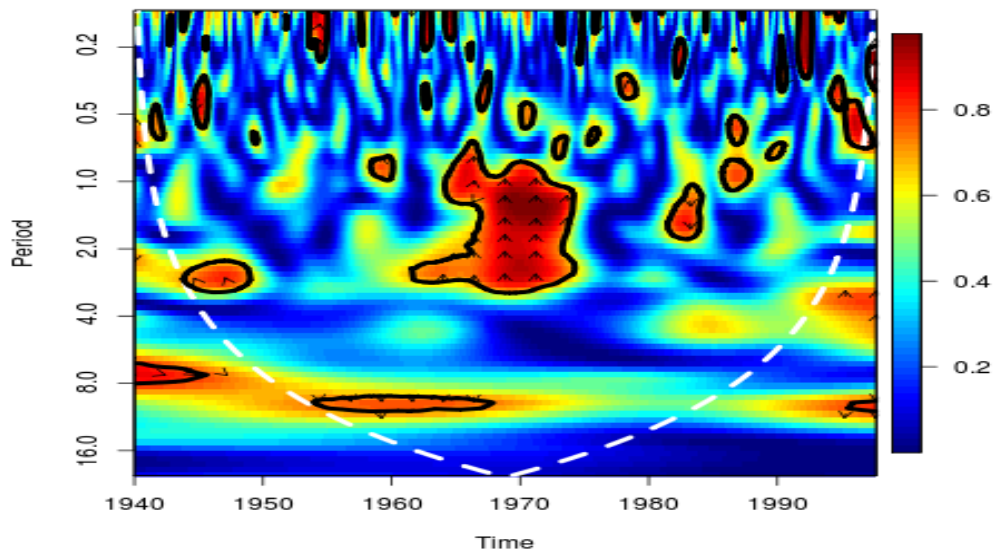
Figure 22: The wavelet coherence (and phase shift) of DM2 drought mode with teleconnections: (a) ENSO and (b) IOD. Downward arrows mean the teleconnection leads DM2, and vice versa. Left facing arrow means the teleconnection and DM2 are in phase, and vice versa
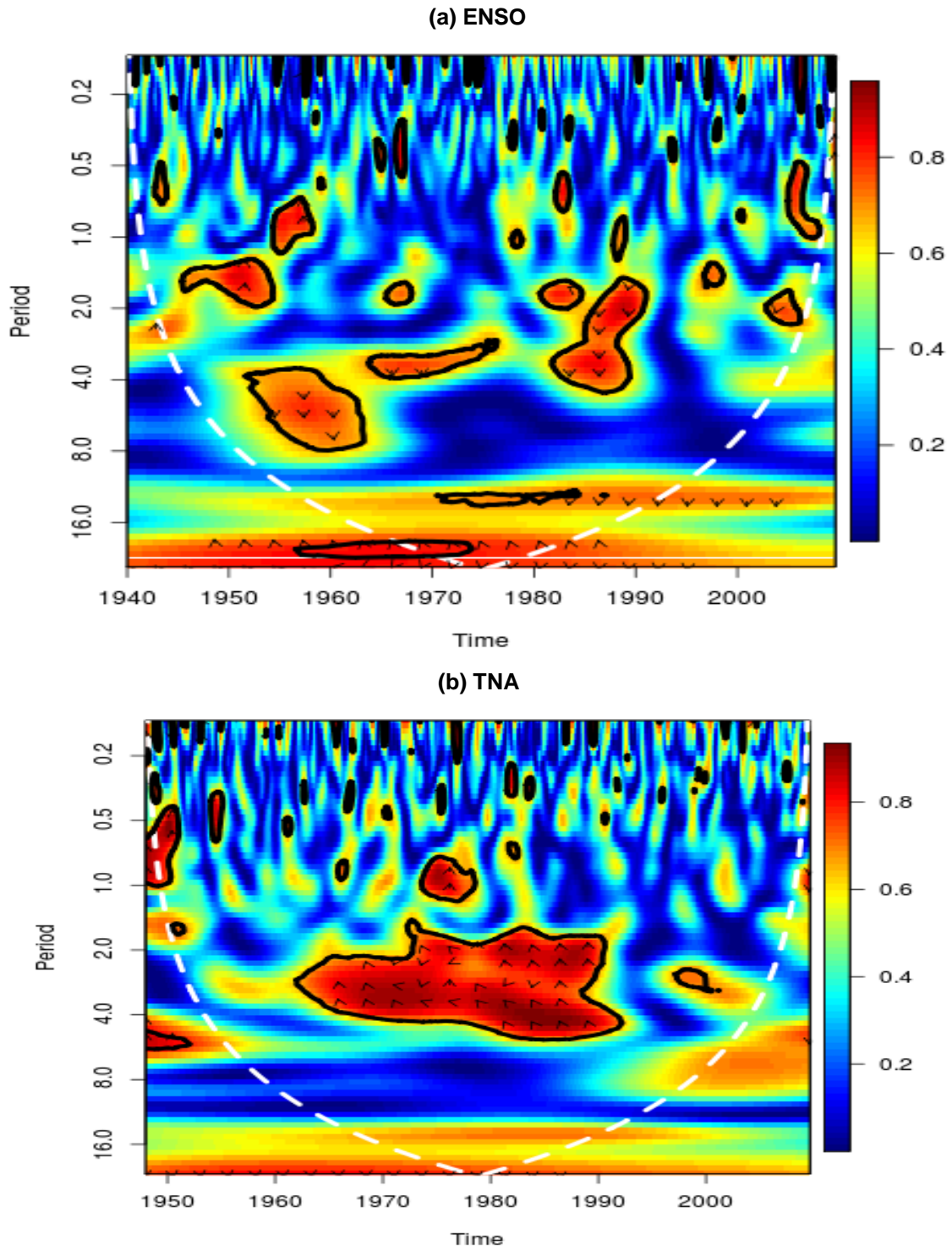
Figure 23: The wavelet coherence (and phase shift) of DM3 drought mode with teleconnection (a) ENSO and (b) TNA. Downward arrows mean the teleconnection leads DM3, and vice versa. Left facing arrow means the teleconnection and DM3 are in phase, and vice versa
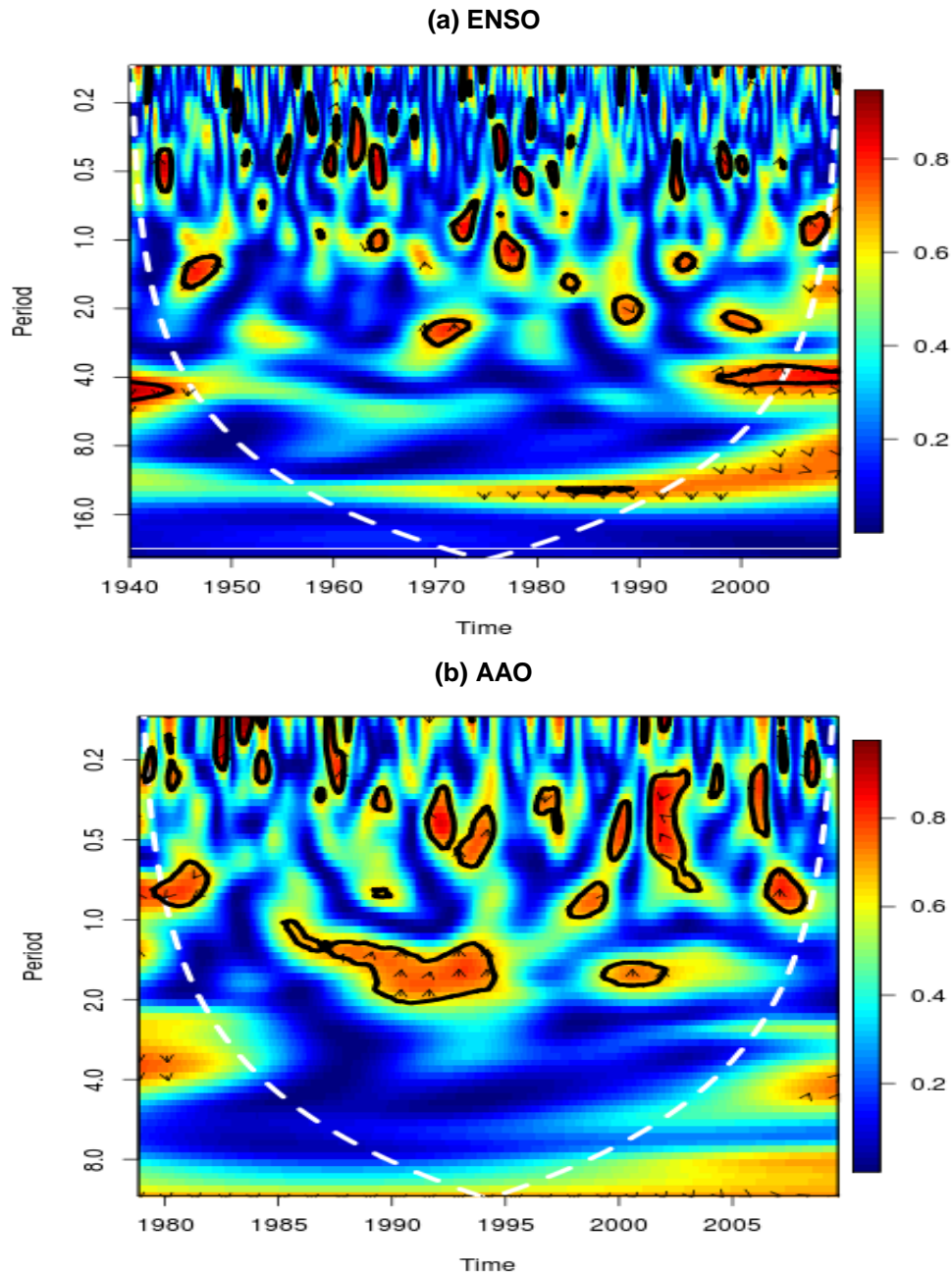
(a) ENSO

(b) AAO

Figure 24: The wavelet coherence (and phase shift) of DM4 drought modes (principal factors) with teleconnections: (b) ENSO and (b) AAO. Upward arrow means the teleconnection leads DM4, and vice versa. Left facing arrow means the teleconnection and DM4 are in phase, and vice versa

3.4 Relationship Between Atmospheric Teleconnection and Drought Patterns in Summer Over Southern Africa

This section examines the relationship between atmospheric teleconnections and each of the 12 drought patterns presented in Chapter 2. In the examination, we focus on austral summer (DJF) because it is the rainy season for most part of southern Africa, and we consider the most important atmospheric teleconnections (or climate indices such as ENSO, IOD, AAO and BEN) for studying or predicting rainfall (or drought) over the region during this season.

As an indication of the relationship between the drought pattern and atmospheric teleconnections, Figure 25 presents the frequency of overlapping between the drought patterns and the active phases of the teleconnections in summer. Node 1 and Node 12 show a substantial and consistent relationship with ENSO but not with other teleconnections (IOD, AAO, and BEN). For instance, 83% (five events) of

Node 1 occurrences coincide with the positive phase of ENSO (El Niño), while 100% (three events) of Node 12 occurrences happen during the negative phase of ENSO (La Niña). Although Node 1 also shows a substantial relationship with other teleconnections, the relationship is not consistent. For example, the pattern features well during the active phases of BEN (83%) but occurs in both positive (50%) and negative (33%) modes of the teleconnection. It also features well during the active phases of IOD (66%) but in both positive (33%) and negative (33%) phases. Node 12, on the other hand, shows no relationship with IOD, a weak relationship with BEN (< 34%), and an inconsistent relationship with AAO (< 34% in negative and < 34% in positive modes). No other drought pattern shows substantial and consistent relationships with ENSO or with other teleconnections.

Node 6 and Node 8 exhibit a consistent relationship with ENSO (i.e. positive and negative modes, respectively), but the two nodes feature less than 29% and 34%, respectively, of their occurrences during ENSO events. Nodes 9, 10 and 11 have a substantial relationship with ENSO, but they appear in both positive and negative modes of ENSO. In some cases, two opposite drought patterns feature in the same phase of a teleconnection (i.e. Nodes 4 and 9 in positive IOD; Node 3 and Node 9 in negative AAO). This makes it difficult to relate any of these patterns with the teleconnection. Hence, the most consistent message from the discussion is that Nodes 1 and 2 are the only drought patterns solely induced by ENSO events. However, this does not indicate that all ENSO events will produce Node 1 or Node 12.
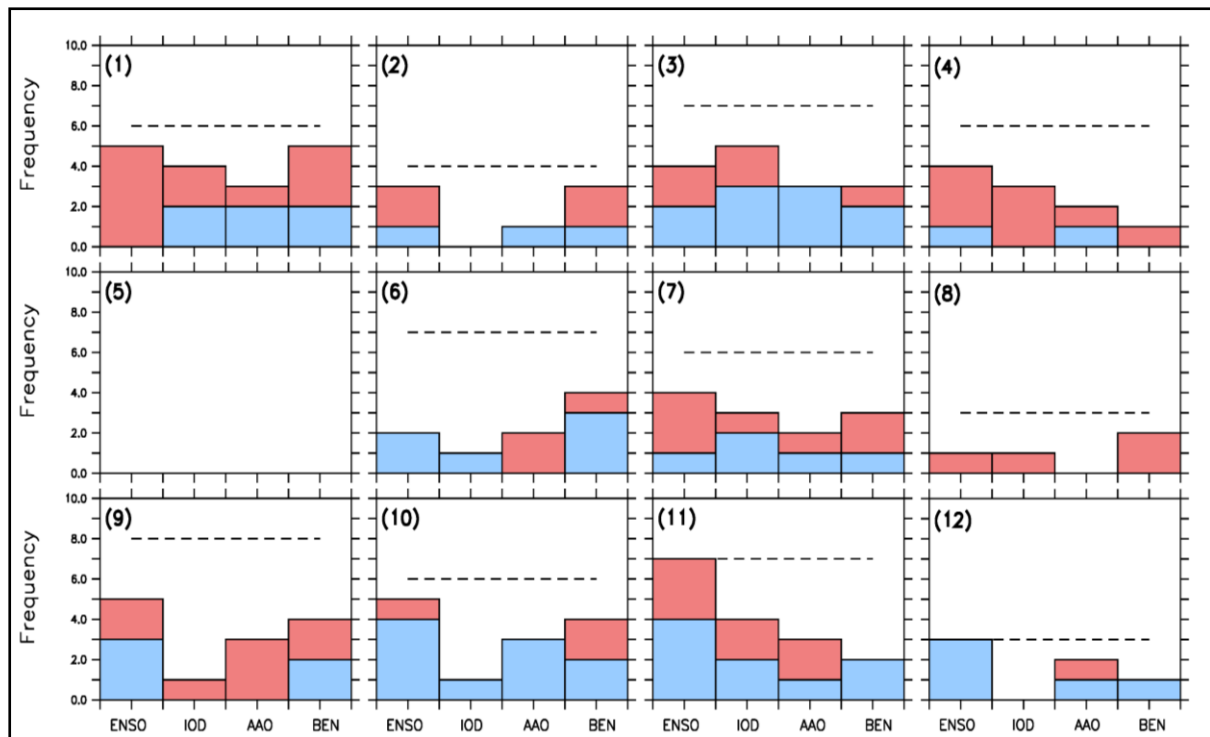
Figure 25: The frequency of overlapping between the drought patterns (shown in Figure 7) and the active phases (positive: red; negative: blue) of atmospheric teleconnections (i.e. climate indices: ENSO, IOD, AAO and BEN) in DJF. The total number of each drought event is indicated with dashed

Figure 26 presents the composite of DJF SST anomalies for each drought pattern. For Node 1, the SST pattern features a warm pool (positive anomalies) over the central Pacific Ocean. This SST pattern has been identified as the central Pacific ENSO (Kao and Yu 2009; Yeh et al. 2012), dateline ENSO (Larkin and Harrison 2005), El Niño Modoki (Ashok et al. 2007), warm pool El Niño (Kug et al. 2009), and El Niño Type 3 (EN3) (Hoell et al. 2014; Johnson 2013). However, in agreement with Hoell et al. (2014), the SST pattern is characterised with warm Indian and tropical Atlantic SST.

Node 4 is also associated with warm pool over the Pacific Ocean, but the warming is confined to the equatorial eastern Pacific Ocean. This SST pattern, which is usually called the eastern Pacific El Niño or canonical El Niño, is classified as El Niño Type 4 (EN4) by Hoell et al. (2014). It is accompanied with warm SST over the tropical Atlantic and tropical Indian Ocean. Hence, Node 1 and Node 4 drought patterns are caused by different flavours of El Niño events.
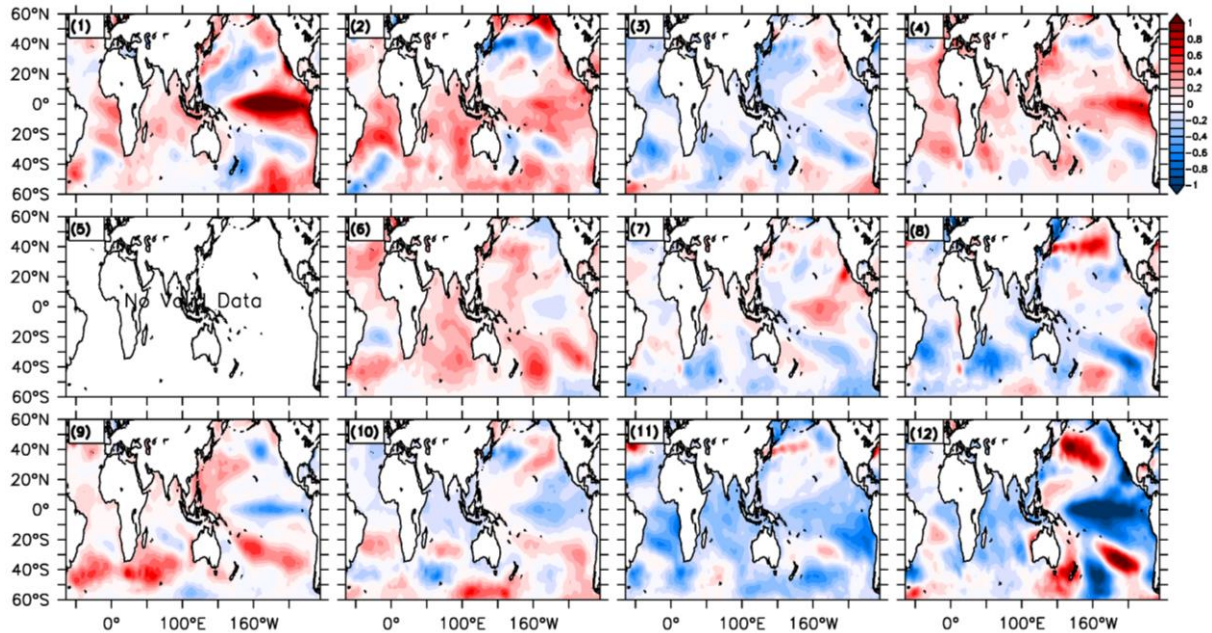
Figure 26: Composite of SST (°C) anomalies associated with the SOM drought patterns (shown in Figure 7) during summer (DJF) in 1950–2013

In contrast, the SST anomaly pattern for Node 12 features cold SST over the equatorial and central Pacific (i.e. La Niña event). This SST pattern, which features cold tropical Atlantic and Indian Oceans, is called La Niña Type 1 (LN1) in Hoell et al. (2014). Node 9 is also characterised with an SST anomaly pattern that shows maximum cooling over the central Pacific Ocean and features maximum warming over the southern Atlantic and southern Indian Oceans. The SST pattern corresponds to La Niña Type 4 (LN4) in Hoell et al. (2014). Many authors (i.e. Hoell et al. 2014; Johnson 2013) have shown that LN1 dominated the La Niña pattern prior 1990 while LN4 dominated afterward. This is consistent with the shifting of southern African droughts (from all-wet drought patterns to all-dry patterns; Figure 26), in that Node 12 that is associated with LN1 dominated prior 1990 but has not featured since 1990. Meanwhile Node 6 that is associated with LN4 has been becoming more frequent since 1990.

Figure 27 presents the composites of DJF rainfall and temperature fields for the extremely different drought pattern (Nodes 1, 4, 9 and 12). A comparison of Nodes 1 with 9 shows that, in general, dry conditions (i.e. SPEI < 0) are associated with warming and rainfall deficit, while wet conditions (i.e. SPEI< 0) are induced by cooling and rainfall surplus. This agrees with the general relationship between rainfall and land surface temperature that an increase in rainfall will lower soil temperature (e.g. Lyon 2009; Trenberth and Shea 2005). However, there are conditions that deviate from this norm. For example, Node 1 shows areas of surplus rainfall with dry condition (SPEI < 0) because of the associated warming. The warming (possibly caused by higher insolation or advection of warmer dry air) produces higher evapotranspiration that exceeds the rainfall surplus and thereby causes a water balance deficit (SPEI < 0) over the areas. For a similar reason, Node 12 features some areas of rainfall deficit with wet conditions (SPEI > 0) due to the associated cooling, which reduces the evapotranspiration and causes a water balance surplus (SPEI > 0) over the areas. For a better understanding of the dynamics behind the rainfall and temperature changes that induce the drought patterns, Figure 28 and Figure 29 present the composite of anomalies in vertical wind, moisture transport and moisture flux convergence for the extremely different drought patterns (Nodes 1, 4, 9 and 12) during DJF.

The pattern of vertical wind anomalies (Figure 28) for Node 1 is consistent with changes in the corresponding SST anomalies (shown in Figure 26), except over the Atlantic Ocean. The pattern features an increase in convection over the warm SST areas (i.e. over the eastern and central Pacific Ocean and over the central Indian Ocean), but the maximum increase is over the central Pacific Ocean. It also features a decrease in convection over the cold SST areas (i.e. over the western Pacific Ocean) and shows no changes over the Atlantic Ocean despite the warm SST over the ocean. Most importantly, the vertical wind pattern shows a decrease in convection over southern Africa, with a local maximum decrease at 0° and at 20°N. Figure 3.20 shows that the decrease in convection is associated with a moisture flux divergence over the subcontinent. The subsidence is consistent with the rainfall deficit and temperature increase, and hence with the dry conditions (SPEI <0) over the subcontinent.

For Node 12, the vertical velocity pattern is almost a mirror image of Node 1 over the Pacific Ocean and Atlantic Ocean, but not over the Indian Ocean or over southern Africa. The pattern shows an increased convection that extends from the central Indian Ocean to southern Africa, and the maximum increase is over south Mozambique (Figure 29). This is consistent with the maximum moisture flux convergence over the area (Figure 29). Comparing Node 12 with Node 1, it seems that the increased convection in Node 12 only replaces the decreased convection at 0° in Node 1 pattern, but not at 20°S.

Contrary to expectation, Node 12 also features a maximum decreased convection at around 20°N, as in the Node 1 pattern. The decreased convection is consistent with the moisture divergence over the area. Hence, there are only two major consistent changes in dynamics of Node 1 and Node 12 apart from the changes in vertical motion at 0°N. First, the nodes have opposite patterns of vertical motion over the Pacific Ocean (in agreement different mode of ENSO); second, they feature opposite regional temperatures (warm and cool, respectively) over southern Africa and over the surrounding oceans (i.e. both Indian and Atlantic Oceans). The link between these two dynamic changes is not clear and remains a subject of future study.

For Node 9, over the Pacific Ocean, the vertical wind pattern resembles that of Node 12 though with a lower magnitude. But, over the Indian Ocean and southern Africa, it is a mirror image of Node 12. For instance, in contrast to Node 12, the Node 9 pattern features a decreased convection that extends from the Indian Ocean to Mozambique, and an increased convection that extends from south of 20°S over the continent to the Indian Ocean. The pattern is consistent with the location of moisture flux convergence (Figure 29), rainfall surplus, cooling (Figure 29), and wet condition (SPE < 0; Figure 26) south of 20°S over the subcontinent. It is also consistent with the location of the moisture flux divergence (Figure 29), rainfall deficit, warming (Figure 27), and wet condition (SPE < 0; Figure 27) north of 20°S.

For Node 4, the magnitude of the vertical wind changes is weak over the Pacific Ocean, especially when compared with those of other nodes (Figure 29). The weak magnitude is not consistent with the corresponding SST pattern, which shows a strong canonical El Niño pattern (Figure 26). Nevertheless, the magnitude is higher over the Indian Ocean and southern Africa than over the Pacific Ocean (Figure 29). In the vertical wind pattern, an enhanced convection extends from 30°S to 5°N and covers the Eastern Africa and western topical Indian Ocean, but convection is supressed south of 20° N over the subcontinent. The associated moisture flux field (Figure 29) shows a strong moisture flux convergence supporting the enhanced convection, and a weak moisture flux divergence in the area of the supressed convection. However, the location of the enhanced convection is consistent with the cooling and rainfall surplus over the wet areas (i.e. SPEI > 0), while the location of the supressed convection is consistent with the warming and rainfall deficit over the dry areas (SPE < 0).
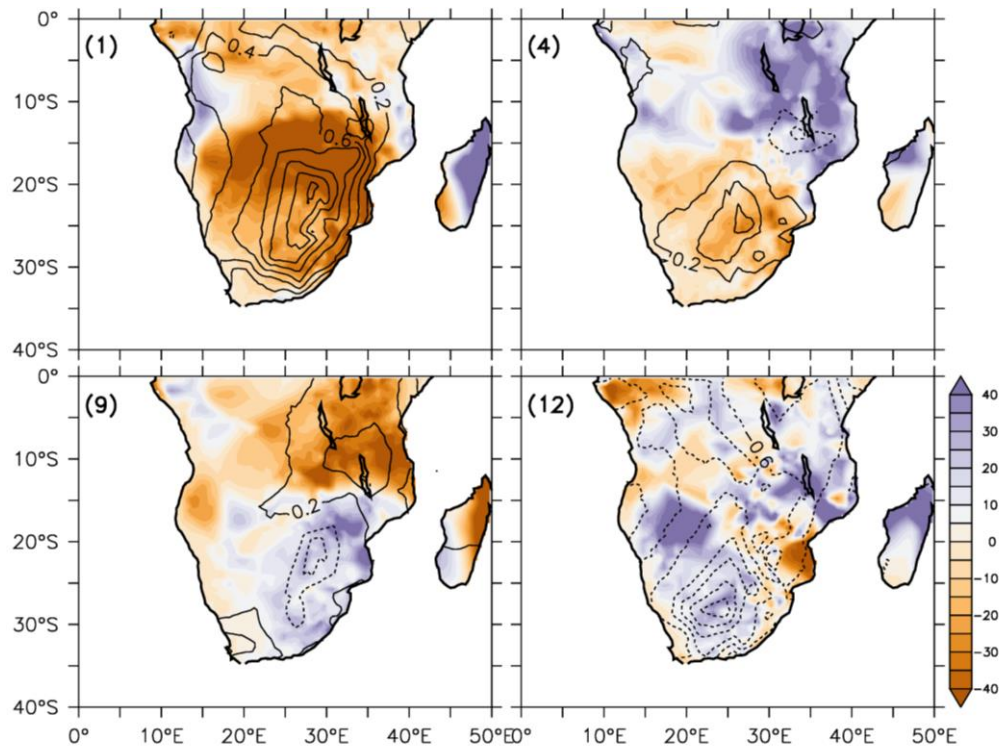
Figure 27: Composite of rainfall anomalies (colour; mm/month) and temperature anomalies (°C) associated with the four extremely different drought patterns (i.e. Nodes 1, 4, 9 and 12, shown in Figure 7) during summer (DJF) in 1950–2013
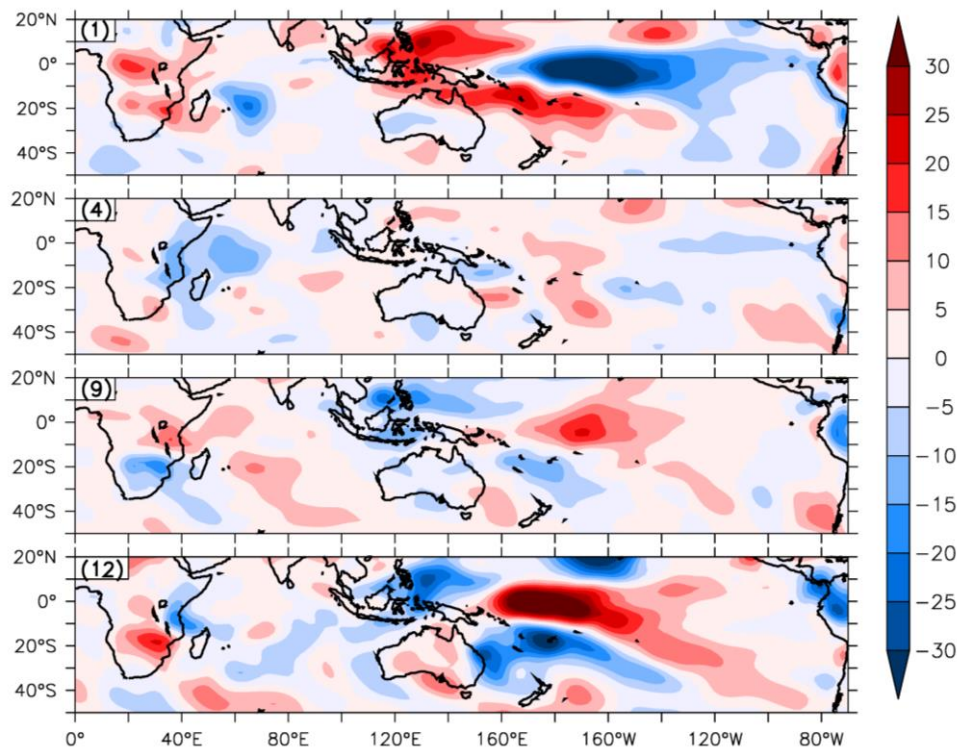
Figure 28: The composites of vertical wind (omega) anomalies (× 10³ Pa·s⁻¹) associated with the four extremely different drought patterns (Nodes 1, 4, 9 and 12, shown in the Figure 7)
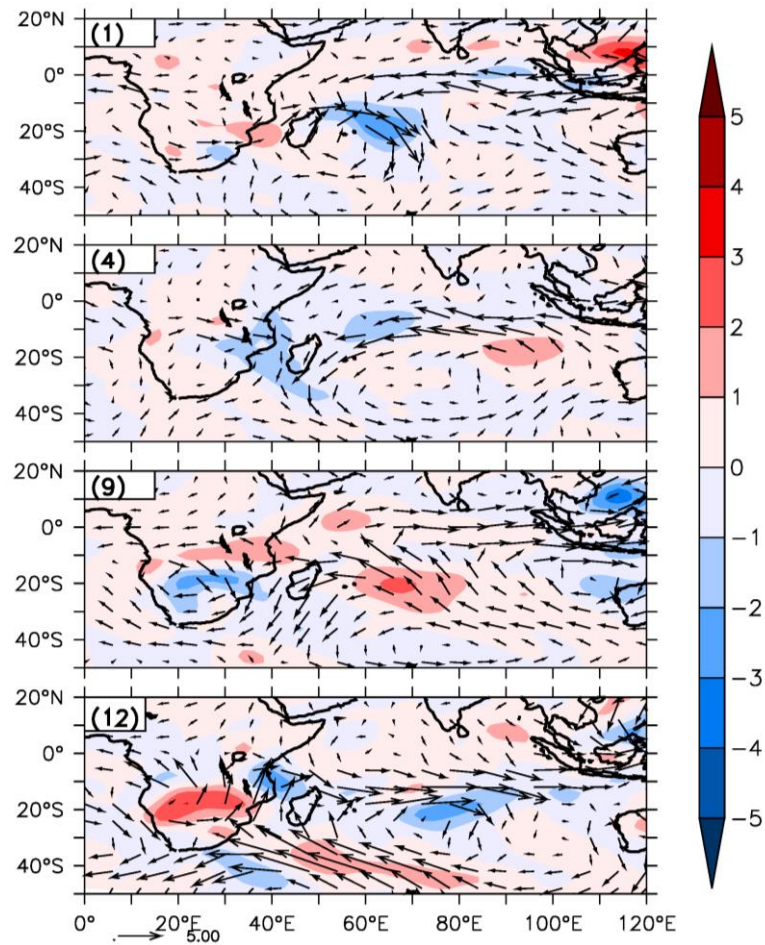
Figure 29: The composites of moisture flux (arrows; m·s⁻¹) and moisture flux convergence (colour; × 10⁶·s⁻¹) for the extremely different drought patterns (Nodes 1, 4, 9 and 12, shown in Figure 7)

3.5   Conclusion

This chapter examined the relationship between southern African droughts and atmospheric teleconnections using three approaches. In the first approach, we followed the conventional way by calculating a spatial correlation between the ENSO index and the SPEI over the subcontinent. In the second approach, we used wavelet analysis to examine the temporal structure of the correlation between each drought mode and each atmospheric teleconnection. In the third approach, we obtained the number of times each drought pattern (identified in the previous chapter) overlapped the active phases of each atmospheric teleconnection. The results obtained can be summarised as follows:

- The results of the first approach indicate the existence of a strong dipole correlation between ENSO and droughts (SPEI) over southern Africa, with the positive correlation values (up to +0.6) over the tropical area and the negative values (up to −0.6) over the subtropical area. The link between ENSO and droughts (SPEI) is due to the influence of ENSO on both temperature and rainfall fields, but the influence of ENSO is stronger on temperature than on rainfall.

- The wavelet coherence analysis confirms that ENSO influences droughts over most regions in southern Africa, but it also indicates that the influence of IOD on DM2 drought mode is as important as that of ENSO, while the influence of TNA on DM3 is more important than that of ENSO.

- The results of SOM analysis show that only 20% of drought patterns (Nodes 1 and 12) are induced solely by ENSO; other drought patterns are caused by complex interactions among the atmospheric teleconnections. Node 1 drought pattern occurs during El Niño events, while 100% of Node 12 occur during the La Niña events.

4 ASSESSMENT OF CLIMATE MODELS IN SIMULATING REDs OVER SOUTHERN AFRICA

4.1 Introduction

Climate models are viable tools for understanding the intricacy of the Earth's climate system (including droughts). Using some equations (derived from physical, chemical and biological laws) to represent the Earth's system processes, climate models can simulate past and future states of climate system over any time range from a few hours to many centuries (McGuffie and Henderson-Sellers 2005). Hence, climate model simulations can be analysed to study characteristics of droughts, investigate the mechanisms controlling droughts, and project impacts of future climate change on droughts. However, before applying a climate model simulation for these studies, it is essential to give a credible simulation of past climate, because the reliability of the simulation depends on how well the model reproduces the past climate.

Many studies have applied global climate models (GCMs) to simulate and study characteristics of southern African droughts. For instance, Joubert and Mason (1996) used GCM simulations to show that drought may be less common over a bulk of southern Africa, with the exception of parts of South Africa and Mozambique where there is a likelihood of more frequent droughts. Lyon (2009) also indicated a drying trend over the region during the austral summer (DJF), though he concluded that the trend was model dependent. The results from these studies are far from perfect. The GCM simulations lack regional details due to their coarse resolution, which is typically around 200 km. Therefore, it is necessary to investigate characteristics of southern African droughts using RCMs, which generally have much higher resolutions (~40 km) than GCMs. However, the present study assesses and compares the capability of some GCMs and RCMs in reproducing the characteristics of southern African droughts and in replicating the influence of atmospheric teleconnections on the droughts.

In the previous chapters, we identified and describe the characteristics of REDs over southern Africa (Chapter 2) and discussed the physical mechanism controlling the droughts (Chapter 3). In Chapter 4, we assess the capability of GCMs and RCMs in reproducing the observed characteristics of REDs and in linking them to the drivers. The assessment is presented in three parts. The first part (Section 4.2) shows how GCMs and RCMs reproduce the link between ENSO and drought distribution over southern Africa, and how downscaling of GCM simulations with the RCMs may improve (or depreciate) the simulation of the link. The second part (Section 4.3) shows how well the models reproduce the spatial-temporal characteristics of the drought modes. The third part discusses the capability of the RCMs in simulating drought patterns. For a more comprehensive and technical discussion of the materials in the chapter, readers are referred to Meque and Abiodun (2014), Ujeneza and Abiodun (2014), Meque (2015), and Meque and Abiodun (2017).

4.2 Model and Data

In addition to CRU observation and ERAINT reanalysis data sets (described in previous chapter), GCM and RCM simulation data sets were analysed. The GCM simulation data sets are from the Coupled Model Intercomparison Project Phase 5 (CMIP5) (Taylor et al. 2012). Table 3 provides the information of the ten GCM simulations used in the study. The GCMs were selected because their outputs have temperature and rainfall data that covers the longest periods within the study period. However, the model data sets have different spatial resolution and cover different time periods. For uniformity, the simulation data were regridded to the same resolution as for the CRU data set, and only simulation data for 1956–2009 was used in the study. The RCM simulation data set are results of the CORDEX (Giorgi et al. 2009, Jones et al. 2011). The ten CORDEX RCMs used in this study (Table 4) were driven by the ERAINT and GCMs. Their simulations cover the entire African domain (Figure 30) with a horizontal grid spacing of 0.44°. The results of the ERAINT, GCMs and RCMs were compared with the CRU observation over the southern African region (Figure 13) and over three selected areas (see Figure 13): Limpopo area (LP: 27°–32°E, 20°–25°S), north-eastern South Africa (NS: 19°–25°E, 30°–26°S) and over the north-eastern highlands of Tanzania (TZ: 35°–39°E, 5°–2°S).
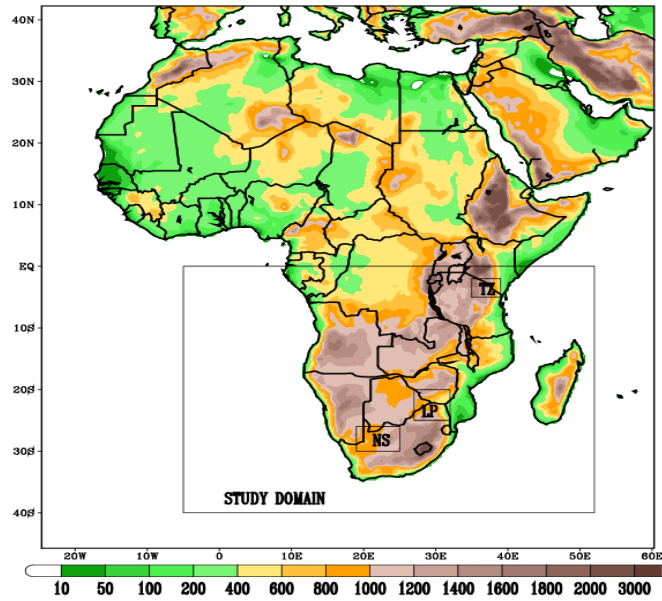
Figure 30: The simulation domain of CORDEX Africa showing the African topography (metres) and the southern African domain used in this study. The boxes inland (LP, TN and NS) indicate the three subregions in which time series data are investigated. The boxes inland (LP: 27°–32°E, 20°–25°S; NS: 19°–25°E, 30°–26°S; and TZ: 35°–39°E, 5°–2°S) indicate the three subregions (i.e. Limpopo area, North-eastern South Africa and North-eastern highlands of Tanzania, respectively) in which time series data are investigated

Table 3: A description of all GCMs used in this study

Model Name	Resolution	Period	Modelling Group	Country
GFDL-ESM2M	2.6° × 2.1°	Jan 1956–Dec 2005	NOAA/Geographical Fluid Dynamics Laboratory	USA
MIROC-ESM-CHEM	2.8° × 2.8°	Jan 1850–Dec 2005	Japan Agency for Marine-Earth Science and Technology, Atmospheric and Oceanic Research Institute, National Institute for Environmental studies	Japan
MIROC5	1.4° × 1.4°	Jan 1860–Dec 2009	National Institute for Environmental studies, Atmospheric and Oceanic Research Institute, Japan Agency for Marine-Earth Science and Technology	Japan
CanESM2	2.8° × 2.7°	Jan 1950–Dec 2005	Canadian Centre for Climate Modelling and Analysis	Canada
BNU-ESM	2.8° × 2.8°	Jan 1950–Dec 2005	College of Global Change and Earth Systems Science, BNU	China
GFDL-ESM2G	2.6° × 2.1°	Jan 1956–Dec 2005	NOAA/Geographical Fluid Dynamics Laboratory	USA
CNRM-CM5	1.4° × 1.4°	Jan 1955–Dec 2005	Centre National de Recherches Météorologique	France
FGOALS-s2	2.8° × 1.66°	Jan 1960–Dec 2005	LASG, Institute of Atmospheric, Chinese Academy of Science	China
HadGEM2-CC	1.9° × 1.25°	Jan 1950–Dec 2005	Hadley Centre for Climate Prediction and Research at the Meteorological Office	UK
Bcc_csm1	2.8° × 2.8°	Jan 1850–Dec 2012	Beijing Climate Center (BCC), China Meteorological Administration	China

Table 4: A description of RCMs used in this study. All models have a 0.44° × 0.44° grid resolution

Model Name	Modelling Group	Country
CCLM	Potsdam Institute for Climate Impact Research (PIK)	Germany
CNRM	Centre National de Recherches Météorologique	France
CRCM5	Canadian Centre for Climate Modelling and Analysis	Canada
RACMO2	Royal Netherland Meteorological Institute (KNMI)	Netherland
RCA35	Rossby Centre Regional Atmospheric Model – Swedish Meteorological Institute (SMHI)	Sweden
REMO	Max Planck Institute for Meteorology, DKRZ, DWD, GKSS	Europe
REGCM3	International Centre for Theoretical Physics	Italy
WRF3	NCAR, NCEP, FSL, AFWA	Worldwide
PRECIS	UK Meteorological Office	UK
ARPEGE	Centre National de Recherches Meteorolo–Giques	France

4.3 Simulating the Link Between ENSO and Summer Droughts in Southern Africa

4.3.1 The relationship between ENSO and drought (SPEI)

This section evaluates how well the RCMs simulate the link between ENSO and droughts (SPEI) over southern Africa. Figure 31 shows a strong correlation between ENSO and droughts over southern Africa for both observations and simulations.

In the CRU result (Figure 31a), the correlation between ENSO and SPEI shows a marked dipole pattern over southern Africa with positive values (r ≥ 0.6) over the eastern part of the tropical area (north of 15°S) and negative values (r ≤ −0.6) over the subtropical area (south of 15°S). The correlation is weak (r = ±0.3) over the western part of the tropical area. It is also weak over the south-western tip of southern Africa. The RCM simulations show different patterns of the correlation between the ENSO and southern African droughts. In some RCMs (i.e. ARPEGE), the simulated correlation pattern is close to the observed (or ERAINT) pattern, but in other RCMs (i.e. CRCM) the pattern is different.

Among the RCMs, ARPEGE simulates the best correlation pattern, although its result is closer to the ERAINT pattern than it is to the CRU pattern. The main shortcoming in the ARPEGE correlation pattern is that it shows a stronger correlation than observed over the entire southern Africa, even over the south-west, where CRU shows no correlation. However, the best performance of ARPEGE here is consistent with Kalognomou et al. (2013), who showed that ARPEGE consistently outperforms all CORDEX RCMs over southern Africa in all seasons. The good performance of ARPEGE in simulating the link between ENSO and southern African droughts may be because ARPEGE is a global stretch-grid model. This may help the model to yield a better simulation of the Walker circulation, and to experience no shock at the lateral boundaries between the driving data (ERAINT) and RCM dynamics.

RegCM3 also captures the general pattern of the observed correlation between ENSO and droughts, but its area of significant correlation is confined to the central area of southern Africa. The model fails to reproduce the negative correlation over Namibia and southern Angola, where it shows a positive correlation. Only HIRHAM and REMO show a good correlation over Namibia and southern Angola; other RCMs (including ARPEGE) either show a weaker correlation or show opposite correlation when compared to the observed pattern. Nevertheless, HIRHAM and REMO simulate poor correlation patterns elsewhere, especially over the eastern side of southern Africa. This agrees with a previous study (Haensler et al. 2011a) that showed that the REMO model has a better skill in the drier areas (i.e. the south-west) than in the more humid areas (south-east and north-east) of southern Africa. In the

RCA model, the areas of significant correlation are scattered over southern Africa, but in WRF the area of significant correlation is displaced south with few patches over southern Namibia and Botswana. CRCM portrays the most striking correlation pattern; it shows no correlation to weak correlation over the entire southern Africa. Hence, among the CORDEX RCMs, CRCM shows the lowest capability in linking ENSO with the southern African droughts. Hernandez-Diaz et al. (2013) also reported that CRCM has cold biases over most areas in southern Africa.

There is a good agreement between ERAINT and RCM 850 mb mean winds over southern Africa in DJF (Figure 31). South of 15°S, the wind pattern is characterised with strong anti-cyclonic wind over the southern Atlantic Ocean (i.e. west of southern Africa) and strong easterlies transporting warm, moist air from the Indian Ocean to the subcontinent. North of 15°S, the wind pattern is characterised by strong north-easterlies in the east and westerlies in the west, producing convergence flow at the centre. The major difference between ERAINT and RCM wind patterns is that the westerlies are stronger in the RCM (except HIRHAM) than in ERAINT. It is difficult to link the wind pattern with the ENSO-drought correlation pattern, but generally, in the ERAINT and RCM (except in CRCM), the area of negative correlation experiences easterly winds (from Indian Ocean), while the area of positive correlation experiences north-easterly or westerly flow.
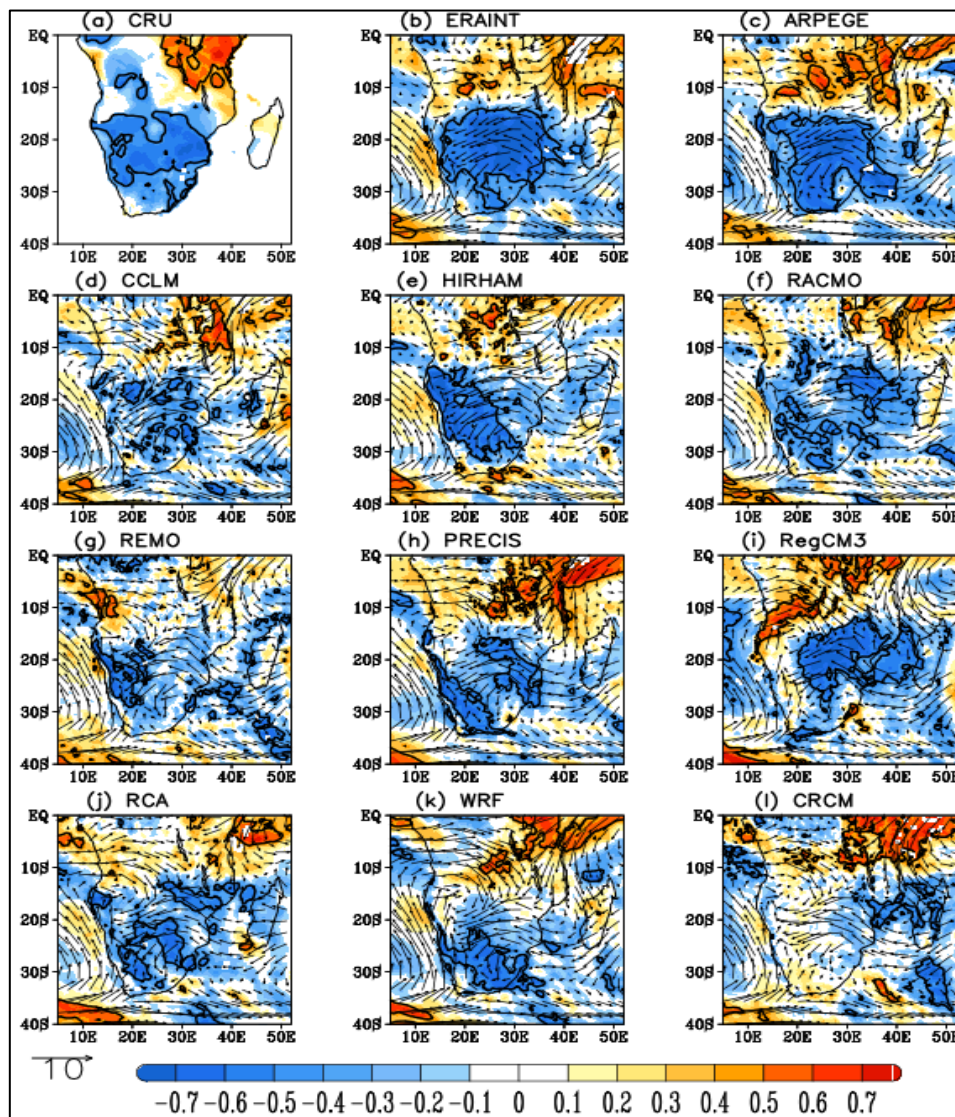
Figure 31: The coefficient of correlation between ENSO and drought (SPEI) over southern Africa in summer (DJF, 1989–2008), as observed (CRU and ERAINT) and simulated (CORDEX RCMs). The contours show areas where the correlation is significant at 95% using the t-test. The corresponding 850 hPa winds are shown in the background; the arrow at lower left corner indicates 10 m/s wind speed

4.3.2   The influence of ENSO on precipitation and temperature

We examine how well the models simulate the relationship between ENSO and the two climate variables (precipitation and temperature) used in computing the drought index (SPEI). The correlation between ENSO and precipitation over the study area shows a good resemblance with that of ENSO and drought (compare Figure 31 and Figure 32). The general pattern shows positive correlations (r ≈ 0.5) over the tropical region and negative correlation (r ≈ −0.6) over the subtropical region. The significant negative correlation over central parts of southern Africa suggests that a warm ENSO event will induce lower rainfall over southern Africa, while a cold ENSO event will produce above-normal rainfall conditions, which is consistent with the findings from previous studies over the region. As in CRU data, most RCMs show negative correlation over central parts of southern Africa. The ARPEGE best captures this well-known feature over southern Africa. In line with Figure 31, the HIRHAM and REMO models show a strong correlation over Namibia. The weakness of the CRCM in capturing the link between ENSO and droughts is also reflected in capturing the link between ENSO and rainfall.
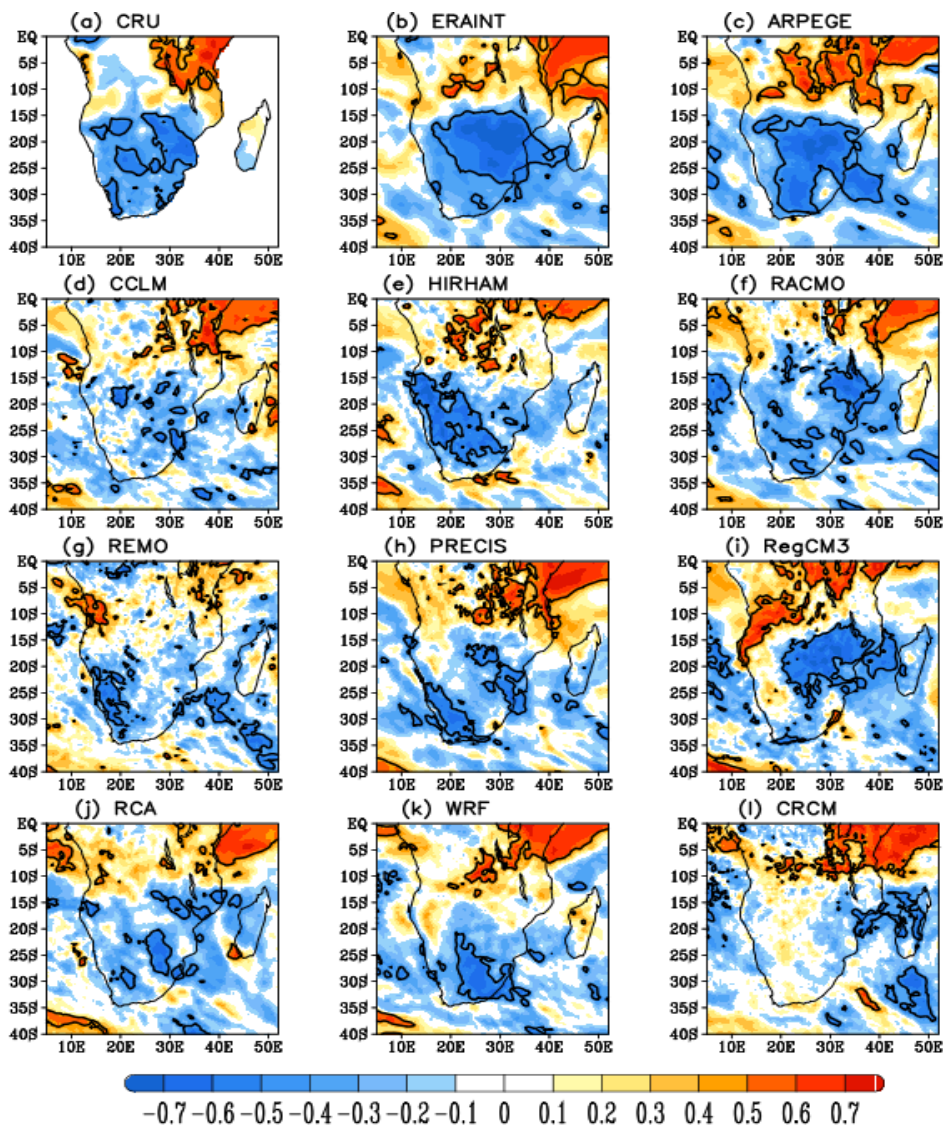
Figure 32: The coefficient of correlation between ENSO and precipitation over southern Africa in summer (DJF), as observed (CRU and ERAINT) and simulated (CORDEX RCMs). The contours show areas where the correlation is significant at 95% using the t-test

The CRU data shows a significant positive correlation between ENSO and temperature in DJF over the bulk of southern Africa (Figure 33). During El Niño years, the convergence zone that normally reaches 20°S in January (i.e. during the austral summer) is weakened and shifted to the east and north, resulting in dry conditions over the subcontinent (Mason 2001). In comparison to the observations, the ARPEGE continues to show a high reliability in simulating the relationship between ENSO and temperature over southern Africa, but performs poorly over Angola, where ERAINT does not perform well either.
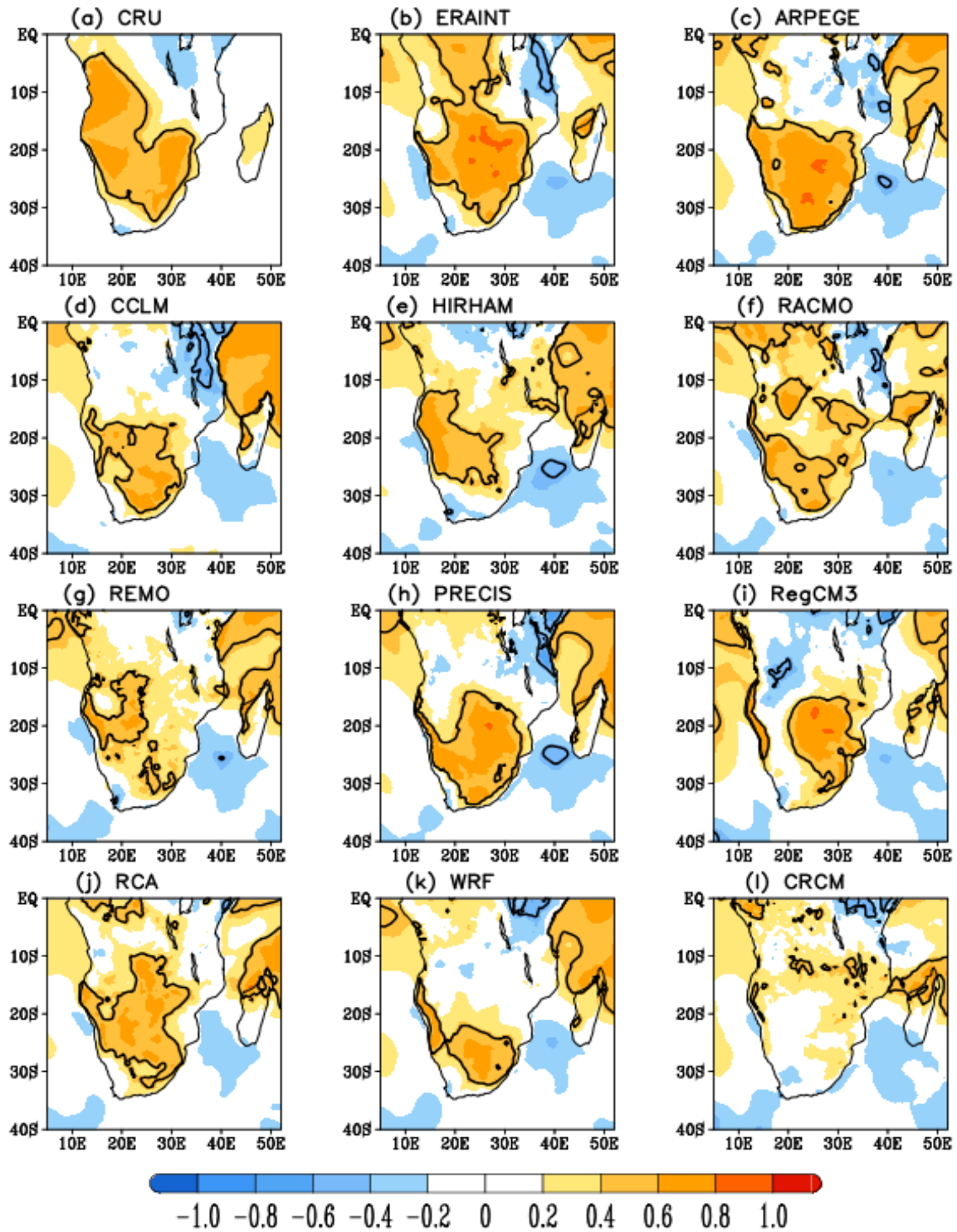
Figure 33: The coefficient of correlation between ENSO and temperature over southern Africa in summer (DJF), as observed (CRU and ERAINT) and simulated (CORDEX RCMs). The contours show areas where the correlation is significant at 95% using the t-test

Figure 34 compares the influence of ENSO on rainfall, temperature, and drought over the three selected areas (see Figure 30): Limpopo area (LP: 27°–32°E, 20°–25°S), north-eastern South Africa (NS: 19°–25°E, 30°–26°S) and over the north-eastern highlands of Tanzania (TZ: 35°–39°E, 5°–2°S). Over Limpopo (the drought corridor), the correlation between ENSO and temperature (r ≈ 0.7) is stronger than the correlation between ENSO and rainfall (r ≈ −0.5; Figure 34a). The same is true over the north-eastern South Africa (Figure 34b), but the reverse is the case over the north-eastern highlands of Tanzania (Figure 34c). ERAINT results also show that the influence of ENSO is stronger on temperature (or on SPEI) than on rainfall over the two areas. All RCMs (except HIRHAM) simulate this characteristic. However, most RCMs (i.e. CCLM, HIRHAM, RACMO, REMO, RCA, CRCM and WRF) grossly underestimate the link between ENSO and drought (rainfall and temperature) over the three areas (Limpopo, north-eastern South Africa and north-eastern highlands of Tanzania).
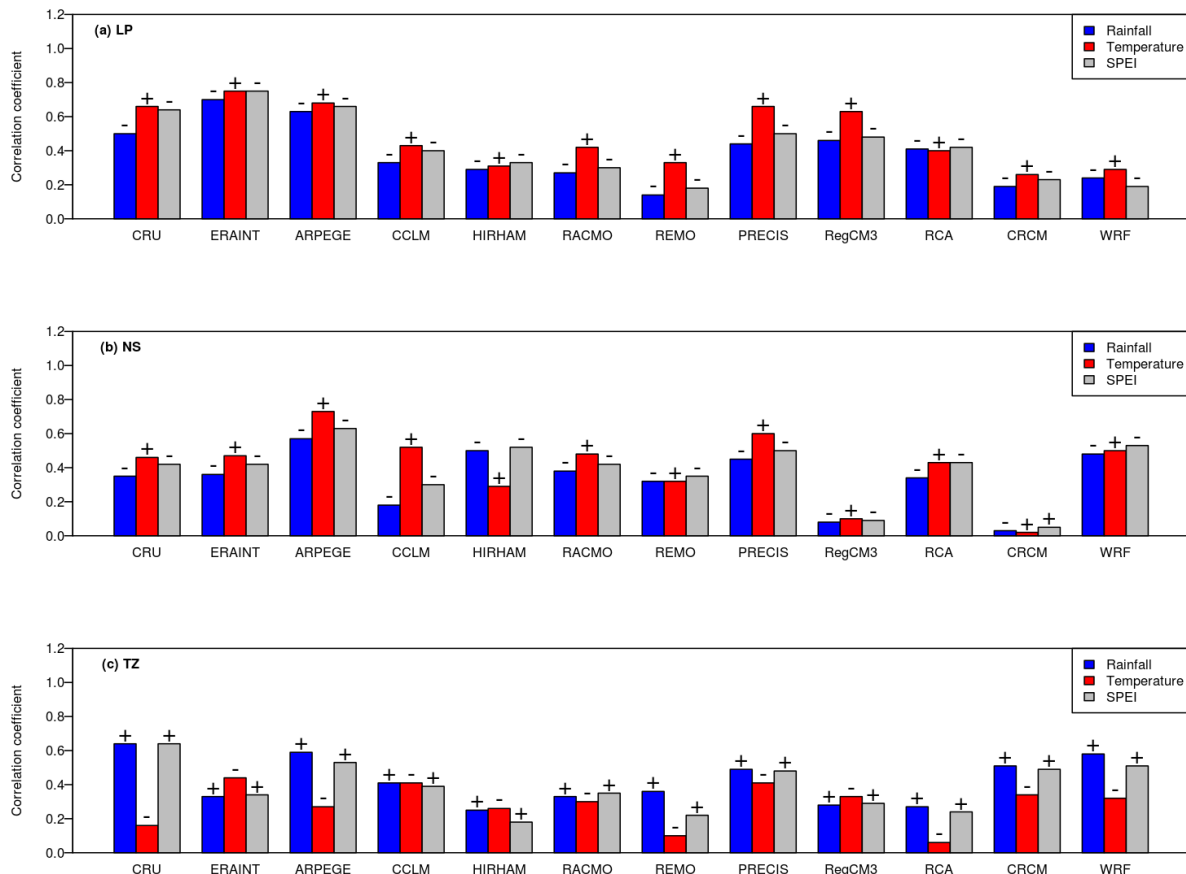
Figure 34: The coefficient of correlation between ENSO and climate variables (rainfall, temperature and SPEI) over (a) Limpopo (LP), (b) north-western South Africa (NS), and (c) North-eastern Tanzania (TZ). The signs of the correlation coefficients are indicated on the bars

4.3.3 Composite of SPEI, precipitation and temperature during El Niño and La Niña events

For a better understanding of the impact of ENSO on southern African droughts, we present the composites of SPEI, precipitation, and temperature during El Niño and La Niña conditions (Figure 35 and Figure 36). Within our study period (1989–2008), there were six El Niño events (1991/92, 1994/95, 1997/98, 2002/03, 2004/05 and 2006/07) and six La Niña events (1995/96, 1998/99, 1999/2000, 200/01, 2005/06 and 2007/08). Figure 35 shows the composite of SPEI for the La Niña events. The figure shows that the cold phase of ENSO (La Niña) is associated with positive SPEI (wet conditions) over the subtropical southern Africa and negative SPEI (dry conditions) over the north-eastern tropical area.

The RCMs (except CRCM) show similar patterns as the observations, but the magnitude of the SPEI anomalies during the La Niña and El Niño events are weaker than the observed; only ARPEGE produces the magnitude of SPEI anomalies that is comparable with observation. Contrary to observation, some RCMs (e.g. REMO, PRECIS and RegCM3) simulate no changes in SPEI over the Drakensberg Mountains (around the Kingdom of Lesotho) during the La Niña and El Niño conditions. High elevation areas, such as the Drakensberg Mountains, usually experience higher precipitation with lower temperatures (i.e. lower PET) than the surroundings; this might reduce the severity of drought over the mountains, and some models might find it difficult to simulate this process.
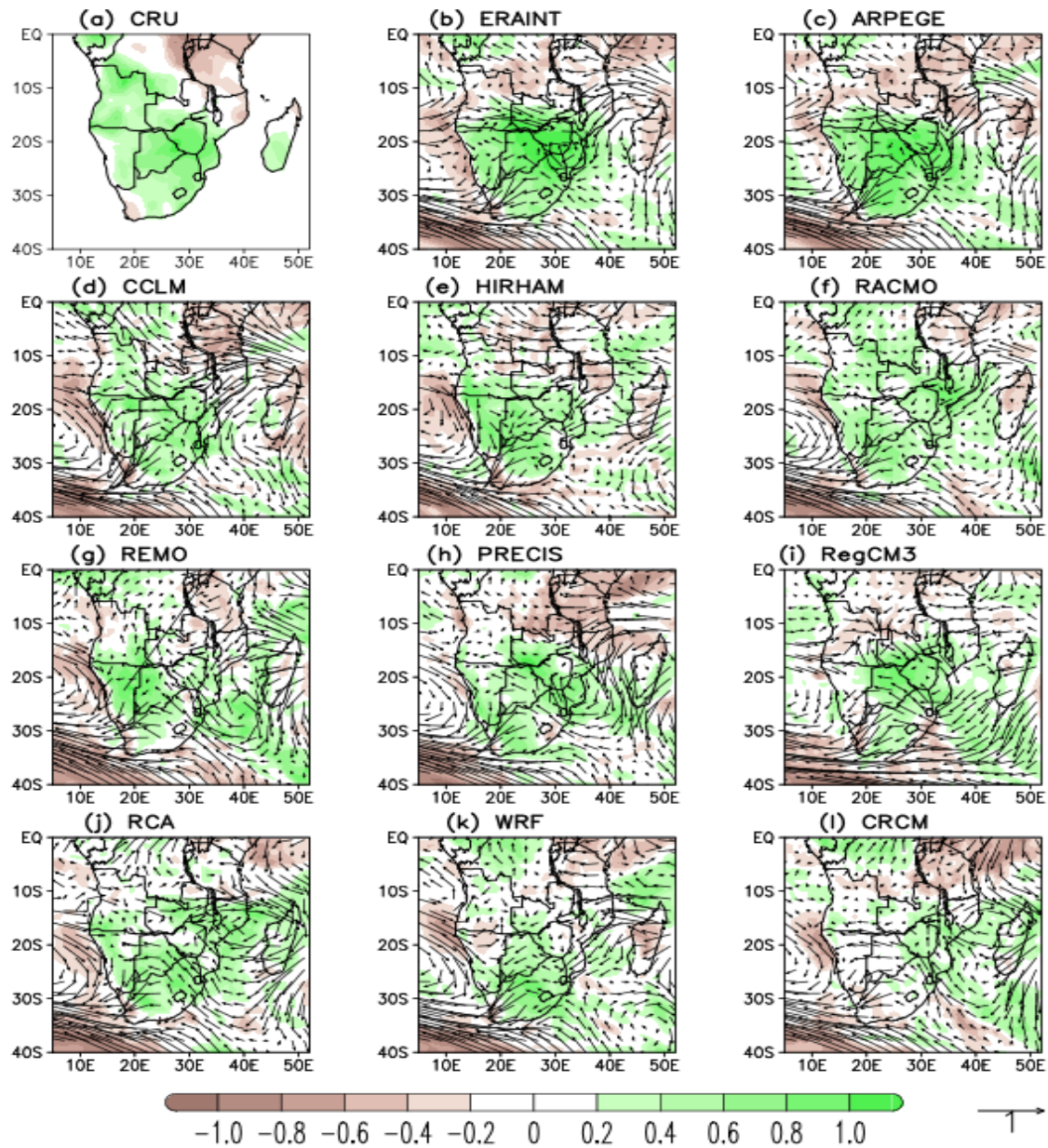
Figure 35: The composite of drought index (SPEI) and wind anomalies at 850 hPa in December–January of La Niña years

43
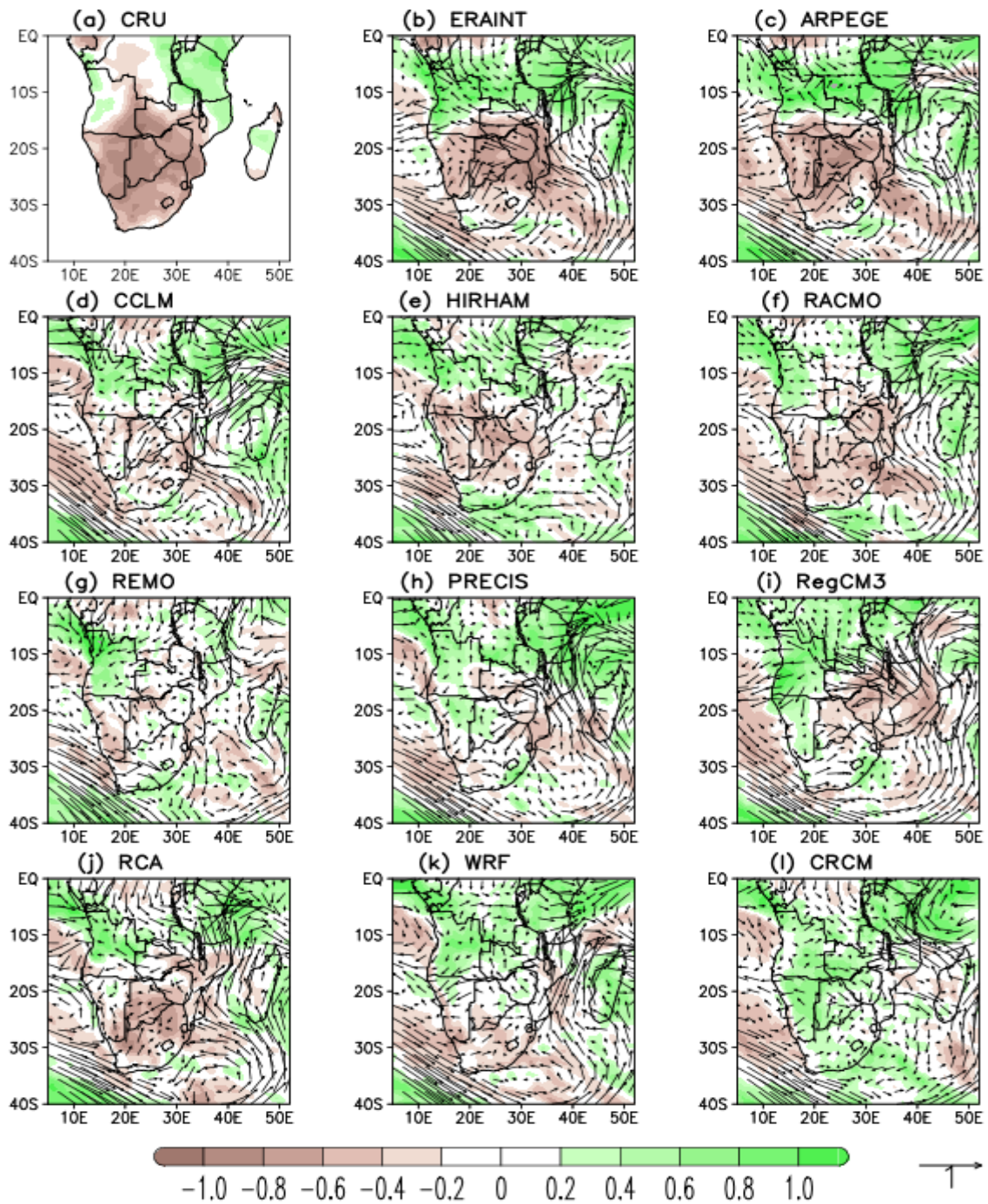
Figure 36: The composite of drought index (SPEI) and wind anomalies at 850 hPa in December–January of El Niño years

4.3.4   The influence of boundary conditions

This section investigates the sensitivity of the simulated link between ENSO and southern African drought to the GCM simulations used as boundary forcing. We used the RCA model to examine the influence of boundary conditions. The RCA was chosen because it was the only model available with different GCM forcing. However, as shown in the previous section, RCA also gives a credible simulation of the link when forced with ERAINT; hence, the model is also suitable for the sensitivity experiment.

Figure 37 represents the GCM simulated links between ENSO and SPEI, Figure 38 shows the link after the GCM simulations are dynamically downscaled with RCA, while Figure 39 gives the added value of the downscaling to the simulated link when compared with observation. The added value (δ), which is

a measure of difference between GCM and RCM errors, was computed according to Di Luca et al. (2012; 2013) as:

$$\delta = \left(r_{GCM} - r_{OBS}\right)^2 - \left(r_{RCM} - r_{OBS}\right)^2 \dots\dots\dots\dots\dots\dots\dots\dots\dots\dots\dots\dots (1)$$

where, r_{OBS}, r_{GCM} and r_{RCM} represents the correlation between ENSO and SPEI in observation, GCM, and RCM, respectively. A positive value of δ means that the RCA downscaling improves the simulated link, while a negative value indicates that the RCM downscaling does not improve the simulated link.

With or without the downscaling, the correlation patterns for ERAINT are the same (Figure 37a and Figure 38a) and the added value of the downscaling is negative over most areas in southern Africa (Figure 39a), except over a small area in the northern part of Angola. Hence, downscaling ERAINT results with RCA adds no value to the simulated link between ENSO and southern African droughts. While the downscaling improves the simulated link for some GCMs (i.e. CCMA, CNRM and MIROC), it adds no substantial value to the simulated link for other GCMs (i.e. NOAA, MPI, NCC and MOHC). Without downscaling, the CCMA simulation fails to simulate the negative correlation over the central part of southern Africa and over the north-eastern part of South Africa and fails to reproduce the positive correlation in the north-eastern part of southern Africa (Figure 37b). The RCA downscaling corrects these biases (Figure 38b) and provides an added value of more than 0.5 over the areas (Figure 39b).

CNRM simulation, on the other hand, fails to simulate the negative correlation pattern over the southern part of South Africa and over Mozambique (Figure 37c). It also fails to simulate the positive correlation over the north-eastern part of southern Africa (Figure 37c). Unfortunately, we do not have the necessary data to diagnose the reason for the poor performance of CNRM in simulating the link; however, it may be due to the boundary conditions or the convective parameterization schemes used in the model.

The RCA downscaling corrects the shortcoming to an extent and provides an added value up to 0.2 over South Africa and up to 0.6 over Tanzania (Figure 38c). MIROC fails to simulate negative correlation in the 20°–30°S zone and the positive correlation over Tanzania (Figure 37e). While the RCA downscaling corrects the MIROC bias in the 20°–30°S zone (with up to 0.8 added value), it does not improve the simulated link over Tanzania (Figure 38e). For the simulations of the remaining four GCMs, the RCA downscaling only provides added values over small areas, i.e. over Tanzania in NOAA (Figure 39d), over the border of Zambia and Tanzania in MPI (Figure 39f), and the northern part of Angola in NCC (Figure 39g). However, it is important to note that the added value of RCA to GCM results decreases as the GCM bias ($bs = r_{GCM} - r_{OBS}$) in simulating the ENSO drought decreases. For instance, ERAINT is already very good in representing the link ($bs < 0.2$, except over Congo) because of data assimilation; hence, RCA is not adding value (δ ≈ −0.4). On the other hand, CNRM is poor in simulating the link ($bs > 0.6$), the RCA added value is substantial ($bs > 0.8$).
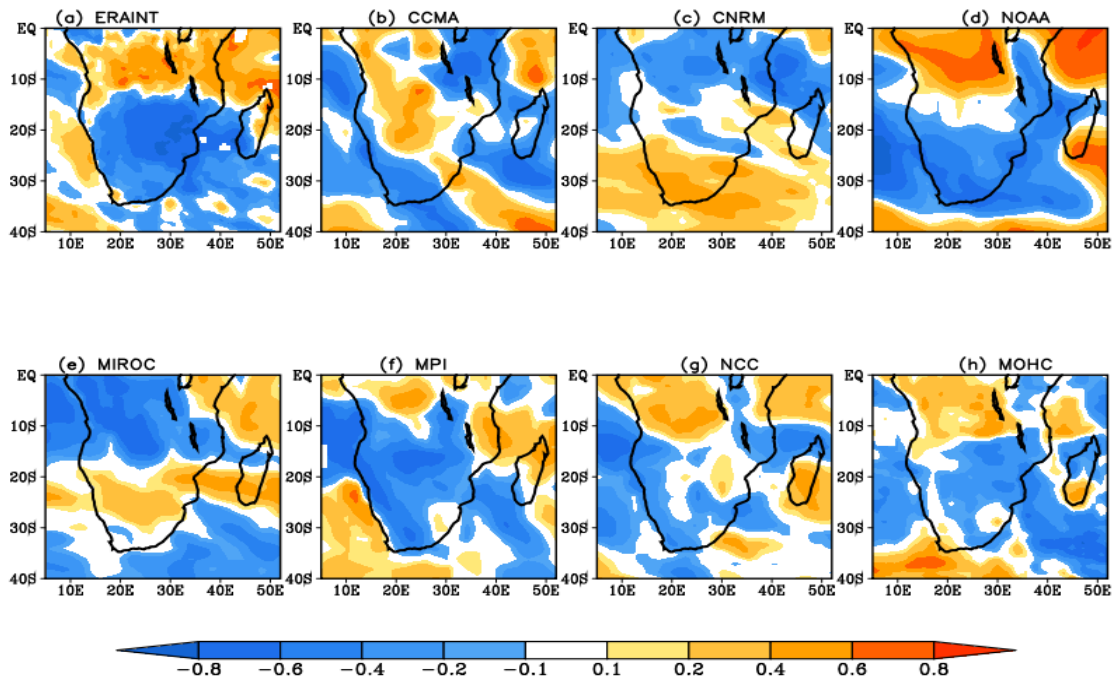
Figure 37: The coefficient of correlation between ENSO (i.e. Nino3.4) and drought index in ERAINT and GCM simulations
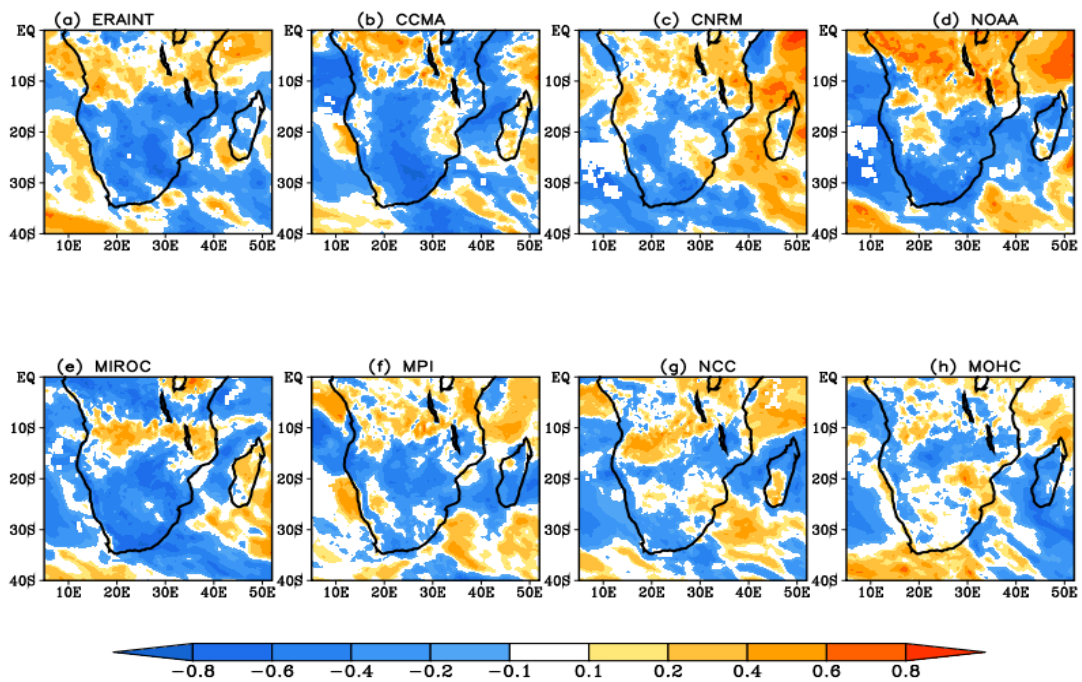
Figure 38: The coefficient of correlation between ENSO (i.e. Nino3.4) and drought index in RCA simulations forced with ERAINT and GCM data sets
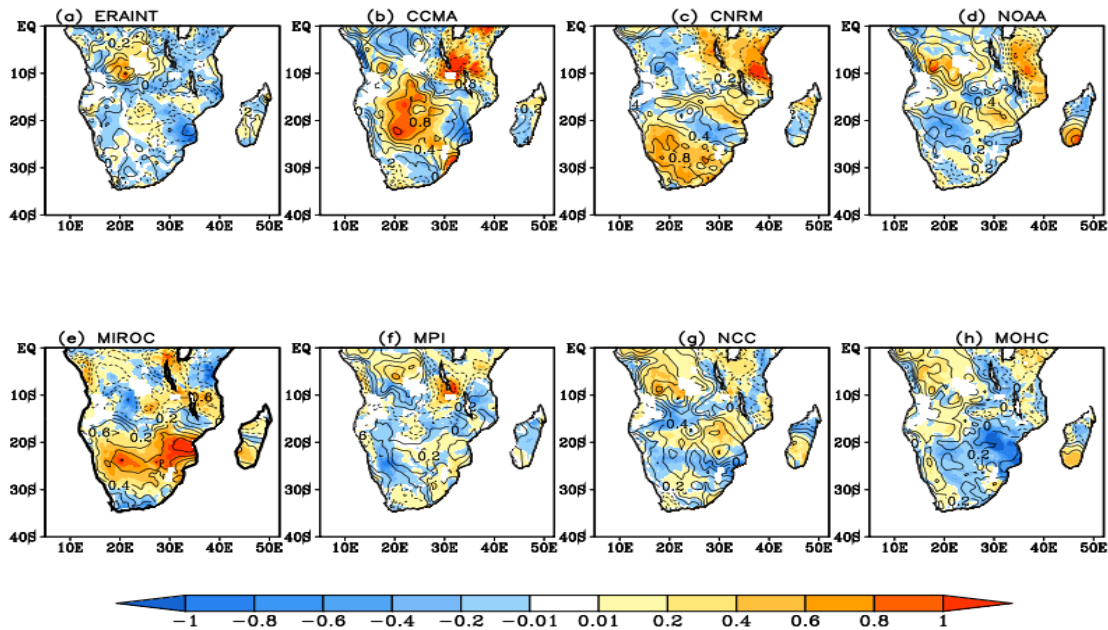
Figure 39: The added value (shaded) of the RCA dynamical downscaling to the simulated link between ENSO and droughts in southern Africa. The GCM biases in simulating the link are indicated with contours; the contour interval is 0.2

Focusing on the drought corridor area in southern Africa, the RCA downscaling improves the simulated ENSO-drought link over the area in some cases and worsens it in other cases (Figure 40). However, none of the RCA downscaling reproduces the magnitude of the observed link. With ERAINT, the RCA downscaling weakens the simulated link because it reduces the influence of ENSO on both rainfall and temperature (Figure 40). In two cases (CNRM and MOHC), the downscaling produces a wrong sign of the correlation between ENSO and the drought index, even though the GCM produce the right sign. This occurs because the RCM compromises the sign of the correlation between ENSO and the rainfall over the area. In some cases, the downscaling improves the simulated correlation between ENSO and the drought index. This is because the RCM improves the simulation between ENSO and rainfall, or between ENSO and temperature, or both. However, downscaling MIROC and NOAA simulations gives the best ENSO-drought link over LP (Figure 40a) and NS (Figure 41a), while downscaling MPI and NOAA simulations gives the best ENSO-drought link over north-eastern Tanzania (Figure 42a).
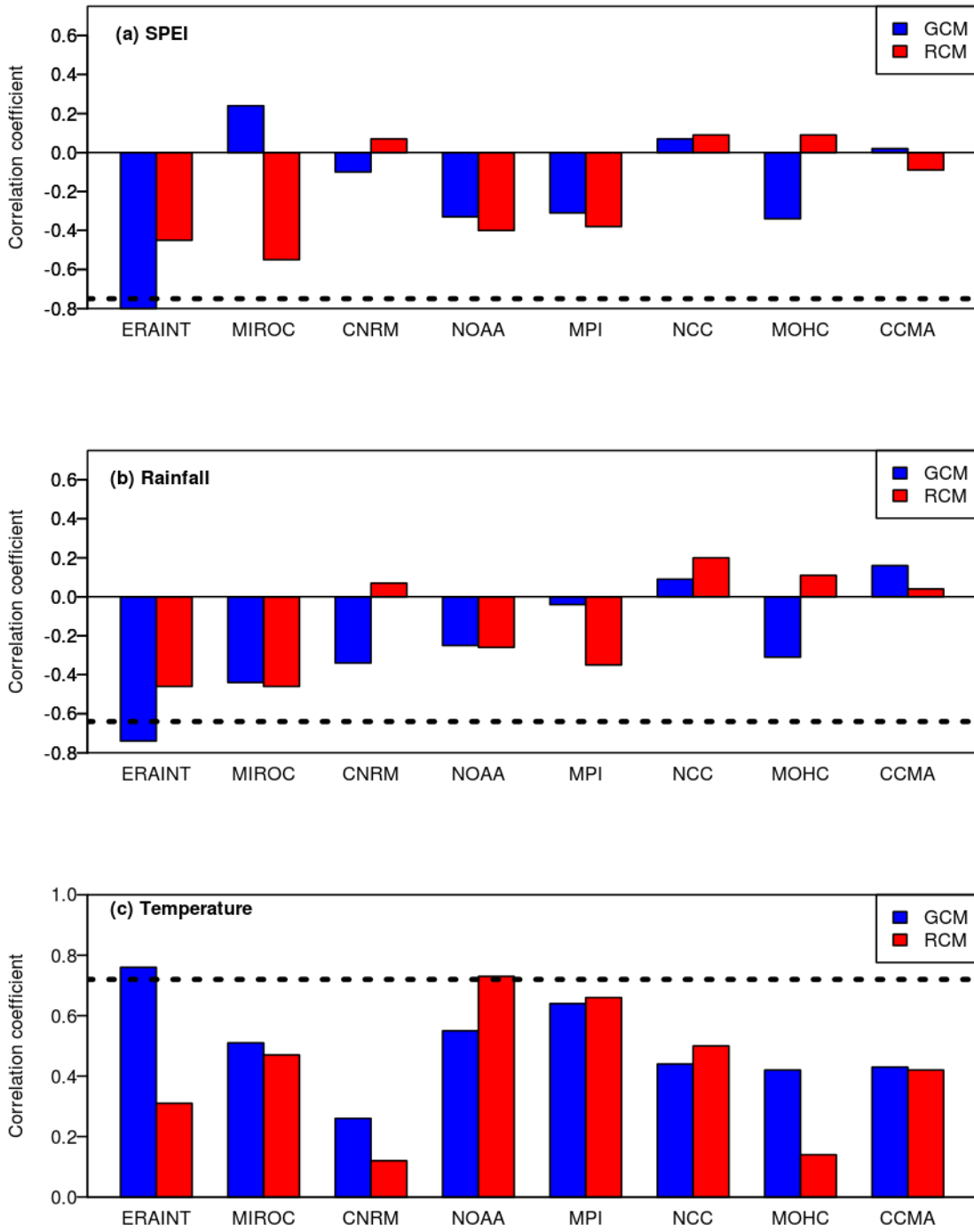
Figure 40: The correlation between ENSO and (a) SPEI, (a) rainfall and (c) temperature (c) over the drought corridor (LP) in southern Africa for both GCM and RCA4. The dotted line represents the value of the CRU data
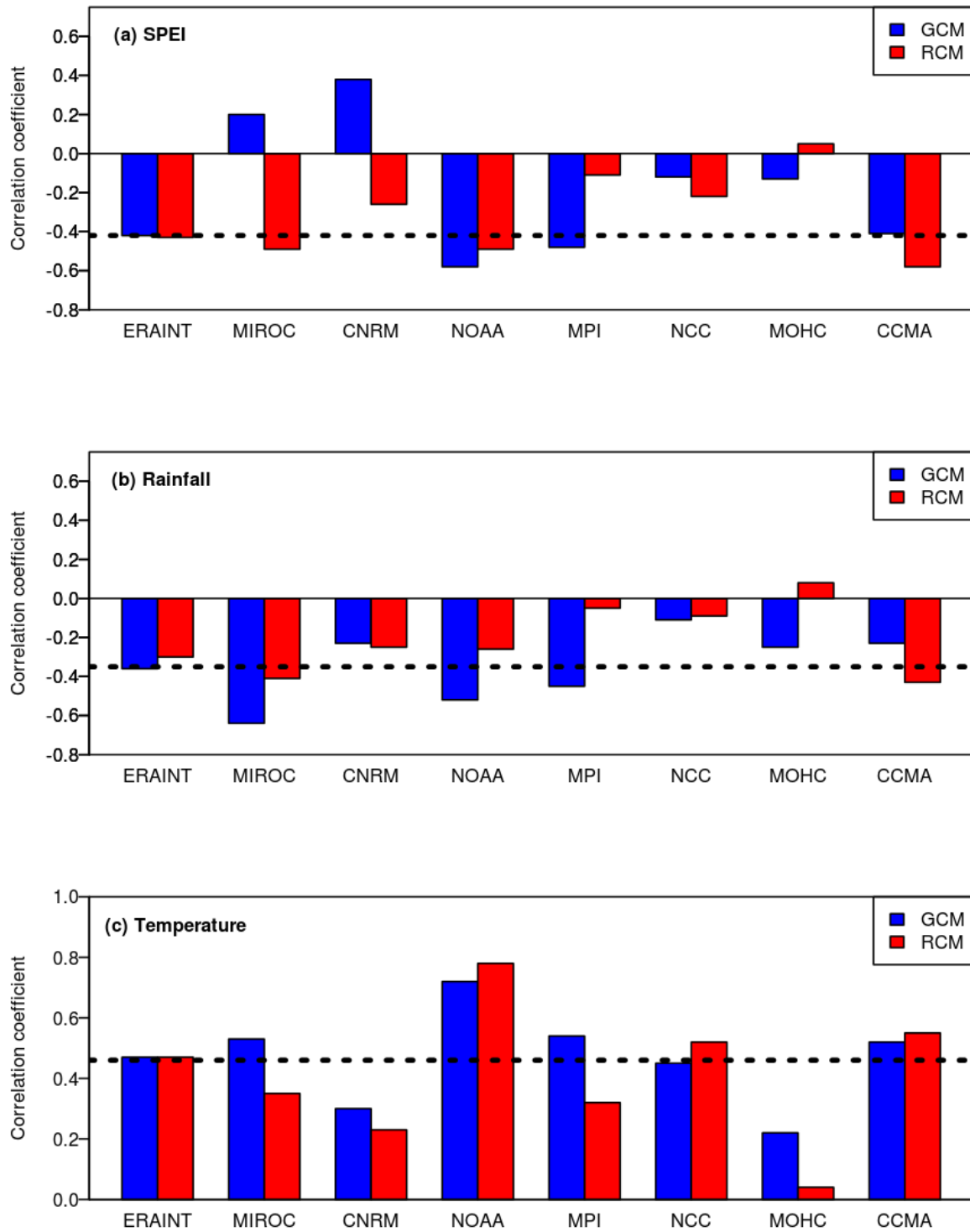
Figure 41: Same as in Figure 40 but over north-western South Africa (NS)
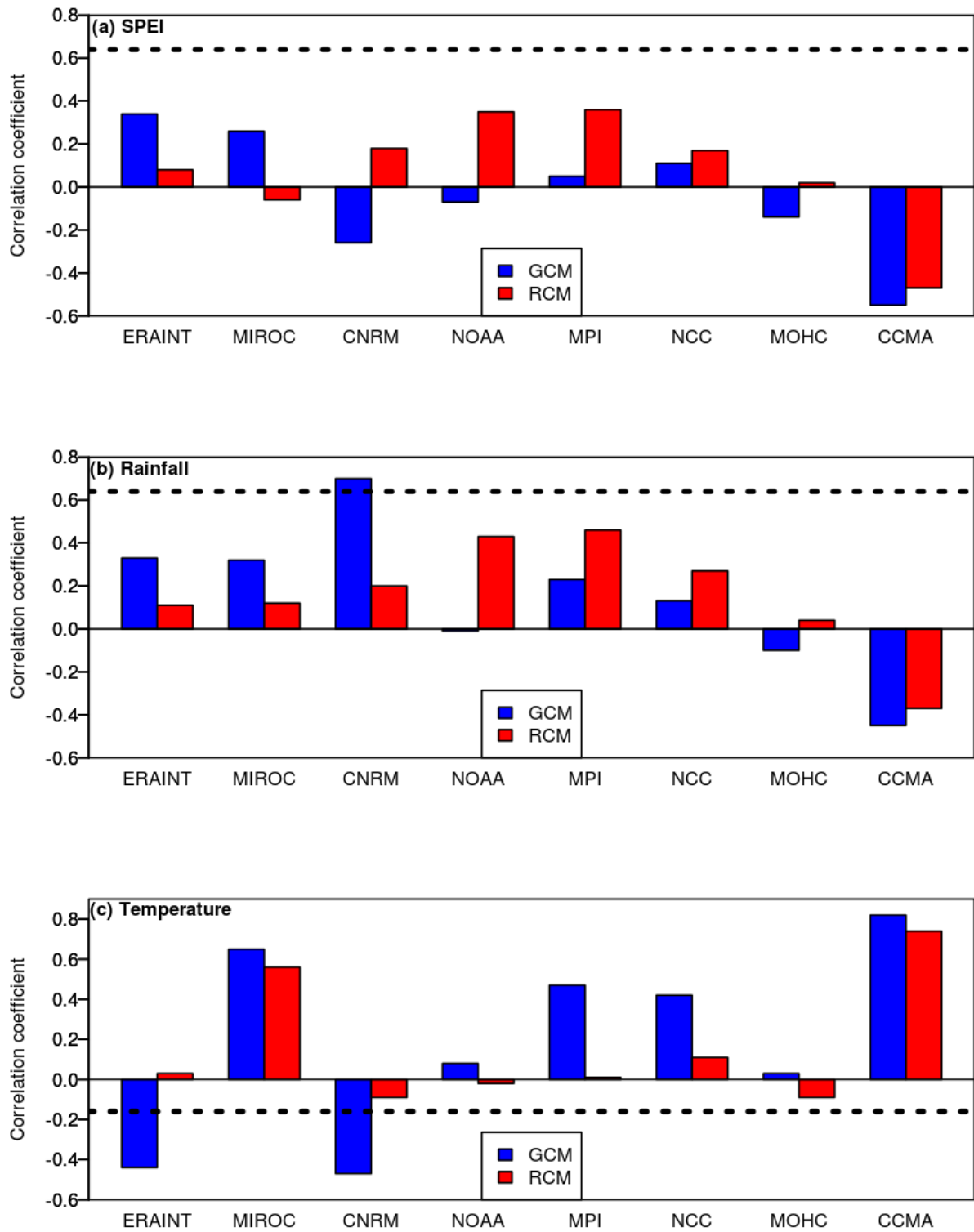
Figure 42: Same as in Figure 40 but over north-eastern Tanzania

4.4   Simulating the Drought Modes

4.4.1   GCM results

Figure 43 and Figure 44 compare the simulated drought modes (i.e. rotated PCA loadings of the three-month and 12-month SPEI, respectively) with the observed. Note that the observed drought modes in these figures are similar to those in Figure 2 and Figure 3 (Chapter 2) despite the difference in the length of the data used. This further establishes the robustness of the four drought modes over the region. In general, the figures show that all the GCMs reproduce the observed principal factors well, though with some notable differences.

With the three-month SPEI, all models show the best performance in reproducing DM1 and the worst performance in reproducing DM4. In DM1, the correlation (r) between the simulated and observed mode is 0.9 for all the GCMs.

In DM2, five GCMs (BCC-CSM, BNUESM, CNRMCM, FGOALS and MIROCESMCH) show a lower correlation (r = 0.8) with observation, but other GCMs maintain the correlation (r = 0.9) as in DM1.

In DM3, HadGEM3 and MIROC5 have the highest correction (r = 0.9), while BNUESM gives the lowest correlation (r = 0.6). The main shortcoming in the DM3 drought mode of BNUESM is that the mode features a dipole loading within the tropics, between the central and eastern part of southern Africa, contrary to the observed mode.

In DM4, BCC-CSM and CanESM2 have the highest correction (r = 0.8), while CNRMCM gives the least correlation (r = 0.3) because it misses the location and orientation of the dipole mode of DM4.

For all GCMs, the agreement between the simulated and observed drought modes in 12-month SPEI is weaker than in the three-month SPEI. For DM1, BNUESM and MIROC5 have the highest correlation (r = 0.8) with the observation, while CanESM2, GFDL2G and GFDL2G have the least correlation coefficient (r = 0.6).

For DM2, CanESM2, GFDL2G and GFDL2G and HadGEM3 feature the highest correlation coefficient (r = 0.7), while BNUESM and FGOAL feature the least correlation coefficient (r = 0.3).

For DM3, FGOAL and MIROC5 show the highest correlation coefficient (r = 0.8), while BCC-CSM show the least correlation coefficient (r = 0.3).

For DM4, FGOAL has the highest correlation (r = 0.7), while GFDL2M has lowest correlation (r = 0.2).

A closer look at Figure 43 and Figure 44 reveals that in all GCMs (except MIROC5, HadGEM2 and CNRMCM at both three- and 12-month scales and BNUESM at three-month scales), the drought mode with the lowest percentage of explained variance (among the selected four drought modes) has the lowest correlation coefficient. This suggests that the drought mode may not be the most comparable with observed drought mode, and the most comparable may not be among the leading four principal factors. Our emphasis in this study is to see how well the first four simulated drought modes in the GCMs agree with the observed.

In general, the GCMs performance with respect to drought mode is encouraging. With the three-month SPEI, all the GCMs simulate the first three drought modes (DM1, DM2 and DM3) with a high correlation (i.e. r > 0.6), while 70% of the GCMs simulate all the observed drought modes with a high correlation.

With the 12-month SPEI, all the models simulate the first drought mode (DM1) with a high correlation coefficient, and 60% of the models simulate at least three of the drought modes with a high correlation coefficient. It is not logical to compare the time variation of the simulated modes (i.e. scores) with the observed, because the simulations used in this study are obtained with coupled models in which the time variation may not synchronize with observation. However, the results here show that the climatology of the dominant drought modes in southern Africa is well reproduced in most GCMs.
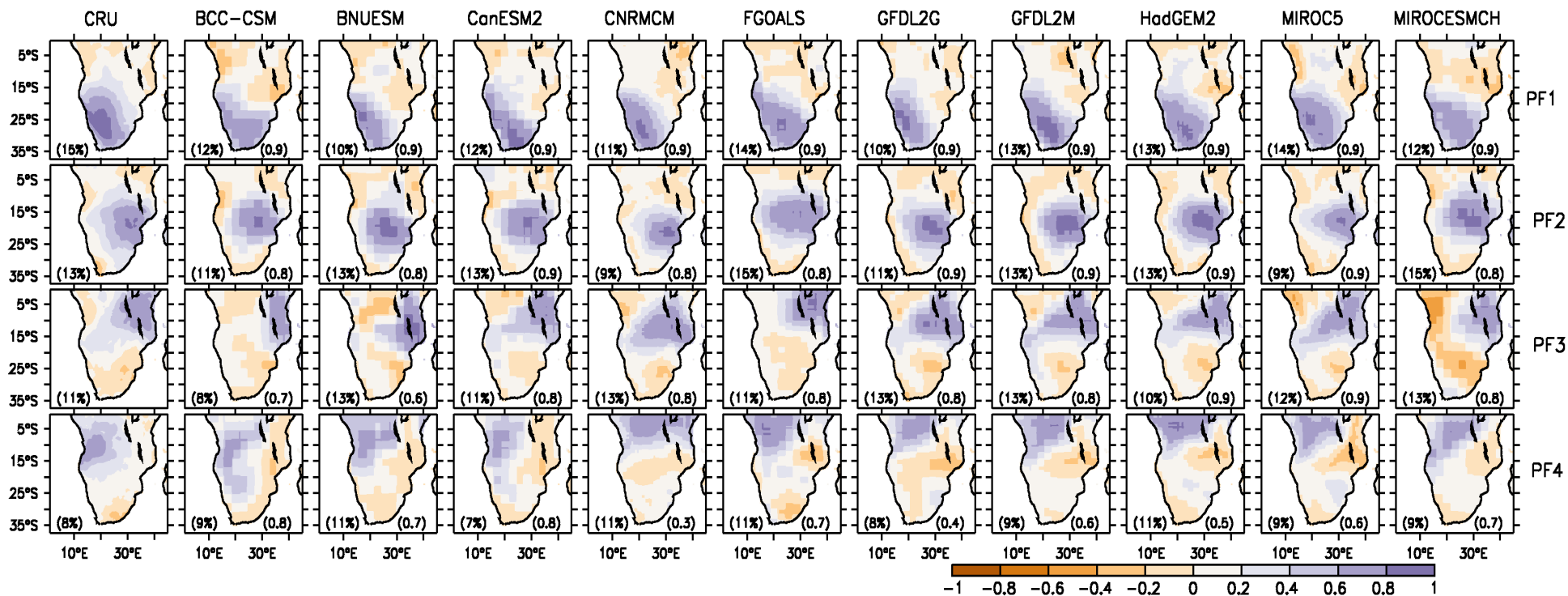
Figure 43: The observed and simulated PCA loadings of three-month SPEI over southern Africa. The percentage of variance explained by each principal factor is indicated at the lower left corner of the panel. The spatial correlation between observed and simulated loadings for each model is shown at the lower right corner of the model's panel
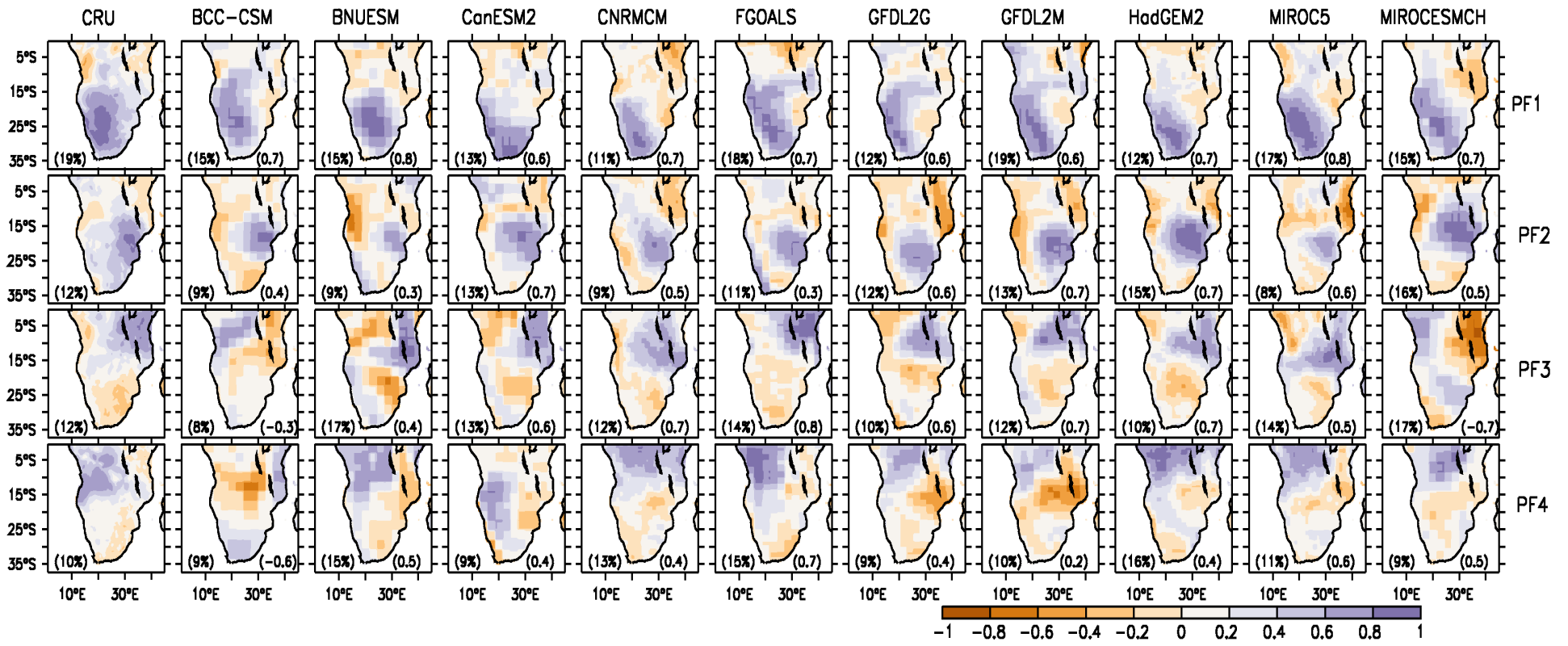
Figure 44: Same as Figure 43 but for 12-month SPEI

4.4.2   RCMs results

Spatial variation

The RCM simulated drought modes are compared with the observed at three- and 12-month scales (Figure 45 and Figure 46, respectively). Note that the observed four modes obtained in this case differ from those obtained previously in Section 3.2.1. The period of availability of RCM simulation data sets is much shorter (1989–2007) than for the GCM (1956–2002). Hence, in order to accommodate the required dimensions for the PCA (time-number of grid cells), we reduced the area of the region of study (fewer grid cells). As a result, the drought mode named DM3 in our previous discussions, whose strongest features are over Tanzania, has been replaced by a new drought mode. In general, all models performed better at three-month than at 12-month scale.

As with the GCMs, all RCMs also performed better at the three-month scale than at the 12-month scale. At three-month scale, the first three drought modes are well simulated by all RCMs despite some differences in the performance of the models.

For DM1, the correlation between the simulations and observation was between 0.6 and 0.9, with RCA35, REMO and WRF3 showing the least performance (r = 0.6). It was between 0.7 and 0.8 for DM2 and between 0.7 and 0.9 for DM3. The RCMs struggled in reproducing DM4. In this regard, CNRM and RACMO2 (r = 0.5) performed worst, while CCLM, REGCM3, REMO and WRF3 performed best (r = 0.7).

At 12-month scale, the performance of the models in simulating drought modes was generally lower than at three-month scale. For DM1, only three models captured spatial modes of the drought mode well (r > 0.5). WRF3 performed best (r = 0.8) while RACMO2 performed worst (r = 0.4). All the RCMs models reproduced DM2 at high correlations (r = 0.8 and 0.7), except RACMO2 (r = 0.5). For DM3, REGCM3 showed the least correlation with the observed (r = 0.6) while CNRM, CRCM5 and REMO the highest (r = 0.8). For DM4, all models captured the mode well, except CNRM (r = 0.4). CCLM and RCA35 showed the highest correlation with observation (r = 0.8).
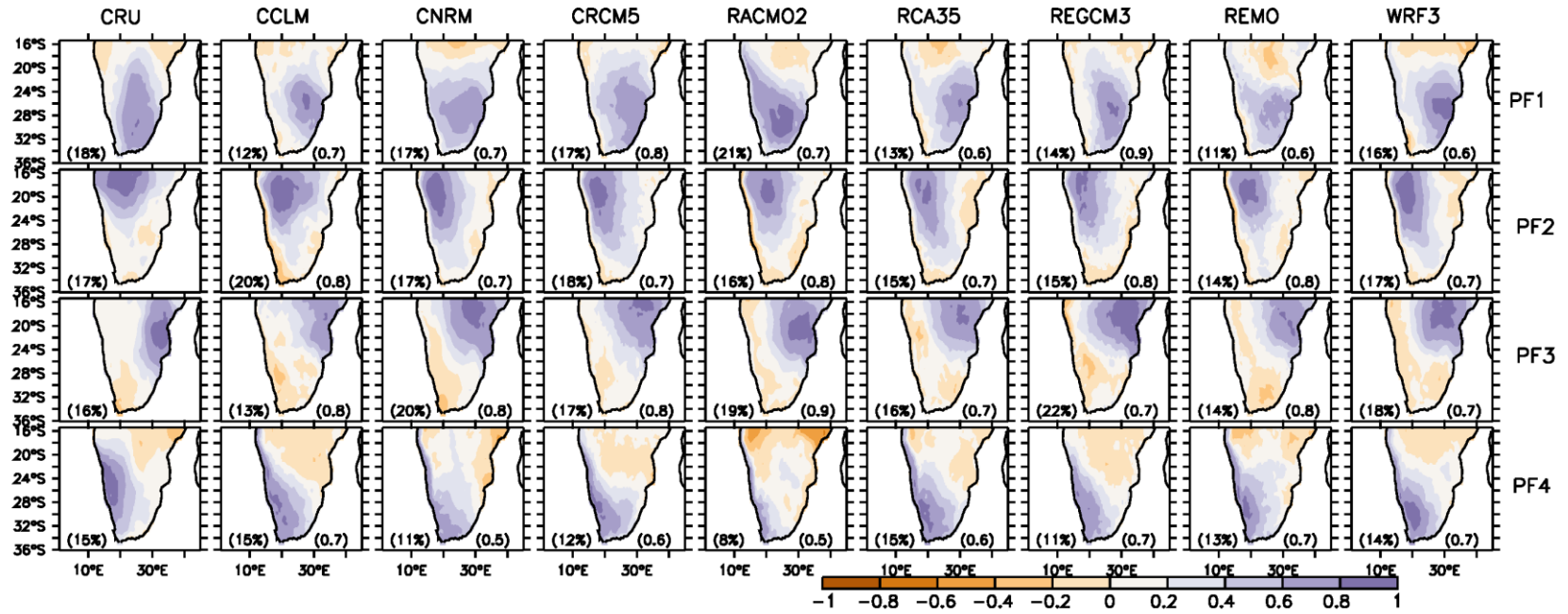
Figure 45: The observed and simulated PCA loadings of three-month SPEI over southern Africa by RCMs. The percentage of variance explained by each principal factor is indicated at the lower left corner of each panel. The spatial correlation between observed and simulated loadings for each model is shown at the lower right corner of the model's panel
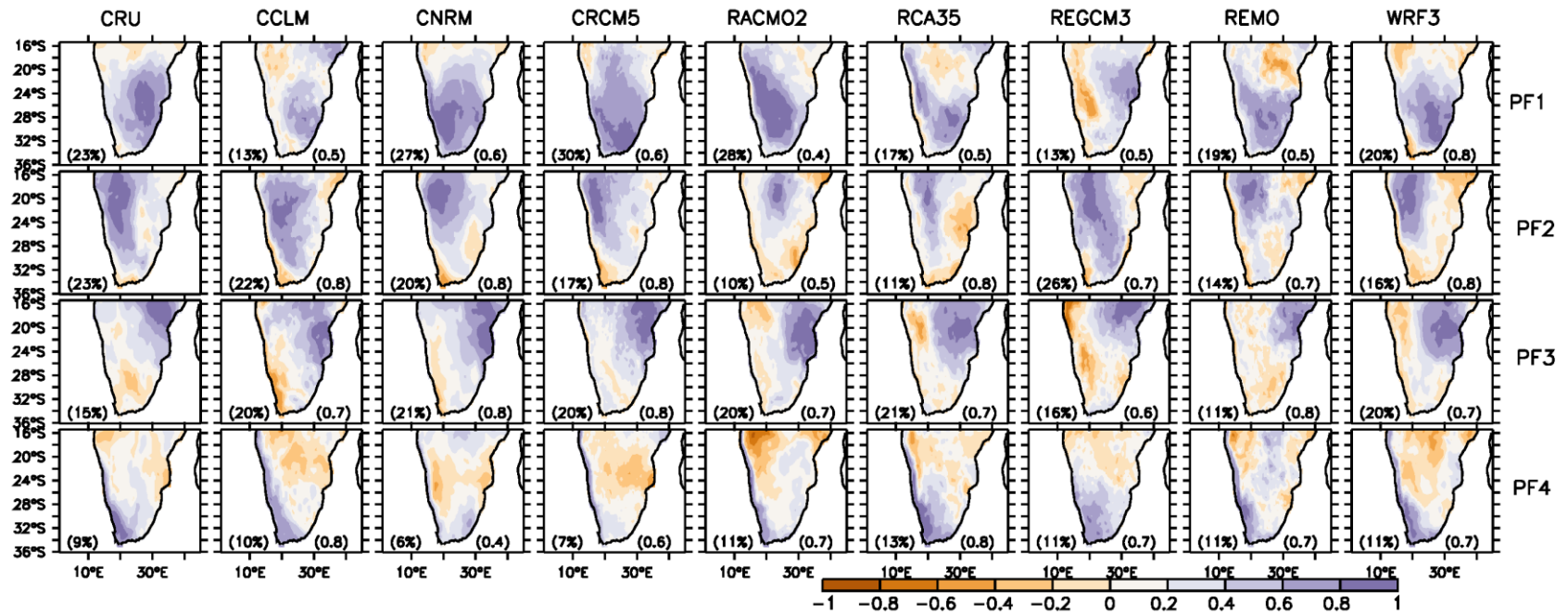
Figure 46: Same as Figure 45 but for 12-month SPEI

Temporal variation

Figure 47 and Figure 48 show the seasonal correlation of observed and simulated drought modes at both 3 and 12-month scales, respectively. In both figures, the correlations are plotted versus the normalised standard deviation (i.e. Taylor diagram). The normalised standard deviation is obtained by dividing the standard deviation of simulated score with the observed one. The vertical and the horizontal lines represent the normalised standard deviation, while the top curve shows the variation of the correlation. Figure 47 and Figure 48 indicate that RCMs capture the temporal variability of drought modes better at 12-month scale than at three-month scale, despite the better performance of the models in simulating the spatial structure of the drought modes better three-month scale than at 12-month.
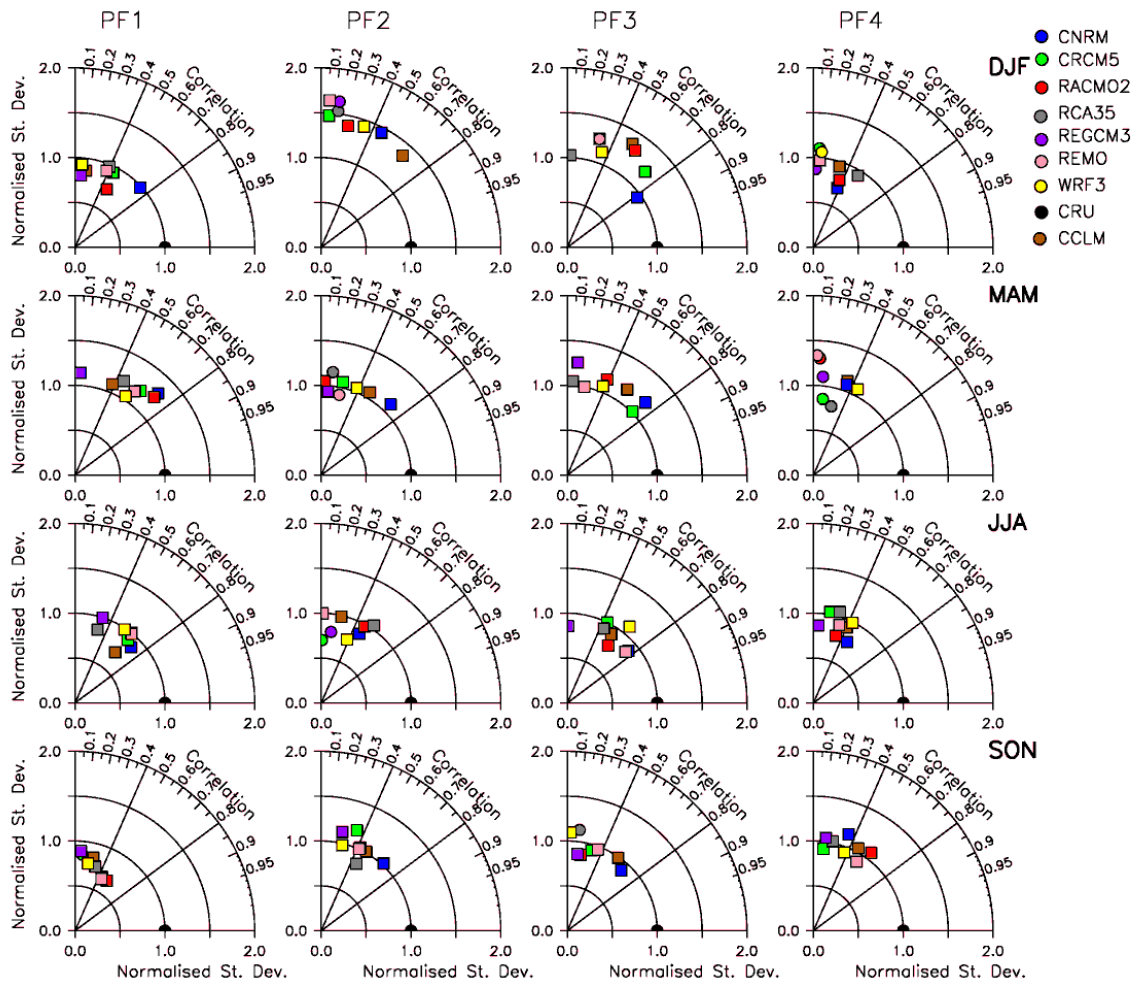
Figure 47: Taylor plots of the correlation between observed and simulated PCA scores (from RCMs driven by reanalysis) of three-month SPEI over southern Africa. Positive correlations are represented by the circles while the squares stand for negative correlations
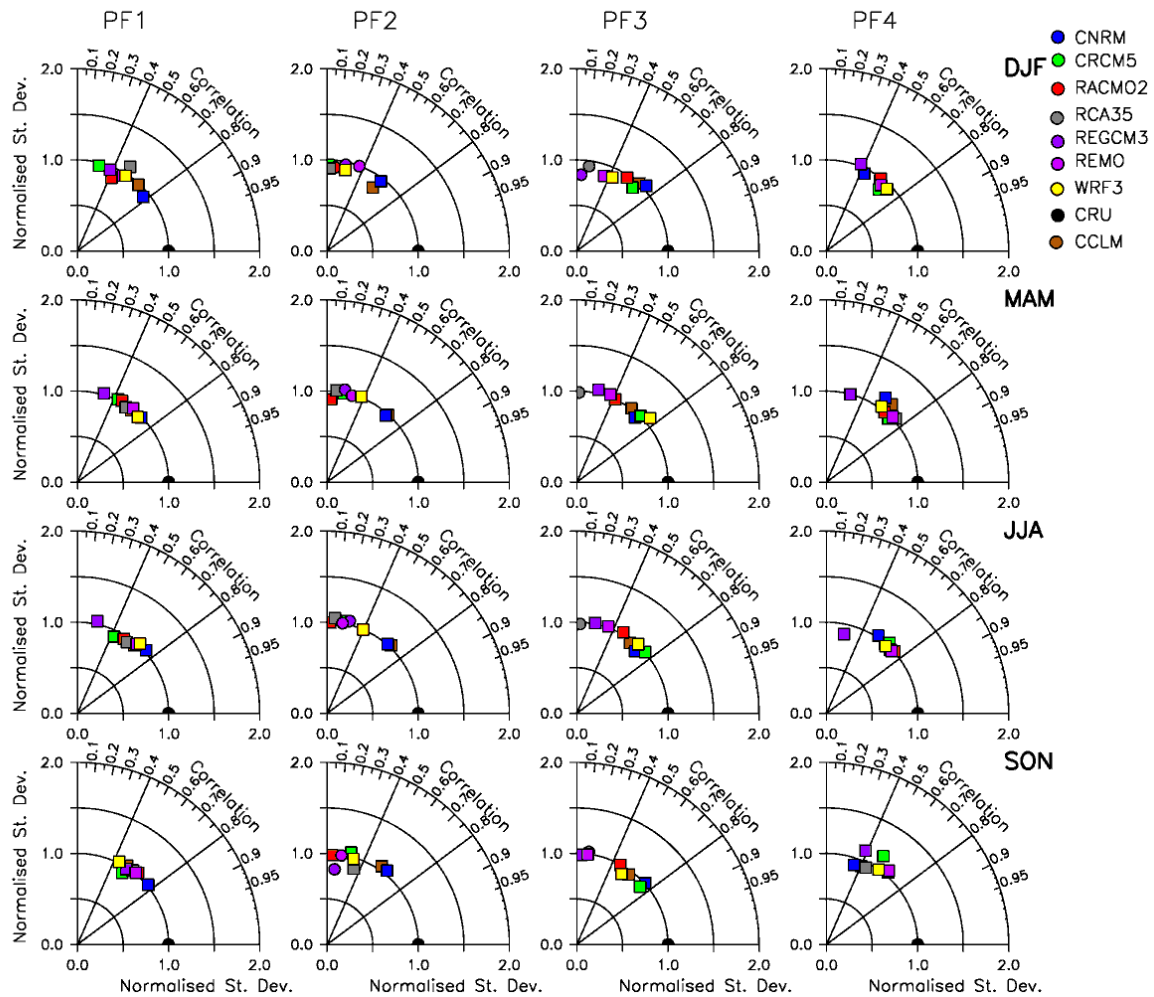
Figure 48: Same as Fig 4.18 but for the 12-month SPEI

4.5 Simulating the Drought Patterns

The section assesses how well CORDEX RCMs simulate the drought patterns. For the assessment, we aggregated the SPEI data from CRU, ERAINT and the then RCMs data sets, then used SOM to classify the aggregated SPEI data into 12 dominant patterns (nodes). The contribution of each RCM to each node is compared with that of CRU and ERAINT.

4.5.1 The drought patterns

Figure 49 shows that the observed and simulated drought patterns over southern Africa can be broadly grouped into three groups as discussed in Chapter 2 (Figure 7). These drought patterns are essentially identical to those obtained using CRU only. For instance, Node 5 from Figure 49 is characterised by negative SPEI values over the central southern Africa, which is roughly the same drought pattern presented in Figure 7. However, some differences between the drought patterns shown in Figure 49 and Figure 7 can be spotted. For example, the negative SPEI values in Node 12 displayed in this study do not cover much north of 10°S as shown in Figure 7. These differences are inevitable since the two studies use two different periods and the drought patterns presented here include observations model outputs.
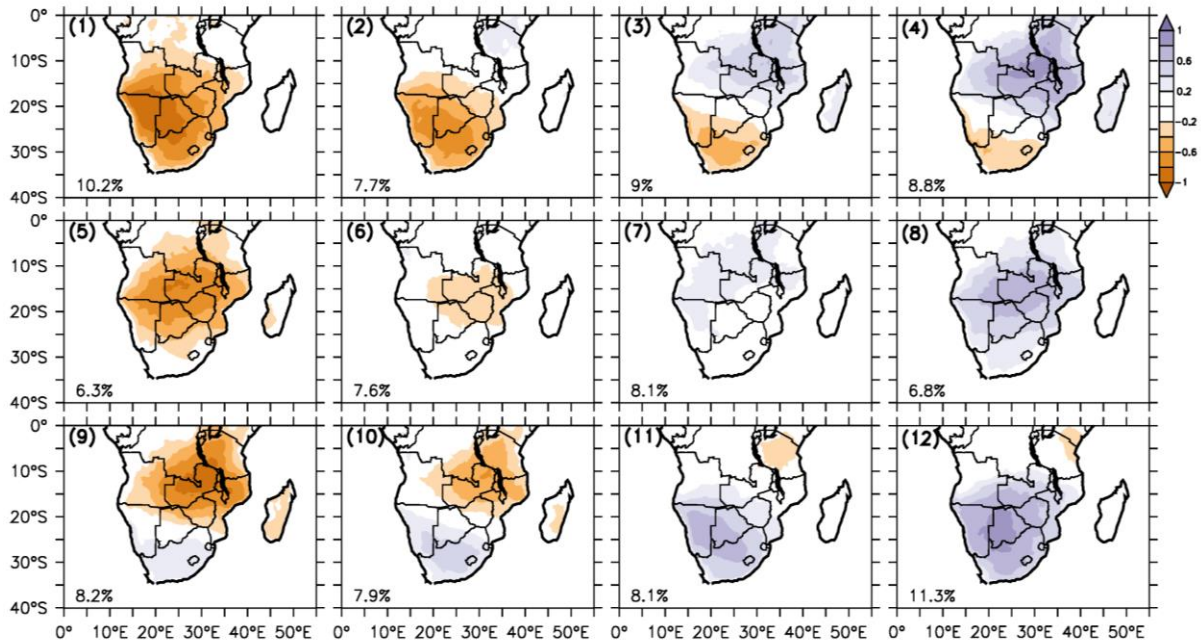
Figure 49: Drought modes generated by a 4 × 3 SOM array using the combined SPEI values from the 12 data sets (CRU, ERAINT and then CORDEX RCMs). The mode number is shown on the top left corner of each panel and the frequency of the mode is shown on the lower left corner

4.5.2   The seasonal distribution

There are some discrepancies between observations and reanalysis data sets in terms of seasonal distribution of the drought patterns (Figure 50). In the observations, Pattern 3 is the most frequent (11 events) followed by Pattern 12 (ten events), while in the reanalysis data set, Pattern 12 is the most recurrent (11 events) followed by Pattern 1 (ten events). Furthermore, in the CRU data set, Patterns 8 and 9 never occur during the austral summer period, whereas in the reanalysis, these patterns are reported in all seasons throughout the entire study period.
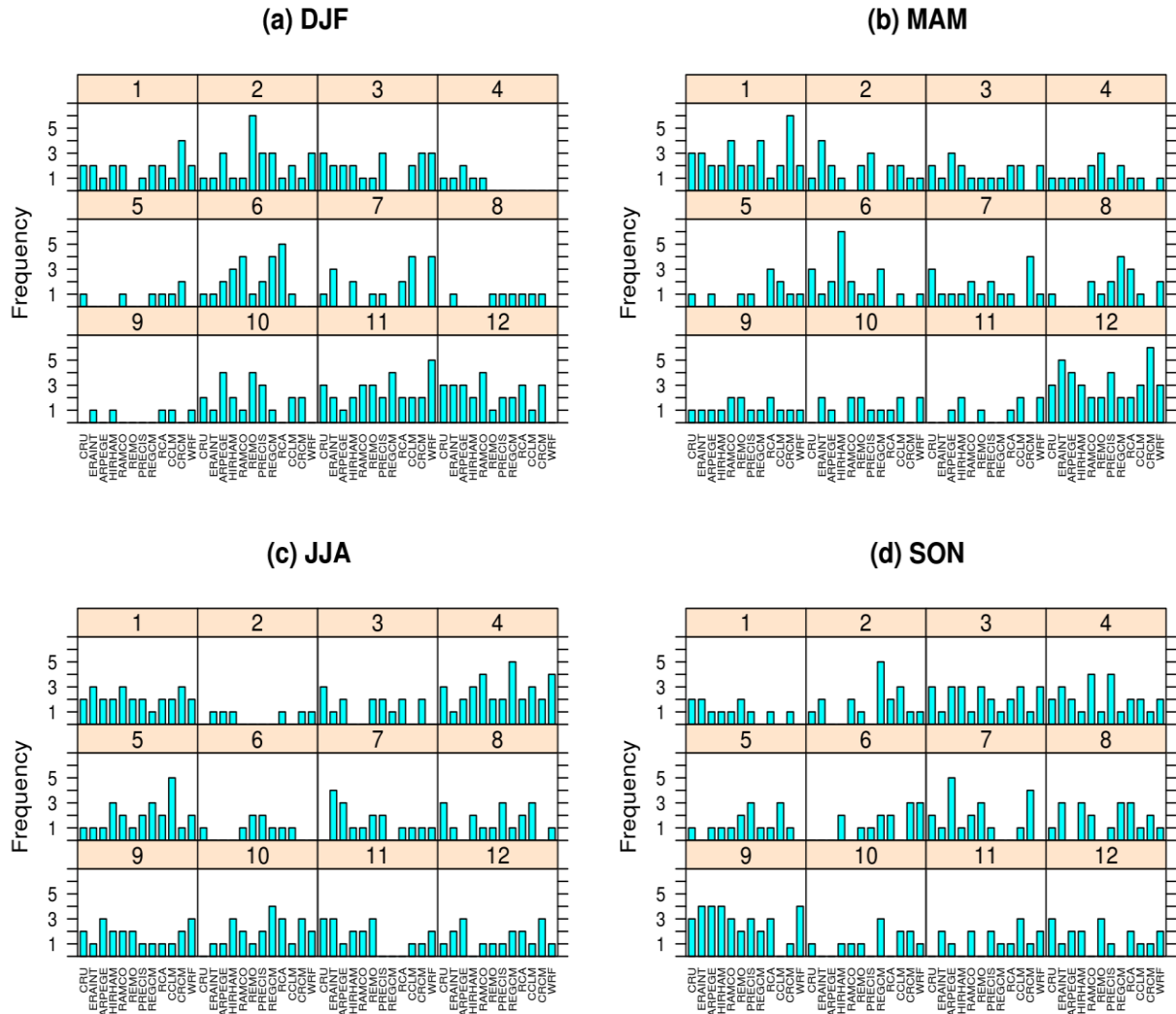
Figure 50: Seasonal frequency of the drought patterns during the 1990–2008 period for all 12 data sets including Observation, Reanalysis and ten RCMs participating in the CORDEX project

The ARPEGE model is more in agreement with the observation than any other RCM (as shown in Figure 51). It has the highest correlation coefficient (r = 0.58) with the observations and possesses the lowest root-mean-square-error (α ≈ 0.75). The model outperforms the reanalysis data set (ERAINT), which shows a much lower correlation coefficient (r = 0.52) with the observations. Previous studies (e.g., Kalognomou et al. 2013) have also reported the good performance of ARPEGE over southern Africa.

On the other hand, HIRHAM has the weakest correlation (r = 0.21) with the reference data (CRU), followed by the RCA model, which has a correlation coefficient of 0.25. Overall, the normalised standard deviation of all the models varies from approximately 0.5 to 0.75. The REMO model seems to exhibit the lowest amplitude of SPEI values while CCLM and RCA show the highest amplitude. ARPEGE an RAMCO are the only models not reporting Patterns 8 and 9 during the austral summer. Other RCMs capture the non-occurrence of either Pattern 8 (HIRHAM and WRF) or Pattern 9 (REMO, PRECIS, RegCM and CRCM).
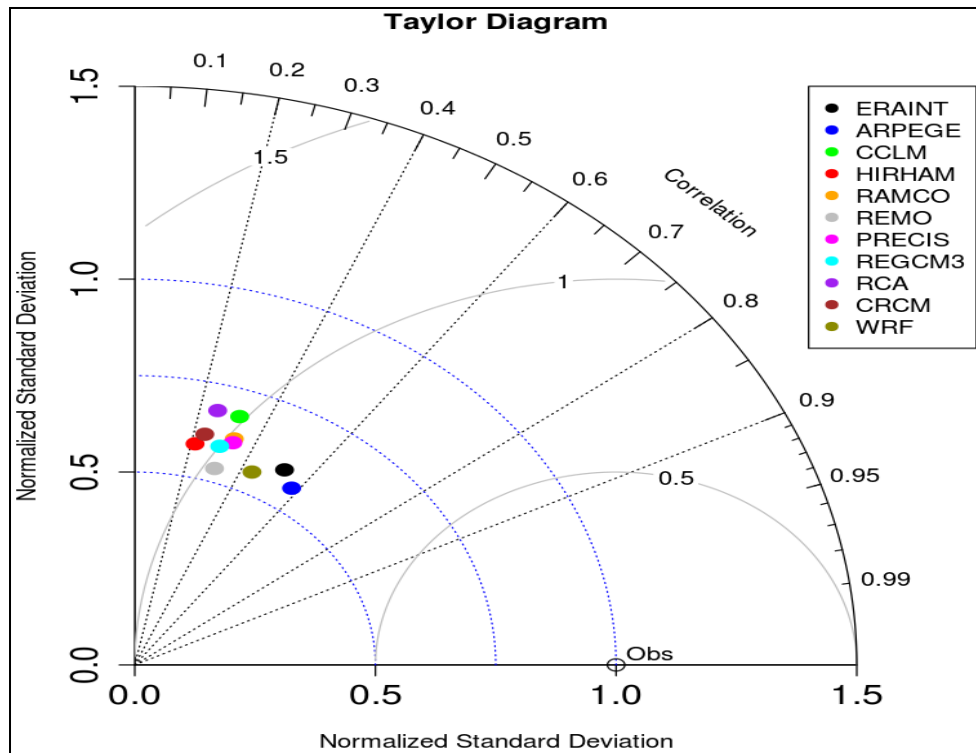
Figure 51: Taylor diagram for area-average monthly SPEI values over the entire southern Africa during the period 1990–2008. The SPEI values from CRU (open circle along the x-axis) are used as the reference data

Figure 52 shows that the reanalysis data set and ARPEGE model (Figure 52b and c, respectively) have the most comparable features with the CRU data set. All the data sets depict the major dry and wet events in southern Africa. For example, the three data sets agree that during the 1991/92 severe drought event, southern Africa was under the effect of Drought Pattern 1, which represents dry conditions across the entire region. All the data sets show that this pattern persisted for two consecutive seasons (austral summer and autumn) during the 1991/92 season, affecting the entire growing season in southern Africa.

Furthermore, the data sets collectively reveal that Drought Pattern 1 has the highest probability of persisting in the following season whenever it occurs. However, there is inconsistency among the data sets. For instance, the three data sets disagree on the number of transient drought patterns. While CRU reports only three patterns (Patterns 2, 5 and 11), ERAINT shows eight (Patterns 3, 4, 5, 6, 8, 9, 10 and 11) and the ARPEGE model reports three patterns (Patterns 8, 9, and 10), which are completely different from those in the CRU data set.
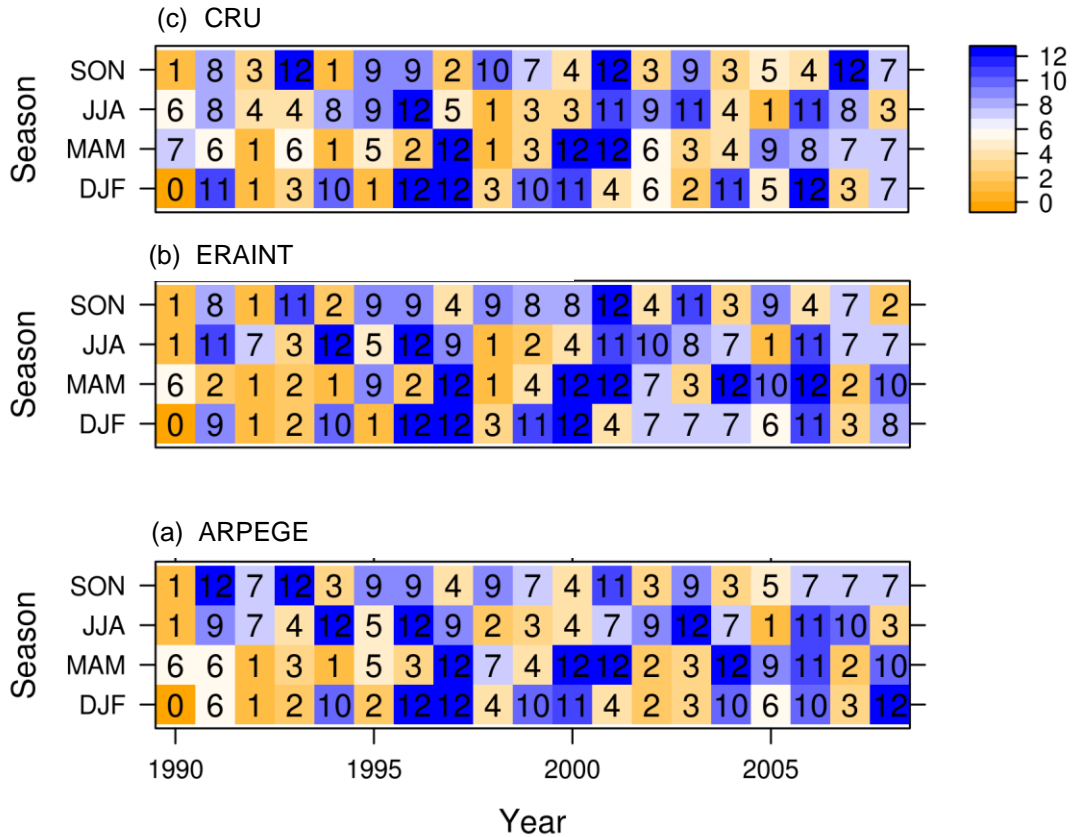
Figure 52: Seasonal occurrence of the drought patterns in observation, reanalysis, and ARPEGE. Each number represents a drought pattern type

We used phase synchronization to examine how well ERAINT and ARPEGE capture the changes in the drought patterns. Following Mistra (1991), the synchronization is calculated as:

$$\eta = \left(\frac{n - n'}{n}\right) \times 100\%$$

where n′ is the number of seasons the simulated (i.e. ERAINT or RCM) drought patterns that are out of phase with the observed drought patterns, and n is the total number of seasons under study.

All the RCMs have poor phase synchronization with the observation. None of them show synchronization above 50% (Figure 53). The ARPEGE model features the highest synchronization (η = 46.7%) among all the models (including the reanalysis data set); RegCM3 has the worst (η = 10.75). Despite the weak phase synchronization, some models captured the general distribution of the wet and dry patterns as in the observation. For instance, during the 1996/97 season, CRU data set shows a persistence of Node 12 during the austral summer and autumn and REMO model shows a persistence of Node 11 during the same period. Given that Node 11 is also markedly a wet node, we can infer that the model captured the event.

62
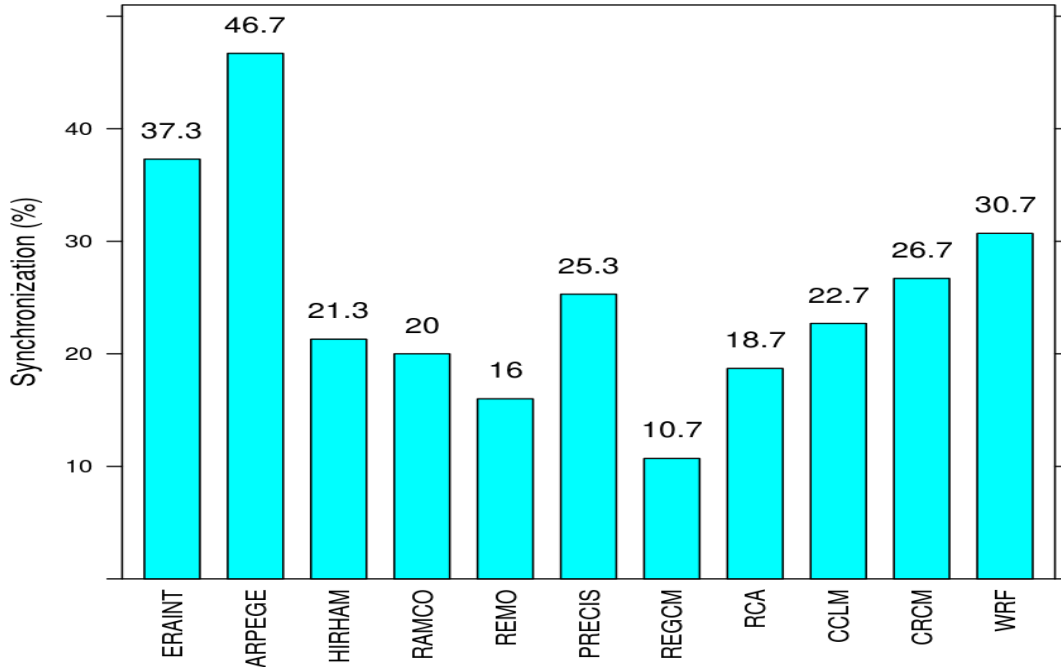
Figure 53: Synchronization (%) of nodes between 11 data sets (Reanalysis and ten RCMs) with the observations during the entire study period (1990–2008)

4.5.3 Composite anomalies of SSTs

Figure 54 presents the composite analyses of the SST anomalies for the two most common drought patterns (Node 1 and 12). The composites of SST anomalies for Node 1 are positive over the central equatorial Pacific Ocean. This is a typical characteristic of the so-called Central Pacific El Niño or El Niño Modoki or even EN3 (Hoell et al. 2014; Johnson, 2013). Conversely, the SST anomalies during the occurrence of Drought Pattern 12 are negative over the equatorial eastern Pacific, resembling the La Niña LN4 conditions described in Hoell et al. (2014).

The ERAINT data set captures the SST anomalies associated with the two drought patterns. Most of the CORDEX RCMs show the same feature of SST anomalies associated with Drought Pattern 1 as the observation, with the exception of CCLM and REMO. The REMO model does not reproduce the SST anomalies associated with Node 1 while the CCLM model shows negative SST anomalies off the coast of Peru, which is contrary to El Niño conditions. With regard to Node 12, all CORDEX RCMs show La Niña conditions in the Pacific Ocean, with the exception of the WRF model that never captures this pattern.

(a)

(b)
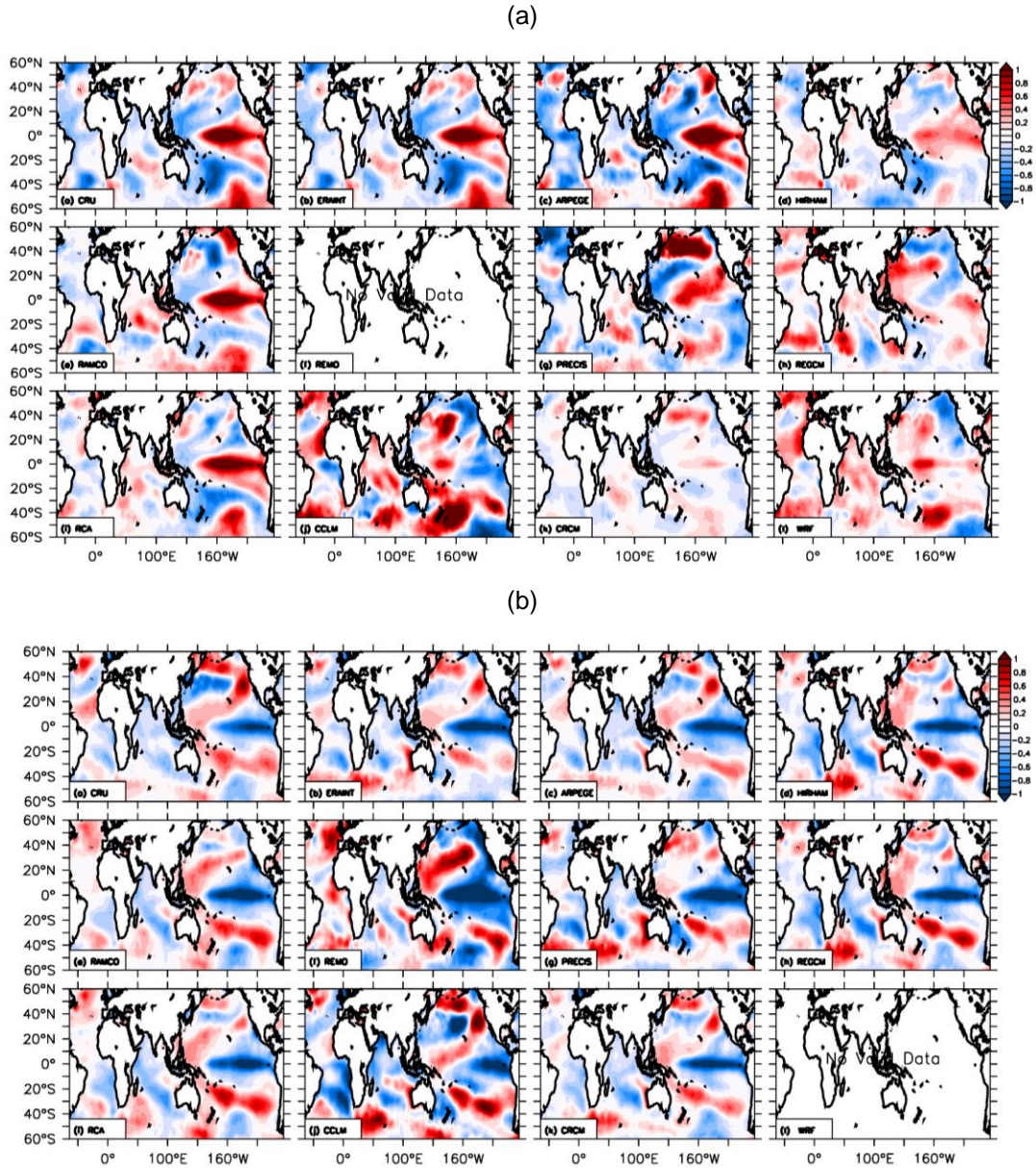
Figure 54: Composite of SST anomalies (°C) associated with (a) Nodes 1 and (b) Node 12 during austral summer period for the CRU, ERAINT and the 10 RCMs

4.6 Conclusion

In this chapter, we examined the capability of GCMs and RCMs to simulate characteristics of southern African droughts and reproduce the link between droughts and some atmospheric teleconnections. The results obtained can be summarised as follows:

- Only a few CORDEX RCMs simulate the influence of ENSO on southern African drought as observed. In this regard, the ARPEGE model shows the best simulation. The differences in the performance may be due to their lateral boundary conditions. The ARPEGE model is a variable-resolution model. This stretching capability would allow a better interaction between large-scale and small-scale features in the ARPEGE model, and consequently a better representation of the rain-producing systems in southern Africa.

- The RCA-simulated link between ENSO and southern African droughts is sensitive to the global data set used as the lateral boundary conditions. In some cases, using RCA to downscale GCM simulations adds value to the simulated link between ENSO and the droughts, but in other cases the downscaling adds no value to the link. The added value of RCA to the simulated link decreases as the capability of the GCM to simulate the link increases. This study suggests that downscaling GCM simulations with RCMs over southern Africa may either improve or depreciate the simulated ENSO-drought link over the region.

- The GCMs give remarkable representation of the drought modes, but they perform better in reproducing the drought modes at three-month scale than at 12-month scale. About 70% of GCMs simulate all drought patterns well at three-month scale, while only 60% of GCMs simulate three of the drought patterns well at 12-month scale.

- The RCMs also simulate the spatial characteristics of the drought modes better at three-month scale than at the 12-month scale, but they capture the temporal variability of the drought modes better at 12-month scale than at three-month scale.

- The RCMs give realistic simulations of the drought patterns over southern Africa, but they have difficulty in simulating the temporal variability of the drought patterns. However, ARPEGE model performs best in simulating the drought patterns and the temporal variability.

5   FUTURE PROJECTIONS OF REDs OVER SOUTHERN AFRICA

5.1   Introduction

There is a concern that the ongoing global warming may increase the severity of droughts in southern Africa, because many studies have shown that drought intensity increases with temperature (Dai et al. 2004; Dai 2011; Sheffield and Wood 2008; Vicente-Serrano et al. 2010a; 2010b; Washington and Preston 2006). For example, Dai et al. (2004) showed that in the period 1972–2004, the warming increased global dry areas by 20–38%. Dai (2011) found that the temperature increase of 1–3°C in 1950–2008 decreased the annual rainfall in most parts of Africa. The IPCC Fourth Assessment Report (IPCC, 2007) projected a continuous increase in global mean surface air temperature over the 21st century owing to the increase of anthropogenic greenhouse gas concentration (Meehl et al. 2005), suggesting an increase in drought frequency, severity and spatial extension in future, especially in southern Africa. However, most of these studies based their future projections on GCMs simulations (with coarse resolution) and characterised the droughts with precipitation anomaly only. To obtain more physically based drought projections, the present study used high-resolution simulations (from a CORDEX RCM) and a drought index (SPEI) that accounts for influence of the global warming on droughts.

In previous chapters, we identified and described characteristics of REDs over southern Africa (Chapter 2), investigated the mechanism controlling the droughts (Chapter 3), and assessed the capability of some GCMs and RCMs in simulating the droughts and their links with atmospheric teleconnections (Chapter 4). In the present chapter, we project the future characteristics of southern African droughts under two climate forcing scenarios [Representative Concentration Pathway (RCP4.5 and RCP8.5; i.e. the mid- and high-level emission scenarios, respectively)]. The characteristics considered here include drought intensity, coverage, frequency, modes and patterns. To identify the influence of temperature in characterising the future droughts, the SPEI projections are compared with those of SPI. To ensure the results are relevant for agriculture and water resources planning, the drought projections are provided at three-month, 12-month, and 24-month scales. While the short-time droughts (three-month) are usefully for agricultural purposes, the longer time scale droughts (e.g. 12-month and 24-month) are needed for water resources managements.

5.2   Model Simulations

All climate simulation data sets were obtained by downscaling eight GCM projections over southern Africa using the Rossby Centre Regional Atmospheric Model (called RCA), developed by the SMHI in Sweden. RCA participated in the CORDEX project (www.cordex.org). RCA simulations were chosen for this study because the model has the largest number of simulations available in the CORDEX website. As discussed in the previous chapter (Chapter 4), RCA gives a credible simulation of southern Africa droughts and realistically reproduces the link between the droughts and atmospheric teleconnections. The description of the RCA simulations analysed for the study is summarised in Table 5.

Table 5: Description of all GCMs downscaled in RCA simulations used for this study

RCA Simulation	Forcing Global Data Set	
	Name and Institution	Resolution
R_ERAINT	The ERA-Interim reanalysis from the ECMWF	0.8° × 0.8°
R_CCCMA	The CanESM2 GCM from the Canadian Centre for Climate Modelling and Analysis (CCCMA)	2.8° × 2.8°
R_CNRM	The CNRM-CM5 GCM from the Centre National de Recherches Meteorolo–Giques/Centre Européen de Recherche et de Formation Avancée en Calcul Scientifique	1.4° × 1.4°
R_GFDL	The NOAA-GDFL GCM from NOAA Geophysical Fluid Dynamic Laboratory	2.5° × 2.0°
R_HADGEM	The HadGEM2-ES GCM from UK Met Office Hadley Centre	1.9° × 1.3°
R_ICHEC	The ICHEC-EC GCM from the EC-EARTH Consortium	1.25° × 1.25°
R_MIROC	The MIROC5 GCM from the Atmosphere and Ocean Research Institute (University of Tokyo), National Institute for Environmental studies and Japan agency for Marine-Earth Science and Technology	1.4° × 1.4°
R_MPI	The MPI-ESM-LR GCM from the Max Planck Institute for Meteorology	1.9° × 1.9°
R_NCCN	The NorESM1-month GCM from Norwegian Climate Centre	2.5° × 1.9°

5.3 Droughts Intensity

Figure 55 presents the interannual variation of the seasonal droughts, averaged over southern Africa for the past and future climates (1951–2100). There are notable differences in the SPEI and SPI projections (Figure 56). The SPEI projection suggests a continuation of a negative trend or a dry condition (that features toward the end of past climate) into the future under both RCP4.5 and RCP8.5 scenarios. On the other hand, the SPI projection shows neither trend nor any persistent dry condition for both scenarios, except for a weak negative trend in JJA and SON between 2050 and 2100. In addition, with SPEI, the projected droughts are more severe under RCP8.5 than RCP4.5. For example, by 2100, the model ensemble mean is about −0.8 (DJF), −1.0 (MAM), −1.5 (SON) and 2.5 (JJA) in the RCP4.5 scenario, but about −1.5 (DJF), −2.0 (MAM), −2.5 (SON) and 3.5 (JJA) under the RCP8.5 scenario. However, with SPI, there are no distinctions in the projected SPI values under the two scenarios. Furthermore, while SPEI indicates that the severity of future drought may exceed that of the 1996 drought, SPI suggests that the magnitude of the most severe future droughts may not exceed that of 1996 drought. These results are also true for both 12-month and 24-month droughts (Figure 56).
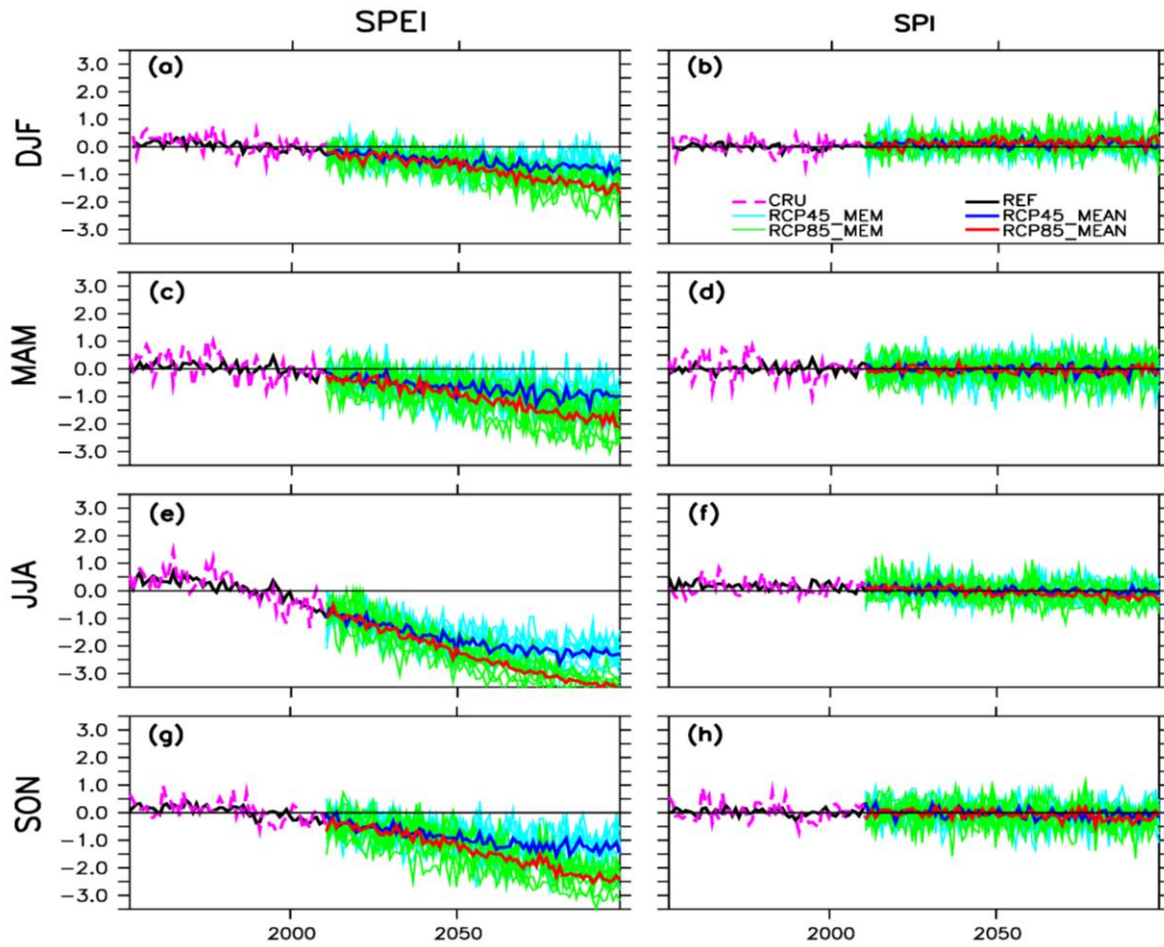
Figure 55: Interannual variability of seasonal droughts, obtained using three-month SPEI (left panels) and SPI (right panels), over southern Africa in summer (DJF), autumn (MAM), winter (JJA) and spring (SON) of 1951–2100, as observed (CRU) and simulated (REF: past climate; RCP4.5_MEM and RCP4.5_MEM: ensemble mean for RCP4.5 and RCP8.5 scenarios, respectively; RCP4.5_MEAN and RCP4.5_MEAN: ensemble mean for RCP4.5 and RCP8.5 scenarios, respectively)
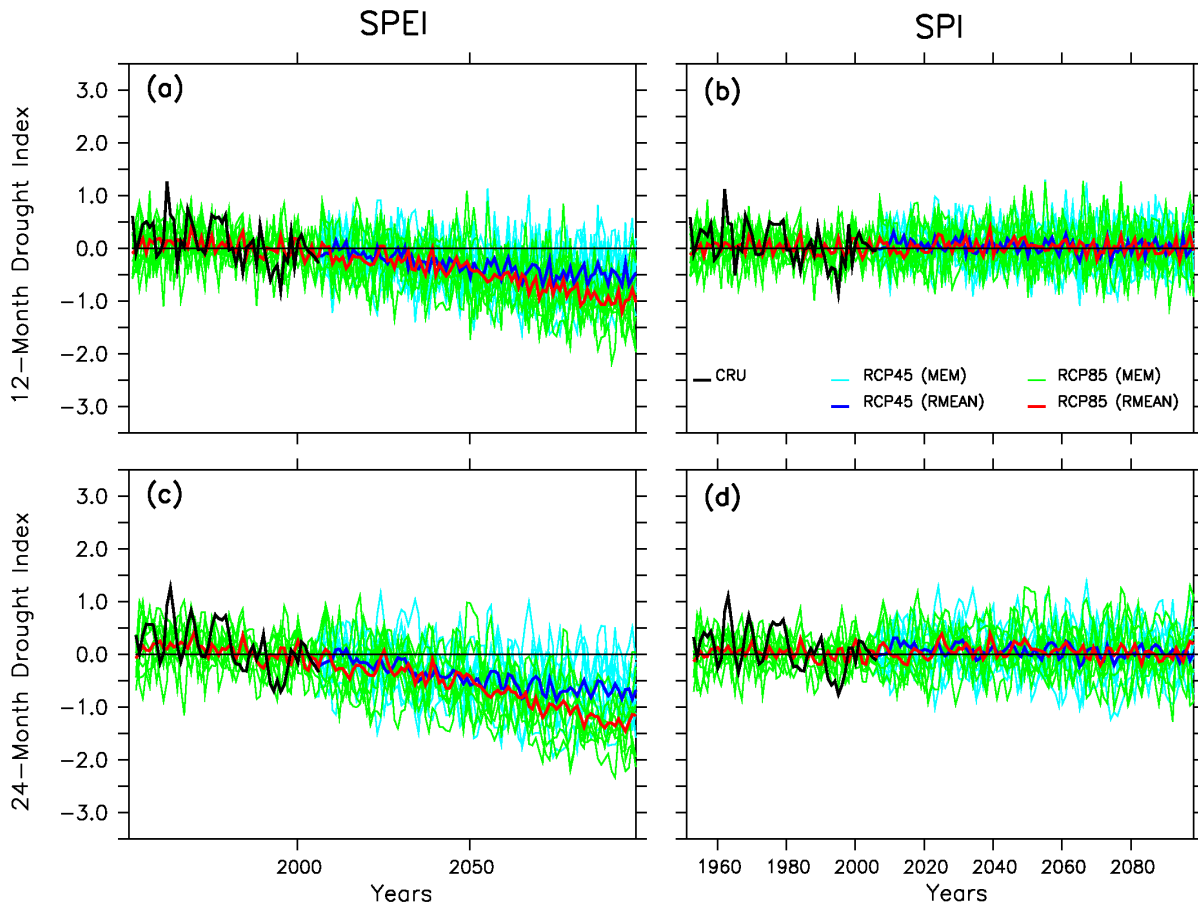
Figure 56: Future projections of drought intensity over southern Africa under RCP4.5 and RCP8.5 scenarios. The drought intensity is obtained with SPEI (left panels) and SPI (right panels) at 12- and 24-month scales (ending in February) from RCA simulations (REF: past climate; RCP4.5_MEM and RCP4.5_MEM: ensemble mean for RCP4.5 and RCP8.5 scenarios, respectively; RCP4.5_MEAN and RCP4.5_MEAN: ensemble mean for RCP4.5 and RCP8.5 scenarios, respectively). CRU observations for present-day climate are indicated

5.4   Drought Coverage

Here we discuss interannual variation in the area covered by moderate drought over southern Africa for past and future climate using both SPEI and SPI (1951–2100). For both indices, a moderate drought is defined as a condition in which the drought index (SPI or SPEI) is less than or equal to −1.0. The drought coverage is expressed as the percentage of southern African landmass covered with drought (Figure 57 and Figure 58). Figure 57 shows a good agreement between the results of SPEI and SPI especially in DJF. This implies that there may not be a significant difference in using SPEI or SPI to estimate drought coverage for this season. The two drought indices disagree in the other seasons, with the highest discrepancy occurring in JJA, when SPEI shows drought coverage of more than 60% and SPI shows less than 25%. The main reason for this discrepancy is that it is difficult to calculate SPI over southern Africa in JJA when the long-term mean rainfall over most of the region is very close to zero. However, with SPEI drought coverage, the ensemble mean shows a positive trend in all seasons, especially since 1990.

The climate models project a general increase in the SPEI drought coverage, but there is no trend in SPI drought coverage. While SPI suggests that the percentage of drought area may not exceed 30% in 2100, SPEI indicates that, depending on the scenarios and seasons, the percentage of drought area may be up to 90%. However, for the SPEI drought area, the enhancement in the drought coverage is projected to be

69

higher in RCP8.5 scenario than in RCP4.5 scenario. For example, the projection shows that by 2100, the percentages of SPEI drought areas may be about 40% (in DJF), 50% (in MAM), 60% (in SON), and 80% (in JJA) under the RCP4.5 scenario, but about 60% (in DJF), 70% (in MAM), 80% (in SON), and 98% (in JJA) under RCP8.5 scenario. The difference between the drought indices features at the 12-month and 24-month drought scale projections (Figure 57). For both drought indices, the projections suggest a general increase in drought coverage, but the increase is more discernible with SPEI than with SPI. While SPEI projects that future droughts coverage may be up to 80% of the subcontinental area, SPI indicates that the most widely spread future drought may not cover more up to 50% of the subcontinental area.
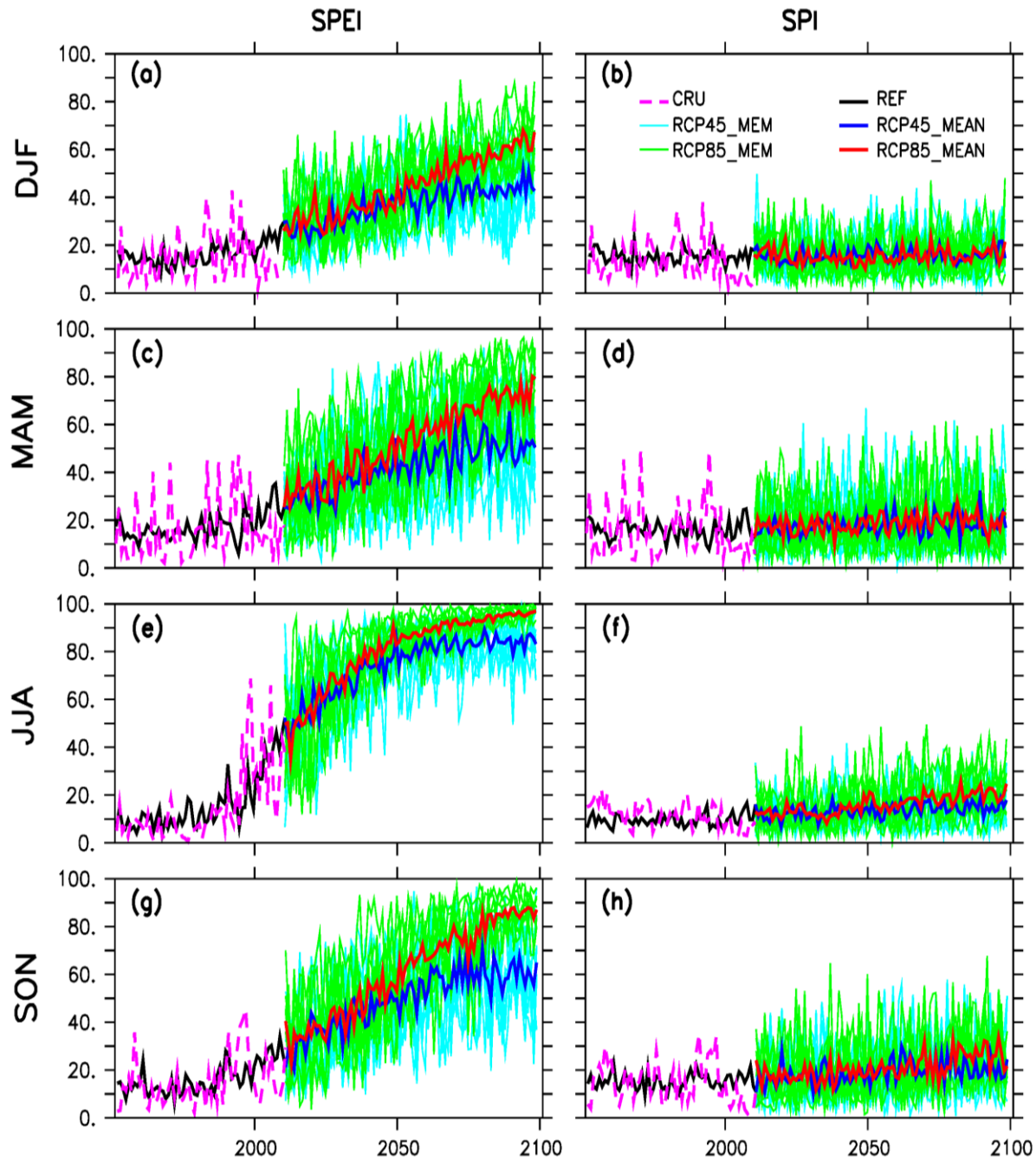
Figure 57: Same as Figure 55, except for percentage of southern African landmass experiencing seasonal drought
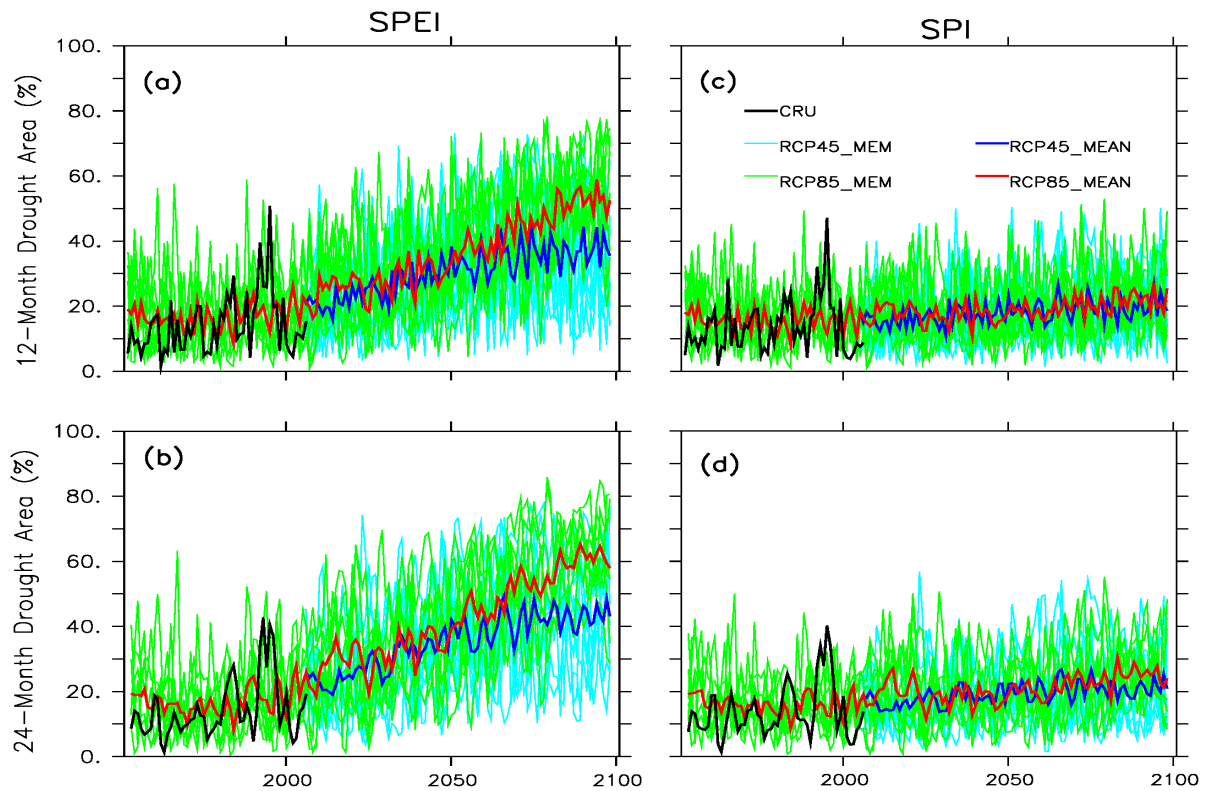
Figure 58: Same as Figure 56, except for percentage of southern African landmass experiencing seasonal drought

5.5   Drought Frequency

The future projection shows an increase in frequency of SPEI drought event over the entire subcontinent for both RCP4.5 and RCP8.5 scenarios (Figure 59–Figure 63). Both scenarios show that the maximum increase occurs in JJA. However, the projection generally shows a higher increase in the drought frequency for RCP8.5 than for RCP4.5 and this is consistent with previous sections, which indicate that a larger area may experience droughts under RCP8.5 than under RCP4.5. However, the situation is different with SPI drought projections. With SPI drought, the models project a lower increase (than that of SPEI drought) and there are no substantial differences between the future projections under RCP8.5 and RCP4.5 scenarios.
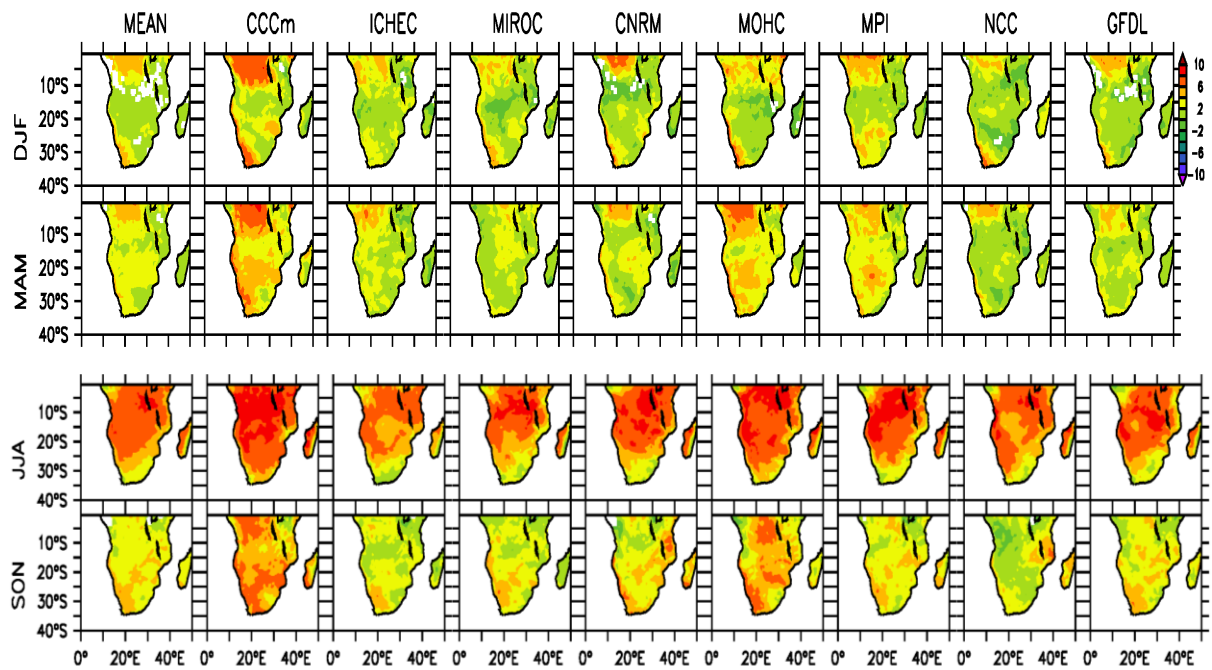
Figure 59: Projected changes in number of seasonal drought (three-month SPEI < −1; number per decade) over southern Africa in 1931–2065 under the RCP4.5 scenario, with reference to 1971–2005
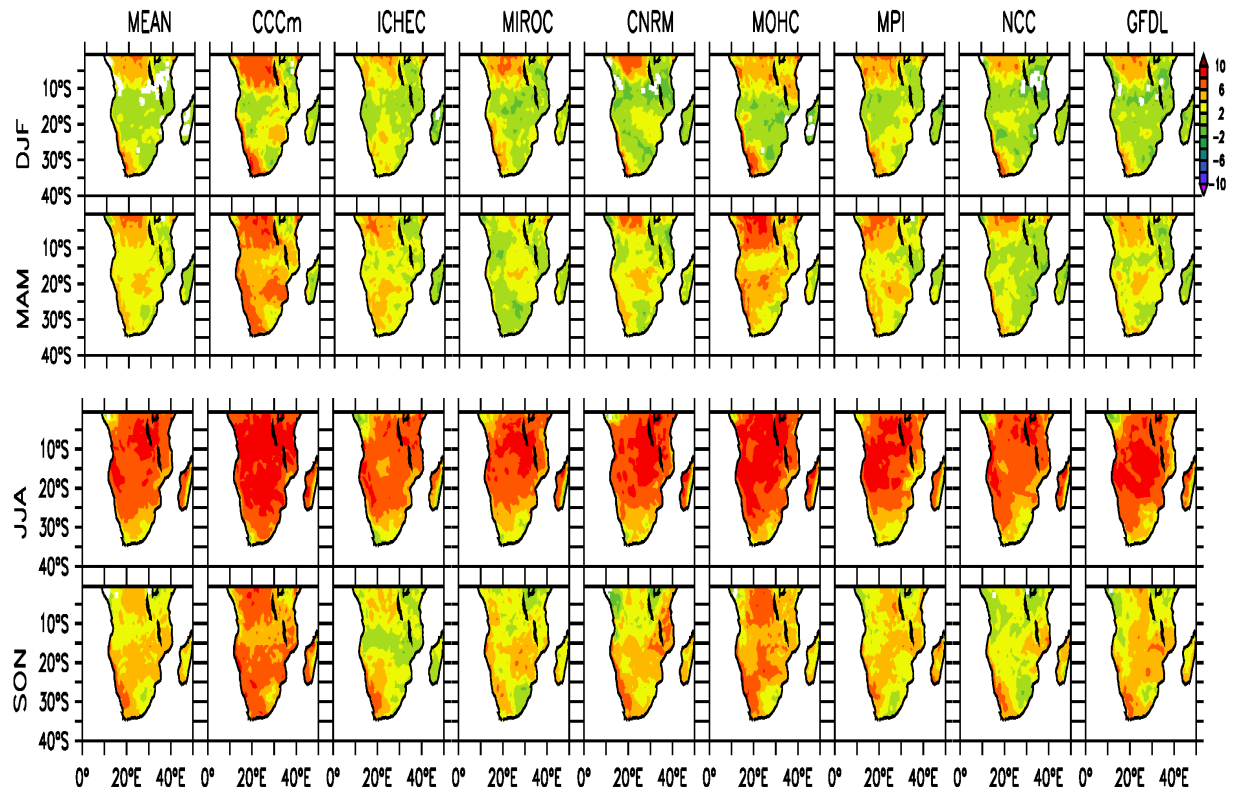
Figure 60: Same as Figure 59, except for RCP8.5 scenario
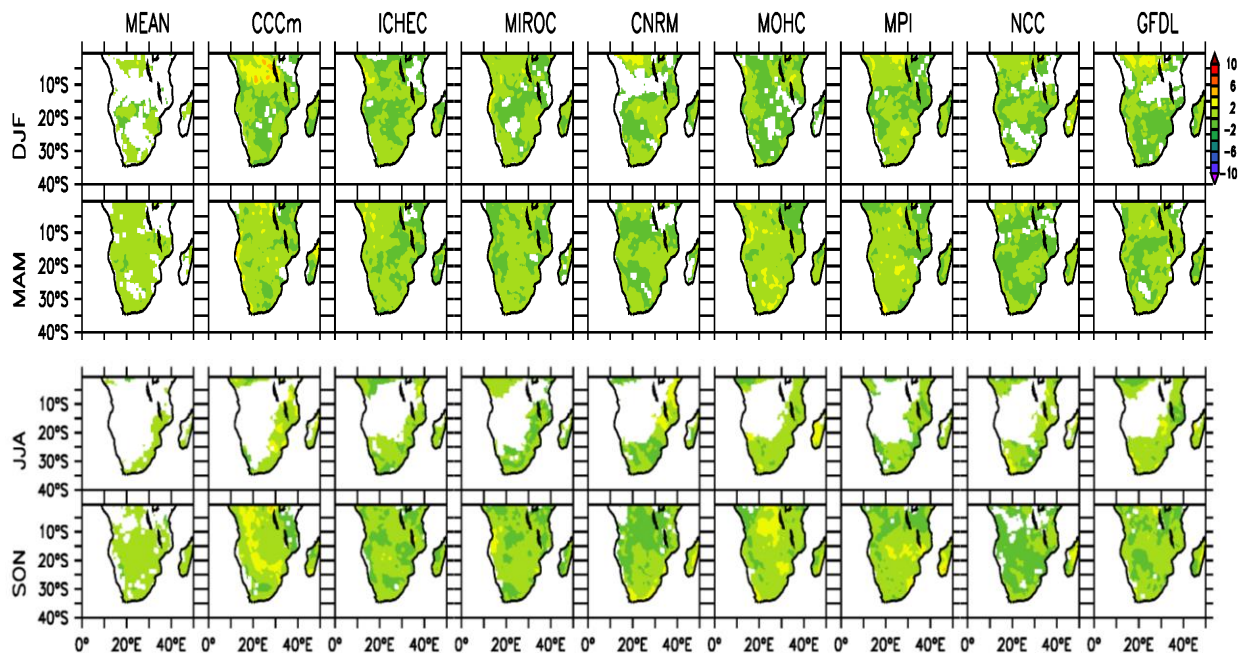
Figure 61: Projected changes in number of seasonal drought (three-month SPI < −1; number per decade) over southern Africa in 1931–2065 under the RCP4.5 scenario, with reference to 1971–2005. The white area indicates no data
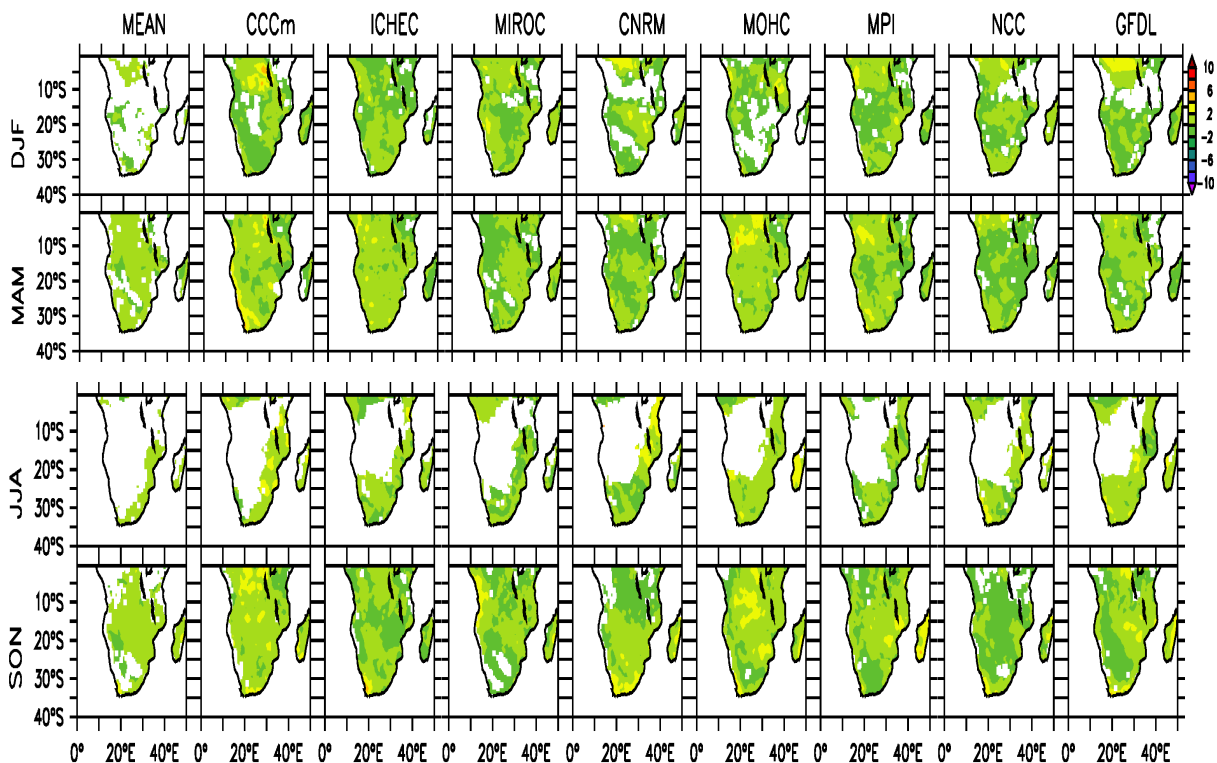
Figure 62: Same as Figure 61, but for RCP8.5 scenario

5.6   The Drought Modes

The drought modes for past and future climates (i.e. 1951–2100 under RCP4.5) have similar structures (compare Figure 63 and Figure 64). This suggests that the climate change may not substantially alter the structure and the spatial structure of the drought modes in the future. However, while the future drought modes are the same in both climates, there are some changes in the contribution of individual drought mode in the two climates. The direction of the changes varies with the drought modes and with the simulations. For example, while R_CCMA projects an increase of about 3% in DM3 contribution, R_NCC projects a decrease of about 1%.

Figure 59–Figure 62 show the projected changes in drought intensity and frequency over the core areas of the drought modes. Consistent with the future projections of drought intensity, a future increase in drought intensity (SPEI and SPI) is projected over the core of each drought mode in both RCP4.5 and RCP8.5 scenarios. However, the magnitude of the increase varies widely with the drought mode. For instance, with SPEI, while the ensemble mean projection is between −1.0 and 1.5 (RCP4.5 and RCP8.5 respectively) over DM3 and DM4 areas, it is between −0.5 and −0.2 over DM2 core. This suggests that the future impacts of climate change on the drought modes differ. The impacts may induce more intensive droughts in DM3 and DM4 modes than in DM1 and DM2 modes. For this projection, the SPI results are consistent with those of SPEI, except that the magnitude of the increase in drought intensity is weaker with SPI. However, in contrast with SPEI results, SPI suggests that the climate change may increase the intensity of pluvial in the DM2 mode. In the mode, the ensemble mean projection for SPI is between +2 and +5 (RCP4.5 and RCP8.5 respectively) in 2100.

The RCA ensemble mean projects an increase in the frequency of drought (i.e. SPEI < −1.0) over core areas of the four drought mode for both scenarios (Figure 65–Figure 68), but the magnitude of the increase varies over the areas. And for each mode, the increase also varies with the forcing scenarios. For example, for DM1, the projected increase in drought frequency is about 3 events·decade^{-1} in the two future periods (2046–2065 and 2081–2100) under RCP4.5 scenario, but it ranges from 3 events·decade^{-1} (in the 2046–2065 period) to 5.5 events·decade^{-1} (in 2081-2100) under RCP8.5. On the other hand, for DM2, the projected increase ranges from 0.1 event·decade^{-1} (in the 2046–2065 period) to 1.0 event·decade^{-1} (in 2081–2100) under RCP4.5, but from 1 event·decade^{-1} (in the 2046–2065 period) to 2 events·decade^{-1} (in 2081–2100) under RCP8.5. However, there is a better agreement among the simulations on the direction of change in drought intensity for DM3 for DM2.
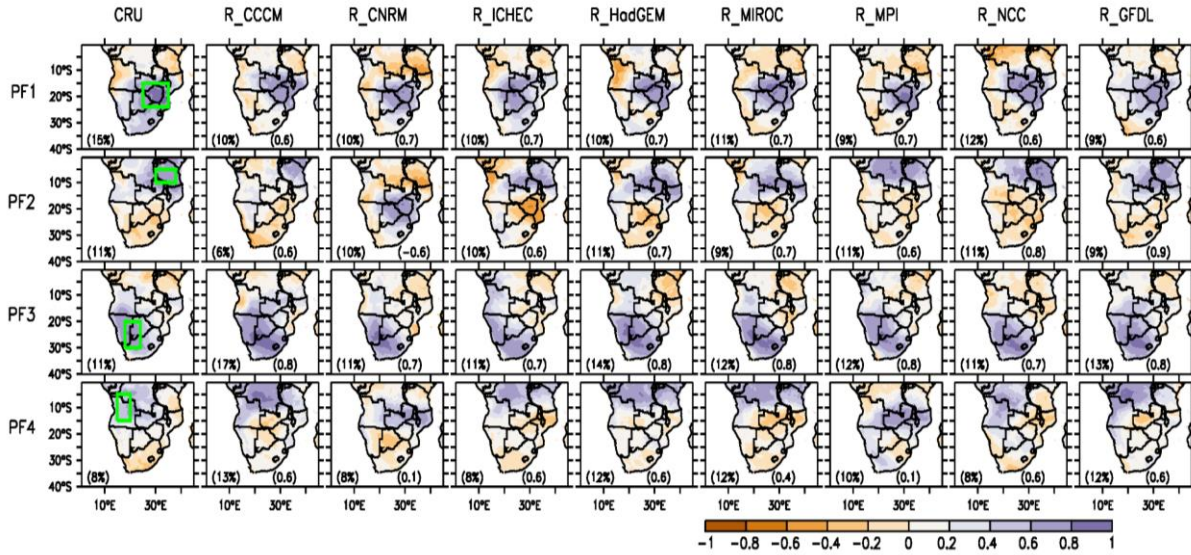
Figure 63: Drought modes over southern Africa, as obtained with PCA of 12-month SPEI for observed (CRU) and simulated RCA simulations (1951–2014). The percentage of variance explained by each drought mode (principal factor) is indicated at the lower left corner of the panel. The spatial correlation between observed and simulated mode for each model is shown at the lower right corner of the model's panel. The green rectangle shows the core area of each drought mode
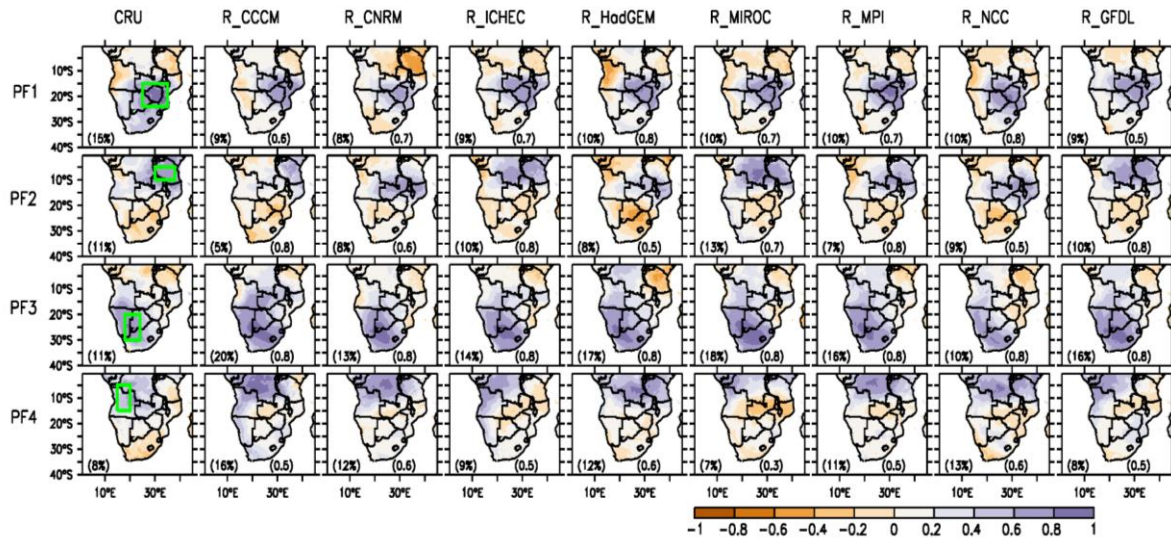
Figure 64: Same as Figure 63, except for 1951–2100 under RCP4.5. CRU analysis is for 1951–2014
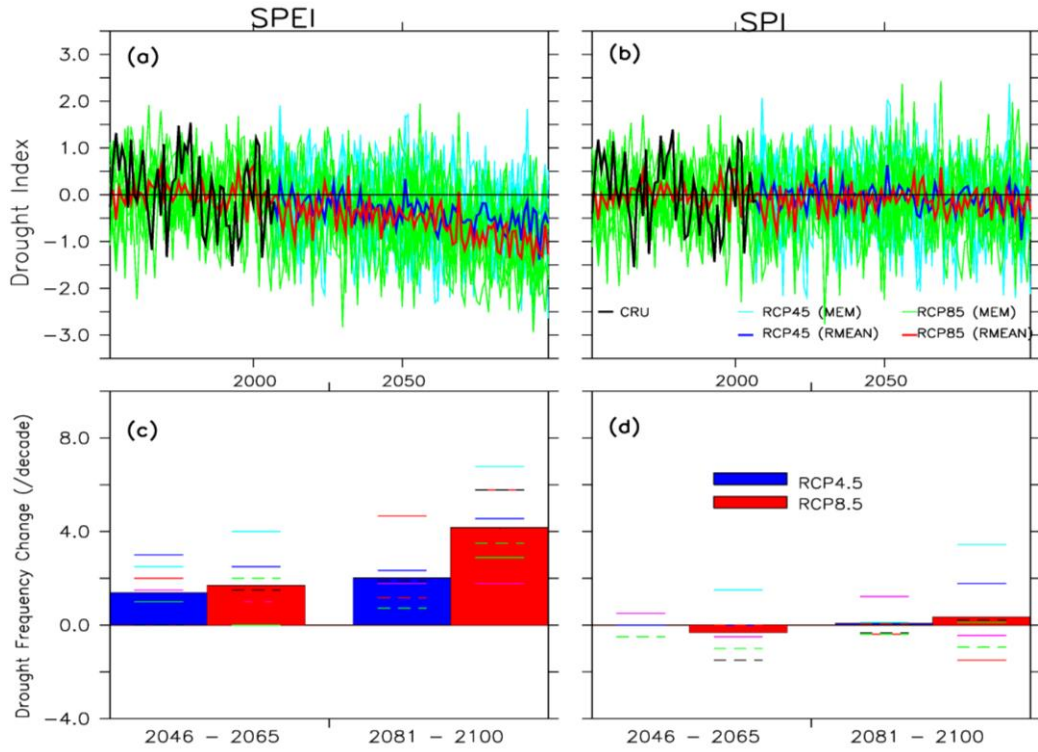
Figure 65: Future projections of drought over the core area of DM1
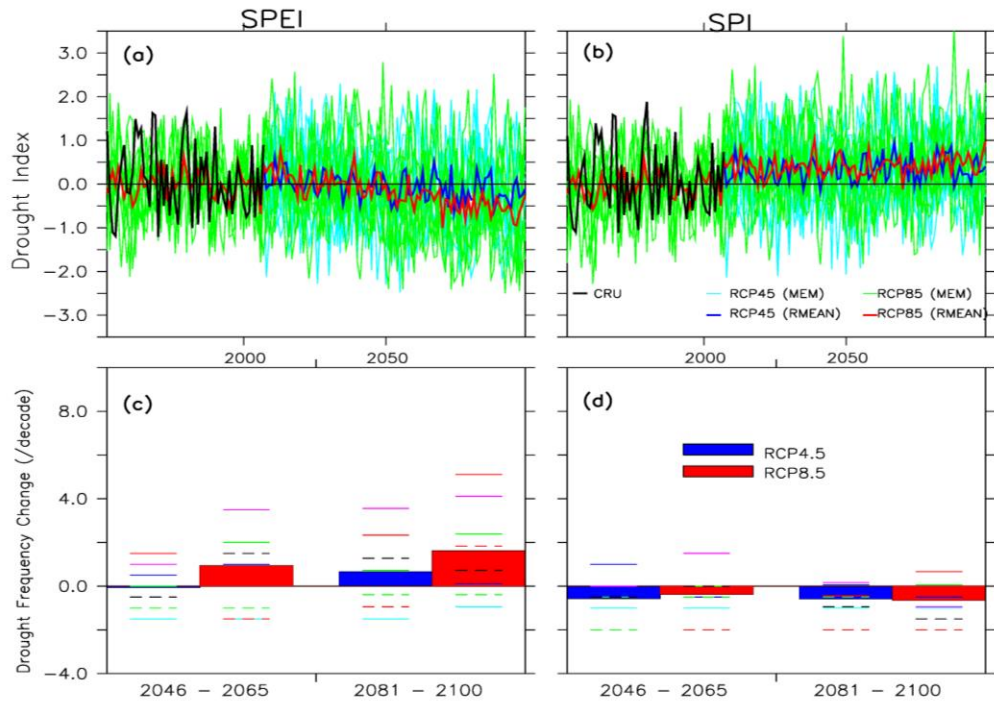
Figure 66: Future projections of drought over the core area of DM2
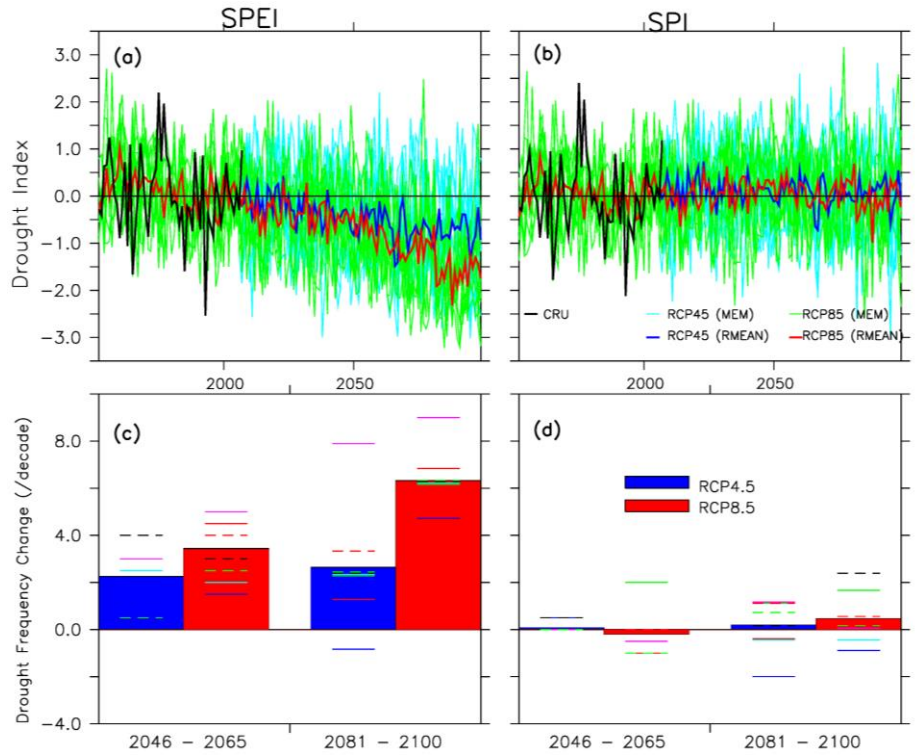
Figure 67: Future projections of drought over the core area of DM3
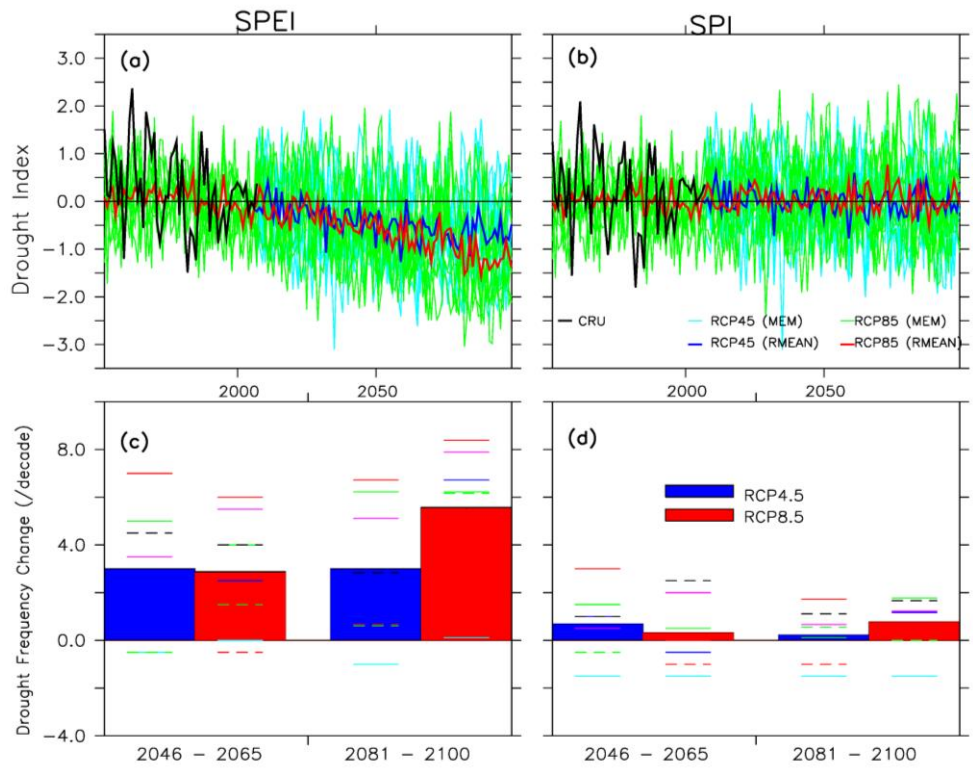
Figure 68: Future projections of drought over the core area of DM4

5.7 Drought Patterns

Here, we examine how the future characteristics of DJF drought patterns may differ from the past. For this purpose, we combined DJF droughts (SPEI) from CRU observation (1971–2005) and RCA simulations (1971–2005; 2031–2065 under both RCP4.5 and RCP8.5 scenarios) as a data set, and then applied SOMs on the data set to classify the patterns into 20 groups based on their similarities. Figure 69 shows results of the SOM classification. The figure suggests that some common drought patterns in the past climate may disappear in the future climate, while some new drought pattern may emerge in the future. For example, Node 15 drought pattern (typifying mild all-wet condition), which occurred about 4 events·decade^{-1} in the past decade, is projected to be less frequent under the RCP4.5 future scenario (< 1 event·decade^{-1}) and completely disappear under RCP8.5 future scenario. On the other hand, Node 1 drought pattern (showing severe all-dry condition), which never occurs in the past climate, is projected to be a common feature in under RCP4.5 scenario (2 events·decade^{-1}) and with a higher frequency under RCP8.5 scenario (3 events·decade^{-1}). However, the frequency of some drought patterns (Nodes 4 and 4, dipole patterns) are projected to remain unchanged in future climate under both RCP4.5 and RCP8.5 scenarios.

(a)

78
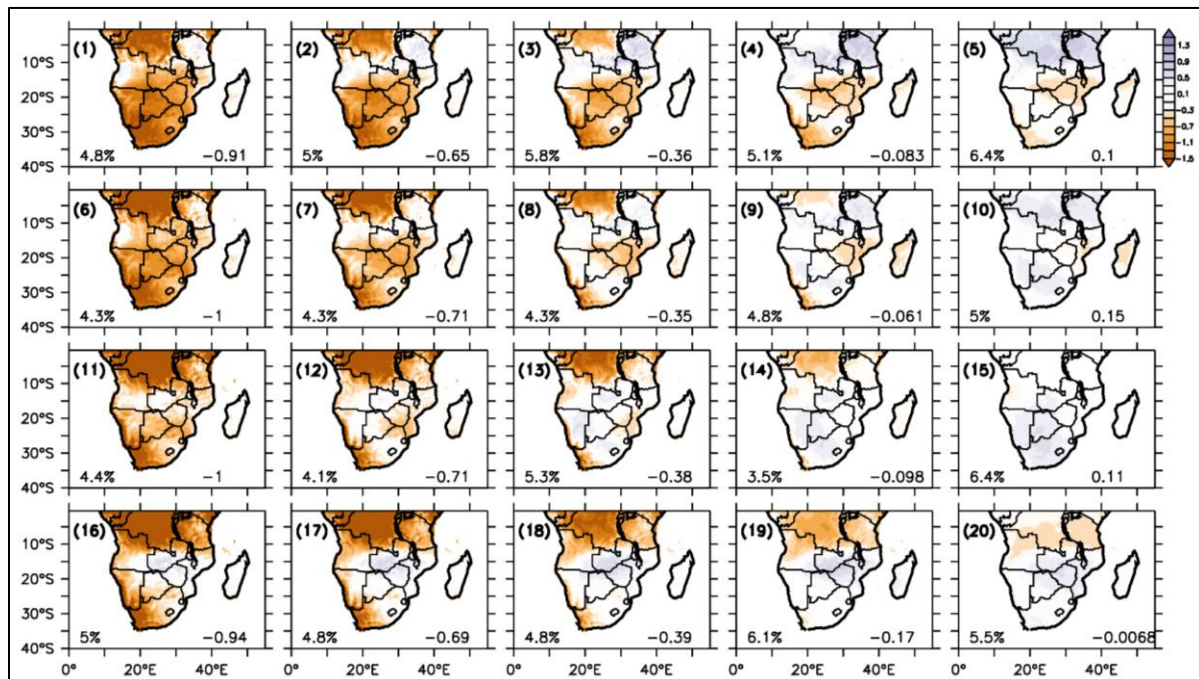
(b)
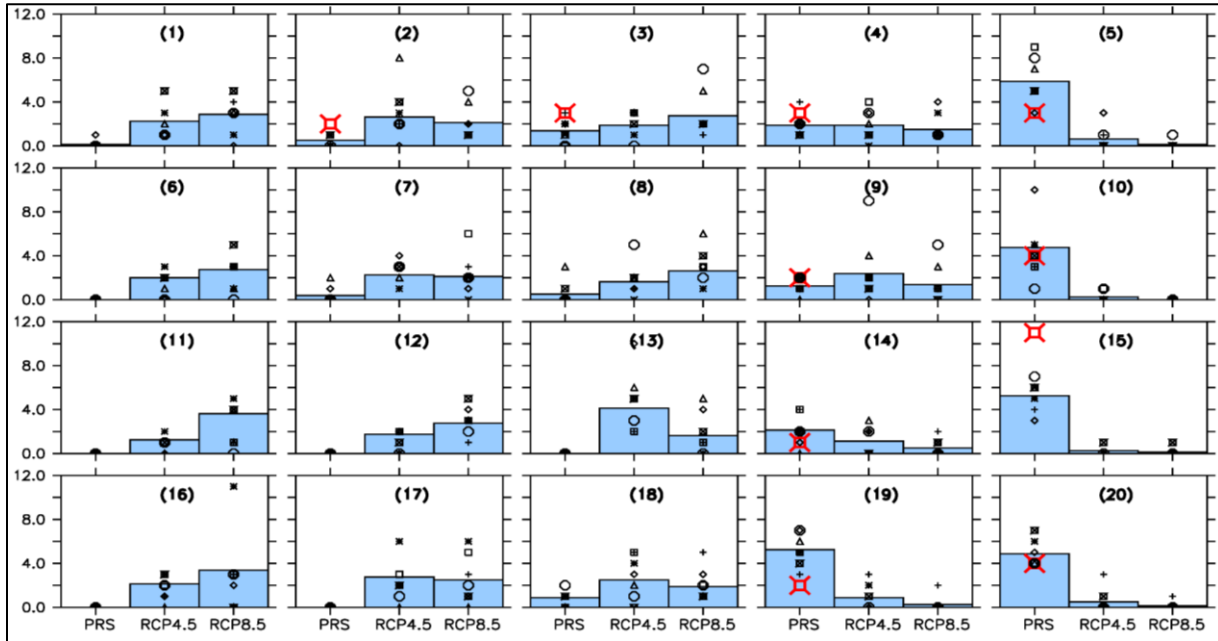
Figure 69: (a) The SOM classification of three-month drought patterns (SPEI) over southern Africa in past climate (1971–2005) and projected future climate (2031–2065) under RCP4.5 and RCP8.5 scenarios; (b) The frequency of the drought patterns during the present-day (1971–2005) and future (2031–2065, under RCP4.5 and RCP8.5 scenarios) climates. In (b), red makers indicate the CRU results, the black markers indicate model simulations, and the bars indicate ensemble mean of the simulations

5.8   Conclusions

This chapter projected future changes in the characteristics of southern African droughts. The projections focused on changes in drought intensity, coverage, frequency, modes, and patterns under two future climate scenarios (RCP4.5 and RCM8.5). Future climate simulations from an RCM that gives realistic representation of southern Africa droughts were analysed for the study. The analysis can be summarised as follows:

- The projections indicate that impacts of global warming would increase drought intensity, area coverage, and frequency over southern Africa. The increase is more pronounced under the RCP8.5 scenario than under the RCP4.5 scenario. However, there are also substantial differences in projection of SPEI and SPI droughts. The SPEI droughts are more intense, more frequent, and wider than the SPI droughts.

- The model projects no significant changes in the spatial structure of the four drought modes over southern Africa. However, more severe droughts are projected over the core areas of the drought modes, but the magnitude of the severity is higher for DM3 and DM4 modes than for DM1 and DM2 modes.

- The projections suggest that all-dry drought pattern would become more frequent in the future, while the all-wet drought pattern would become less frequent, but the frequency of dipole drought patterns would remain unchanged under both RCP4.5 and RCP8.5 scenarios.

79

6   IMPACT OF FORESTATION ON DROUGHTS OVER SOUTHERN AFRICA

6.1   Introduction

The impacts of climate change are projected to be severe in southern Africa. For instance, a warming of about 2–3°C by 2050 is projected over the borders of South Africa and Botswana, and the warming may exceed 4°C over some parts of the interior by the end of the century (Archer et al. 2010; Boko et al. 2007; Hudson and Jones 2002; Midgley et. al. 2007). In addition, a drier condition is projected over many areas of southern Africa in the future (Haensler et al. 2011b; Ringrose et al. 2002). Forestation has been suggested as a reasonable, effective, and affordable climate change mitigation option because of its biogeochemical benefits (Lenton and Vaughan 2009). It can sequester atmospheric carbon dioxide (a major greenhouse gas) and offset fossil fuel emissions (Virgilio and Marshall 2009). Under the United Nations Framework Convention on Climate Change (UNFCC) and the Kyoto Protocol, many efforts have been put into implementing forest-related carbon mitigation projects. The Clean Development Mechanism and Reducing Emissions from Deforestation and Forest Degradation (REDD) have also created financial incentive to store carbon in forests. Therefore, forestation does not only offer emission reductions, but it also creates economic opportunities that may generate monetary returns through carbon trading markets. In addition, forestation may also offer ancillary benefits, such as more sustainable livelihoods for local communities or opportunities for environmental conservation (Canadell and Raupach 2008; Topfer 2001). Most of these efforts, however, often overlook the biophysical effects of forestation on regional climate.

Studies have shown that the biophysical effects of forestation on climate can be harnessed in mitigating regional climate change. Using regional climate simulations, Chen et al. (2012) and Gálos and Jacob (2012) show that forestation may induce a nett cooling and reduce the severity of drought over the USA and Hungary, respectively. Abiodun et al. (2012) showed that forestation may reduce the projected warming over the forested region in West Africa. Despite these favourable effects, forestation may also induce negative impacts on the regional climate. For instance, Abiodun et al. (2012) showed that in West Africa, forestation may enhance the global warming north of the forested area. Swann et al. (2012) also showed that forestation in mid-latitude regions could produce regional warming and remotely modify atmospheric circulations. Hence, forestation may have both positive and negative feedbacks at different scales, and these feedbacks can modify the projected climate change signals. Despite the natural and commercial forestation activities in South Africa, no study has investigated the biophysical impacts of forestation on the regional climate in future. Hence, as part of the project, this study examined the potential impacts of forestation on future climate in southern Africa.

In previous chapters, we identified and characterised REDs over southern Africa (Chapter 2), examined the mechanisms that drive droughts (Chapter 3), assessed the capability of climates models to reproduce the droughts and the drought-driving mechanisms, and projected future changes in characteristics of the droughts. In the present chapter, we used climate model simulations to investigate the impact of forestation on the southern African droughts. The model simulations are described in Section 6.2. The impacts of forestation on precipitation, temperature and droughts are presented in Section 6.3, and the major findings are summarised in Section 6.4. The materials reported in the chapter are published in Naik and Abiodun (2016) and Naik (2015). For more detailed and comprehensive results, readers are referred to these publications.

6.2   Model Simulations

Model simulations data sets were analysed for the study. The model simulation data sets comprise two GCMs and two CORDEX RCMs simulations. The two GCMs are the Met Office Hadley Centre Model (HADGEM2-ES, hereafter HAD; Martin et al. 2011) and the Max Planck Institute for Meteorology Model (MPI-ESM-LR, hereafter MPI; Giorgetta et al. 2013). The simulations for both GCMs (HAD and MPI) were

obtained from the CMIP5 and were used to provide the initial and lateral boundary conditions for the two regional models. The two CORDEX regional models are the International Centre for Theoretical Physics (ICTP) Regional Climate Model version 4.3 (hereafter, RegCM; Pal et al. 2007) and the Weather Research Forecasting Model version 3.1.1 (hereafter, WRF; Skamarock et al. 2008a; 2008b).

Each RCM was applied to perform three experiments (Table 6). The first experiment (PRS) simulated the past climate, the second experiment (GHG) simulated the future climate without forestation, and the third experiment (FRS) simulated the future climate with potential forestation. The first two experiments (PRS and GHG) used the present-day land-cover patterns (Figure 70a and Figure 70c) in simulating the present-day (1970—2004) and the future (2030—2064) climate, respectively. The future climate experiments (GHG and FRS) were based on increasing greenhouse gas concentrations under the intermediate-range RCP4.5 scenario (Thomson et al. 2011).

The forestation experiment (FRS) used land-cover patterns in which the biophysically suitable areas in Eastern Cape are forested (Figure 71b and Figure 71d). This represents a future climate with the influence of natural bush encroachment and human-induced forestation in Eastern Cape. The forestation area was delineated based on results of previous studies (*i.e.* Gush et al. 2002) that mapped the distribution of quaternary catchments and identified regions where the mean annual precipitation (exceeds 650 mm) as sufficient to sustain forestation. Each RCM simulation was initialised and forced with the corresponding GCM simulation (i.e. RegCM with HAD, and WRF with MPI).

All simulations were run for 35 years (1970–2014 and 2030–2064), but the simulation of first year was discarded as spin up and the simulations of remaining 34 years (1971–2014 and 2031–2064) were analysed. We analysed the PRS simulation to evaluate the performance of the models in simulating the southern African climate, used the difference between PRS and GHG (*i.e.* GHG minus PRS) results to obtain the projected future climate change, and used the difference between GHG and FRS results (*i.e.* FRS minus GHG) to assess the impacts of the forestation on the future climate. Only the results of the last analysis (*i.e.* FRS minus GHG) are presented in this report. However, the focus of the present discussion will be on impacts of forestation (*i.e.* FRS minus GHG).

Table 6: Summary of the experiments performed with each regional climate model in the study

Experiment	Boundary condition forcing	Land-cover pattern
PRS	Present day (1970–2005)	Present day
GHG	Future (2030–2065) RCP4.5	Present day (Figure 2a & c)
FRS	Future (2030–2065) RCP4.5	Forestation and bush encroachment along the eastern margin of South Africa (Figure 2b & d)
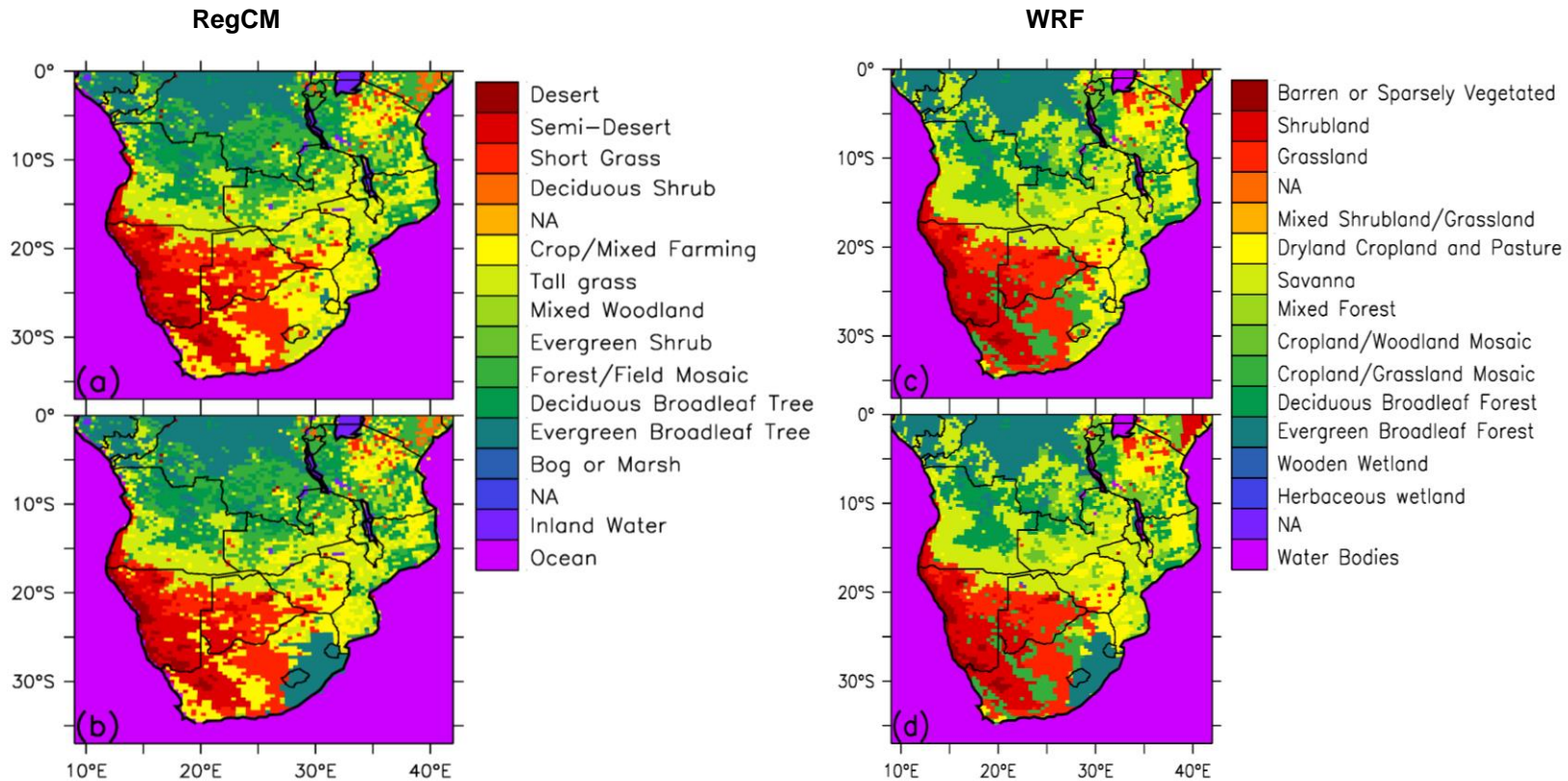
Figure 70: Land-cover types used for the present-day and future climate simulations (PRS and FRS, respectively) in the study. The land-cover types in left panels (a and b) are used in the RegCM simulations, while those in the right panels are used in the WRF simulation. The top panels (a and c) show the land-cover types used in for PRS simulation, while the lower panels (b and d) show those used in FRS simulations; the circles highlight the forested area. In the legend, "NA" means that the colour is not applicable for the model but applicable to the other model

6.3   Potential Impacts of Forestation on Rainfall and Temperature

The RCMs show that the forestation induces both warming and cooling over southern Africa, but the spatial distribution of the warming and cooling varies with the seasons, and slightly differs in the models (Figure 73). Although both models indicate that the peak of the warming resides over the forested area in all the seasons, the magnitude of the warming is higher in MAM than in JJA and the warming covers a wider area in RegCM than in WRF. For instance, with WRF, the warming of 0.1°C is confined to the Eastern Cape area in all the seasons, but with RegCM, it extends to the central part of southern Africa in DJF and JJA, and to the Western Cape area in MAM. There is a better agreement between the models on the spatial distribution of the cooling, which is most visible over Namibia and Botswana in MAM; however, the magnitude of the cooling is higher in RegCM (about −0.2°C) than in WRF (about −0.15°C). The forestation also induces wet and dry patterns over the subcontinent. The spatial distribution of the wet and cooling follows that of the warming and cooling in some seasons but differs in other seasons. But, in general, the forestation induces wet conditions over the forested area, except in the RegCM simulation, where it induces a dry condition along the eastern coast in JJA and MAM. In MAM, both models agree that the forestation enhances rainfall over Botswana in MAM. In other seasons, WRF shows that the forestation still increases the rainfall over Botswana, but RegCM suggests that the forestation decrease rainfall over the country. Both models also agree that the forestation induces a dry condition over south-western regions of the subcontinent during MAM and over the southern regions of the subcontinent during JJA and SON, but the magnitude of the drying differs between the RCMs. The difference in the degree of warming or drying produced by the forestation in the models may be partly attributed to subtle differences in the characteristics of the vegetation that the forest replaced in the simulations (Figure 71).

The impacts of the forestation on the rainfall and temperature fields can be linked to the biophysical influence of the forestation on the surface energy balance and on the atmospheric dynamics. For instance, the warming over the forested area can be attributed to the influence of forestation on the albedo (Table 7 and Table 8). The forestation decreases albedo (*i.e.* by −0.02 in MAM), thereby increasing the nett solar radiation at the surface (*i.e.* by 4.60 W·m^{-2} in MAM). The increase in the nett solar radiation enhances the sensible heat flux from the surface. While the increase in the sensible heat flux over the forested area is consistent with the warming over the area, the maximum increase in the sensible heat flux in MAM agrees with the region of peak warming during this season. In addition, the increase in rainfall over the forested can be attributed to both the albedo effect and the dynamic effect of the forestation. With the albedo effect, the increase in the nett solar radiation enhances the latent heat flux, but only in DJF (by 2.92 W·m^{-2}) and SON (by 3.52 W·m^{-2}), when the soil moisture is sufficient. This is consistent with the increase in surface moisture (*i.e.* specific humidity) and rainfall in the two seasons. With the dynamic effect, the increase in temperature and in surface friction induced by the forestation encourages convergence and cyclonic flow over the forested area, thereby producing more rain (Figure 73). This is supported by the decrease in surface pressure and increase in boundary layer height following the forestation. However, while the dynamic effect increases the rainfall in all seasons, the albedo effect only contributes to the rainfall increase in DJF and MAM. That explains why the rainfall increase is higher during DJF and MAM than in other seasons (SON and JJA). The simulated nett cyclonic flow around the forestation area is consistent with the enhance rainfall over the area.

The reactions of the models to the forestation are similar over the forested area. For instance, the models agree that the decrease in albedo (following the forestation) would increase the nett radiation (i.e. additional energy) at the surface, although the increase is higher in WRF (≈ 13.1 W·m^{-2}) than in RegCM (5.0 W·m^{-2}), because the decrease in albedo is larger in the former (≈ -7.5%) than in the later (≈ −2.2%).

Both models also indicate that forestation would enhance the Bowen ratio, meaning that the greater fraction of the additional energy is partitioned for warming the atmosphere rather than for moistening it.

Nevertheless, the models show different increase in the Bowen ratio (the value is higher in RegCM; hence, the fraction that goes for the warming is higher in RegCM than in WRF). The difference in the Bowen ratio may be attributed the dissimilarity in the way land-cover processes and parameters are represented in the models. However, due to the different the Bowen ratio, the models produce opposite changes in the surface air relative humidity. While RegCM suggests a decrease in the relative humidity ($\approx$ −1.5%), WRF indicates an increase (+0.5%). Nevertheless, both models agree that the forestation would increase the annual rainfall, though the magnitude of the increase is lower in RegCM ($\approx$1.34 mm·month^{-1}) than in WRF ($\approx$12.9 mm·month^{-1}). The RCMs also agree that the forestation would induce a warmer boundary layer; but, due to the difference in the Bowen ratio, the warming is higher in RegCM ($\approx$ 0.18°C) than in WRF (0.15°C), and the increase in boundary layer is higher in the former ($\approx$ 56 m) than in the later (23 m).

These results are consistent with those in Mackellar et al. (2008), where a cooling due to increase in surface albedo (from land-cover changes over southern Africa) was found to initiate a change in circulation through large-scale subsidence (as indicated by increased geopotential heights). As a consequence of this, moisture convergence reduced, and rainfall also decreased in some areas. In the present study, forestation produces opposite changes to those in Mackellar et al. (2008) because it decreases surface albedo. While the influence of forestation on temperature (*i.e.* warming) found in our study agrees with what Swann et al. (2012) found in mid-latitude regions, it contradicts what Abiodun et al. (2012) found over West Africa. With Abiodun et al. (2012), the forestation induced cooling over West Africa (despite the decrease in albedo following the forestation) because it increased evaporation, which in turn increased cloud amount and reduced incoming solar radiation and sensible heat flux. However, in agreement with all the previous studies, the results here suggest that the impacts of the forestation are not limited to the forested area. Through its influences on atmospheric circulation, the forestation remotely modifies the regional temperature and rainfall.
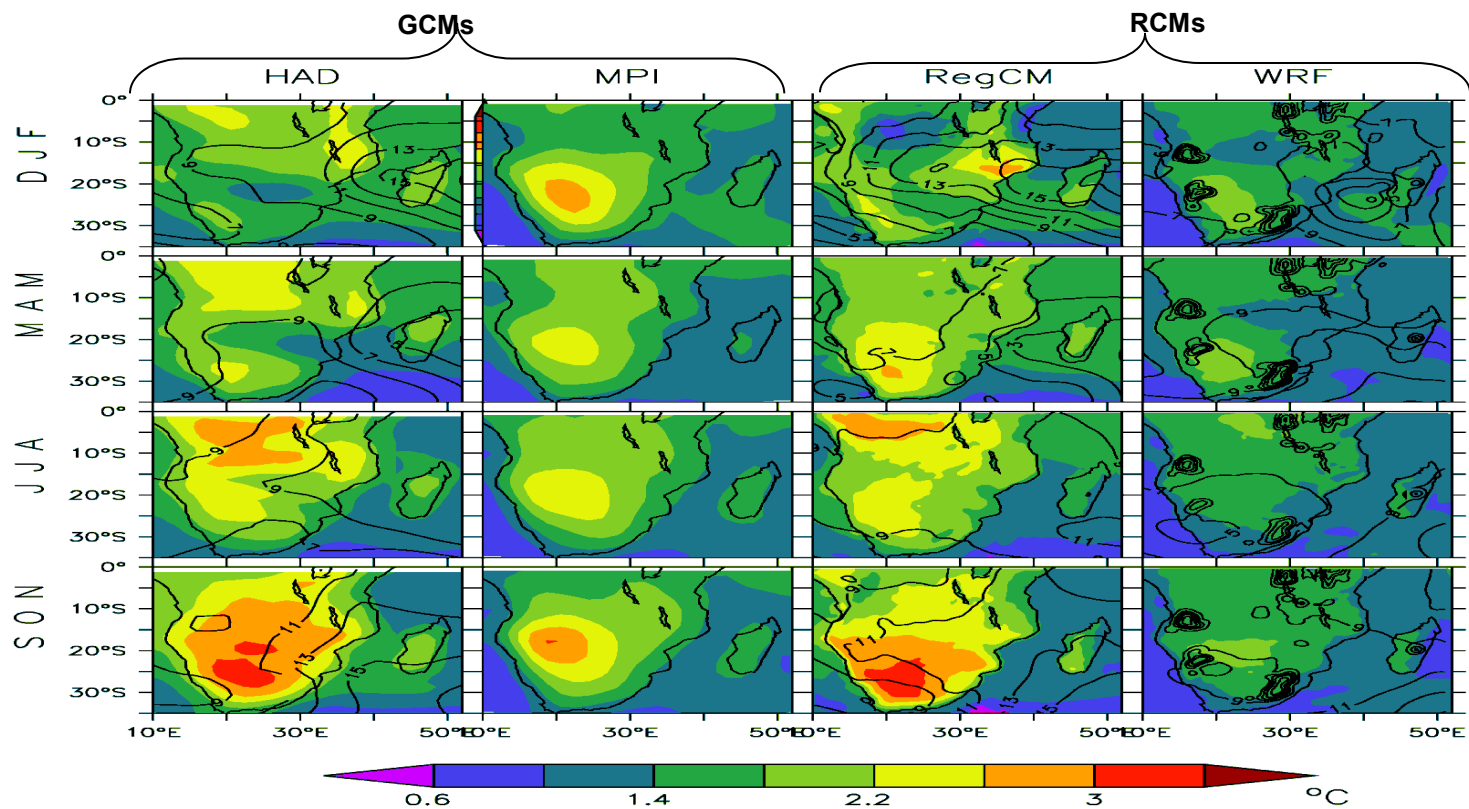
Figure 71: Projected future (2031–2064) changes in mean air temperature (shaded; °C) and 850 hPa geopotential height (contours: metres; the contour interval is 2 m). The changes are relative to the period 1971–2004, as simulated by the GCMs (HAD and MPI) and RCMs (RegCM and WRF)
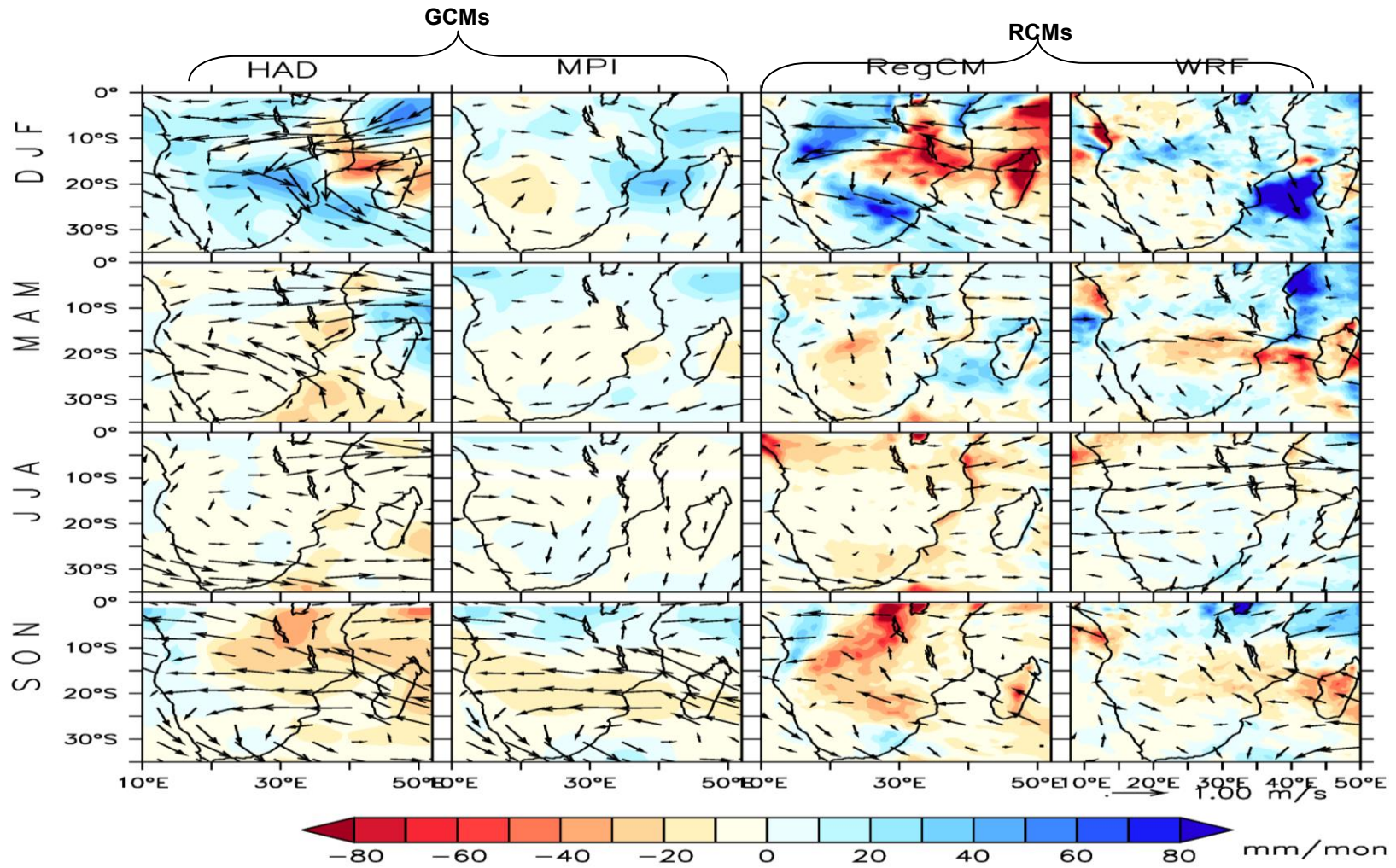
Figure 72: Projected future (2031–2064) changes in mean rainfall (shaded; mm·month⁻¹) and in 850 hPa winds (arrows), relative to the period 1971–2004, as simulated by the GCMs (HAD and MPI) and RCMs (RegCM and WRF). The bottom arrows are the wind speed scale
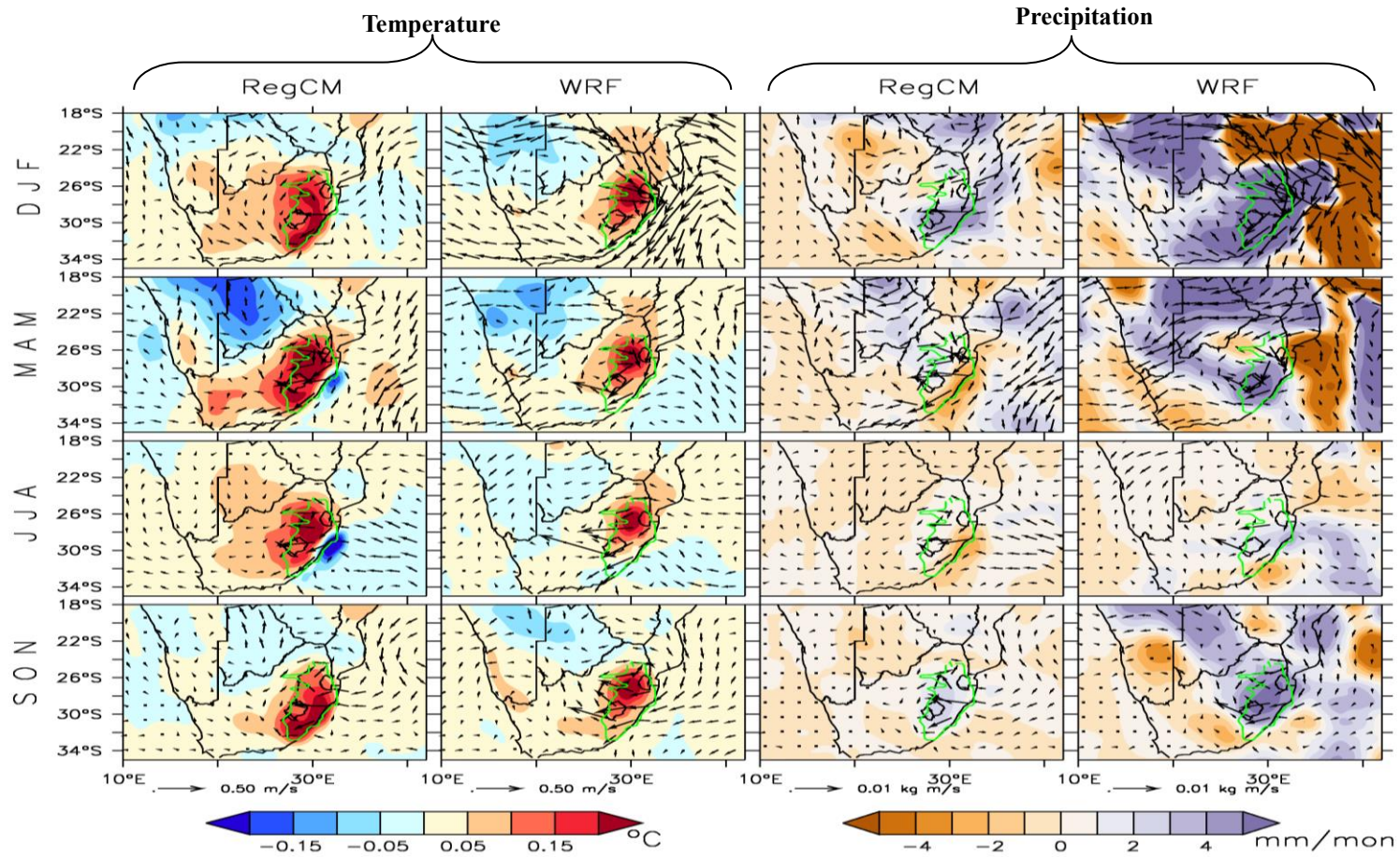
Figure 73: The simulated impacts of forestation (i.e. FRS minus GHG) on surface air (2 m) temperature (°C, shaded; first two left panels) and rainfall (mm·month⁻¹; last two right panels) for different seasons (DJF, MAM, JJA, and SON) in the period 2031–2064, as simulated by RegCM and WRF. The corresponding changes in 850 hPa winds (arrows; vector difference between FRS and GHG) are overlaid on the temperature plots, while the corresponding changes in moisture flux (arrows; vector difference between FRS and GHG) are overlaid on the rainfall plots. The bottom arrows are the scales of wind speed and magnitude of the moisture flux

Table 7: RegCM simulations over the forested area in each season (DJF, MAM, JJA, and SON): the mean (μ) and standard deviation (σ) of the climate averaged variables in the present-day climate (PRS); the projected future climate change (GHG–PRS, Δ); and the impact of the forestation on the future climate (FRS-GHG, ψ). The climate variables considered are temperature (Temp), rainfall (Rain), specific humidity (Q), relative humidity (RH), latent heat flux (LHF), surface downward shortwave flux in air (RSDS), nett shortwave energy flux (RSS), surface albedo (Albedo), sensible heat flux (SHF), surface drag force (Drag), maximum wind speed at 10 m height (Wind), moisture content of the soil layers (MRSO), planetary boundary layer thickness (PBL) and Bowen ratio. The significant climate change values (i.e. Δ > σ) are in bold. If a climate change value is significant, but the additional impact of forestation will make the overall future climate change signal not significant (i.e. Δ + ψ < σ), the impact of forestation value (ψ) is underlined. If the impact of climate change is not significant, but the additional impact of forestation will make the overall future climate change signal significant (i.e. Δ + ψ > σ), the impact of forestation value (ψ) is in bold

Variables	DJF				MAM				JJA				SON			
	PRS				PRS				PRS				PRS			
	μ	σ	Δ	ψ	μ	σ	Δ	ψ	μ	σ	Δ	ψ	μ	σ	Δ	ψ
Temperature (°C)	24.59	0.52	**1.72**	0.19	23.87	0.49	**1.81**	0.21	20.07	0.78	**5.62**	0.16	22.44	0.84	**2.35**	**0.19**
Rain (mm·month⁻¹)	73.79	42.92	10.10	3.49	31.63	25.87	−0.12	−0.23	17.76	20.64	13.75	**0.04**	51.98	29.37	0.62	2.06
Q (g·kg⁻¹)	11.33	0.49	**1.46**	0.05	9.57	0.47	**0.78**	−0.12	6.61	0.48	**3.75**	−0.09	9.17	0.41	**1.02**	0.05
RH (%)	84.85	2.53	1.12	−0.78	77.91	2.13	−1.95	**−2.10**	71.61	4.21	**4.35**	<u>−2.06</u>	80.05	3.31	−2.17	−0.99
LHF (W·m⁻²)	139.70	3.70	**4.49**	2.98	97.62	3.88	0.83	**−7.06**	63.87	4.37	**34.58**	−6.66	119.70	4.09	0.13	3.52
RSDS (W·m⁻²)	219.40	15.67	−9.92	−4.43	174.00	10.46	3.08	−2.79	142.50	8.67	**34.54**	−1.50	207.40	10.34	2.58	−1.96
RSS (W·m⁻²)	228.90	10.14	−6.37	3.83	170.90	6.85	1.32	4.37	135.10	4.78	**37.19**	5.34	209.50	6.37	0.99	**6.42**
Albedo	0.08	0.00	0.00	**−0.02**	0.09	0.00	0.00	**−0.02**	0.09	0.00	0.00	**−0.03**	0.08	0.00	0.00	**−0.02**
SHF (W·m⁻²)	33.85	5.06	**−5.88**	<u>1.09</u>	9.43	3.48	1.10	**5.52**	−4.11	3.05	**14.65**	4.36	24.47	3.80	1.65	2.02
Drag	0.07	0.10	0.00	0.04	0.12	2.05	0.01	0.20	0.04	0.02	**0.09**	0.09	0.19	0.34	0.04	−0.01
Wind (m·s⁻¹)	1.97	0.75	−0.26	−0.50	2.05	0.68	0.03	**−0.87**	4.68	1.12	**−2.60**	−2.10	1.51	0.63	0.44	−0.68
MRSO (kg·m⁻²)	29.98	1.26	0.78	**5.00**	26.96	1.07	**−1.16**	3.13	24.35	2.34	1.46	**2.89**	28.61	1.76	−1.08	**4.56**
PBL (m)	742.90	37.76	**−43.71**	<u>47.94</u>	646.40	31.31	10.53	**72.43**	665.70	45.87	−8.70	49.08	758.30	46.61	13.19	**54.66**
Bowen ratio	0.25	0.05	−0.05	0.01	0.08	0.04	0.01	**0.08**	−0.08	0.05	**0.17**	0.08	0.21	0.06	0.03	0.02

Variables	DJF				MAM				JJA				SON			
	PRS				PRS				PRS				PRS			
	μ	σ	Δ	ψ	μ	σ	Δ	ψ	μ	σ	Δ	ψ	μ	σ	Δ	ψ
Temperature (°C)	17.14	0.48	**1.37**	0.20	14.41	0.65	**1.40**	0.14	10.51	0.63	**5.30**	0.12	15.49	0.78	**1.39**	0.15
Rain (mm·month⁻¹)	208.20	35.23	−1.78	33.30	89.96	42.68	6.67	7.69	31.69	11.70	**64.94**	1.76	117.20	25.85	4.84	8.81
Q (g·kg⁻¹)	9.78	0.40	**0.90**	0.20	7.76	0.51	**0.85**	0.18	4.65	0.34	**3.96**	0.08	6.99	0.41	**0.71**	0.13
RH (%)	80.21	9.52	−0.55	0.14	74.18	9.39	0.58	0.92	60.34	9.20	**14.42**	0.61	65.38	8.20	0.59	0.27
LHF (W·m⁻²)	124.30	3.73	2.42	**9.16**	78.44	3.92	1.04	**7.09**	39.00	2.60	**40.48**	5.94	77.14	4.12	2.57	**9.74**
RSS (W·m⁻²)	240.80	10.81	−0.09	**11.60**	166.20	10.42	−1.12	9.92	132.80	4.27	**32.32**	12.19	220.70	8.28	0.76	**18.83**
Albedo	0.18	0.00	0.00	**−0.07**	0.19	0.00	0.00	−0.07	0.21	0.00	**−0.03**	−0.08	0.20	0.01	0.00	**−0.08**
SHF (W·m⁻²)	51.36	3.64	−0.58	**4.67**	23.75	3.18	−0.04	**3.71**	14.51	1.71	**9.20**	4.55	58.57	4.94	−1.27	**8.86**
Wind (m·s⁻¹)	5.78	2.93	0.91	−0.93	9.07	3.13	−1.67	−1.38	24.25	6.21	**−16.85**	−3.53	6.97	5.58	−0.86	−1.37
PBL (m)	540.20	22.62	−6.08	19.65	458.20	21.84	−11.78	14.81	489.10	21.87	**−42.66**	<u>23.71</u>	613.20	35.95	−17.78	33.92
Bowen ratio	0.43	0.03	−0.01	0.00	0.33	0.04	0.00	0.01	0.48	0.10	**−0.15**	0.03	0.88	0.23	−0.03	0.00

6.4   Potential Impacts of Forestation on Summer Drought

This section discusses how forestation can alter the projected changes in southern African summer drought in the future under the RCP 4.5 scenario. For the past climate (PRS), the RCMs models agree with CRU that the drought frequency over southern Africa ranges from about 1–2 events·decade^{-1} (Figure 74a and Figure 74b).
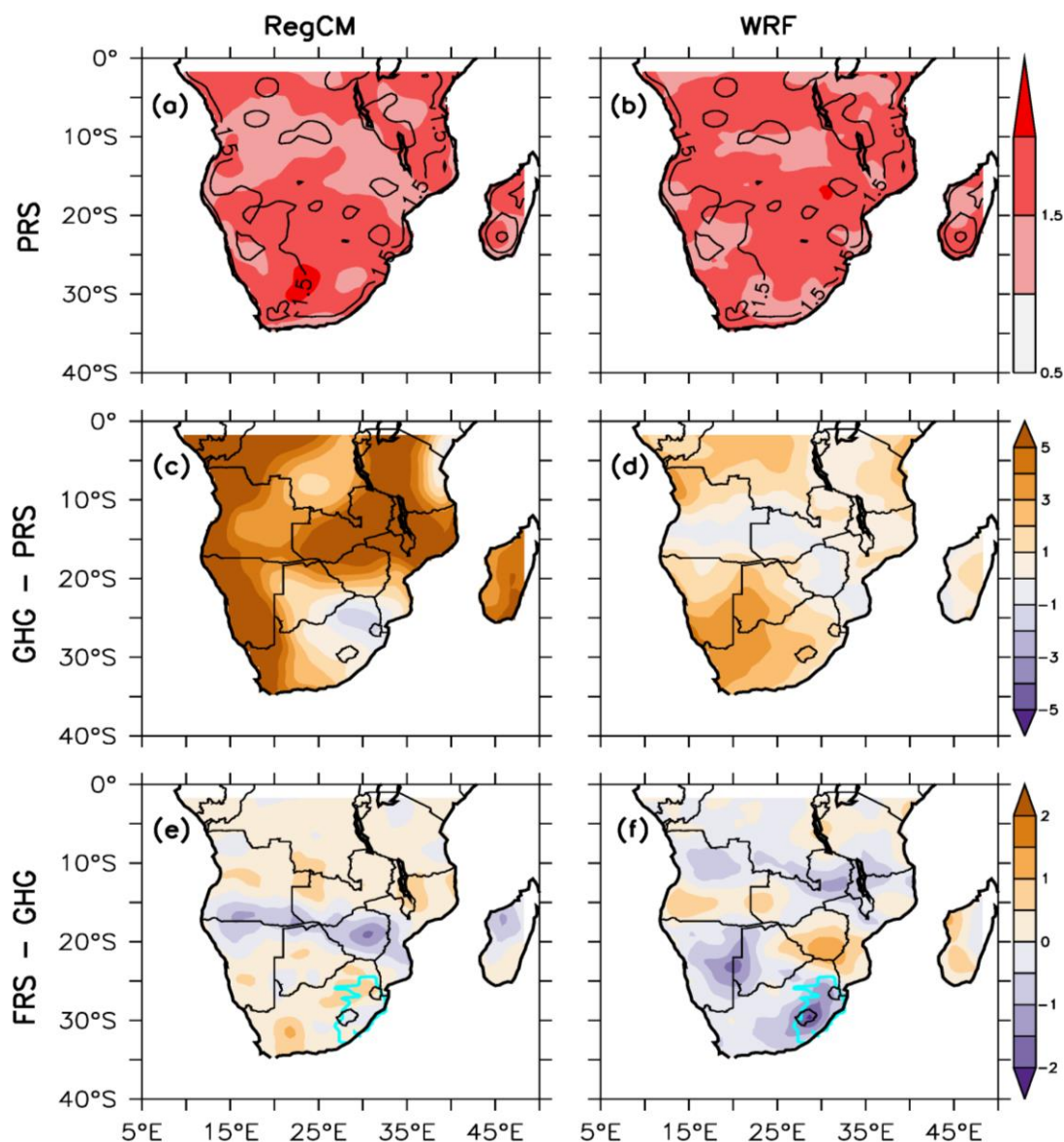
Figure 74: The potential impacts of forestation on summer (DJF) droughts (i.e. three-month SPEI < 1.5). The top panel shows the observed (CRU; contour) and simulated (RegCM and WRF; shaded) drought frequency (number of event per decade) in the present-day climate. The middle row shows the projected future changes in the drought frequency (event per decade) under the RCP4.5 scenario (i.e. GHG–PRS). The bottom row shows the impact of the forestation (i.e. FRS minus GHG) on the projected future drought frequency event per decade); the forested area is enclosed with blue line

With the elevated GHG concentration, both models project a future increase in the summer (DJF) drought frequency, and the spatial distributions of the increase are similar in the models. However, the magnitudes of the increase are generally larger in RegCM than in WRF (Figure 74c and Figure 74d). For instance, the largest increase, which occurs over northern Botswana, northern Mozambique, as well as the south-western regions of South Africa and Namibia, is about 5 events·decade^{-1} in RegCM,

but about 1-3 events·decade^{-1} in WRF. RegCM also shows a decrease in the drought frequency (about −2 events·decade^{-1}) over the north-eastern region of South Africa that is not simulated by WRF. With the forestation, the spatial distribution of the projected changes in the drought frequency differs between the models (Figure 74e and Figure 74f). For instance, WRF shows that the forestation decreases the drought frequency by about 5 events·decade^{-1} over much of the forested areas and over South Africa. However, this does not occur in RegCM simulations over the forested areas and, over parts of South Africa, where an increase in the drought frequency of about one event/decade occurs. RegCM and WRF also differ in the drought signal over adjacent regions, such as the Kalahari Desert, Zimbabwe, and parts of Mozambique. Thus, although both RCMs show that forestation may alter the characteristics of drought frequency in the future, from the divergent response to forestation, it is not clear as to where the forestation might alleviate or enhance the projected drought signal over southern Africa.

6.5   Summary and Conclusion

This chapter applied two RCMs (RegCM and WRF) to investigate the potential impacts of forestation on future climate in southern Africa. Forced with GCM simulations, the RCMs were used in three experiments: PRS (present-day climate), GHG (future climate without forestation) and FRS (future climate with forestation). The study first evaluated the performance of the RCMs (using PRS), and then presented the projected future changes (GHG minus PRS) before discussing the impacts on the forestation (FRS minus GHG). The results of the study can be summarised as follows:

- Both models give a realistic simulation of essential features of the southern African climate, but with some biases. The maximum bias in the temperature field (about 2°C in RegCM and about 4°C in WRF) occurs over the south-west of South Africa in summer, while the maximum bias in the rainfall field (about 75 mm·month^{-1} in RegCM and about 50 mm·month^{-1} in WRF) occurs over Zimbabwe in summer.

- The RCMs project warming over the entire subcontinent in all seasons, in both models the maximum warming occurs over south-west of South Africa, but with RegCM the maximum warming occurs in SON (3.2°C), and with WRF it occurs in DJF and MAM (2.0°C). In summer, RegCM projects drier summer conditions over Mozambique in the future, but WRF projects the wetter summer condition over the same area.

- Forestation enhances the projected warming and rainfall over the forested area but reduces them elsewhere. These changes are largely due to the albedo effect and dynamic effect of the forestation on the atmosphere. The darker forest (relative to pre-existing vegetation cover) decreases the surface albedo and increases the amount of solar radiation absorbed at the surface. This extra energy in the system increases the amount of sensible and latent heat, and increases the temperature and rainfall, respectively.

- The RCMs project that the elevated GHG could increase in drought frequency in summer over southern Africa in future. Forestation could alleviate the occurrence of these droughts over some regions but enhance it over other areas in southern Africa.

The potential biophysical impacts of forestation on future climate and extreme events have previously been illustrated over West Africa (Abiodun et al. 2012a; 2012b; Oguntunde et al. 2014). However, over southern Africa, while many studies have projected the future climate change, the influence of ongoing forestation activities in the region has previously not been included. This research provides a preliminary assessment of the potential climatic impacts of forests on the future climate in southern Africa. The results indicate, in the very least, a substantial sensitivity of the climate change projections to natural and commercial forestation activities and suggest that human management of forests could have some potential for regional climate regulation. However, our results illustrate that the impacts of forestation on regional climate are complex and that potentially unintended biophysical effects could occur. Thus, forestation projects in southern Africa should not only be viewed from the perspective of carbon storage alone. Rather, the biophysical effects need to be carefully weighed against the biogeochemical benefits (i.e. carbon sequestration).

7   DROUGHT MONITORING SYSTEM OVER SOUTHERN AFRICA

7.1   Introduction

Southern Africa has experienced severe droughts in the past few decades such as the 1991/92 droughts) (Meque and Abiodun 2014). The socio-economic impacts of these droughts have motivated many studies on southern African droughts. While some of the studies focused on monitoring the droughts (e.g. Unganai and Kogan 1998a; 1998b), some attempted to understand the spatial and temporal characteristics of the droughts (e.g. Dube and Jury 2003; Jury and Mwafulirwa 2002; Mulenga et al. 2003; Ujeneza and Abiodun 2014), while others concentrated on how to improve the seasonal forecasting of the droughts (e.g. Jury et al. 1999; Landman and Mason 1999; Unganai and Mason 2002). For example, Rouault and Richard (2003) developed a South African Drought Atlas to assist seasonal forecasting of drought over the country. A Drought Atlas can help improve drought monitoring and forecasting because we can learn from the past drought events or compare real-time drought pattern with similar past conditions (Rouault and Richard 2003). However, the Drought Atlas (developed in 2003) is now more than a decade old; hence, it may not account for some recent drought patterns. In addition, the Drought Atlas only covers South Africa, meaning that it does not show REDs over the subcontinent. Furthermore, the atlas used SPI to characterise the droughts, so it may underestimate the severity of the droughts as it has not considered the influence of temperature variability on the droughts. Hence, to address these shortcomings, the present project updates the Drought Atlas. It extends the atlas dates to 2015, uses SPEI that accounts for influence of both precipitation and potential evapotranspiration in characterising the droughts, and extends the atlas domain to cover the entire southern Africa. In addition, it includes future projections of the droughts under two possible climate change scenarios (RCP4.5 and RCP8.5).

The atlas (Figure 75) is an interactive online system, publicly available at: http://hail.csag.uct.ac.za/droughtmonitor/atlas.php. Depending on the user's interests, the atlas can be used to obtain information on past droughts and projected future changes in droughts characteristics over southern Africa, some of which are discussed in the in previous chapters. The present chapter provides detailed guidelines on how use the system and shows sample maps from the atlas. The online drought system has three options: Drought Monitoring, Drought Atlas, and Future Projections (Figure 75).
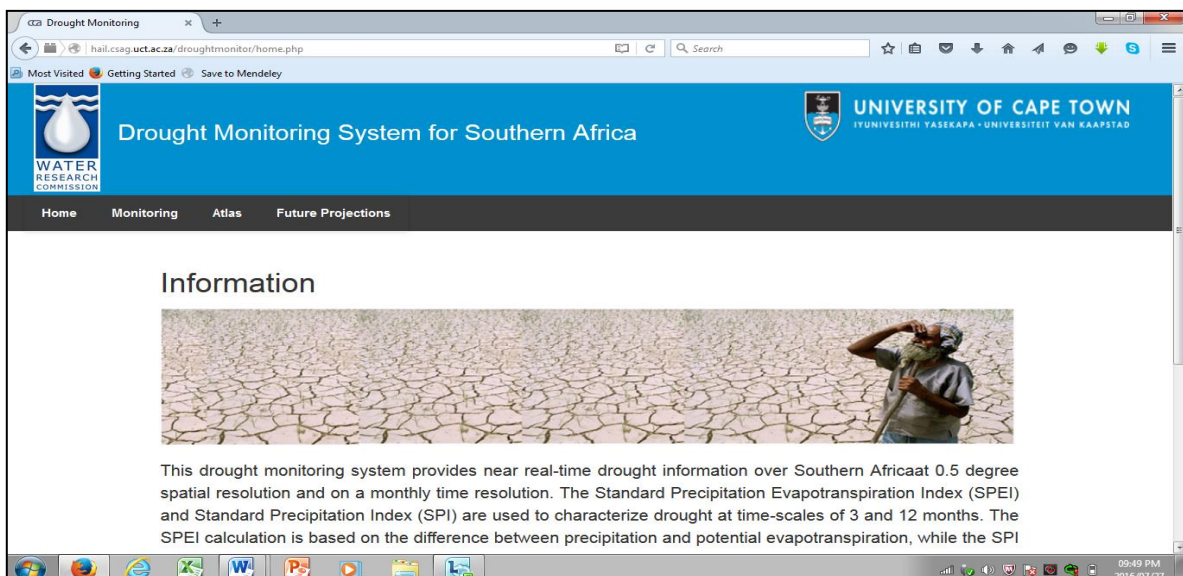
Figure 75: A screen shot of the project website portal

7.2   Drought Monitoring Option

The Drought Monitoring option provides near real-time drought information over southern Africa at 0.5-degree spatial resolution and on a monthly time resolution. The SPEI and SPI are used to characterise drought at time scales of three and 12 months. The SPEI calculation is based on the difference between precipitation and potential evapotranspiration, while the SPI is based on precipitation amount. The potential evapotranspiration is calculated with the Hargreaves method (PET) using maximum and minimum temperature. The calibration period for SPEI and SPI calculations is January 1971–December 2000. Monthly mean rainfall from the Global Precipitation Climatology Centre and monthly temperature (maximum and minimum) data from data sets are used for the NOAA NCEP CPC GHCN_CAMS gridded data set. The database is updated during the first days of the following month based on the reliable sources of climatic data.

The drought monitoring is suitable for near real-time monitoring and early warning purposes. The system produces spatial and temporal drought plots. The spatial option gives the spatial variation of drought index at three-month or 12-month scales. To retrieve this information, the user needs to specify the desired drought index (SPI or SPEI), drought scale (three-month or 12-month), the ending month, and the year of interest. An example of the spatial drought plot produced for a three-month SPI ending in February 2014 is shown in Figure 76. The information from this type of plot will indicate the drought hot spot, intensity, and coverage for the given period. From the plot one can deduce whether the region is experiencing patches of small-scale droughts or a RED. If it is a RED, a comparison of the map with those of previous months will provide information on temporal characteristics of the RED. For instance, it will show if the RED is expanding or reducing, moving or static, or if it is intensifying or weakening. Such information could help in seasonal prediction the drought coverage for the next month.
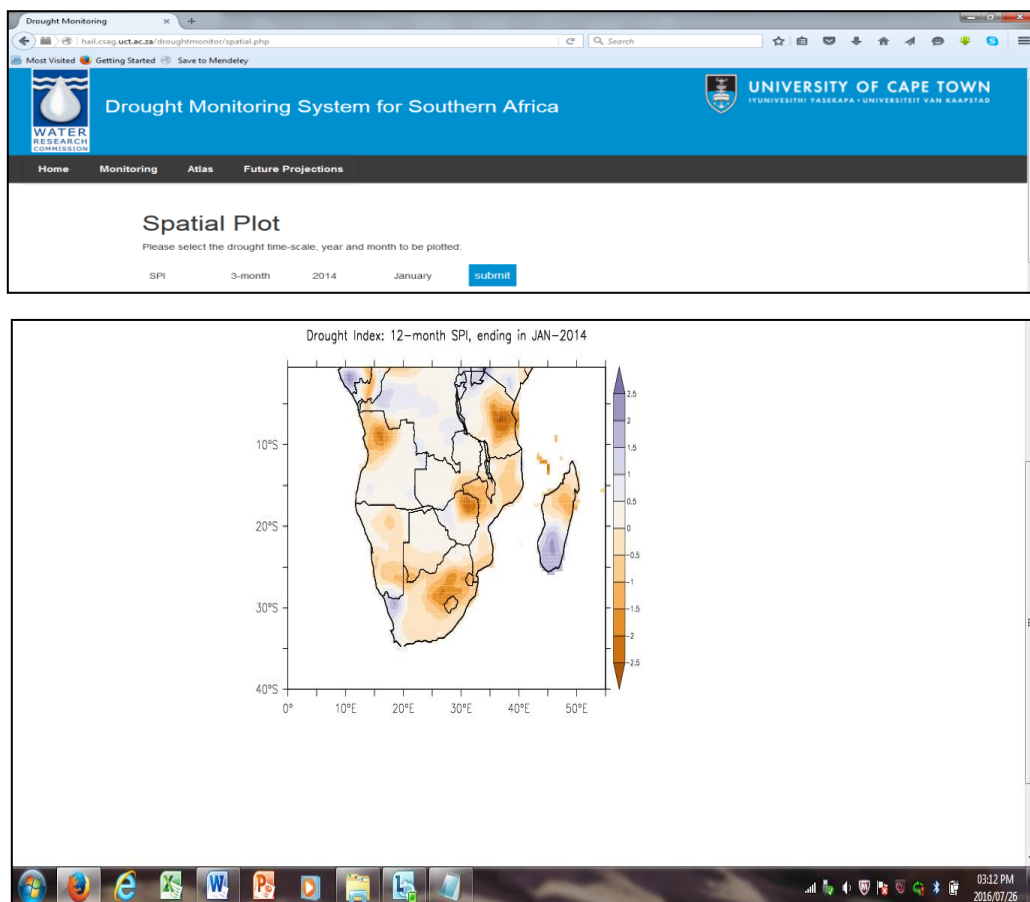
Figure 76: A screen shot of the spatial drought plot from the project website

The temporal plot option displays variation of drought index at three-month or 12-month scales, averaged over a given rectangular area or over a selected country. To retrieve the information over an area of interest, the user will specify the needed drought index (SPI or SPEI), the drought scale (three-month or 12-month), the longitude and latitude coordinates of the area, and the start and end of the period of interest. Figure 77 shows an example of a temporal plot for three-month SPI over a domain (15°E–24°W and 36°S–30°S) and a period (January 1952–December 2014). An example of a similar temporal plot for South Africa is shown in Figure 78.

The information from this type of plot clearly shows the temporal characteristics of drought over a selected area. It will also show the drought intensity, peak(s), duration and frequency. It also shows changes to these characteristics of droughts over time. This information could help seasonal predictions of the drought behaviour in the next few months.

Figure 77: A screen shot of the temporal drought plot over a rectangular area (Western Cape), as obtained from the project website
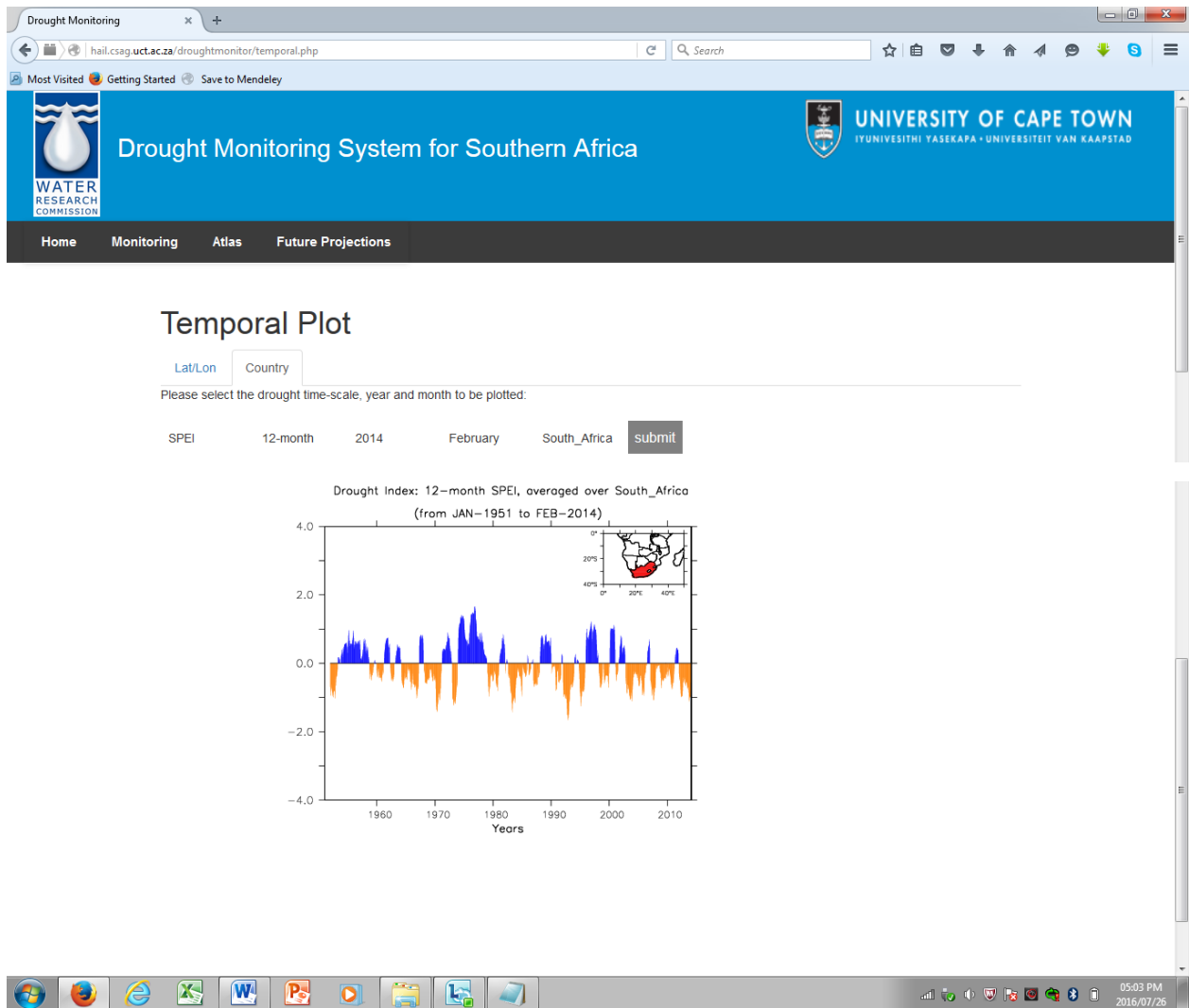
Figure 78: A screen shot of the temporal drought plot over a country (South Africa) as obtained from the project website

7.3   Drought Atlas Option

The Drought Atlas system generates drought maps for some special years or a composite drought pattern for selected years. The maps are generated based on some specified criteria, namely:

- The most widely extensive southern African drought patterns.
- Drought patterns during the positive and negative phases of ENSO.
- Drought patterns during the positive and negative phases of IOD.
- Drought patterns during the joint occurrence of IOD and ENSO.
- Drought patterns during positive and negative phases of Subtropical Indian Ocean Dipole (SIOD).

For example, Figure 79 shows a composite of drought during very strong ENSO (El Niño). Such maps give information on a drought pattern that may occur during a given teleconnection(s). This may aid in seasonal forecasting under similar conditions.
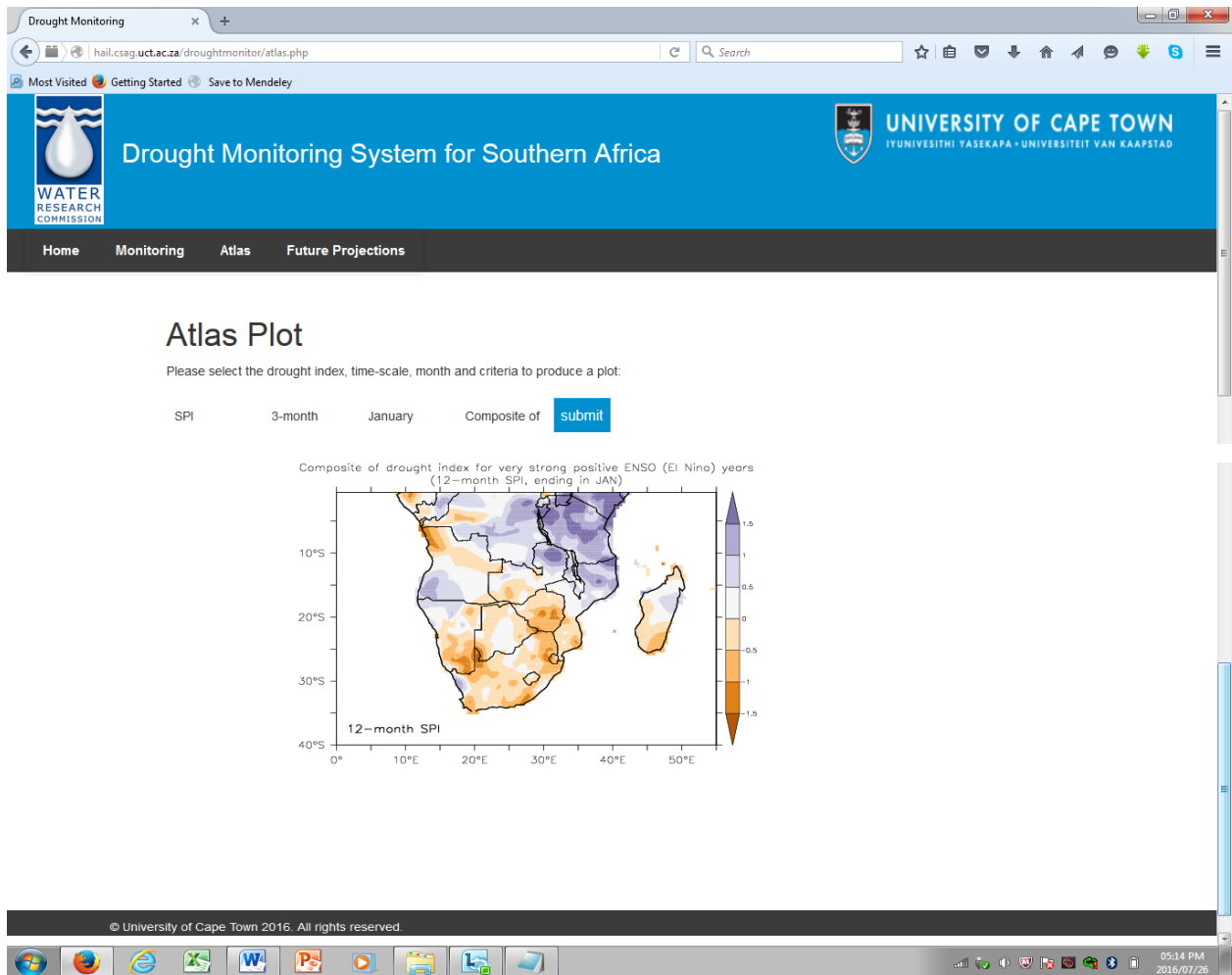
Figure 79: A screen shot of the atlas drought plot over southern Africa (composite of drought index for very strong ENSO years) as obtained from the project website

7.3.1 Southern African drought patterns during positive and negative phases of ENSO years

This part presents overall impacts of ENSO on southern Africa drought patterns. ENSO is a periodic departure of the SSTs in the equatorial Pacific Ocean from the normal. A positive phase of ENSO (i.e. El Niño) is characterised by warmer-than-normal water in the equatorial Pacific Ocean, while a negative phase of ENSO (La Niña) is characterised by cooler than normal water in the equatorial Pacific Ocean.

The composites of southern Africa drought patterns during very strong El Niño years (1983 and 1988), strong El Niño years (1958, 1966 and 1973), and strong La Niña years (1974, 1976 and 1989) were obtained at annual and seasonal scales. The resulting maps are shown in the Appendix.

7.3.2 Southern African drought patterns during positive and negative of IOD years

This part presents the average impacts of IOD events on southern Africa drought patterns. A positive IOD year is characterised by cooler than normal water in the tropical eastern Indian Ocean near Indonesia, and warmer-than-normal water in the tropical western Indian Ocean near Africa, while a negative IOD year is characterised by warmer-than-normal water in the tropical eastern Indian Ocean near Indonesia, and cooler than normal water in the tropical western Indian Ocean near Africa.

To obtain the impacts of positive phase of IOD of drought patterns, 11 years with positive IOD (1961, 1963, 1967, 1972, 1977, 1982, 1983, 1994, 1997, 2006 and 2007) were selected and the composites of the SPEI and SPI for the years were obtained at annual and seasonal scales. To obtain the impacts of negative phase of IOD of the drought patterns, a similar analysis was done but using ten years with

negative IOD years (1958, 1960, 1964, 1971, 1974, 1975, 1989, 1992, 1993 and 1996) were used. The resulting maps are shown in the Appendix.

7.3.3   Southern African drought patterns during joint occurrence of ENSO and IOD events

This presents impacts of joint occurrences of ENSO and IOD events. Some positive IOD events (not all) occur during the same year as an El Niño, and some negative IOD events (not all) occur during the same year as La Niña. It is rare for a positive IOD event to occur in the same year as La Niña (it occurred only once, in 2007, since 1950), and for a negative IOD event to occur during an El Niño year (it occurred only once, in 1993, since 1950). However, the relationship between ENSO and IOD is complicated and remains an active area of research.

To show the influence of joint occurrence of the two phenomena on the southern African drought patterns, we obtained the composite for the drought patterns that occurred during the positive IOD and El Niño years (1963, 1972, 1977, 1982, 1994, 1997 and 2006), and for those that occurred during negative IOD and La Niña years (1964, 1971, 1974 and 1975). This is done for droughts at annual and seasonal scales. The seasonal scale droughts show seasonal variation of the droughts from three months before to three months after the peak of the ENSO event in summer. The resulting maps are presented in the Appendix.

7.3.4   Southern African drought patterns during positive and negative SIOD years

This part presents impacts of SIOD on southern African drought patterns. SIOD is a periodic SST oscillation in which the south-west Indian Ocean (i.e. south of Madagascar) is warmer and then colder than the eastern part (i.e. off Australia). A positive SIOD year is characterised by warmer-than-normal SST south of Madagascar and colder-than-normal SST off Australia. The reverse is the case for a negative SIOD year.

To show the SIOD on the southern African drought patterns, we obtained the composite for the drought patterns during the positive SIOD years (1969, 1974, 1976, 1981, 1982 and 1999), and for those that occurred during negative SIOD years (1958 and 1964). This is done for droughts at annual and seasonal scales. The seasonal scale droughts show seasonal variation of the droughts from three months before to three months after the peak of the ENSO event in summer. The resulting maps are shown in the Appendix.

7.4   Future Projections Plots

The Future Projection Plots provides information on the projected future changes in drought characteristics over a given area or country. The future projection data sets used for this are obtained from CORDEX (http://www.cordex.org). Figure 80 gives an example of such projection over South Africa. This type of plot can help in preparation for future climate change. For instance, the projection in the plot suggests that drought is expected to worsen with the projected climate change. The projected increase in drought frequency and intensity could translate to into a variety of drought-related impacts that can affect key sectors of the South African economy. Effective drought monitoring is essential to improving preparedness for future drought. In addition, information from this map highlights the need to enhance our understanding of the differences between drought indices, especially if the research findings of similar studies are to provide valuable information for drought-related decision-making.
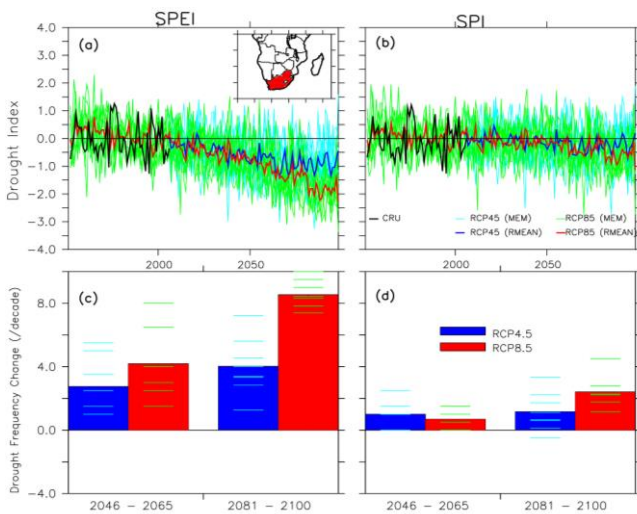
Figure 80: A screen shot of the projected changes (for two RCP futures) in drought characteristics over a country (South Africa) as obtained from the project website

The third section presents the future projection drought intensity and frequency over the entire southern Africa, and over ten southern African countries, namely: South Africa, Angola, Botswana, Madagascar, Lesotho, Mozambique, Namibia, Malawi, Zambia and Zimbabwe. Figure 80 shows a clear distinction between the future projections of drought from SPEI and SPI. With SPEI, an increase in intensity and frequency is projected over all the countries, although the magnitude of the increase differs over the counties. With SPI, an increase in drought intensity and frequency is projected over some countries (e.g. South Africa), while a decrease is projected over other countries (e.g. Zambia).

8   CONCLUSIONS AND RECOMMENDATIONS

8.1   Summary of Products from This Project

In the proposal for this project, three main products were envisaged: scientific papers, a public paper and a drought monitoring system. Detailed information for each of the envisaged products is given in Table 9. All these products have been delivered as envisaged.

8.1.1   Scientific papers

Scientific papers arising from this project are listed in Section 1.1 of the Bibliography. At the time of submission of this report, six papers have been published (three are directly from the project while the other three are extension of the project), one paper is under review, and two papers are in progress. In addition, work from this project has been presented in five talks and five posters at conferences and workshops.

8.1.2   Public paper

Results of from this work have been released as a public paper (http://www.droughtsa.org.za/images/Background_to_current_drought_situation_in_South_Africa.pdf). In addition, public awareness of the project has taken other forms:

- Two student interviews on southern African drought (Section 10.1.6).

- Development and continuous monthly update of the drought information on the drought monitoring website.

8.1.3   A drought monitoring system

The new drought monitoring system is an improvement over the earlier drought system developed by Rouault and Richard (2003) in three ways:

- The previous system used SPI to characterise droughts, but the present system used both SPI and SPEI to characterise droughts. While SPI is based on precipitation only, SPEI is based on the climate water balance (a function on precipitation, potential evapotranspiration and temperature). Hence, SPEI may give a better representation of impact of anthropogenic warming on the droughts.

- The drought maps have been updated to include recent droughts. In addition, the new system has the capability to give near-time monthly drought maps. It also provides future projections of droughts under two climate forcing scenarios.

- The horizontal domain developed of the drought monitoring system has been extended from South Africa to cover the entire southern Africa (and thus characterisation of REDs). Nevertheless, the new system still has the capability to provide drought information over a specific country over the subcontinent or over a targeted boxed area.

Table 9: Main products from the projects

Product	Target Group	Application
Scientific papers	The scientific community in all sectors involved in climate change and its impacts on hydrologic systems, particularly extremes; Working Group I and II of the IPCC	Four scientific papers describing the results on the characteristics REDs, the mechanism controlling the droughts, capability of climate model in simulating the droughts and the future projection of the droughts

Product	Target Group	Application
Public paper	National Water Planning Departments; National and Provincial Disaster Risk Management Agencies; Municipalities; Poor Rural Communities; Informal Urban Communities	One public paper describing the future characteristics of REDs in southern Africa
Improved drought monitoring forecasting system	Users of the SAWS, Climate System Analysis Group (CSAG), and CSIR seasonal forecast	A seasonal forecast of drought occurrence, coverage and intensity

8.2 Conclusions from the Project

The studies reported in Chapters 2–7 have revealed some robust information on the characteristics and drivers of REDs in southern Africa, the capability of contemporary climate models in simulating the droughts, the potential impacts of future anthropogenic forcing (under RCP4.5 and RCP8.5), and the potential impact of forestation on the projected droughts in southern Africa.

8.2.1 Characteristics of REDs

- About 50% of SPEI variance over southern Africa can be represented with four main drought modes (DM1, DM2, DM3 and DM4), which centre over the south-western part of southern Africa, Zimbabwe, Tanzania and Angola, respectively.

- The southern African drought patterns can be generally classified into three groups: An all-dry pattern, which shows a dry condition over the entire southern Africa; an all-wet pattern, which shows a wet condition over the whole region; and a dipole pattern, which shows both wet and dry conditions over the subcontinent.

- The drought patterns give a more robust description of RED characteristics than what drought modes give, because the entire drought mode descriptions fall under dipole drought pattern descriptions.

- Although each drought pattern can occur in any season, some drought patterns have preference for specific seasons. While some droughts patterns persist from season to season, others easily transit to another pattern in the following season.

- There are some distinctions in SPEI and SPI drought patterns in the past climate. The SPEI drought patterns suggests a general shift in the southern African drought from an all-wet condition in 1950s–1970s to an all-dry condition in 1990 (possibly due to the global warming), but in general, this shift does not feature in the SPI drought patterns, suggesting that the SPI may underestimate the influence global warming on southern African droughts.

8.2.2 Drivers of the droughts

- There is a strong dipole correlation between ENSO and droughts (SPEI) over southern Africa; the positive correlation is up to +0.6 over the tropical area and the negative is up −0.6 over the subtropical area. However, the link between ENSO and droughts (SPEI) is due to the influence of ENSO on both precipitation and temperature fields, and the influence ENSO is stronger on temperature than on precipitation.

- While ENSO influences droughts over most regions in southern Africa, the influence of IOD on the DM2 drought mode is as important as that of ENSO, while the influence of TNA on DM3 is more important than that of ENSO.

- Only 20% of drought patterns (all-dry and all-wet patterns) are induced solely by ENSO, other drought patterns are caused by complex interactions among the atmospheric teleconnections. All-dry drought patterns usually occur during El Niño, while all-wet patterns usually occur during the La Niña events.

8.2.3   Simulations of the droughts

- Contemporary GCMs give remarkable simulations of the spatial structure of the drought modes. However, GCMs reproduce the structure better at three-month drought scale than at 12-month drought scale. About 70% of the GCMs simulate all drought patterns well at three-month scale, while only 60% of the GCMs simulate three of the drought patterns well at 12-month scale.

- CORDEX RCMs also simulate the spatial characteristics of the drought modes better at three-month scale than at the 12-month scales, but they capture the temporal variability of the drought modes better at 12-month scale than three-month scale.

- The RCMs give realistic simulation of the drought patterns over southern Africa, but they perform poorly in simulating the temporal variability of the drought patterns. However, ARPEGE model perform best in simulating the drought patterns and their temporal variability.

- Some RCMs simulate the ENSO influence on the southern African drought as observed. In this regard, the ARPEGE (a variable-resolution model) shows the best simulation, possibly because it does have lateral boundary condition problem.

- The RCA model also gives a credible simulation of the ENSO influence on the southern African drought as observed. However, the RCA-simulated link between ENSO and southern African droughts is sensitive to the global data set used as the lateral boundary conditions. In some cases, the RCA downscaling of GCM simulations adds value to the simulated link, but in other cases it does not add value. The added value of RCA to the simulated link decreases as the capability of the GCM to simulate the link increases. This study suggests that downscaling GCM simulations with RCMs over southern Africa may improve or depreciate the simulated ENSO-drought link over the region.

8.2.4   Future projections of the droughts

- The RCA future projections (using ensemble simulations) indicate that global warming would increase droughts intensity, area coverage, and frequency over southern Africa. The increase is more pronounced under the RCP4.5 scenario than under the RCP8.5 scenario. However, there are substantial differences in projection of SPEI and SPI droughts. The SPEI droughts are more intense, more frequent and wider than the SPI droughts.

- The model projects no significant changes in the spatial structure of the four drought modes over southern Africa. However, more severe droughts are projected over the core areas of the drought modes, but the magnitude of the severity is higher for DM3 and DM4 modes than for DM1 and DM2 modes.

- The projections suggest that an all-dry drought pattern would become more frequent in the future, while an all-wet drought pattern would become less frequent, but the frequency of dipole drought patterns would remain unchanged under both RCP4.5 and RCP8.5 scenarios.

8.2.5   Impact of forestation on the droughts

- Forestation enhances the projected warming and rainfall over the forested area but reduces them elsewhere. These changes are largely due to the albedo effect and dynamic effect of the forestation on the atmosphere. The darker forest (relative to pre-existing vegetation cover) decreases the surface albedo and increases the amount of solar radiation absorbed at the surface. This extra energy in the system increases the amount of sensible and latent heat, and increases the temperature and rainfall, respectively.

- The RCMs project that the elevated GHG could increase in drought frequency in summer over southern Africa in future. Forestation could alleviate the occurrence of these droughts over some regions but enhance it over other areas in southern Africa.

8.3 Recommendation

Results of this project can be improved or applied in several ways. For instance, it can be improved by using more observational, reanalysis and simulation data sets that cover a longer time period. Using data sets with a longer time period (i.e. paleo-climate data sets) would give better information on whether the disappearance of the all-wet drought since the last few decades is due to the impact of climate change or it is a part of natural climate variability. Performing the analysis with more data sets will help in quantifying the uncertainties in the results, hence making them more robust for policymaking.

There is a need for additional studies to investigate why the stretched-grid global climate model (SGCM) performed better than the limited-area climate models (i.e. RCMs) in simulating a link between ENSO and southern African droughts. The most plausible reason is that while the lateral boundary condition problem in RCMs could be a bottleneck in simulating the link, there is no boundary condition problem in the stretched-grid global model. A climate model that can function as GCM, SGCM, and RCM is required to study the influence of boundary condition problem in simulating the link between atmospheric teleconnection and southern African droughts. However, results of such experiments will assist the climate model development community (especially in southern Africa) to focus their efforts and resources on areas that will improve the simulations of southern African droughts.

Although the project analysis focused on characteristics of REDs in past climate and in future climate projection, the analysis can be easily extended to forecasting REDs at subseasonal to seasonal scales. The emphases of conventional seasonal forecasting systems in southern Africa have been on rainfall and temperature anomalies. Incorporating the methodology and results of this project into the current seasonal forecasting systems will make the systems provide more relevant and useful information for minimising drought impacts over the subcontinent. Lastly, the results of the project can also be applied in studying impacts of REDs on southern African river basins and in investigating how land-use management (e.g. land-cover changes) can be used to mitigate the impacts.

BIBLIOGRAPHIES

1   Publications, Presentations and Interviews Arising from this Project

1.1   Published and Accepted Papers

Abbar SO and Abiodun BJ (2016) How well do CORDEX models simulate extreme rainfall events over the East Coast of South Africa? *Theoretical & Applied Climatology*. DOI: 10.1007/s00704-015-1714-5.

Abiodun BJ, Abbar SO, Lennard C and Jack C (2015). Using regional climate models to simulate extreme rainfall events in the Western Cape, South Africa. *International Journal of Climatology*. DOI: 10.1002/joc.4376.

Browne-Klutse N, Abiodun BJ, Hewitson BC, Gutowski WJ and Tadross M (2016) Evaluation of two GCMs in simulating rainfall inter-annual variability over southern Africa. *Theoretical & Applied Climatology*. 123, 415–436.

Meque A and Abiodun BJ (2015) Simulating the link between ENSO and summer drought in southern Africa using regional climate models. *Climate Dynamics*. 44, 1881–1900.

Naik M and Abiodun, BJ (2016). Potential impacts of forestation on future climate change in southern Africa. *International Journal of Climatology.* DOI: 10.1002/joc.4652.

Ujeneza E and Abiodun BJ (2015) Drought modes in southern Africa and how well GCMs simulate them. *Climate Dynamics.* 44(5), 1595–1609.

1.2   Submitted Papers

Meque A and Abiodun BJ (2016) Persistence and transition of droughts in Southern Africa. *Climate Dynamics* (submitted).

1.3   Papers in Preparation

Abiodun BJ, Meque A, New M and Rouault M (2016) Potential impacts of climate change on drought modes in southern Africa.

Abiodun BJ, Meque A, New M and Rouault M (2016) Projections of drought patterns over southern Africa from CORDEX RCMs.

1.4   Conference Talks and Posters

Abiodun BJ (June 2014) How well do regional climate models simulate extreme rainfall events in South Africa? 3rd Lund Regional-Scale Climate Modelling Workshop 21st Century Challenges in Regional Climate Modelling.

Abiodun BJ (December 2014) The persistence and transition of drought patterns in southern Africa. Workshop on Paleo-Environmental Change in Africa, Networking and Collaboration Meeting December 24, 2014 K5/2067/1 Report on Deliverable 7 June 2016.

Abiodun BJ and Naik M (June 2014) The potential impacts of forestation in mitigating climate change over southern Africa. 8th ICTP Workshop on the Theory and Use of Regional Climate Models.

Meque A (June 2014) The link between El Niño Southern Oscillation (ENSO) and the southern African rainfall in a regional climate model. 3rd Lund Regional-Scale Climate Modelling Workshop – 21st Century Challenges in Regional Climate Modelling.

Meque A (December 2015) The persistence and transition of drought patterns in southern Africa. The Climate System Analysis Group (CSAG) Weekly Seminar, University of Cape Town, South Africa.

Naik M (June 2014) The potential impacts of forestation in mitigating climate change over southern Africa. 3rd Lund Regional-Scale Climate Modelling Workshop 21st Century Challenges in Regional Climate Modelling.

2 Publications Cited in this Report

Abiodun BJ, Adeyewa ZD, Oguntunde PG, Salami AT and Ajayi VO (2012a) Modeling the impacts of reforestation on future climate in West Africa. *Theoretical and Applied Climatology* 110(1–2): 77–96. DOI: 10.1007/s00704-012-0614-1.

Abiodun BJ, Lawal KA, Salami TA and Abatan AA (2012b) Potential influences of global warming on future climate and extreme events in Nigeria. *Regional Environmental Change* 13:477–491.

Abiodun BJ, Salami AT, Matthew OJ and Odedokun S (2013) Potential impacts of afforestation on climate change and extreme events in Nigeria. *Climate Dynamics* 41(2): 277–293.

Agarwal P and Skupin A (eds.) (2008) *Self-Organising Maps: Applications in Geographic information Science.* John Wiley & Sons, West Sussex.

Andrews ED, Antweiler RC, Neiman PJ and Ralph FM (2004) Influence of ENSO on flood frequency along the California Coast. *Journal of Climate* 17: 337–348.

Araujo J, Abiodun BJ and Crespo O (2014) Impacts of drought on grape yields in Western Cape, South Africa. *Theoretical and Applied Climatology* 123(1–2): 117–130.

Archer E et al. (2010) *South African Risk and Vulnerability Atlas*. Department of Science and Technology.

Ashok K, Behera SK, Rao SA, Weng H and Yamagata T (2007) El Niño Modoki and its possible teleconnection. *Journal of Geophysical Research* 112 (C11): C11, 007. DOI: 10.1029/2006JC003798.

Beguería S and Vicente-Serrano SM (2013) Package "SPEI". DOI: 10.1175/2009JCLI2909.1.http.

Blamey R and Reason CJC (2007) Relationships between Antarctic sea-ice and South African winter rainfall. *Climate Research* 33, 183–193.

Boko M et al. (2007) Africa. Climate Change 2007: Impacts, Adaptation and Vulnerability. Contribution of Working Group II to the Fourth Assessment Report of the Intergovernmental Panel on Climate Change. Cambridge: 433–467.

Boulard D, Pohl B, Cretat B, Vigaud N and Pham-Xuan T (2013) Downscaling large-scale climate variability using a regional climate model: The case of ENSO over southern Africa. *Climate Dynamics* 40: 1141–1168.

Brown JR, Jako C and Hayenes JM (2010) An evaluation of rainfall frequency and intensity over the Australian region in a global climate model. *Journal of Climate* 23: 6504–6525.

Calow RC, Macdonald AM, Nicol AL and Robins NS (2010) Ground water security and drought in Africa: Linking availability, access, and demand. *Groundwater* 48(2): 246–56. DOI: 10.1111/j.1745-6584.2009.00558.x.

Canadell JG and Raupach MR (2008) *Managing Forests for Climate Change Mitigation*. Science, New York, NY, 320(5882): 1456–7. DOI: 10.1126/science.1155458.

Cavos T (1999) Large-scale circulation anomalies conducive to extreme precipitation events and derivation of daily rainfall in northeastern Mexico and southeastern Texas. *Journal of Climate* 12: 1506–1523.

Chen G-S, Notaro M, Liu Z and Liu Y (2012) Simulated local and remote biophysical effects of afforestation over the southeast United States in boreal summer. *Journal of Climate* 25(13): 4511–4522. DOI: 10.1175/JCLI-D-11-00317.1.

Christensen JH et al. (2007) Regional climate projections. Climate Change, 2007: The Physical Science Basis. Contribution of Working Group I to the Fourth Assessment Report of the Intergovernmental Panel on Climate Change, University Press, Cambridge, Chapter 11 847–940.

Compo GP, Whitaker JS and Sardeshmukh PD (2006) Feasibility of a 100-year reanalysis using only surface pressure data. Bulletin of the American Meteorological Society. American Meteorological Society 87(2): 175–190. DOI: 10.1175/BAMS-87-2-175.

Compo GP et al. (2009) NOAA CIRES Twentieth Century Global Reanalysis Version 2. Research Data Archive at the National Center for Atmospheric Research, Computational and Information Systems Laboratory: Boulder, CO. DOI: 10.5065/D6QR4V37.

Compo GP et al. (2011) *The twentieth century reanalysis project. Quarterly Journal of the Royal Meteorological Society* 137(654): 1–28. DOI:10.1002/qj.776.

Cook BI, Bonan GB and Levis S (2006) Soil moisture feedbacks to precipitation in southern Africa. *Journal of Climate* 19(17): 4198–4206.

Dai A (2011) Drought Under global warming: A review. *Wiley Interdisciplinary Reviews: Climate Change* 2(1): 45–65. DOI: 10.1002/wcc.81.

Dai A, Trenberth EK and Qian T (2004) A global dataset of Palmer drought severity index for 1870–2002: Relationship with soil moisture and effects of surface warming. *Journal of Hydrometeorology* 5: 1117–1130.

Dee DP et al. (2011) The ERA-Interim reanalysis: Configuration and performance of the data assimilation system. *Quarterly Journal of the Royal Meteorological Society* 137: 553–597. DOI: 10.1002/qj.828.

Di Luca A, De Elia R and Laprise R (2012) Potential for added value in precipitation simulated by high-resolution nested regional climate models and observations. *Climate Dynamics* 38:1229–1247. DOI: 10.1007/s00382-011-1068-3.

Di Luca A, De Elia R and Laprise R (2013) Potential for small scale added value of RCM's downscaled climate change signal. *Climate Dynamics* 40, 601–618.

Dube LT and Jury MR (2003) Structure and precursors of the 1992/93 drought in KwaZulu-Natal, South Africa from NCEP reanalysis data. *Water SA* 29(2): 201–207.

Engelbrecht FA, McGregor JL and Engelbrecht CJ (2009) Dynamics of the conformal-cubic atmospheric model projected climate-change signal over southern Africa. *International Journal of Climatology* 29: 1013–1033.

Everitt B, Landau S, Leese M and Stahl D (2011) *Cluster Analysis*. 5th ed. John Wiley & Sons, West Sussex.

Farge M (1992) Wavelet transforms and their applications to turbulence. *Annual Review Fluids Mechanics* 24(Holschneider 1991): 395–457.

Fauchereau N, Pohl B, Reason CJC, Rouault M and Richard Y (2009) Recurrent daily OLR patterns in the southern Africa/southwest Indian Ocean region, implications for South African rainfall and teleconnections. *Climate Dynamics* 32:575–591.

Fauchereau N, Trzaska S, Rouault M and Richard Y (2003) Rainfall variability and changes in southern Africa during the 20th century in the global warming context. *Natural Hazards* 29: 139–154.

Gálos B and Jacob D (2012) Regional-scale assessment of the climatic role of forests under future climate conditions. In: Liu, G. (ed). *Greenhouse Gases: Emission, Measurement and Management.* ISBN 979-953-307-224-0, 295–314 pp.

Giannini A, Biasutti M, Held IM and Sobel AH (2008) A global perspective on African climate. *Climatic Change* 90: 359–383. DOI: 10.1007/s10584-008-9396-y.

Giorgetta MA et al. (2013) Climate and carbon cycle changes from 1850 to 2100 in MPI-ESM simulations for the Coupled Model Intercomparison Project phase 5. *Journal of Advances in Modeling Earth Systems*. Wiley Online Library 5(3): 572–597.

Giorgi F, Jones C and Asrar GR (2009) Addressing climate information needs at the regional level: The CORDEX framework. *WMO Bulletin* 58: 175–183.

Gush MB, Scott DF, Jewitt GPW, Schulze RE and Hallowes LA (2002) A new approach to modelling streamflow reductions resulting from commercial afforestation in South Africa. *South African Forestry Journal* 196(November): 27–36.

Haensler A, Hagemann S and Jacob D (2011a) Dynamical downscaling of ERA40 reanalysis data over southern Africa: Added value in the simulation of seasonal rainfall characteristics. *International Journal of Climatology* 31: 2338–2349.

Haensler A, Hagemann S and Jacob D (2011b) The role of the simulation setup in a long-term high-resolution climate change projection for the southern African region. *Theoretical and Applied Climatology* 106(1–2): 153–169.

Hallack-Alegria J, Ramirez-Hernandez J and Watkins Jr DW (2012) ENSO-conditioned rainfall drought frequency analysis in northwest Baja California, Mexico. *International Journal of Climatology* 32: 831–842.

Harrison M (1984) A generalised classification of southern African summer rain-bearing synoptic systems. *Journal of Climatology* 4: 547–560.

Hayes MJ, Svodoba MD, Wilhite DA and Vanyarko OV (1999) Monitoring the 1996 drought using the standardized precipitation index. *Bulletin of the American Meteorological Society* 80: 429–438.

Heddinghaus TR and Sabol P (1991) A review of the Palmer drought severity index and where do we go from here? In *Proceedings of the Seventh Conference on Applied Climatology*. American Meteorological Society, Boston, 242–246.

Hernandez-Diaz L, Laprise R, Sushama S, Martynov A, Winger K and Dugas B (2013) Climate simulation over CORDEX Africa domain using the fifth-generation Canadian Regional Climate Model (CRCM5). *Climate Dynamics* 40: 1415–1433.

Higgins SI and Scheiter S (2012) Atmospheric CO_2 forces abrupt vegetation shifts locally, but not globally. *Nature* 488(7410): 209–12. DOI: 10.1038/nature11238.

Hoell A, Funk C, Magadzire T, Zinke J and Husak G (2014) El Niño–Southern Oscillation diversity and southern Africa teleconnections during austral Summer. *Climate Dynamics.* DOI 10.1007/s00382-014-2414-z.

Holtslag AAM, De Bruijn EIF and Pan H-L (1990) A high resolution air mass transformation model for short-range weather forecasting. *Monthly Weather Review – American Meteorological Society* 118(8): 1561–1575. DOI: 10.1175/1520-0493(1990)118<1561:AHRAMT>2.0.CO;2.

Hong S-Y, Dudhia J and Chen S-H (2004) A revised approach to ice microphysical processes for the bulk parameterization of clouds and precipitation. *Monthly Weather Review – American Meteorological Society* 132(1): 103–120.

Hong S-Y, Noh Y and Dudhia J (2006) A new vertical diffusion package with an explicit treatment of entrainment processes. *Monthly Weather Review – American Meteorological Society* 134(9): 2318–2341. DOI: 10.1175/MWR3199.1.

Hudson DA and Jones RG (2002) Regional climate model simulations of present-day and future climates of southern Africa. Hadley Centre Technical Note N 39, 42 pp.

Ideião SMA and Santos CAG (2005) Analysis of precipitation time series using the wavelet transform. *Sociedade & Natureza* 736–745.

IPCC (2007) The physical science basis. In: Solomon S, Qin D, Manning M, Chen Z, Marquis M, Averyt KB, Tignor M, Miler HL, eds. Contribution of Working Group I to the Fourth Assessment Report of the International Panel on Climate Change Program. Cambridge/New York, NY: Cambridge University Press, 2007, 996 p.

Johnson NC (2013) How many ENSO flavors can we distinguish? *Journal of Climate* 26(13):4816–4827. DOI: 10.1175/JCLI-D-12-00649.1.

Jolliffe I, Trendafilov, N and Uddin M (2003) A modified principal component technique based on the lasso. *Journal of Computational and Graphical Statistics* 12(3): 531–547.

Jolliffe IT (1995) Rotation of principal components: Choice of normalization constraints. *Journal of Applied Statistics* 22: 29–35.

Joubert AM and Mason SJ (1996) Drought over southern Africa in a doubled-CO_2 climate. *International Journal of Climatology* 16: 1149–1156.

Jury MR and Enfield DB (2002) Tropical monsoons around Africa: Stability of El Niño–Southern Oscillation associations and links with continental climate. *Journal of Geophysical Research* 107(C10): 15-1–15-17. DOI: 10.1029/2000JC000507.

Jury MR, Mulenga HM and Mason SJ (1999) Exploratory long-range models to estimate summer variability over southern Africa. *Journal of Climate* 12:1892–1899.

Jury MR and Mwafulirwa ND (2002) Climate variability in Malawi, Part 1: Dry summers, statistical associations and predictability. *International Journal of Climatology* 22(11): 1289–1302. DOI: 10.1002/joc.771.

Kalognomou E et al. (2013) A diagnostic evaluation of precipitation in CORDEX models over southern Africa. *Journal of Climate* 26:9477–9506. DOI: 10.1175/JCLI-D-12-00703.1.

Kao HY and Yu JY (2009) Contrasting eastern-Pacific and central-Pacific types of ENSO. *Journal of Climate* 22(3):615–632. DOI: 10.1175/2008J CLI2309.1.

Karl TR (1986) Sensitivity of the Palmer drought severity index and Palmer's Z-index to their calibration coefficients including potential evapotranspiration. *Journal of Climate Applied Meteorology* 25: 77–86.

Kohonen T, Hynninen J, Kangas J and Laaksonen J (1995) SOM_PAK: The self-organizing map program package version 3.1. Laboratory of Computer and Information Science, Helsinki University of Technology, Finland, 27 pp.

Kug JS, Jin FF and An SI (2009) Two types of El Niño events: Cold tongue El Niño and warm pool El Niño. *Journal of Climate* 22(6):1499–1515. DOI: 10.1 175/2008JCLI2624.1.

Labat D (2005) Recent advances in wavelet analyses: Part 1. A review of concepts. *Journal of Hydrology* 314: 275–288. DOI: 10.1016/j.jhydrol.2005.04.003.

Landman WA and Mason SJ (1999) Operational long-lead prediction of South African rainfall using canonical correlation analysis. *International Journal of Climatology* 19: 1073–1090.

Larkin NK and Harrison DE (2005) On the definition of El Niño and associated seasonal average US weather anomalies. *Geophysical Research Letters* 32(13): L13,705. DOI: 10.1029/2005GL022738.

Legates DR and Willmott CJ (1990) Mean seasonal and spatial variability in gauge-corrected, global precipitation. *International Journal of Climatology* 10:111–127.

Lenton TM and Vaughan NE (2009) The radiative forcing potential of different climate geoengineering options. *Atmospheric Chemistry and Physics Discussions* 9(1): 2559–2608. DOI: 10.5194/acpd-9-2559-2009.

Lyon B (2009) Southern Africa summer drought and heat waves: Observations and coupled model behavior. *Journal of Climate*, 22, 6033–6046.

Lyon B and Mason SJ (2009) The 1997/98 summer rainfall season in southern Africa. Part II: Model Simulations and coupled model forecasts. *Journal of Climate* 22: 3802–3818 DOI: 10.1175/2009JCLI2600.1.

Mackellar NC, Tadross MA and Hewitson BC (2008) Effects of vegetation map change in MM5 simulations of southern Africa's summer climate. *International Journal of Climatology*. DOI: 10.1002/joc.

Makarau A and Jury MR (1997) Predictability of Zimbabwe summer rainfall. *International Journal of Climatology* 17: 1421–1432.

Manatsa D, Chingombe W, Matsikwa H and Matarira CH (2008) The superior influence of Darwin sea level pressure anomalies over ENSO as a simple drought predictor for southern Africa. *Theoretical and Applied Climatology* 92: 1–14.

Manatsa D and Matarira CH (2009) Changing dependence of Zimbabwean rainfall variability on ENSO and the Indian Ocean dipole/zonal mode. *Theoretical and Applied Climatology* 98(3–4): 375–396. DOI: 10.1007/s00704-009-0114-0.

Manatsa D, Mukwada G, Siziba E and Chinyanganya T (2010) Analysis of multidimensional aspects of agricultural droughts in Zimbabwe using the standardized precipitation index (SPI). *Theoretical and Applied Climatology* 102: 287–305. DOI 10.1007/s00704-010-0262-2.

Manatsa D, Reason CJC and Mukwada G (2012) On the decoupling of the IODZM from southern Africa summer rainfall variability. *International Journal of Climatology* 32(5): 727–746. DOI: 10.1002/joc.2306.

Martin GM et al. (2011) The HadGEM2 family of Met Office Unified Model Climate configurations. *Geoscientific Model Development Discussions* 4(2): 765–841. DOI: 10.5194/gmdd-4-765-2011.

Mason SJ (2001) El Niño, climate change and southern African climate. *Environmetrics* 12: 327–345.

Mason SJ and Jury MR (1997) Climatic variability and change over southern Africa: A reflection on underlying processes. *Progress in Physical Geography* 21(1)L 23–50. DOI: 10.1177/030913339702100103.

Maure GA (2013) Effects of biomass-burning aerosol loadings on southern Africa climate. PhD Thesis, University of Cape Town, Cape Town, South Africa.

McEvoy D, Huntington J, Abatzoghou J and Edward L (2012) An evaluation of multiscalar drought indices in Nevada and eastern California. *Earth Interactions* 16: 1–18.

McGuffie K and Henderson-Sellers A (2005) *A Climate Modelling Primer*. John Wiley & Sons.

McHugh MJ and Rogers JC (2000) North Atlantic oscillation influence on precipitation variability around the southeast African convergence zone. *Journal of Climate* 14: 3631–3642.

McKee TB, Doesken NJ and Kleist J (1993) The relationship of drought frequency and duration to time scale. Preprints, Eighth Conference on Applied Climatology, Anaheim, CA, *American Meteorological Society* 179–184.

Meadows M (2006) Global change and southern Africa. *Geographical Research* 44(2), 135–145.

Meehl GA et al. (2007) Climate Change 2007: The physical science basis. Contribution of Working Group I to the Fourth Assessment Report of the Intergovernmental Panel on Climate Change. In S. Solomon, D. Quirion, M. Manning, Z. Chen, M. Marquis, K. Averyt, M. Tignor et al. (eds.), Global Climate Projections (pp. 747–846). Cambridge University Press, Cambridge and New York, NY.

Meque AO (2015) Investigating the link between southern African droughts and global atmospheric teleconnections using regional climate models. PhD thesis, University of Cape Town, Cape Town, South Africa.

Meque A and Abiodun B (2014) Simulating the link between ENSO and summer drought in southern Africa using regional climate models. *Climate Dynamics* 1–20. DOI: 10.1007/s00382-014-2143-3.

Midgley GF et al. (2007) Impacts, vulnerability and adaptation in key South African sectors: An input into the long term mitigation scenarios process. LTMS Input Report 5. Cape Town.

Mishra A, Singh V and Desai V (2009) Drought characterization: A probabilistic approach. *Stochastic Environmental Research and Risk Assessment* 23: 41–55.

Mishra AK and Singh VP (2010) Review paper: A review of drought concepts. *Journal of Hydrology* 391(1–2): 202–216. DOI: 10.1016/j.jhydrol.2010.07.012

Mitchell TD and Jones PD (2005) An improved method of constructing a database of monthly climate observations and associated high-resolution grids. *International Journal of Climatology* 25: 693–712.

Mulenga HM, Rouault M and Reason CJC (2003) Dry summers over northeastern South Africa and associated circulation. *Climate Research* 25: 29–41.

Naik M (2015) Modeling the potential impacts of vegetation change on the future climate of southern Africa. MSc dissertation, University of Cape Town, Cape Town, South Africa.

Nash DJ and Endfield GH (2002) A 19th century climate chronology for the Kalahari region of central southern Africa derived from missionary correspondence. *International Journal of Climatology* 22(7): 821–841. DOI: 10.1002/joc.753.

Ntale HK and Gan TYEW (2003) Drought indices and their application to east Africa. *International Journal of Climatology* 23: 1335–1357. DOI: 10.1002/joc.931.

Oettli P, Tozuka T, Izumo T, Engelbrecht FA and Yamagata T (2013) The self-organizing map, a new approach to apprehend the Madden–Julian Oscillation influence on the intraseasonal variability of rainfall in the southern African region. *Climate Dynamics.* DOI 10.1007/s00382-013-1985-4.

Oguntunde PG, Abiodun BJ, Lischeid G and Merz C (2014) Modelling the impacts of reforestation on the projected hydroclimatology of Niger River Basin, West Africa. *Ecohydrology* 7(1): 163–176. DOI: 10.1002/eco.1343.

Pal JS, Small EE and Eltahir EAB (2000) Simulation of regional-scale water and energy budgets: Representation of subgrid cloud and precipitation processes within RegCM. *Journal of Geophysical Research: Atmospheres* 105(D24): 29579–29594. DOI: 10.1029/2000JD900415.

Pal JS et al. (2007) Regional climate modeling for the developing world: The ICTP RegCM3 and RegCNET. *Bulletin of the American Meteorological Society* 88: 1395–1409.

Palmer CW (1965) *Meteorological Drought.* US Weather Bureau, Washington, DC.

Palmer WC (1968) Keeping track of crop moisture conditions, nationwide: The new crop moisture index. *Weatherwise* 21: 156–161.

Philippon N, Rouault M, Richard Y and Favre A (2011) The influence of ENSO on winter rainfall in South Africa. *International Journal of Climatology.* DOI: 10.1002/joc.3403.

Potop V (2011) Evolution of drought severity and its impact on corn in the Republic of Moldova. *Theoretical and Applied Climatology* 105(3–4): 469–483.

Potop V, Boroneant C, Mozny M, Stepanek P and Skalak P (2013) Observed spatiotemporal characteristics of drought on various time scales over the Czech Republic. *Theoretical and Applied Climatology.* DOI: 10.1007/s00704-013-0908-y.

Rahlao S, Mantlana B, Winkler H and Knowles T (2012) South Africa's national REDD+ initiative: Assessing the potential of the forestry sector on climate change mitigation. *Environmental Science & Policy* 17: 24–32.

Rao SA, Behera SK, Masumoto Y and Yamagata T (2002) Interannual subsurface variability in the tropical Indian Ocean with a special emphasis on the Indian Ocean dipole. *Deep Sea Research Part II: Topical Studies in Oceanography* 49(7–8): 1549–1572. DOI: 10.1016/S0967-0645(01)00158-8.

Ratna SB, Ratnam JV, Behera SK, Ndarana T, Takahashi K and Yamagata T (2014) Performance assessment of three convective parameterization schemes in WRF for downscaling summer rainfall over South Africa. *Climate Dynamics* 42(11–12): 2931–2953.

Ratnam JV, Behera SK, Masumoto Y, Takahashi K and Yamagata T (2012) A simple regional coupled model experiment for summer-time climate simulation over southern Africa. *Climate Dynamics* 39: 2207–2217.

Reason CJC, Hachigonta S and Phaladi RF (2005) Interannual variability in rainy season characteristics over the Limpopo region of southern Africa. *International Journal of Climatology* 25:1835–1853.

Reason CJC and Jagadeesha D (2005) A model investigation of the recent ENSO impacts over southern Africa. *Meteorology and Atmospheric Physics* 89:181–205.

Reason CJC and Rouault M (2002) ENSO-like decadal variability and South African rainfall. *Geophysical Research Letters* 29(13): 11–16.

Reason CJC and Rouault M (2005) Links between the Antarctic oscillation and winter rainfall over western South Africa. *Geophysical Research Letters* 32: L07705. DOI: 10.1029/2005GL022419.

Reason CJC, Rouault M, Melice JL and Jagadhessha D (2002) Interannual winter rainfall variability in SW South Africa and large scale ocean-atmosphere interactions. *Meteorology and Atmospheric Physics* 80: 19–29.

Reynolds RW et al. (2007) Daily high-resolution-blended analyses for sea surface temperature. *Journal of Climate* 20: 5473–5496.

Richard Y, Fauchereau N, Poccard I, Rouault M and Trzaska S (2001) 20th century droughts in southern Africa: Spatial and temporal variability, teleconnections with oceanic and atmospheric conditions. *International Journal of Climatology* 21(7): 873–885. DOI: 10.1002/joc.656.

Richard Y and Poccard I (1998) A statistical study of NDVI sensitivity to seasonal and interannual rainfall variations in southern Africa. *International Journal of Remote Sensing* 19:15, 2907–2920.

Richman MB (1986) Rotation of principal components. *Journal of Climatology* 6: 293–335.

Ringrose S et al. (2002) Climate- and human-induced woody vegetation changes in Botswana and their implications for human adaptation. *Environmental Management* 30(1): 98–109. DOI: 10.1007/s00267-002-2486-0.

Rouault M and Richard Y (2003) Intensity and spatial extension of drought in South Africa at different time scales. *WaterSA* 29(4): 489–500.

Sheffield J and Wood EF (2008) Projected changes in drought occurrence under future global warming from multi-model, multi-scenario, IPCC AR4 simulations. *Climate Dynamics* 31(1): 79–105. DOI: 10.1007/s00382-007-0340-z.

Sivakumar MVK, Motha PR, Wilhite AD and Woods AD (2011) Agricultural Drought Indices. Proceedings of the WMO/UNISDR Expert Group Meeting on Agricultural Drought Indices. World Meteorological Organization.

Skamarock WC and Klemp JB (2008a) A time-split nonhydrostatic atmospheric model for weather research and forecasting applications. *Journal of Computational Physics* 227(7): 3465–3485. DOI: 10.1016/j.jcp.2007.01.037.

Skamarock WC, Klemp JB, Dudhia J, Gill DO and DMBC (2008b) A description of the Advanced Research WRF version 3. NCAR Technical Note NCAR/TN/u2013475.

Swann ALS, Fung IY and Chiang JCH (2012) Mid-latitude afforestation shifts general circulation and tropical precipitation. Proceedings of the National Academy of Sciences of the United States of America 109(3): 712–6. DOI: 10.1073/pnas.1116706108.

Tadross M, Jack C and Hewitson B (2005) On RCM-based projections of change in southern African summer climate. *Geophysical Research Letters* 32(23): L23713. DOI: 10.1029/2005GL024460.

Tao H, Borth H, Fraedrich K, Su B and Zhu X (2014) Drought and wetness variability in the Tarim River Basin and connection to large-scale atmospheric circulation. *International Journal of Climatology* 34(8): 2678–2684. DOI: 10.1002/joc.3867.

Taylor KE, Stouffer RJ and Meehl GA (2012) An overview of CMIP5 and the experiment design, *Bulletin of the American Meteorological Society* 93(4): 485–498, DOI: 10.1175/BAMS-D-11-00094.1, http://journals.ametsoc.org/doi/abs/10.1175/BAMS-D-11-00094.1

Thomson AM et al. (2011) RCP4.5: A pathway for stabilization of radiative forcing by 2100. *Climatic Change* 109(1–2): 77–94. DOI: 10.1007/s10584-011-0151-4.

Thomson MC, Abayomi K, Barnston AG, Levy M and Dilley M (2003) El Niño and drought in southern Africa. *The Lancet* 361: 437–438.

Thornthwaite CW (1948) An approach toward a rational classification of climate. *Geographical Review* 38: 55–94.

Todd M and Washington R (1999) Circulation anomalies associated with tropical-temperate troughs in southern Africa and the southwest Indian Ocean. *Climate Dynamics* 15: 937–951.

Todd MC, Washington R and Palmer PI (2004) Water vapour transport associated with tropical-temperate trough systems over southern Africa and the southwest Indian Ocean. *Journal of Climate* 24: 555–568.

Topfer K (2001) What do we know about reducing greenhouse gas emissions? A simplified guide to the IPCC's "Climate Change 2001: Mitigation".

Torrence C and Webster PJ (1999) Interdecadal changes in the ENSO–Monsoon System. *Journal of Climate* 12: 2679–2690.

Trenberth KE and Shea D (2005) Relationships between precipitation and surface temperature. *Geophysical Research Letters* 32: L14703, DOI: 10.1029/2005GL022760.

Ujeneza E and Abiodun B (2014) Drought modes in southern Africa and how well GCMs simulate them. *Climate Dynamics.* DOI 10.1007/s00382-014-2325-z.

Unganai LS and Kogan FN (1998a) Drought monitoring and corn yield estimation in southern Africa from AVHRR data. *Remote Sensing of Environment* 63: 219–232.

Unganai LS and Kogan FN (1998b) southern Africa's recent drought from space. *Advances in Space Research* 21:507–511.

Unganai LS and Mason SJ (2002) Long-range predictability of Zimbabwe summer rainfall. *International Journal of Climatology* 22:1091–1103.

Usman MT and Reason CJC (2004) Dry spell frequencies and their variability over southern Africa. *Climate Research* 26:199–211.

Vicente-Serrano S, Beguería S and López-Moreno J (2010a) A multiscalar drought index sensitive to global warming: The standardized precipitation evapotranspiration index. *Journal of Climate* 23: 1696–1617.

Vicente-Serrano SM, Beguería S, López-Moreno JI, Angulo M and El Kenawy A (2010b) A new global 0.5° gridded dataset (1901–2006) of a multiscalar drought index: Comparison with current drought index datasets based on the Palmer drought severity index. *Journal of Hydrometeorology* 11(4):1033–1043. DOI: 10.1175/2010 JHM1224.1

Vicente-Serrano SM and López-Moreno JI (2005) Hydrological response to different time scales of climatological drought: An evaluation of the standardized precipitation index in a mountainous Mediterranean basin. *Hydrology and Earth System Sciences* 9: 523–533.

Vicente-Serrano SM et al. (2011) Effects of warming processes on droughts and water resources in the NW Iberian Peninsula (1930−2006). *Climate Research:* 48, 203–212. DOI: 10.3354/cr01002.

Vigaud N, Pohl B and Cretat J (2012) Tropical temperate interactions over southern Africa simulated by a regional climate model. *Climate Dynamics* DOI: 10.1007/s00382-012-1314-3.

Virgilio N and Marshall S (2009) *Forest Carbon Strategies in Climate Change Mitigation: Confronting Challenges through on the Ground Experience*. The Nature Conservancy. Arlington, VA.

Washington R and Downing TE (1999) Seasonal forecasting of African rainfall: Prediction, responses and household food security. *The Geographical Journal* 165(3): 255–274. Retrieved from http://www.jstor.org/stable/3060442

Washington R and Preston A (2006) Extreme wet years over southern Africa: Role of Indian Ocean sea surface temperatures. *Journal of Geophysical Research* 111: 1–15. DOI: 10.1029/2005JD006724.

Wehrens R (2011) Chemometrics with R: Multivariate Data Analysis in the Natural Sciences and Life Sciences. Springer-Verlag, Berlin, Heidelberg.

Wells N, Goddard S and Hayes MJ (2004) A self-calibrating Palmer drought severity index. *Journal of Climate* 17: 2335–2351.

Wilks DS (1995) *Statistical Methods in the Atmospheric Sciences.* Elsevier, New York, NY. 467 pp.

Wolter K and Timlin MS (2011) El Niño/Southern Oscillation behavior since 1871 as diagnosed in an extended multivariate ENSO index (MEI.ext). *International Journal of Climatology* 31:1074–1087.

Yeh SW, Ham YG and Lee JY (2012) Changes in the tropical Pacific SST trend from CMIP3 to CMIP5 and its implication of ENSO. *Journal of Climate* 25(21): 7764–7771. DOI: 10.1175/JCLI-D-12-00304.1.
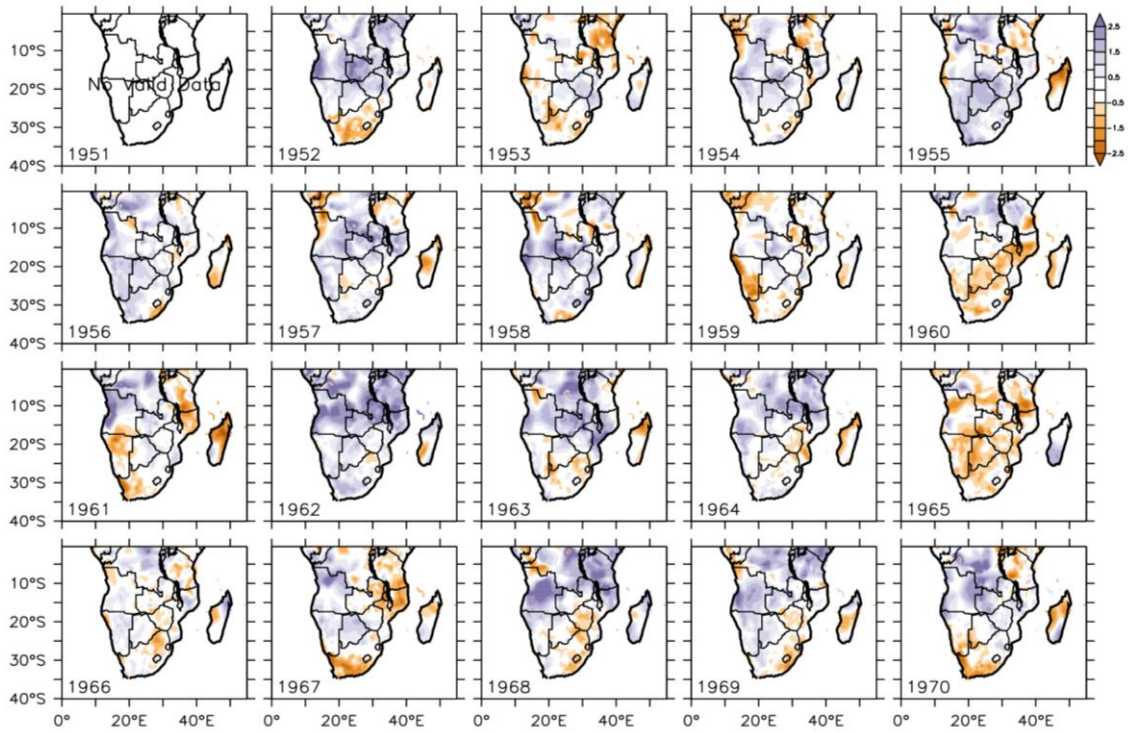
Figure 81: The spatial distribution of annual drought (12-month SPEI, ending in February) over southern Africa for the period 1951–1970
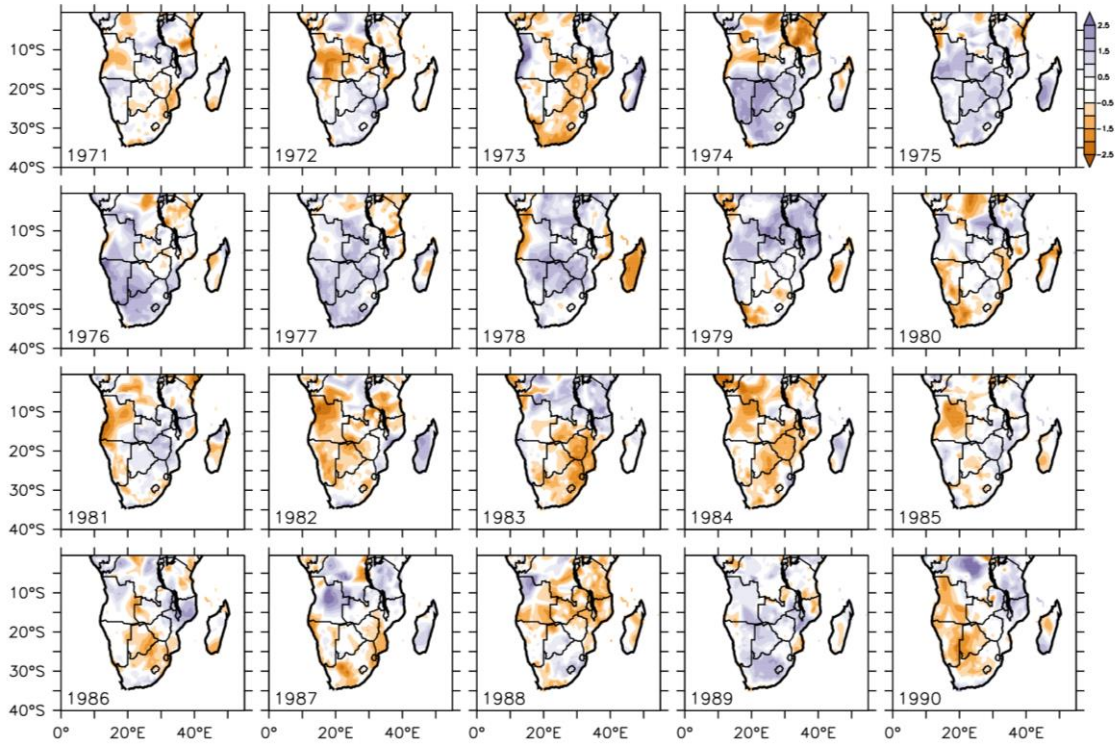
Figure 82: The spatial distribution of annual drought (12-month SPEI, ending in February) over southern Africa for the period 1971–1990
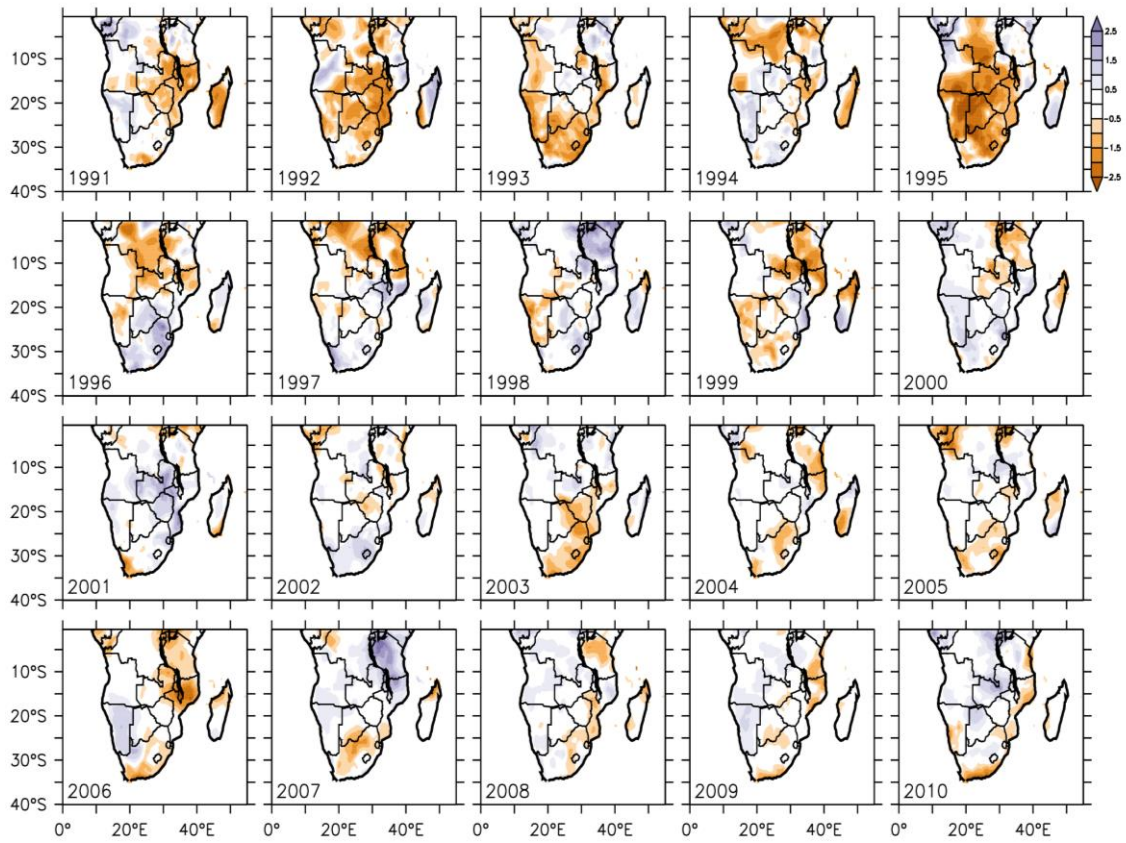
Figure 83: The spatial distribution of annual drought (12-month SPEI, ending in February) over southern Africa for the period 1991–2010
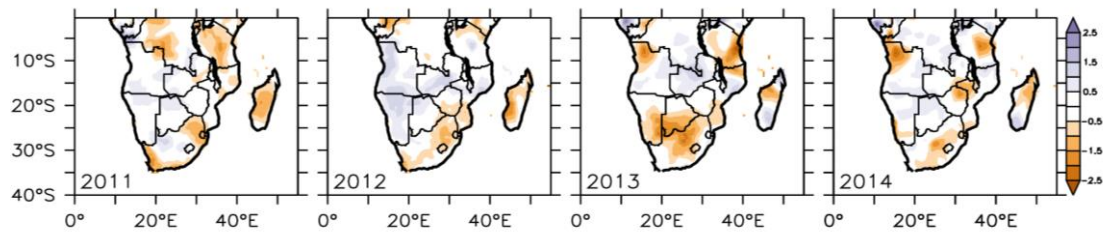
Figure 84: The spatial distribution of annual drought (12-month SPEI, ending in February) over southern Africa for the period 2011–2014
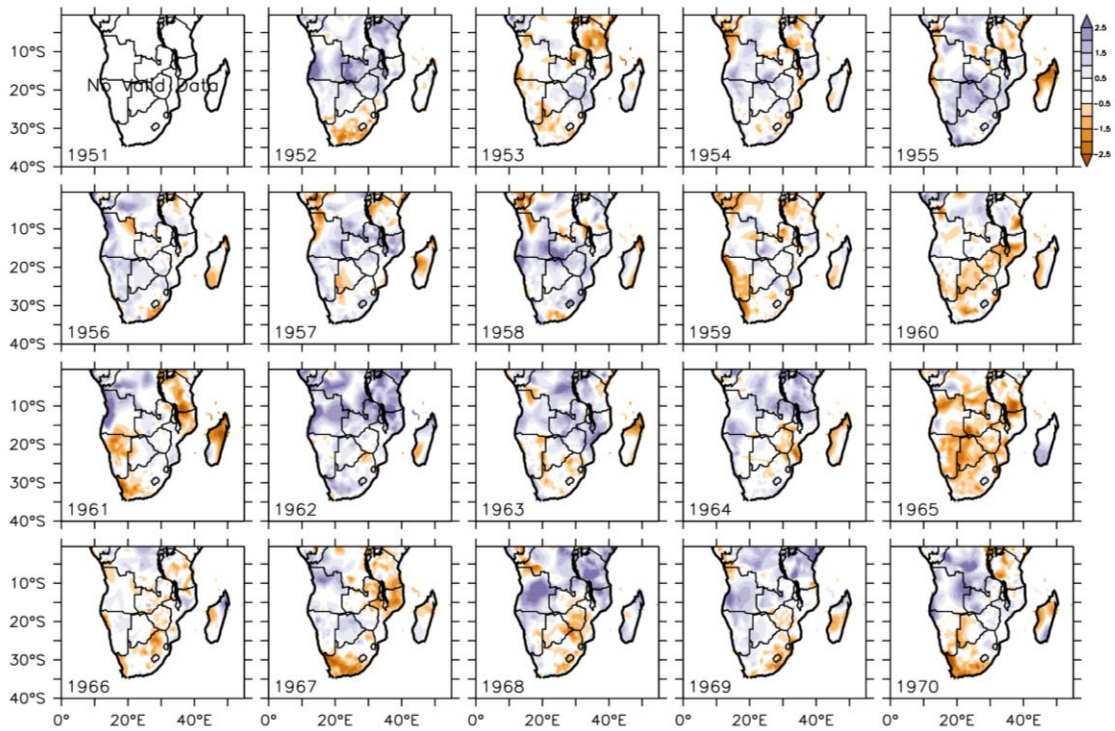
Figure 85: The spatial distribution of annual drought (12-month SPI, ending in February) over southern Africa for the period 1951–1970
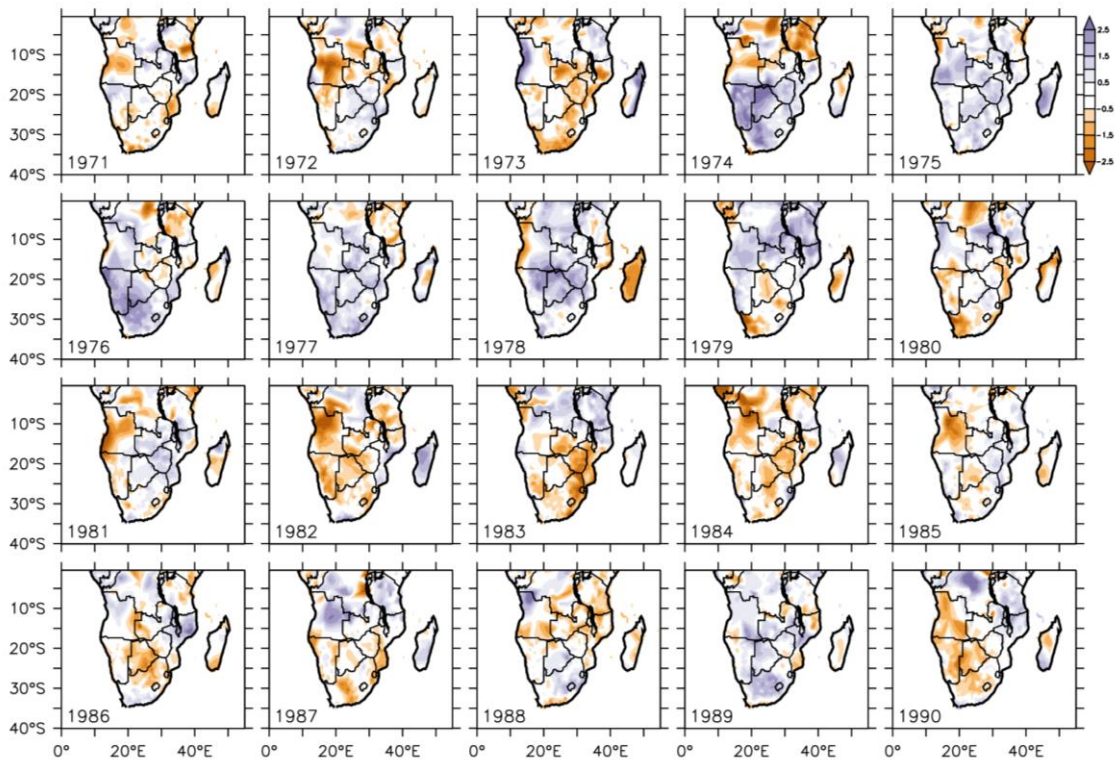
Figure 86: The spatial distribution of annual drought (12-month SPI, ending in February) over southern Africa for the period 1971–1990
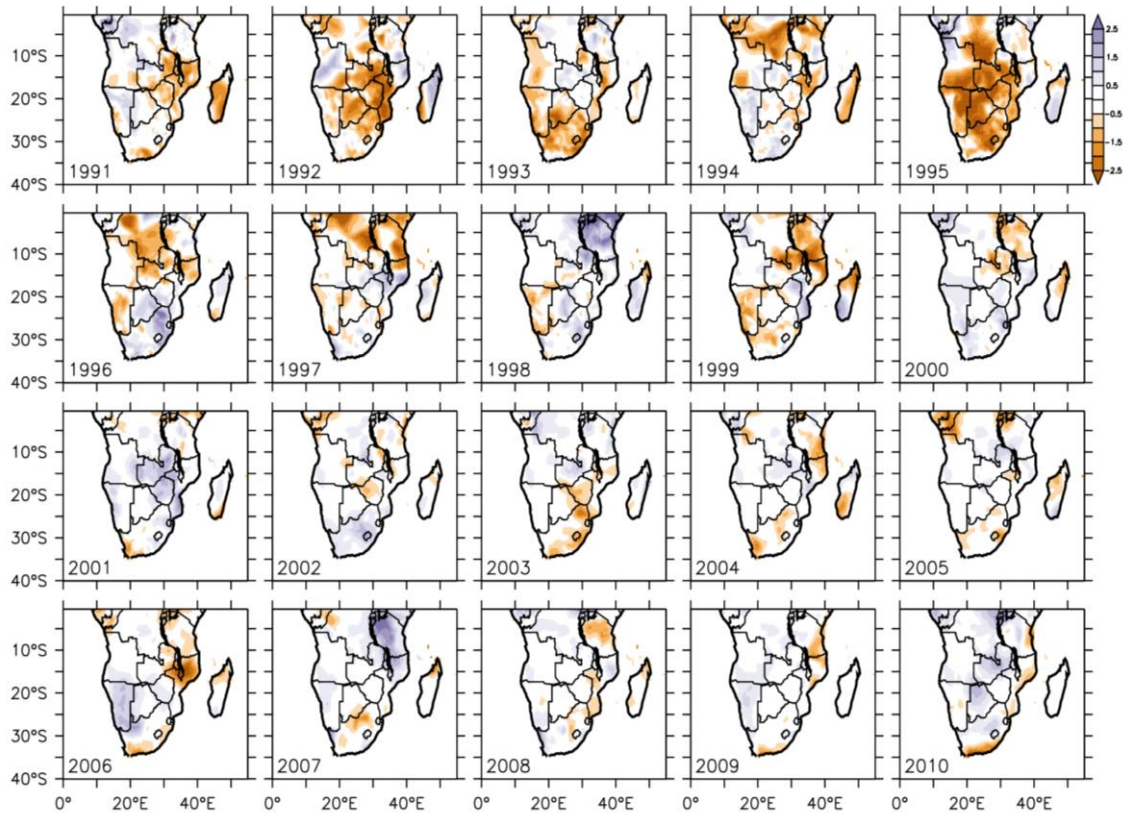
Figure 87: The spatial distribution of annual drought (12-month SPI, ending in February) over southern Africa for the period 1991–2010
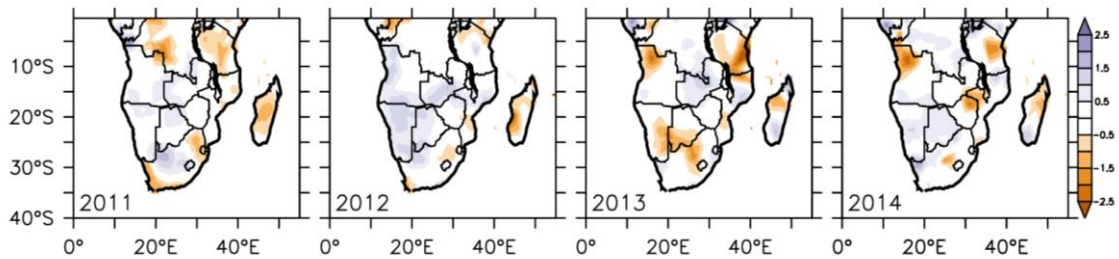
Figure 88: The spatial distribution of annual drought (12-month SPI, ending in February) over southern Africa for the period 2011–2014
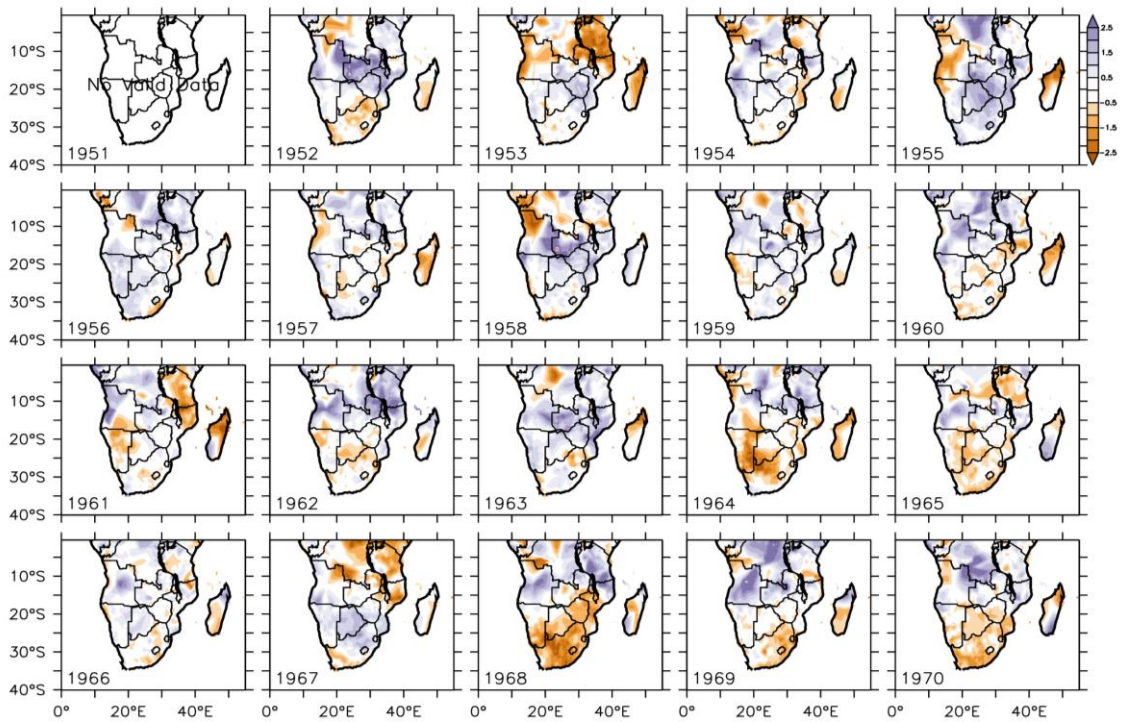
Figure 89: The spatial distribution of summer drought (three-month SPEI, ending in February) over southern Africa for the period 1951–1970
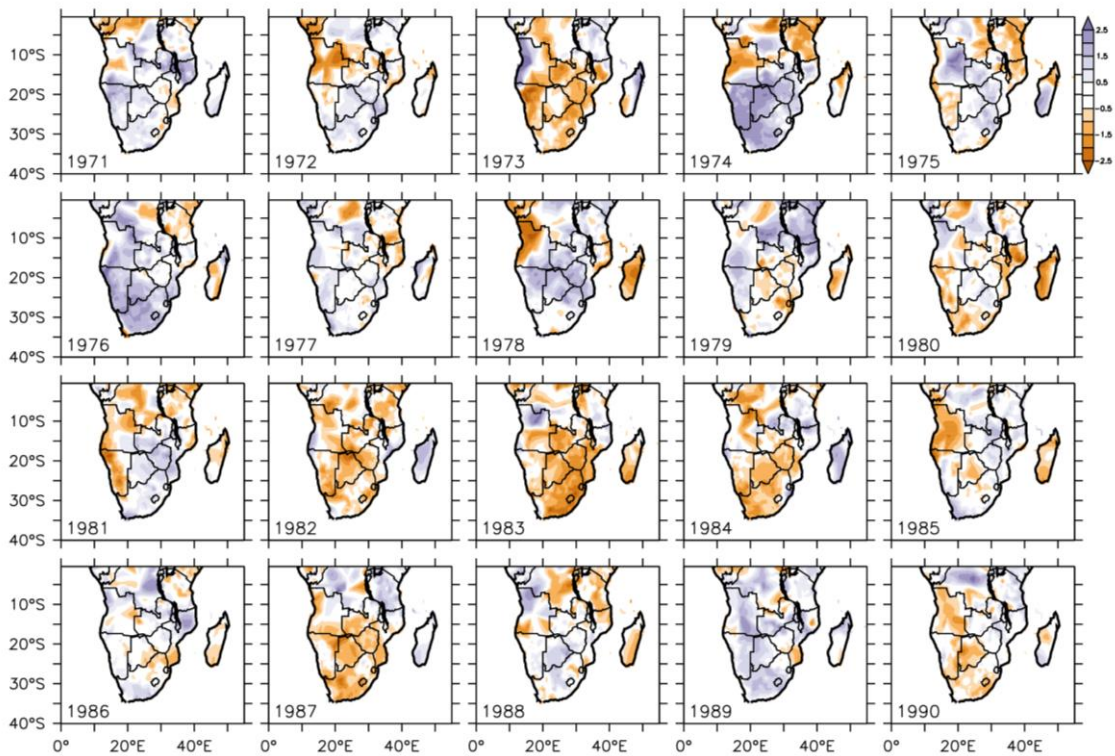
Figure 90: The spatial distribution of summer drought (three-month SPEI, ending in February) over southern Africa for the period 1971–1990

117
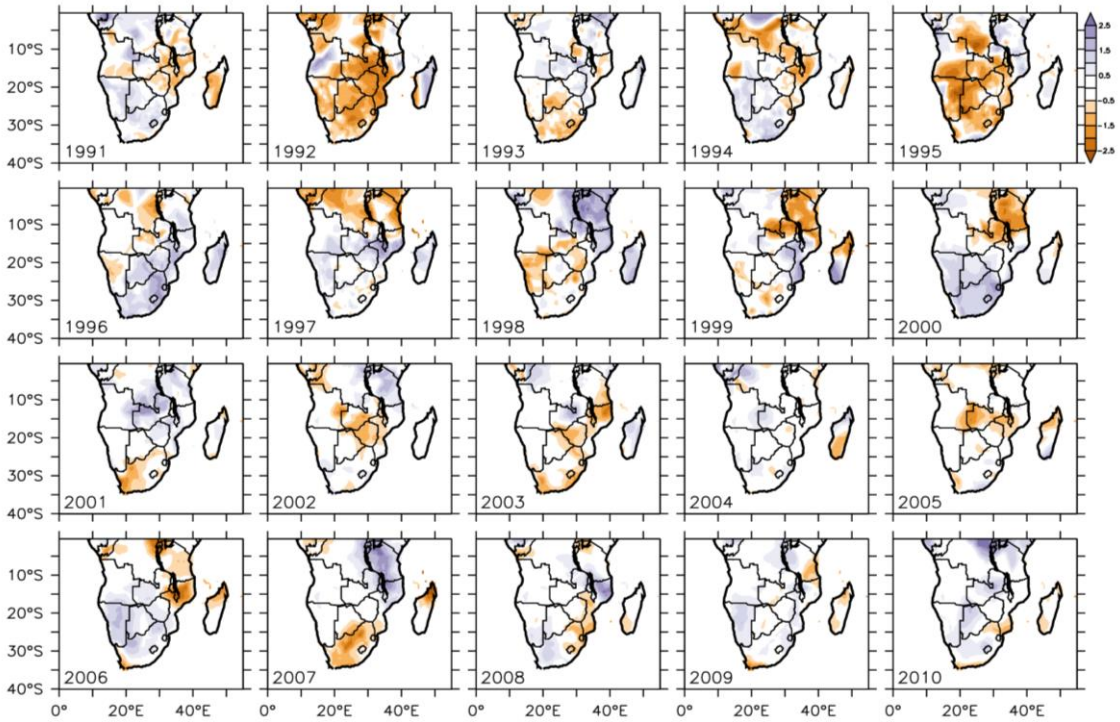
Figure 91: The spatial distribution of summer drought (three-month SPEI, ending in February) over southern Africa for the period 1991–2010
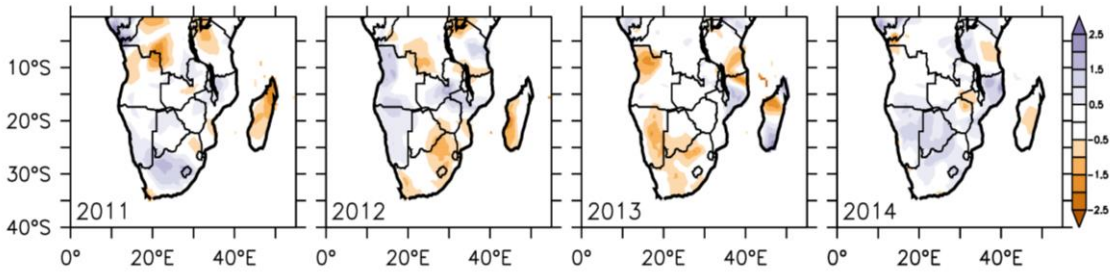
Figure 92: The spatial distribution of summer drought (three-month SPEI, ending in February) over southern Africa for the period 2011–2014
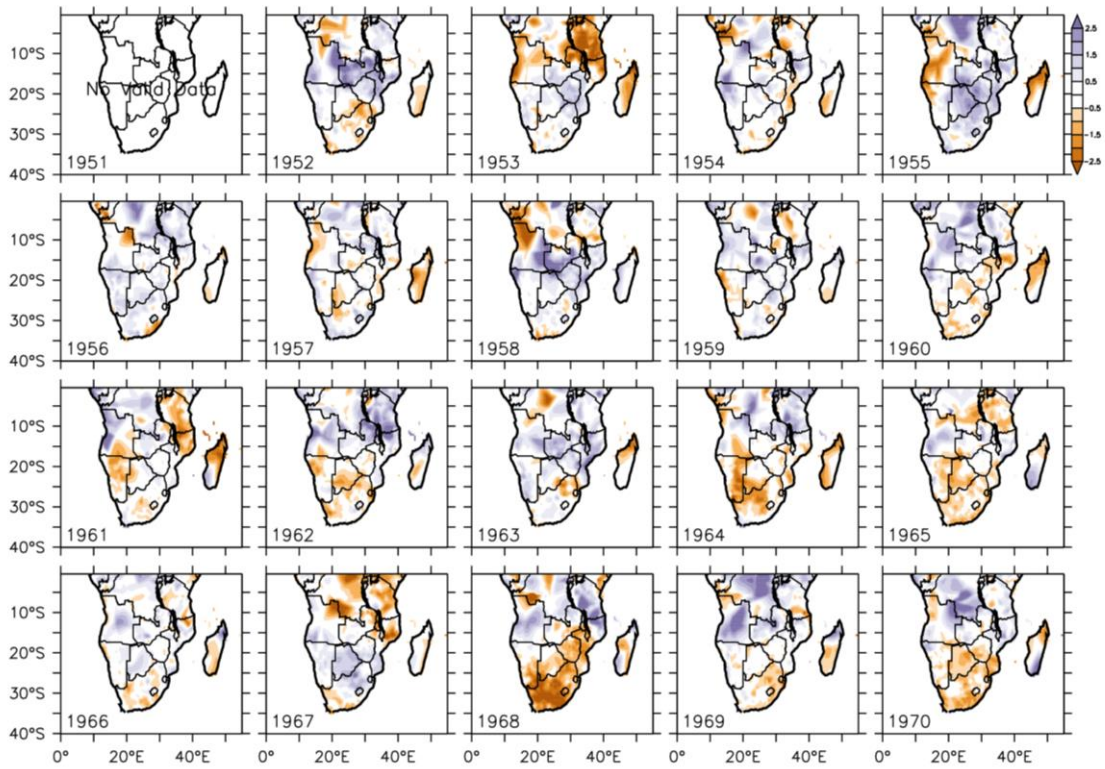
Figure 93: The spatial distribution of summer drought (three-month SPI, ending in February) over southern Africa for the period 1951–1970
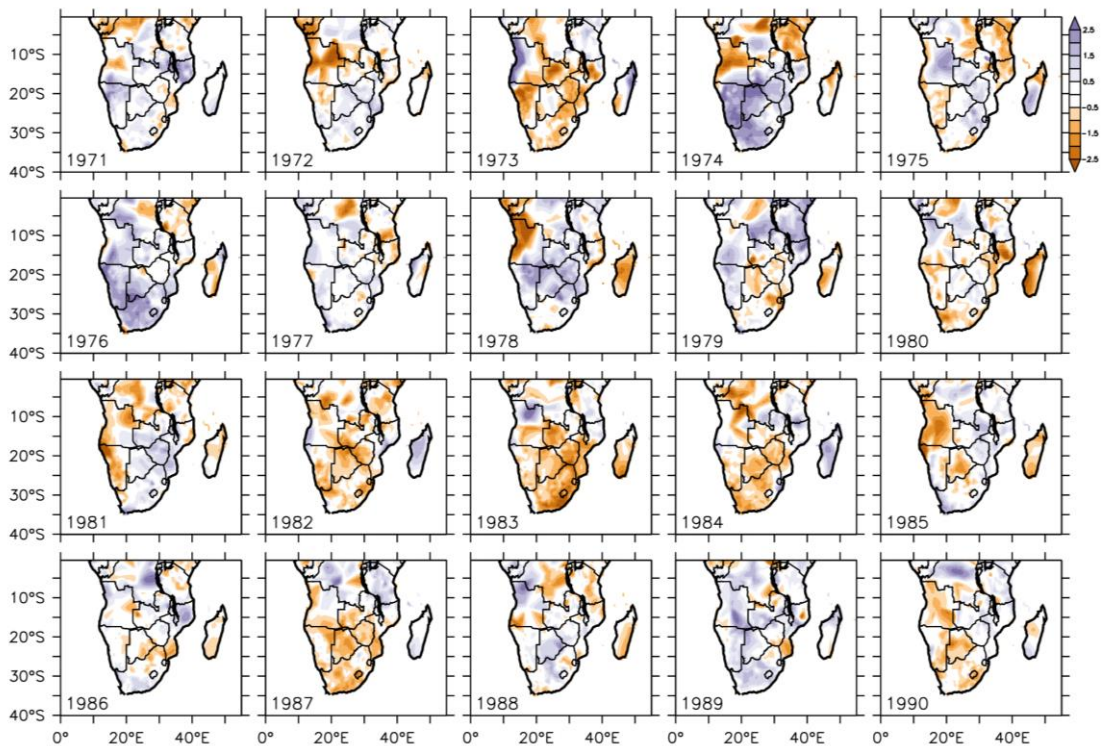
Figure 94: The spatial distribution of summer drought (three-month SPI, ending in February) over southern Africa for the period 1971–1990
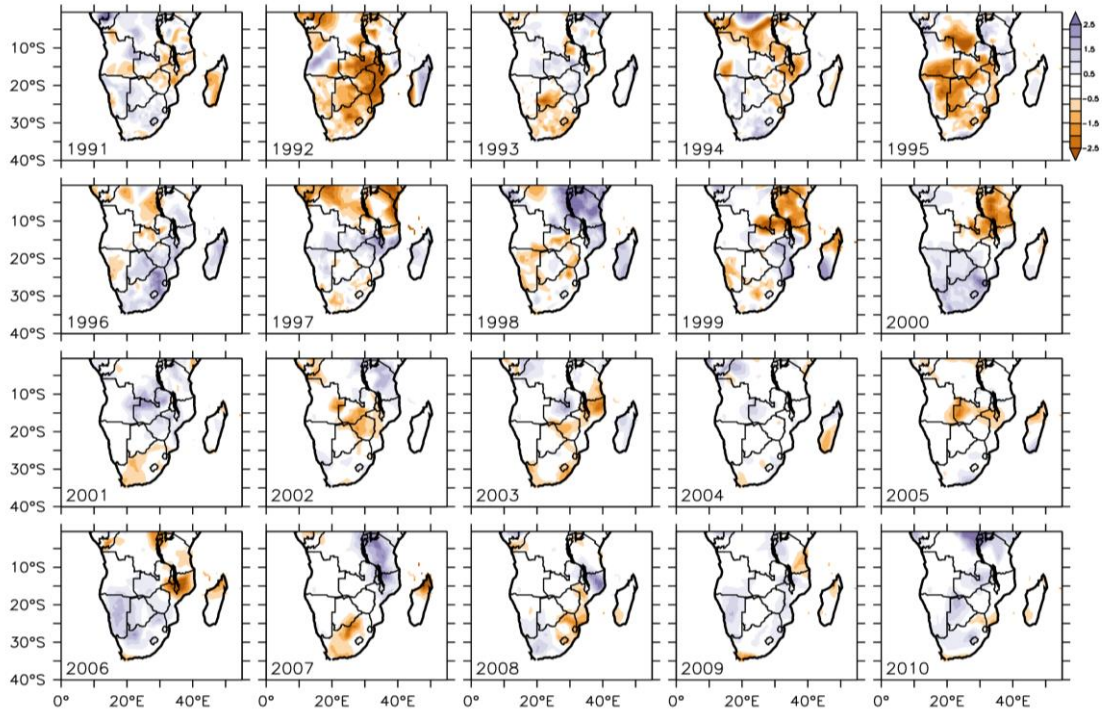
Figure 95: The spatial distribution of summer drought (three-month SPEI, ending in February) over southern Africa for the period 1991–2010
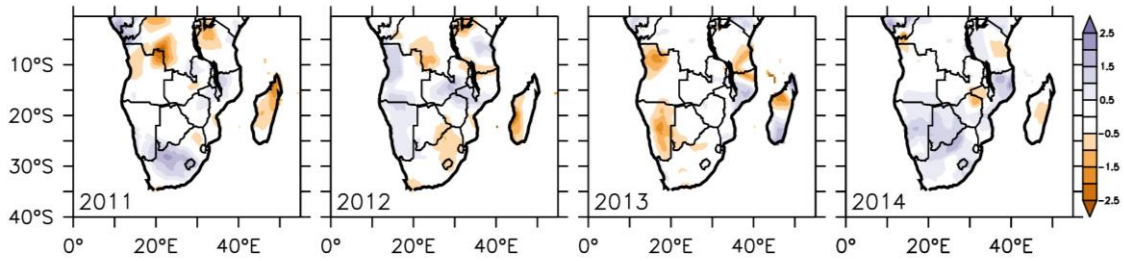
Figure 96: The spatial distribution of summer drought (three-month SPEI, ending in February) over southern Africa for the period 2011–2014
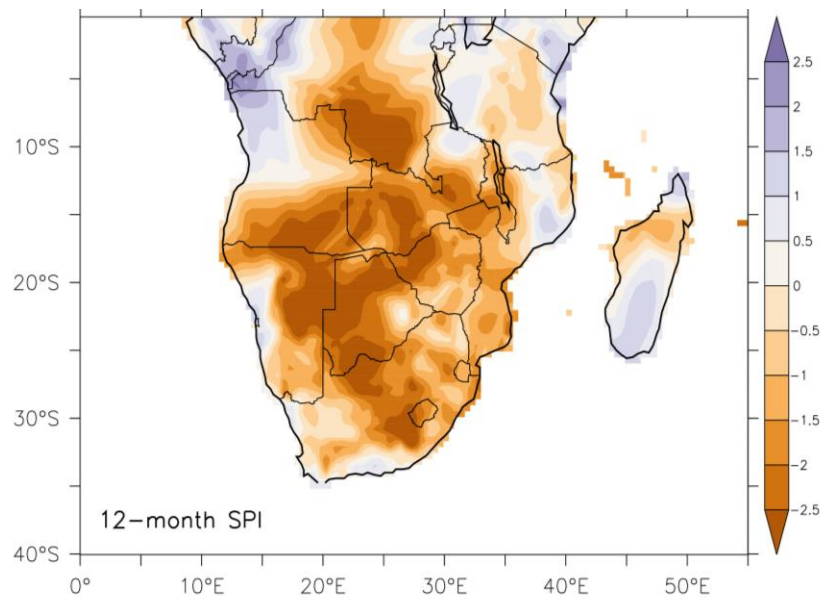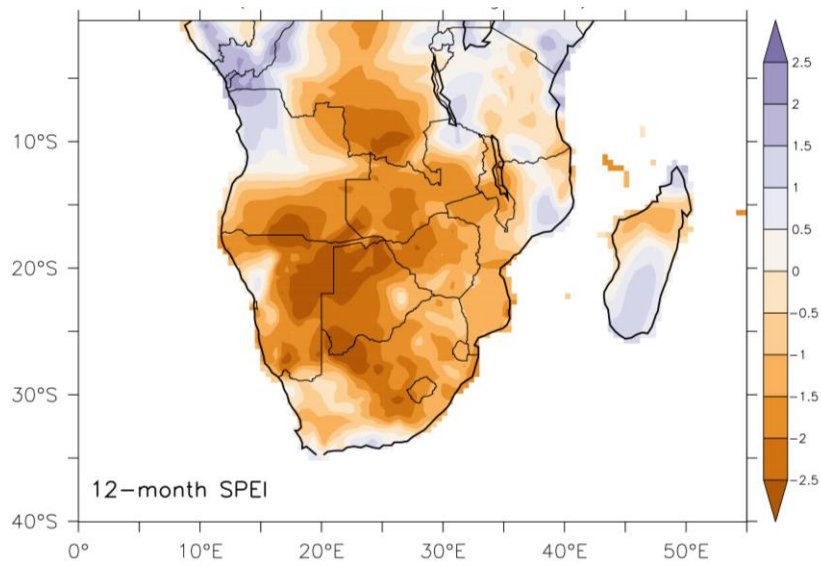
Figure 97: The spatial distribution of the most widely extensive annual droughts over southern Africa as depicted by 12-month SPEI and SPI (ending in February 1995)
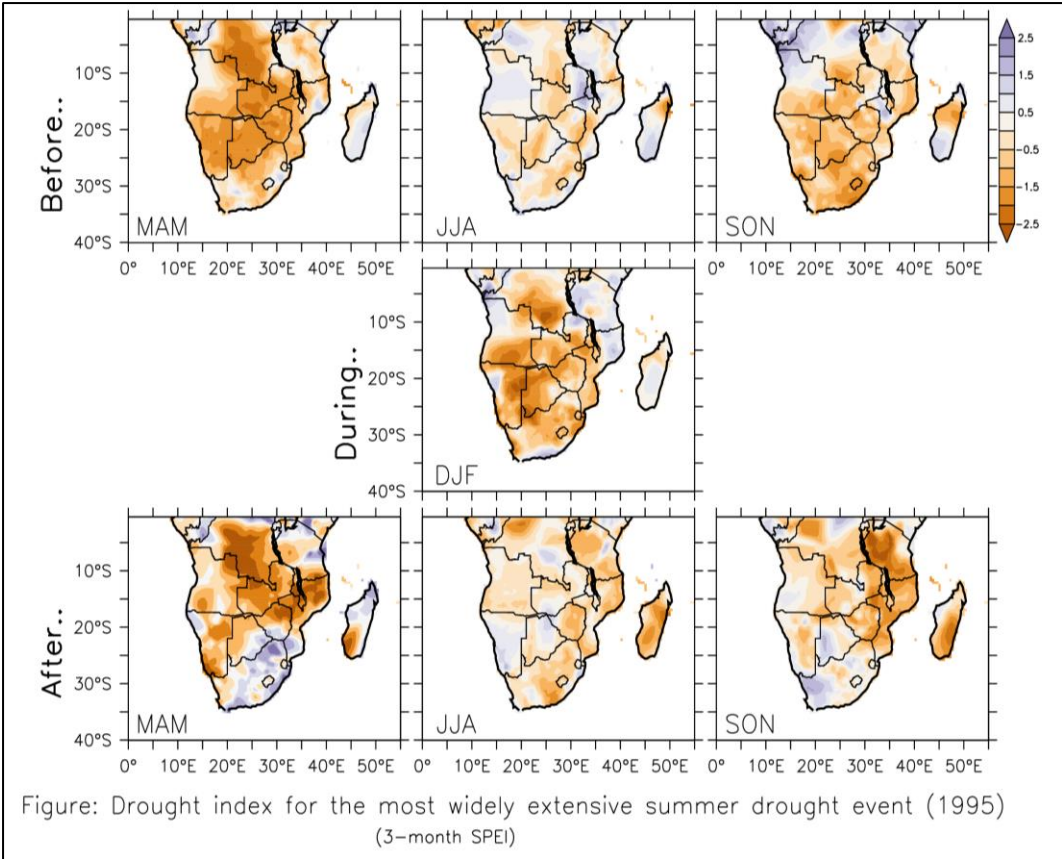
Figure 98: The spatial distribution of seasonal droughts before (top panels), during (middle panel), and after (lower panels) the summer of the most widely extensive drought (1995) over southern Africa, as depicted by three-month SPEI
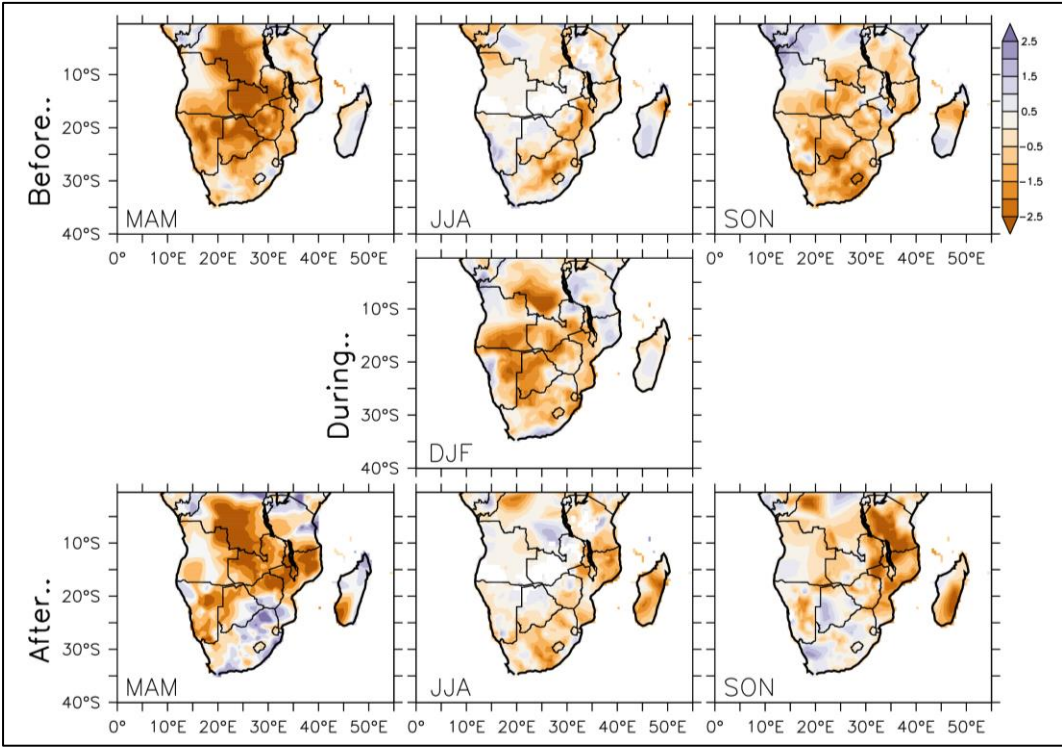
Figure 99: The spatial distribution of seasonal droughts before (top panels), during (middle panel), and after (lower panels) the summer of the most widely extensive drought over southern Africa (1995), as depicted by three-month SPI
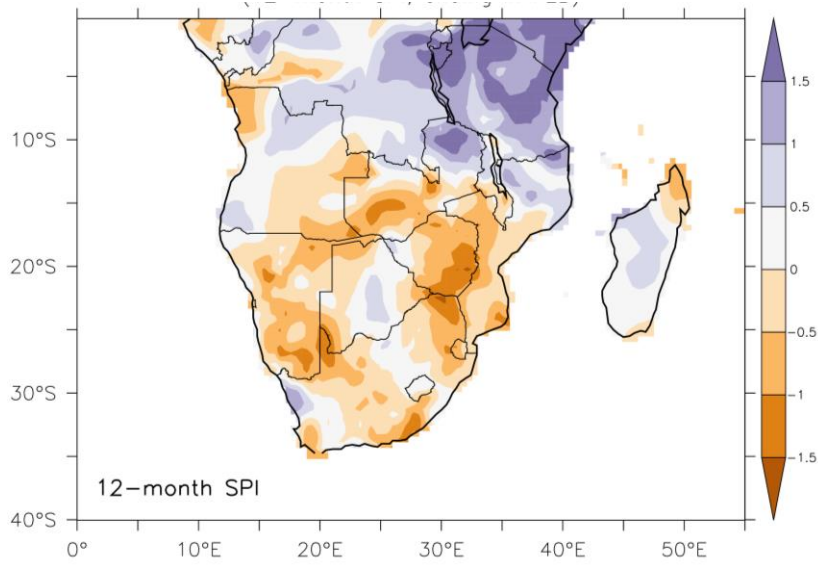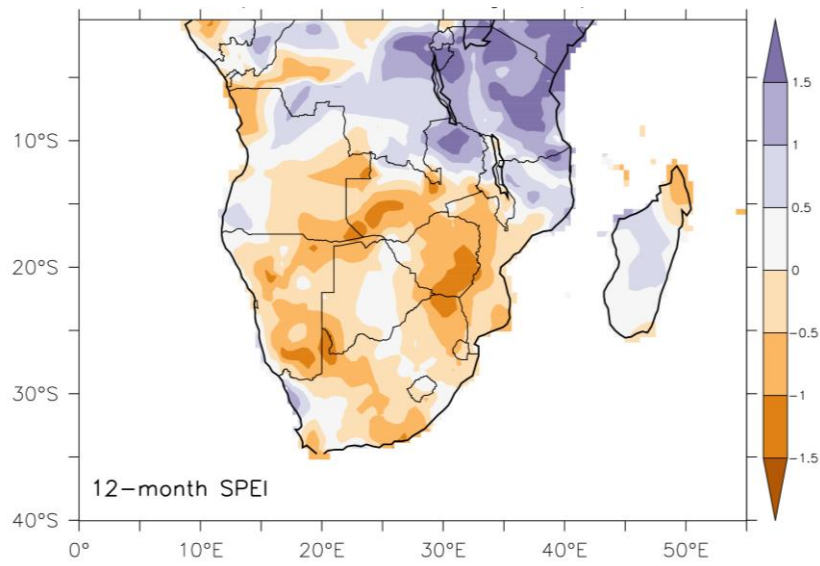
Figure 100: Composite of annual droughts (12-month SPEI and SPI, ending in February) over southern Africa during very strong positive ENSO (El Niño) years (1983 and 1988)
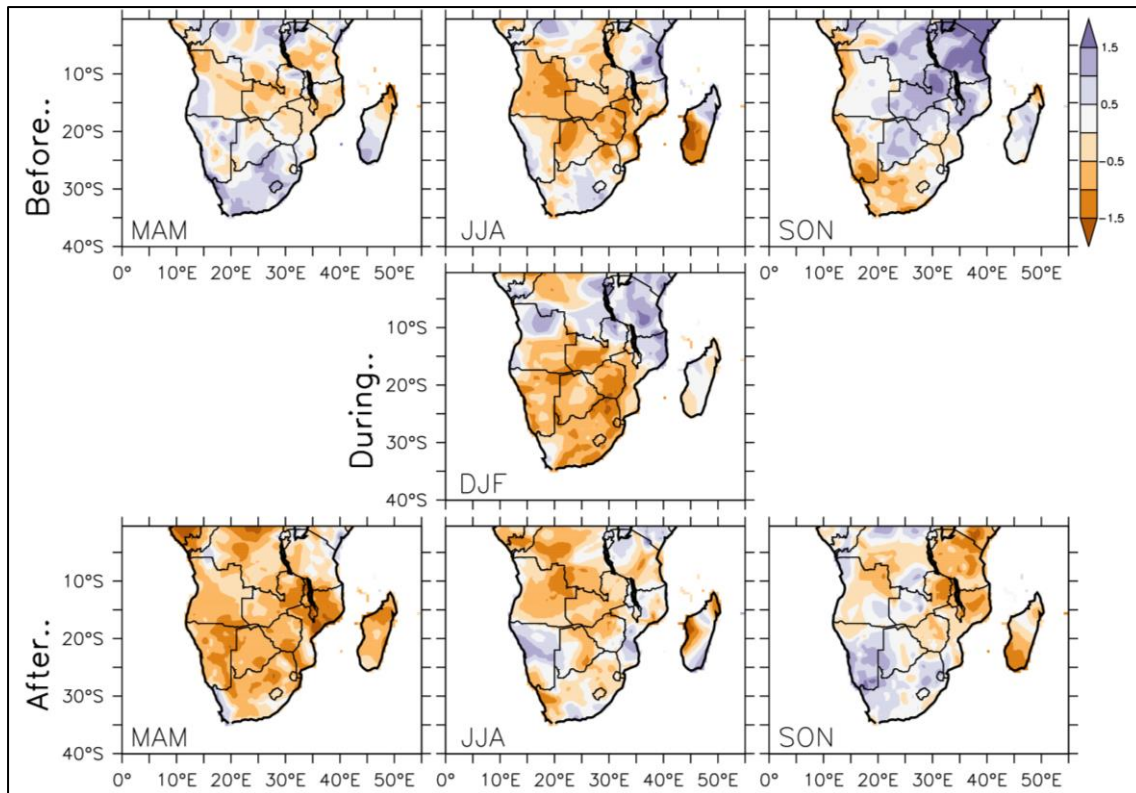
Figure 101: Composite of seasonal droughts (three-month SPEI) over southern Africa before (top panels), during (middle panel), and after (lower panels) the summer of very strong positive ENSO (El Niño) years (1983 and 1988)
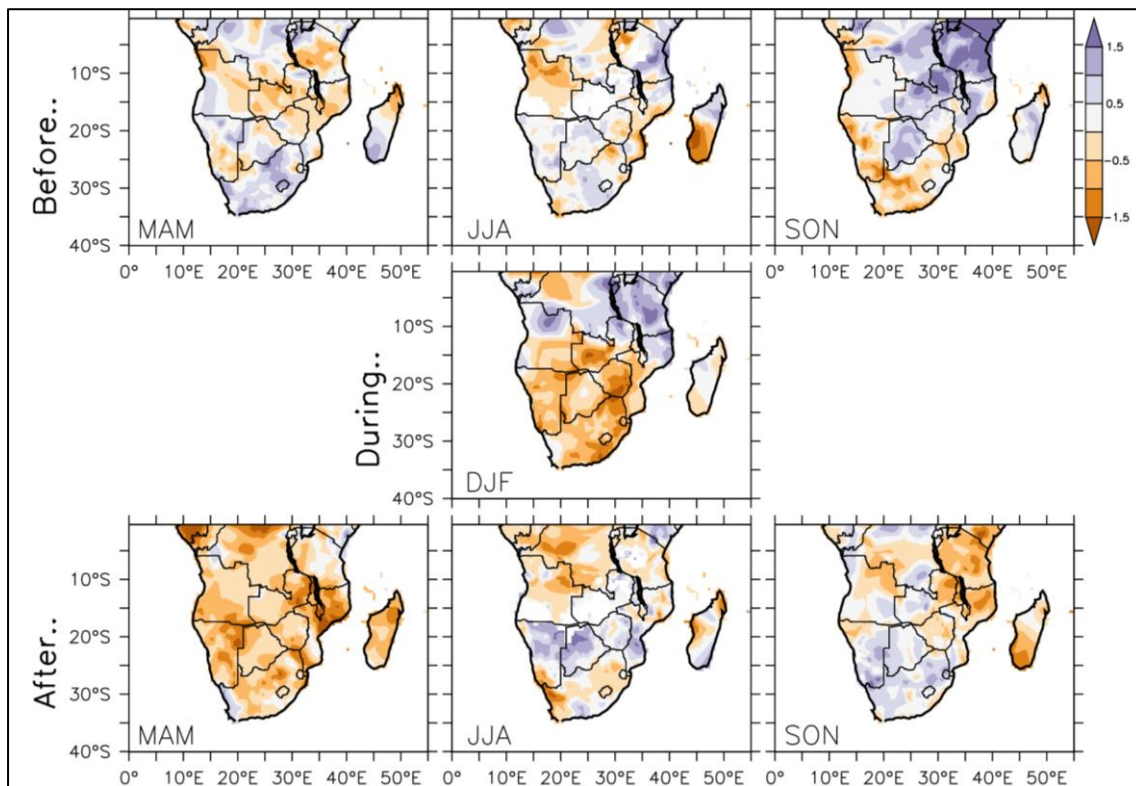
Figure 102: Composite of seasonal droughts (three-month SPI) over southern Africa before (top panels), during (middle panel), and after (lower panels) the summer of very strong positive ENSO (El Niño) years (1983 and 1988)
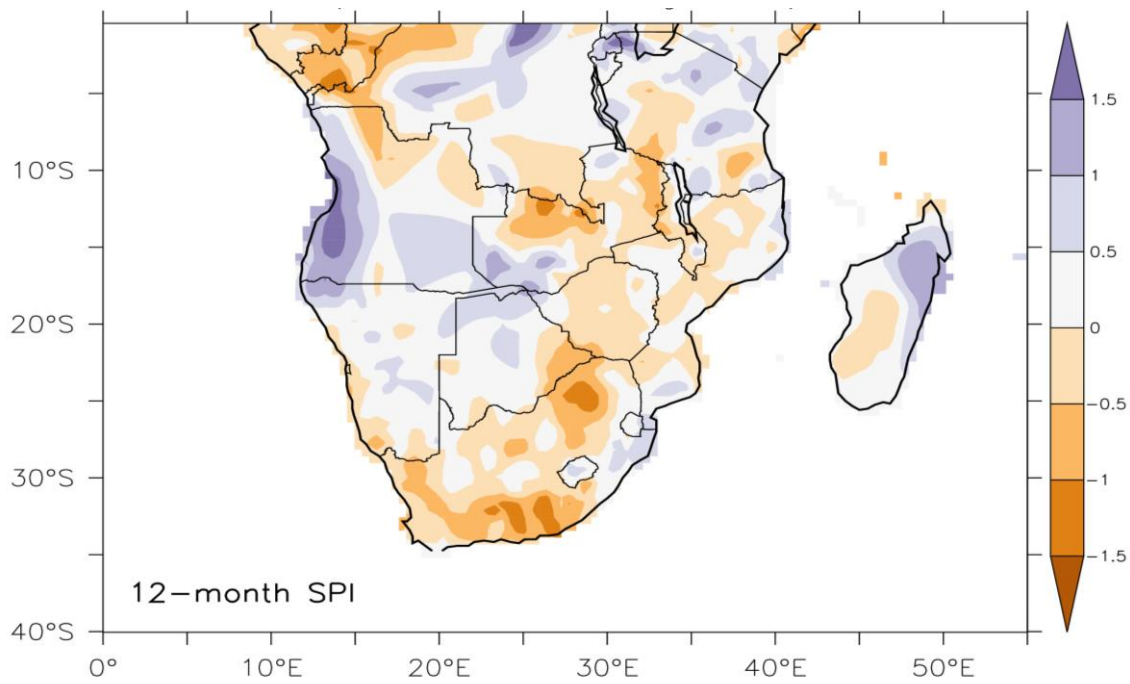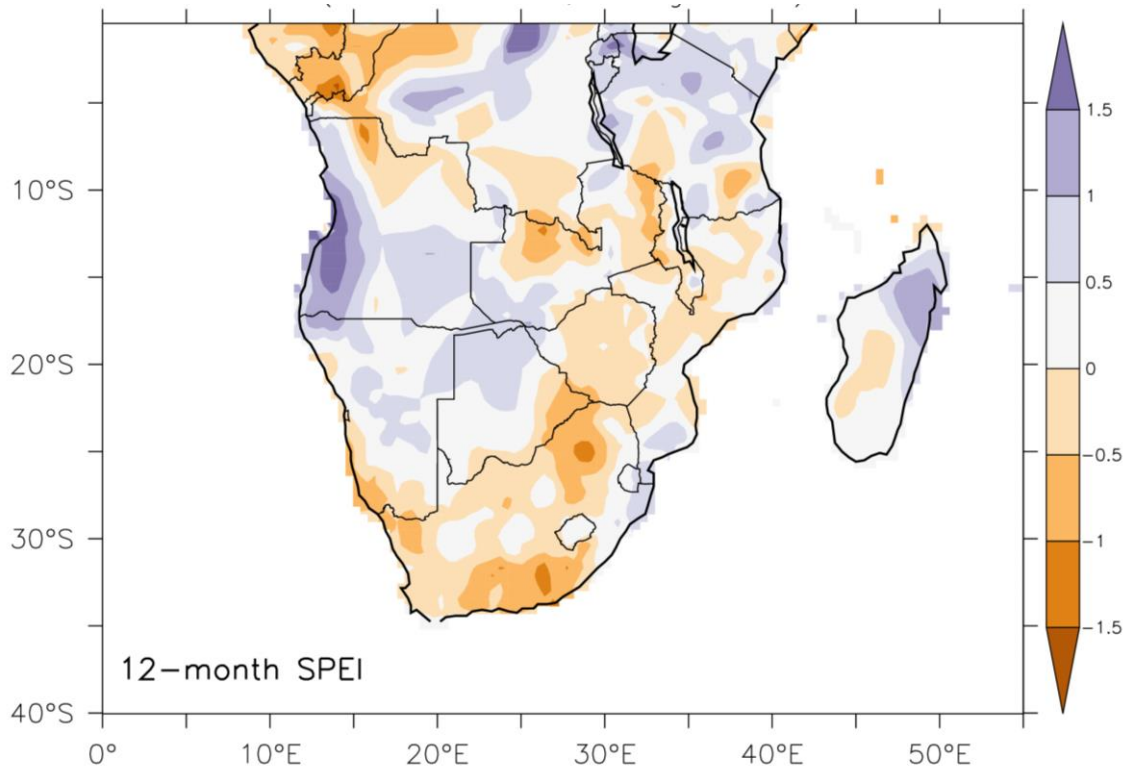
Figure 103: Composite of annual droughts (12-month SPEI and SPI, ending in February) over southern Africa during strong positive ENSO (El Niño) years (1958, 1966, and 1973)
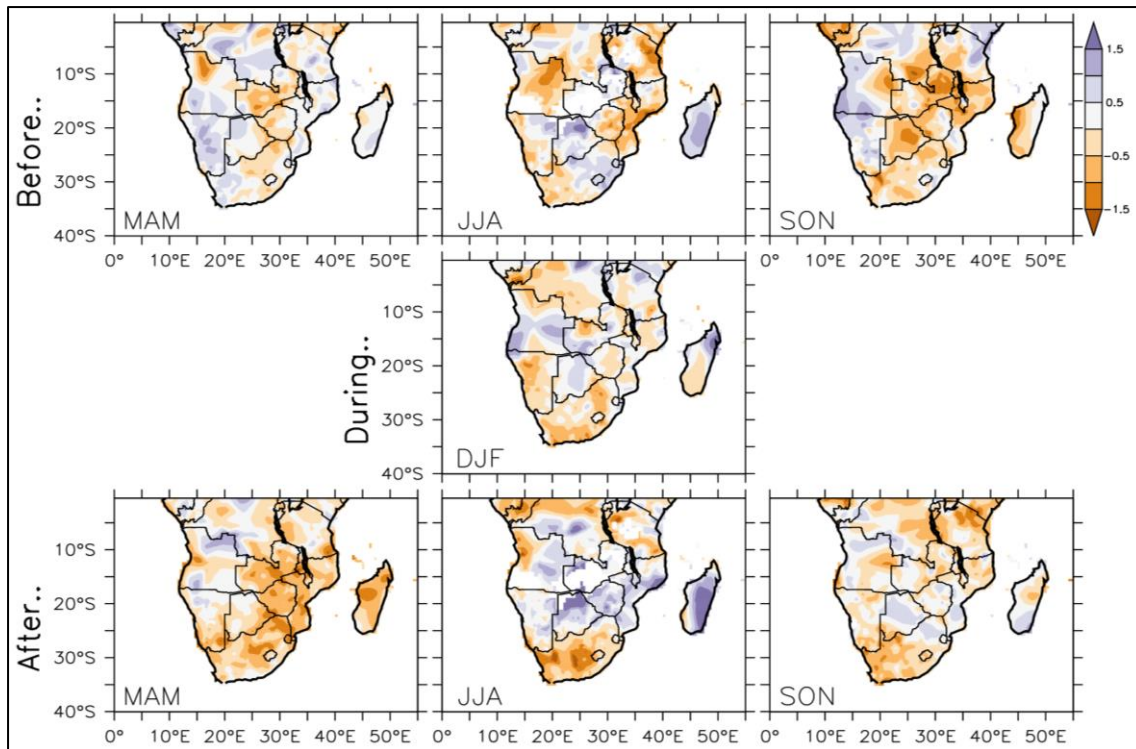
Figure 104: Composite of seasonal droughts (three-month SPEI) over southern Africa before (top panels), during (middle panel), and after (lower panels) the summer of strong positive ENSO (El Niño) years (1958, 1966, and 1973)
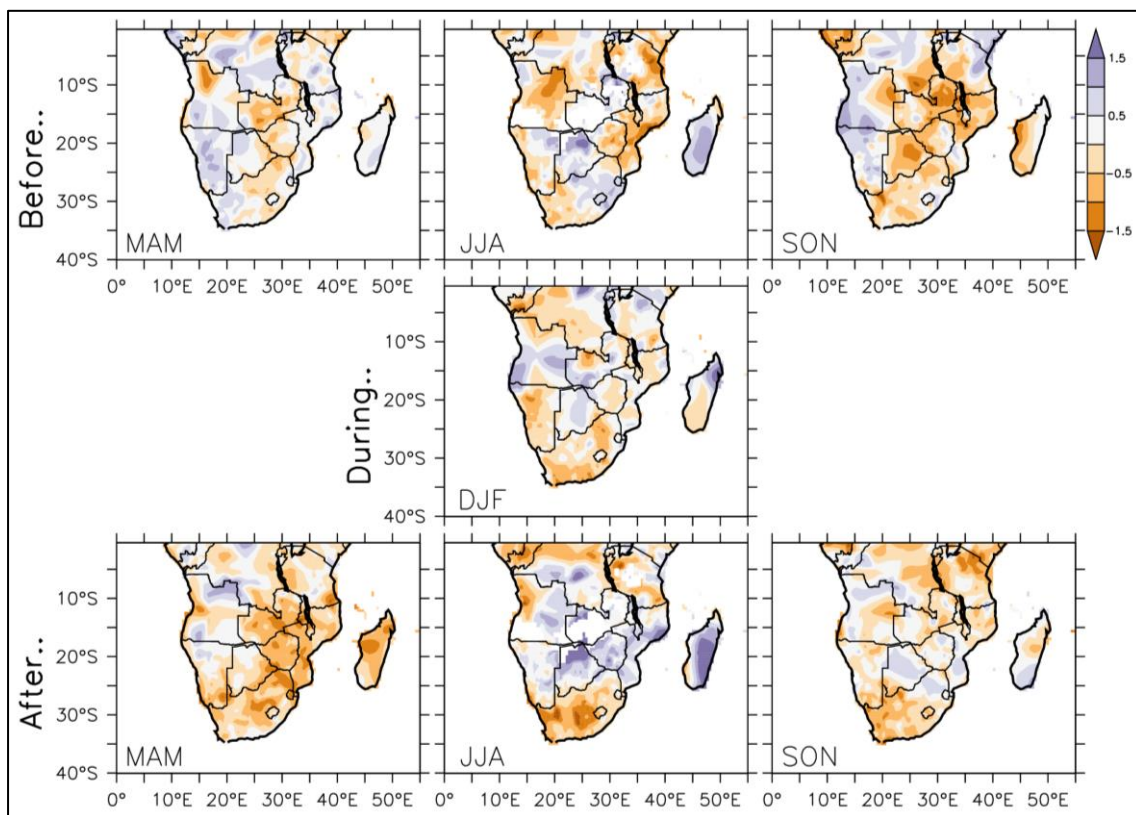
Figure 105: Composite of seasonal droughts (three-month SPI) over southern Africa before (top panels), during (middle panel), and after (lower panels) the summer of strong positive ENSO (El Niño) years (1958, 1966, and 1973)
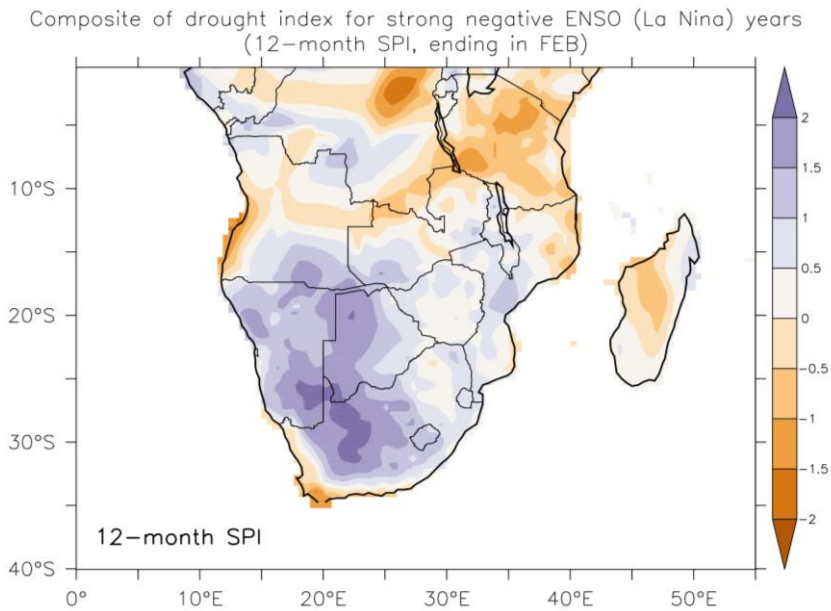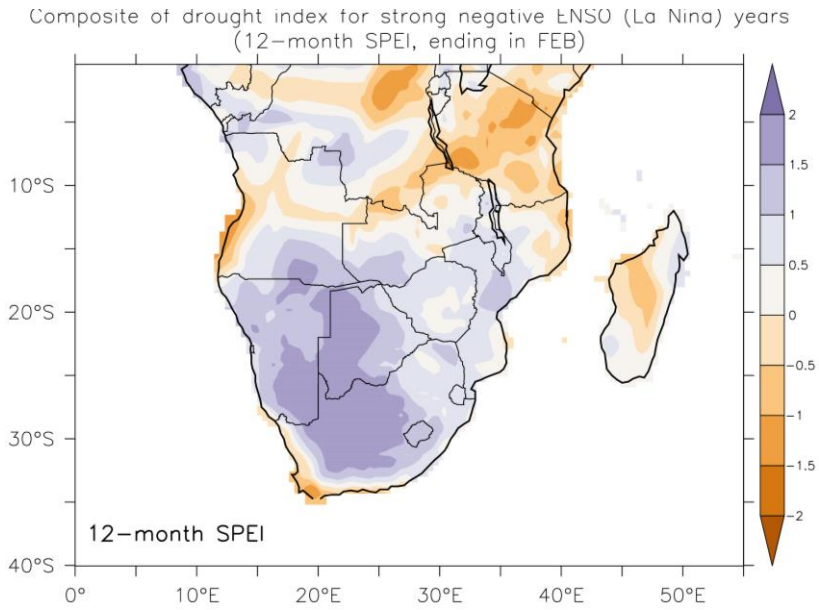
Figure 106: Composite of annual droughts (12-month SPEI and SPI, ending in February) over southern Africa during strong negative ENSO (La Niña) years (1974, 1976, and 1989)
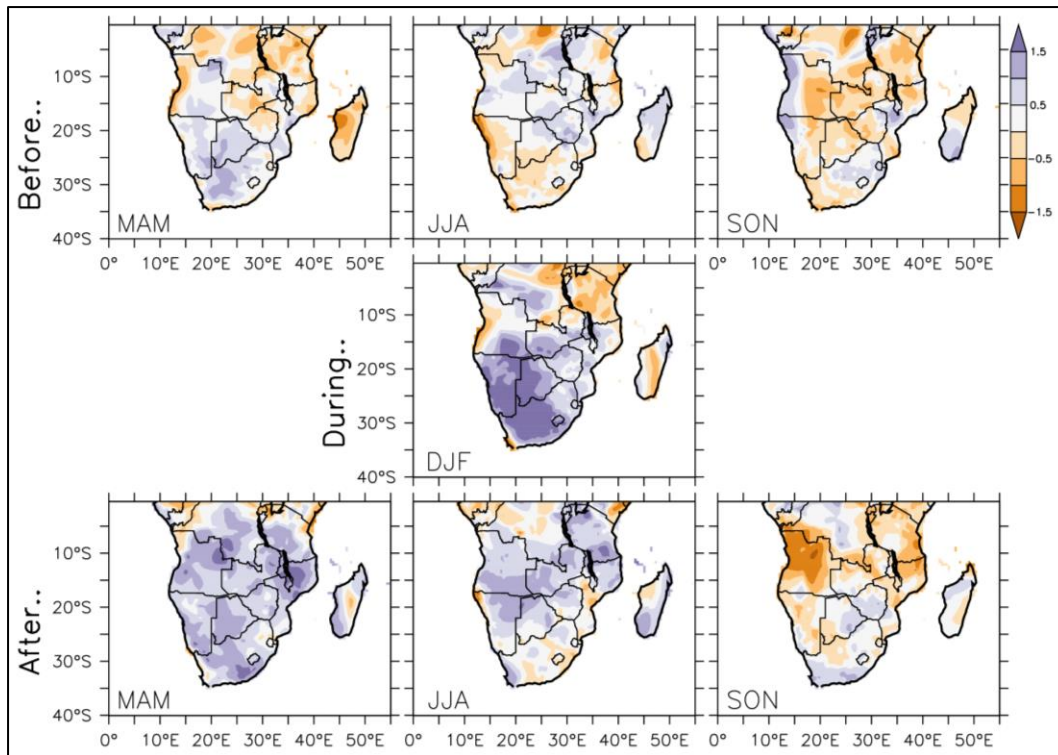
Figure 107: Composite of seasonal droughts (three-month SPEI) over southern Africa before (top panels), during (middle panel), and after (lower panels) the summer of strong negative ENSO (La Niña) years (1974, 1976, and 1989)
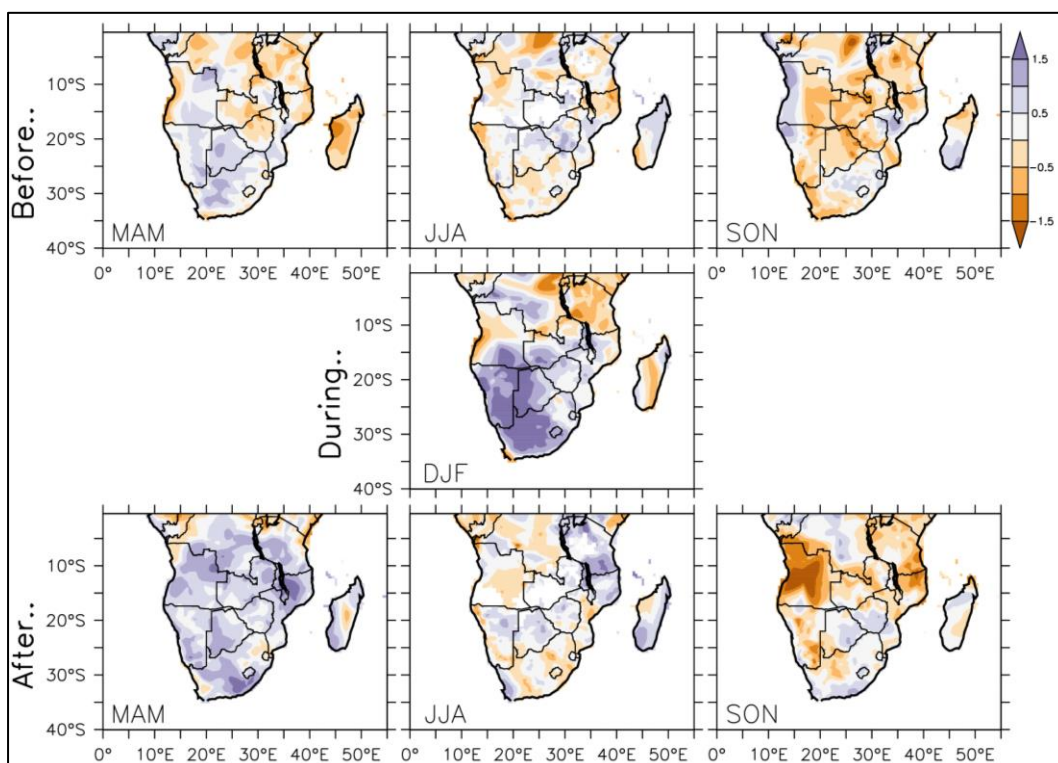
Figure 108: Composite of seasonal droughts (three-month SPI) over southern Africa before (top panels), during (middle panel), and after (lower panels) the summer of strong negative ENSO (La Niña) years (1974, 1976, and 1989)
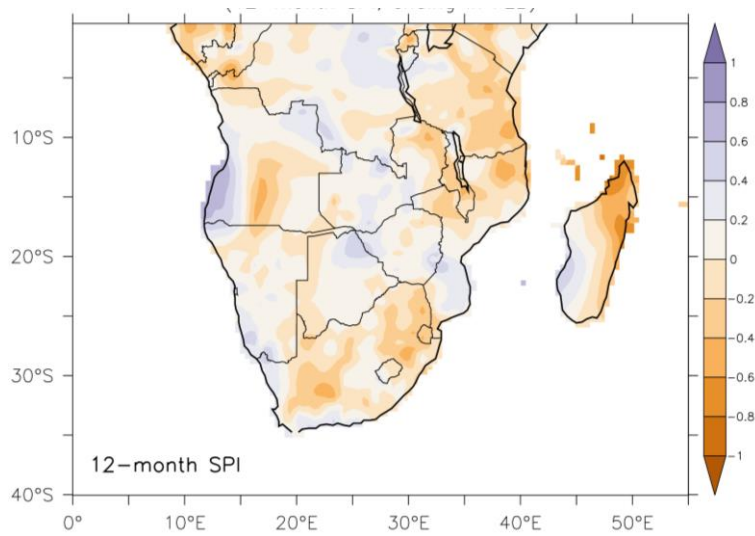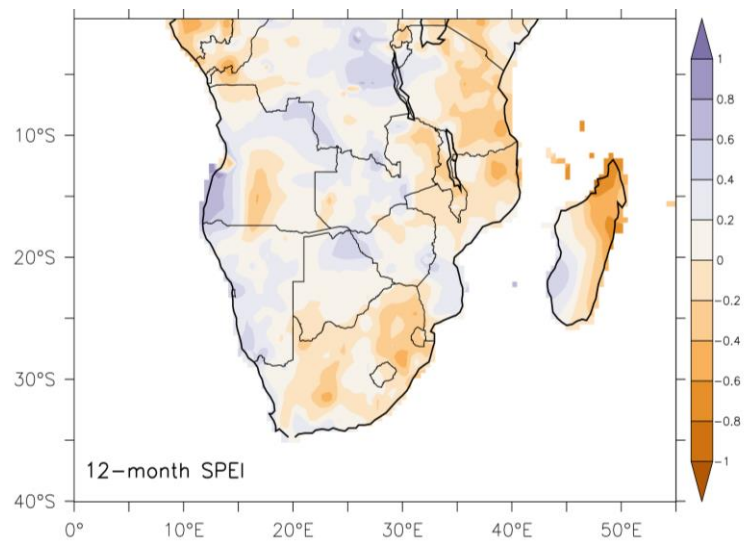
Figure 109: Composite of annual droughts (12-month SPEI and SPI, ending in February) over southern Africa during strong positive IOD years (1961, 1963, 1967, 1972, 1977, 1982, 1983, 1994, 1997, 2006 and 2007)
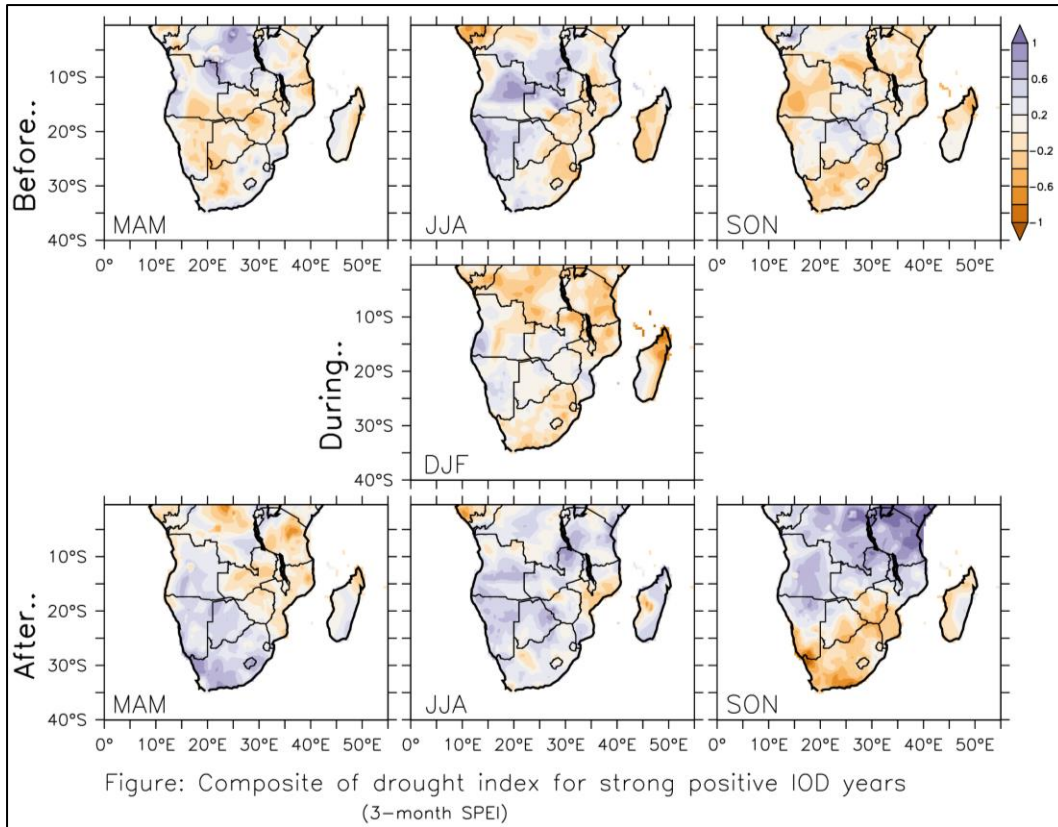
Figure 110: Composite of seasonal droughts (three-month SPEI) over southern Africa before (top panels), during (middle panel), and after (lower panels) the summer of strong positive IOD years (1961, 1963, 1967, 1972, 1977, 1982, 1983, 1994, 1997, 2006 and 2007)
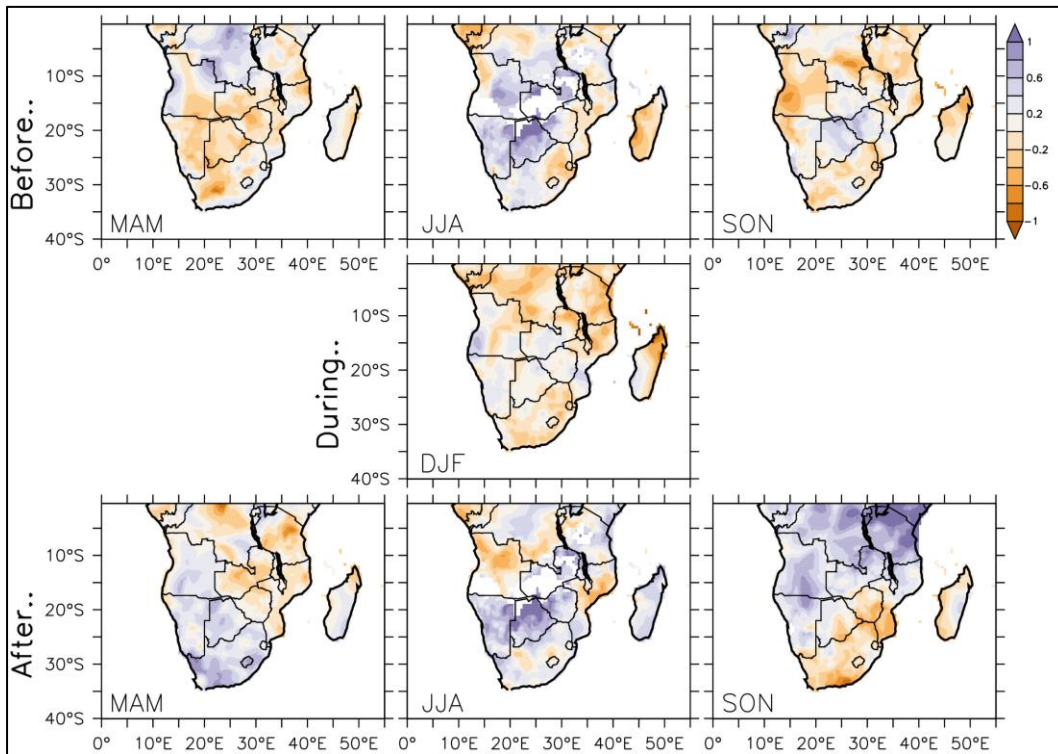
Figure 111: Composite of seasonal droughts (three-month SPI) over southern Africa before (top panels), during (middle panel), and after (lower panels) the summer of strong positive IOD years (1961, 1963, 1967, 1972, 1977, 1982, 1983, 1994, 1997, 2006 and 2007)
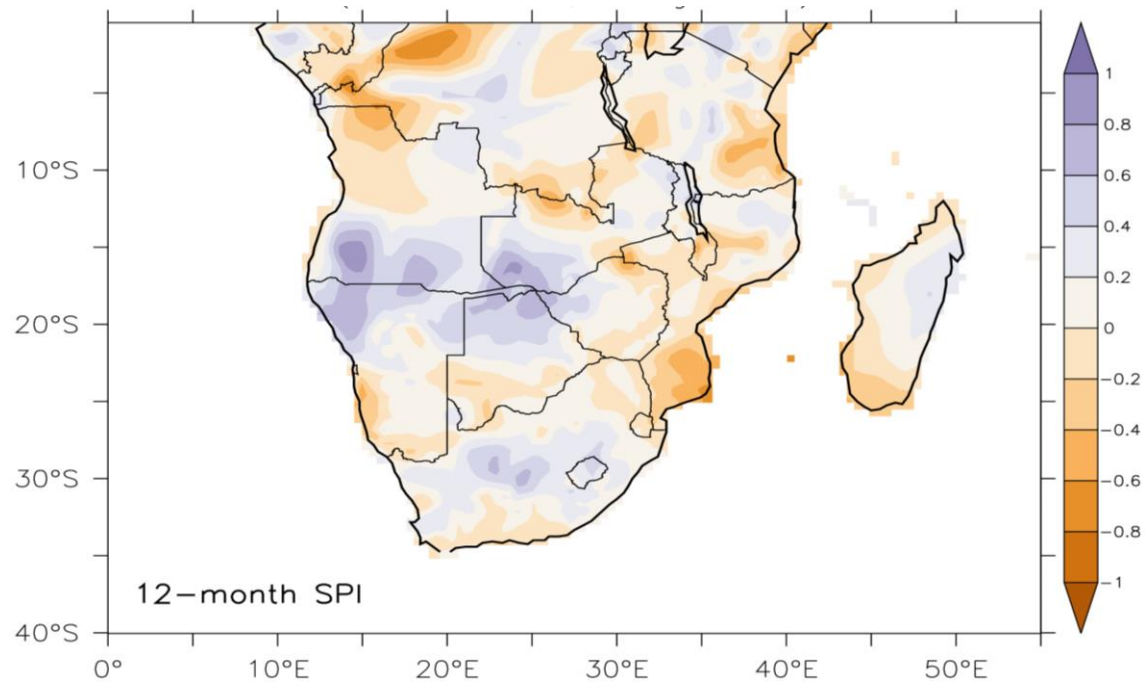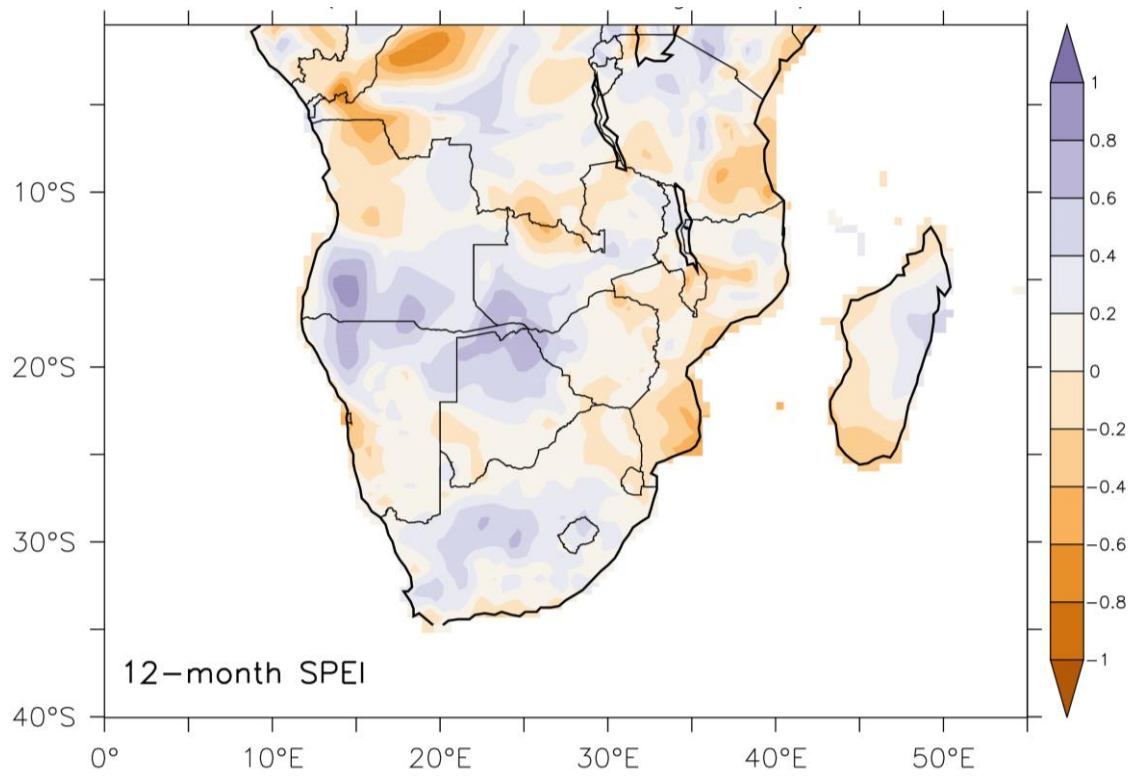
Figure 112: Composite of annual droughts (12-month SPEI and SPI, ending in February) over southern Africa during strong negative IOD years (1958, 1960, 1964, 1971, 1974, 1975, 1989, 1992, 1993, and 1996)
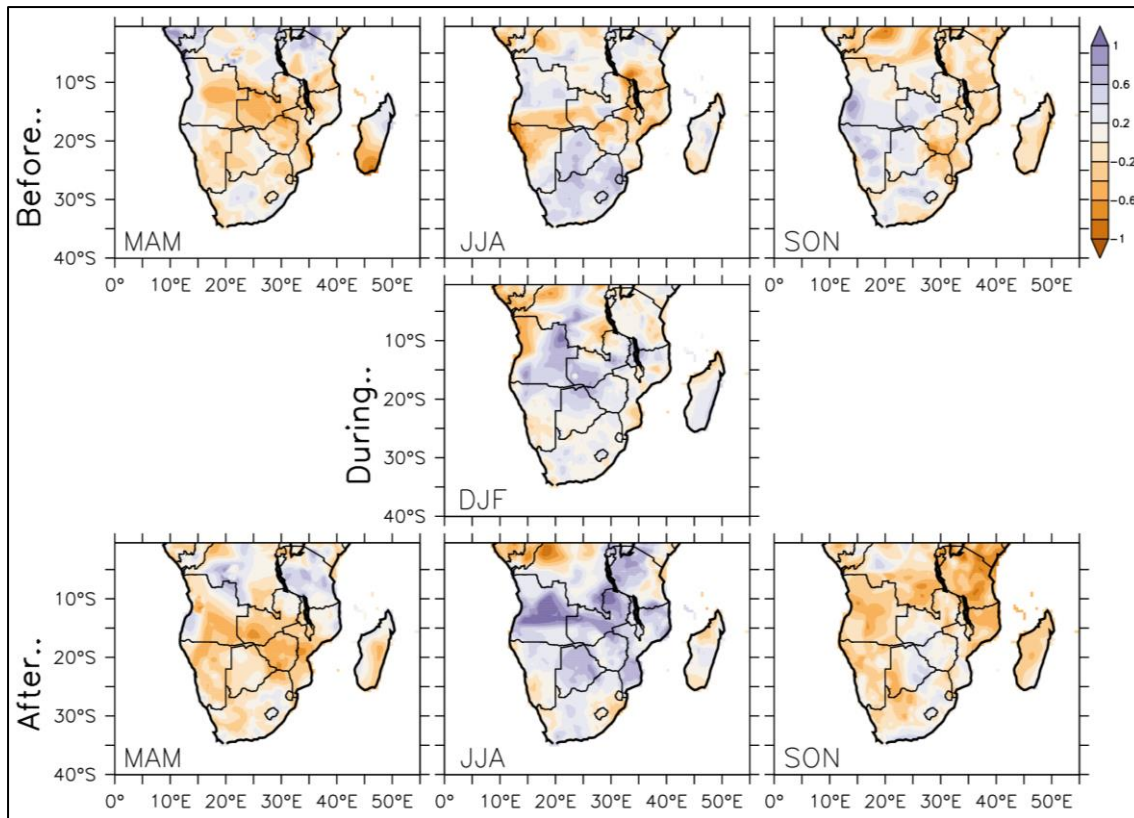
Figure 113: Composite of seasonal droughts (three-month SPEI) over southern Africa before (top panels), during (middle panel), and after (lower panels) the summer of strong negative IOD years (1958, 1960, 1964, 1971, 1974, 1975, 1989, 1992, 1993, and 1996)
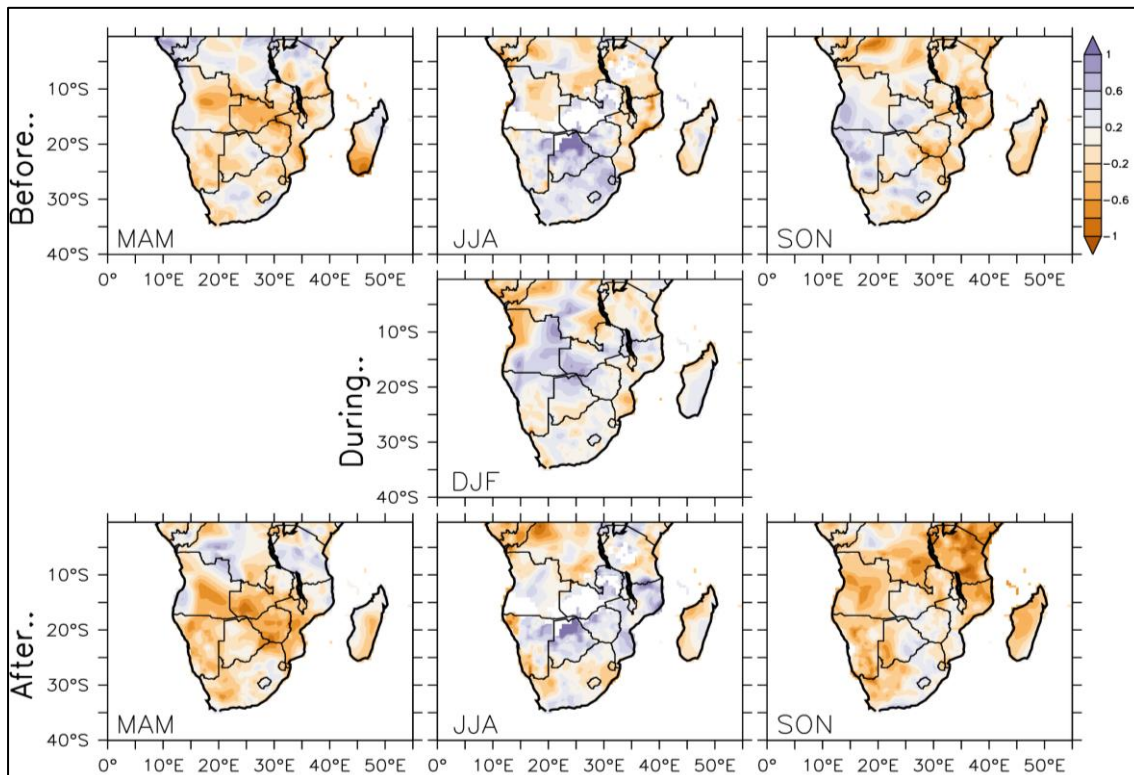
Figure 114: Composite of seasonal droughts (three-month SPI) over southern Africa before (top panels), during (middle panel), and after (lower panels) the summer of strong negative IOD years (1958, 1960, 1964, 1971, 1974, 1975, 1989, 1992, 1993, and 1996)
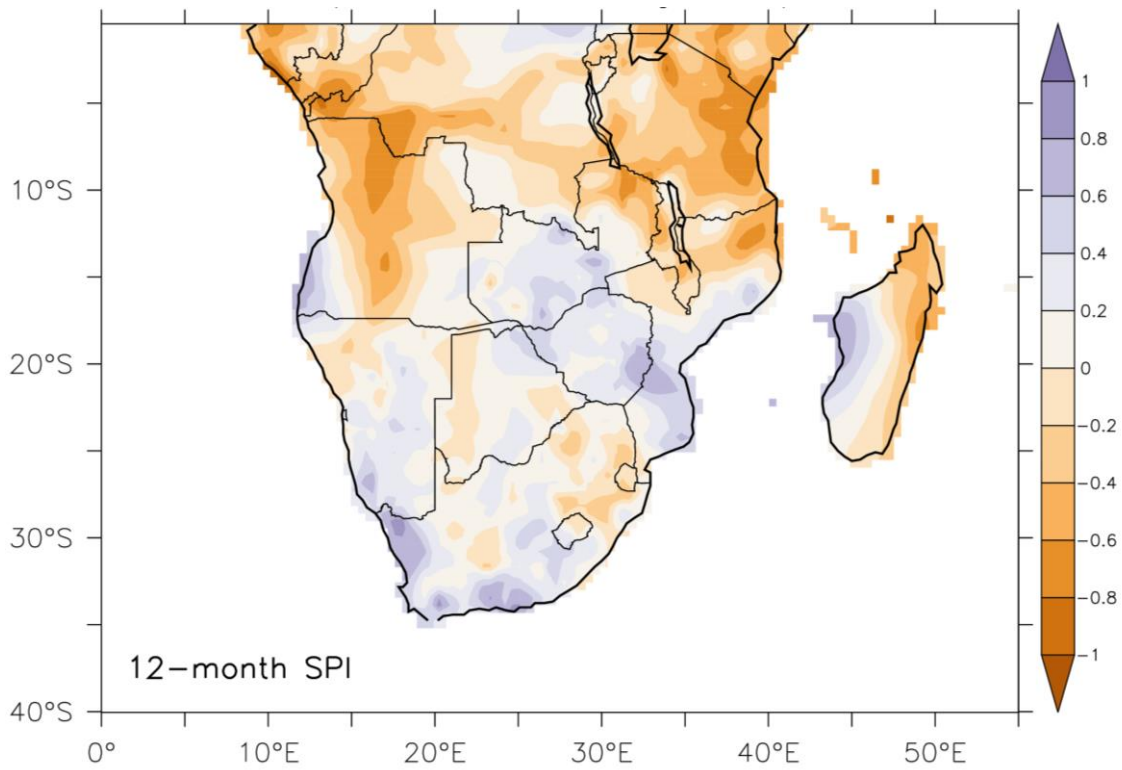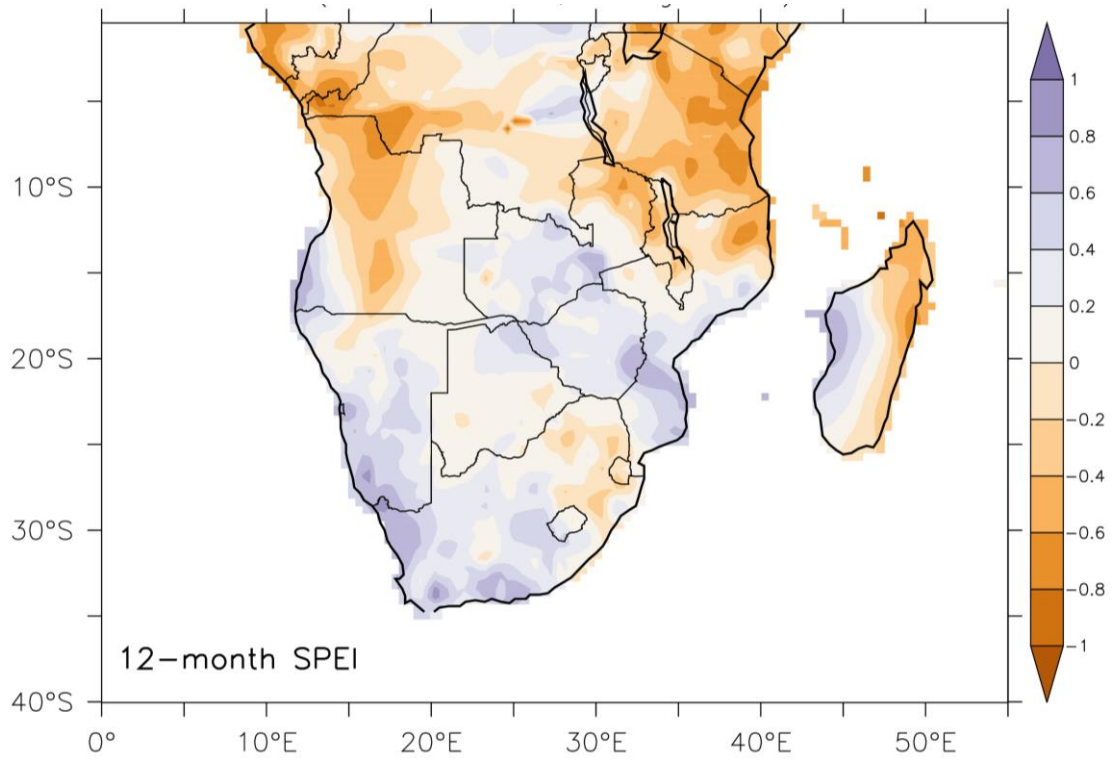
Figure 115: Composite of annual droughts (12-month SPEI and SPI, ending in February) over southern Africa during strong positive IOD and El Niño years (1963, 1972, 1977, 1982, 1994, 1997, and 2006)
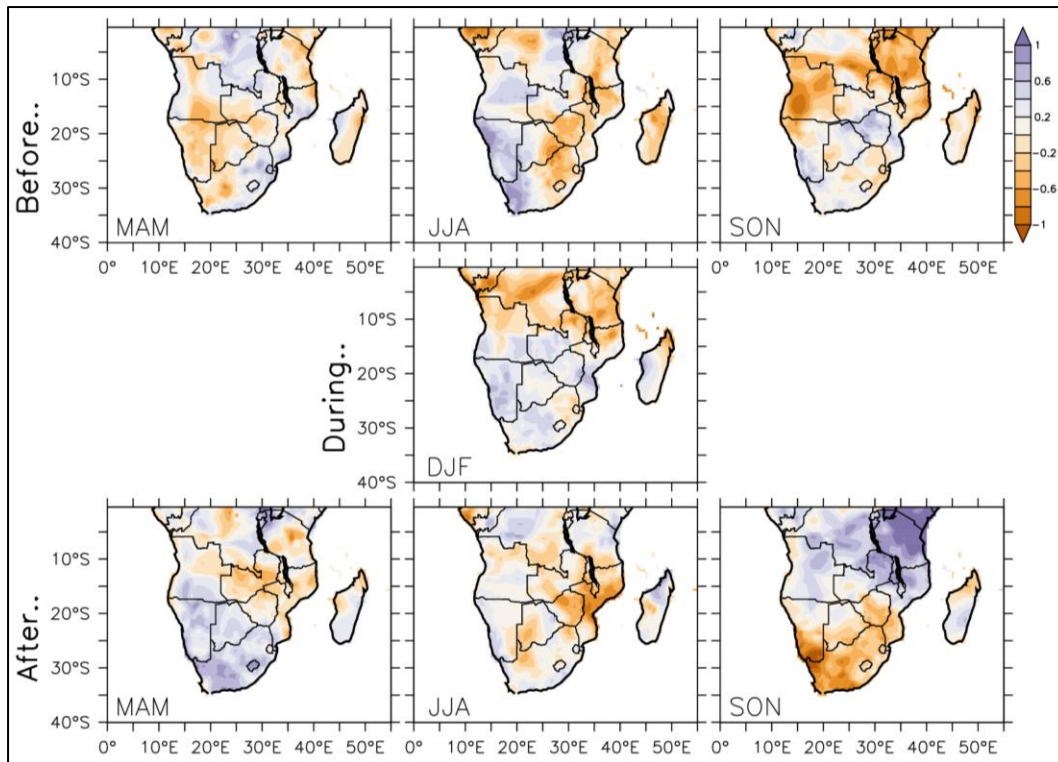
Figure 116: Composite of seasonal droughts (three-month SPEI) over southern Africa before (top panels), during (middle panel), and after (lower panels) the summer of strong positive IOD and El Niño years (1963, 1972, 1977, 1982, 1994, 1997, and 2006)
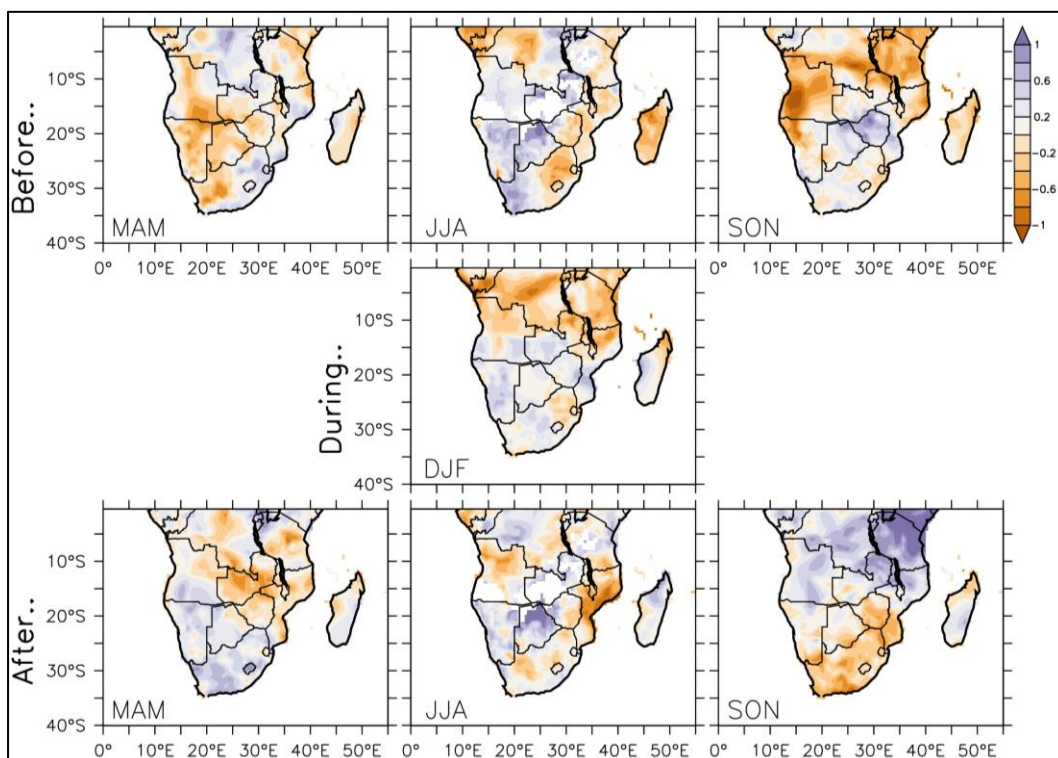
Figure 117: Composite of seasonal droughts (three-month SPI) over southern Africa before (top panels), during (middle panel), and after (lower panels) the summer of strong positive IOD and El Niño years (1963, 1972, 1977, 1982, 1994, 1997, and 2006)
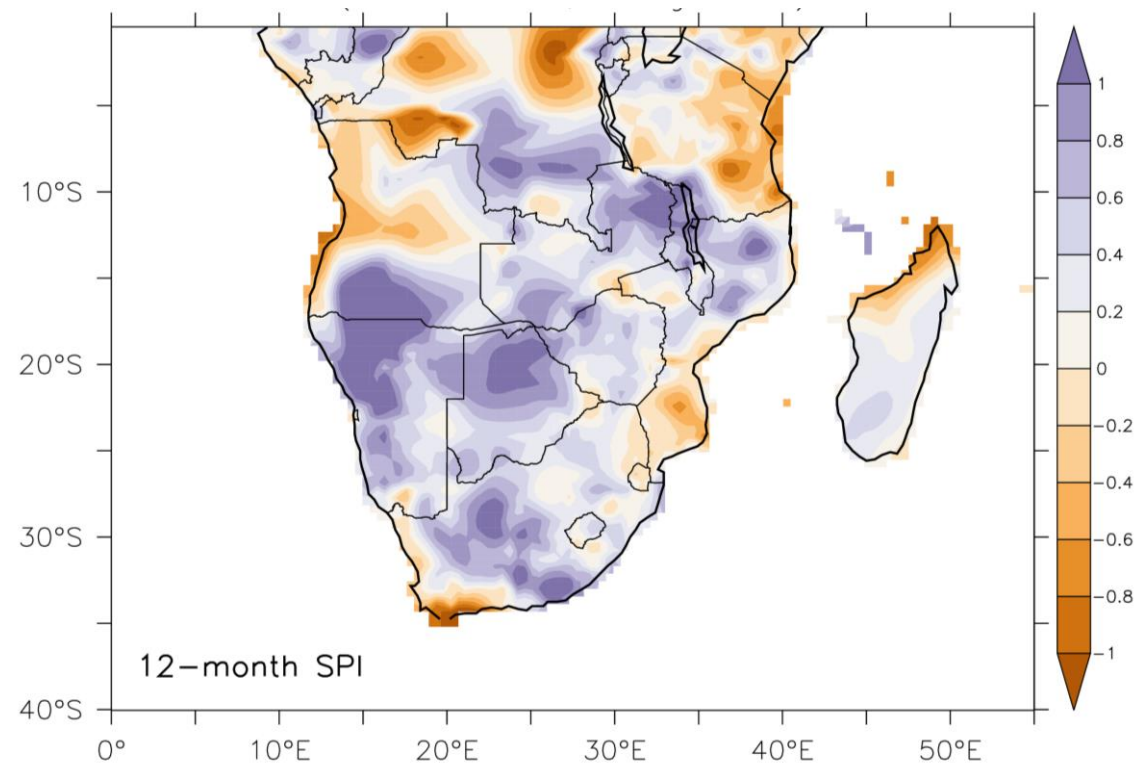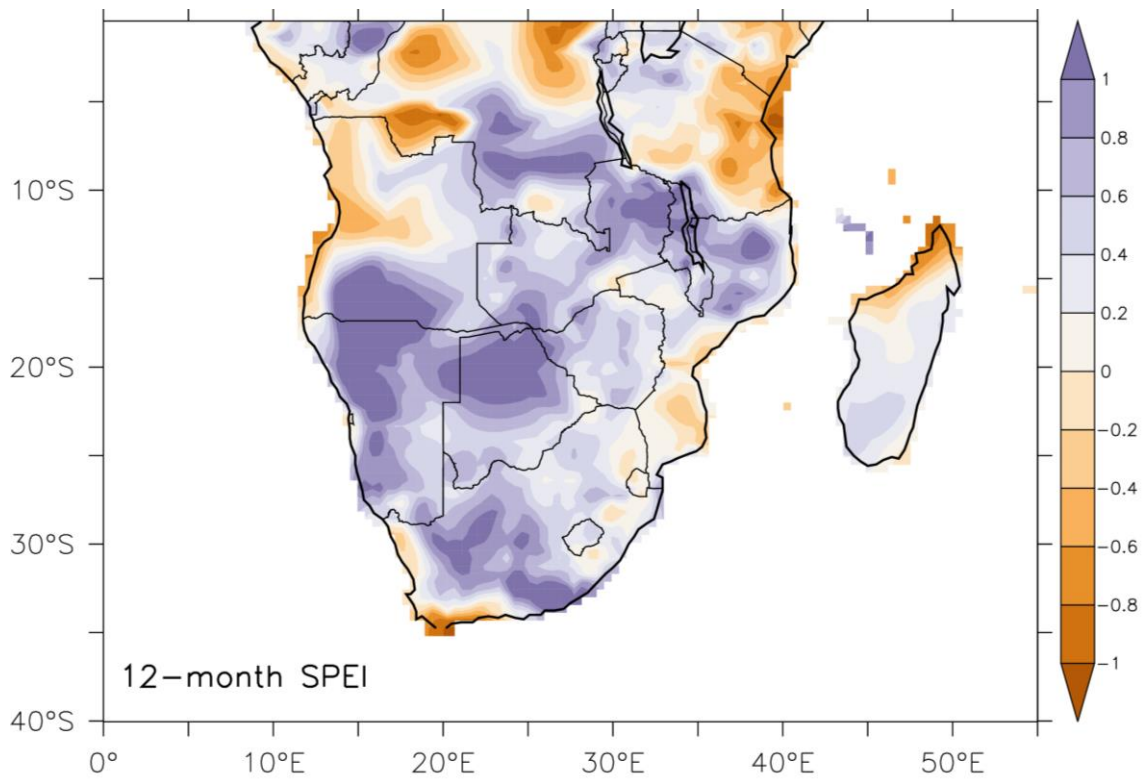
Figure 118: Composite of annual droughts (12-month SPEI and SPI, ending in February) over southern Africa during strong negative IOD and La Niña years (1964, 1971, 1974, and 1975)
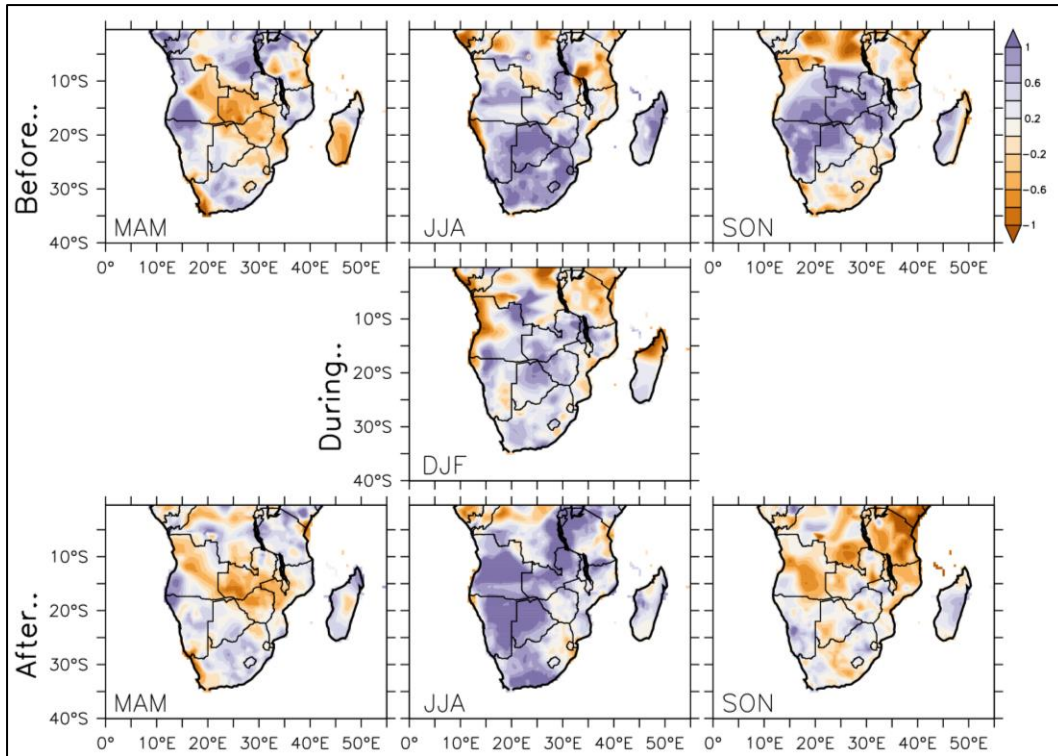
Figure 119: Composite of seasonal droughts (three-month SPEI) over southern Africa before (top panels), during (middle panel), and after (lower panels) the summer of strong negative IOD and La Niña years (1964, 1971, 1974, and 1975)
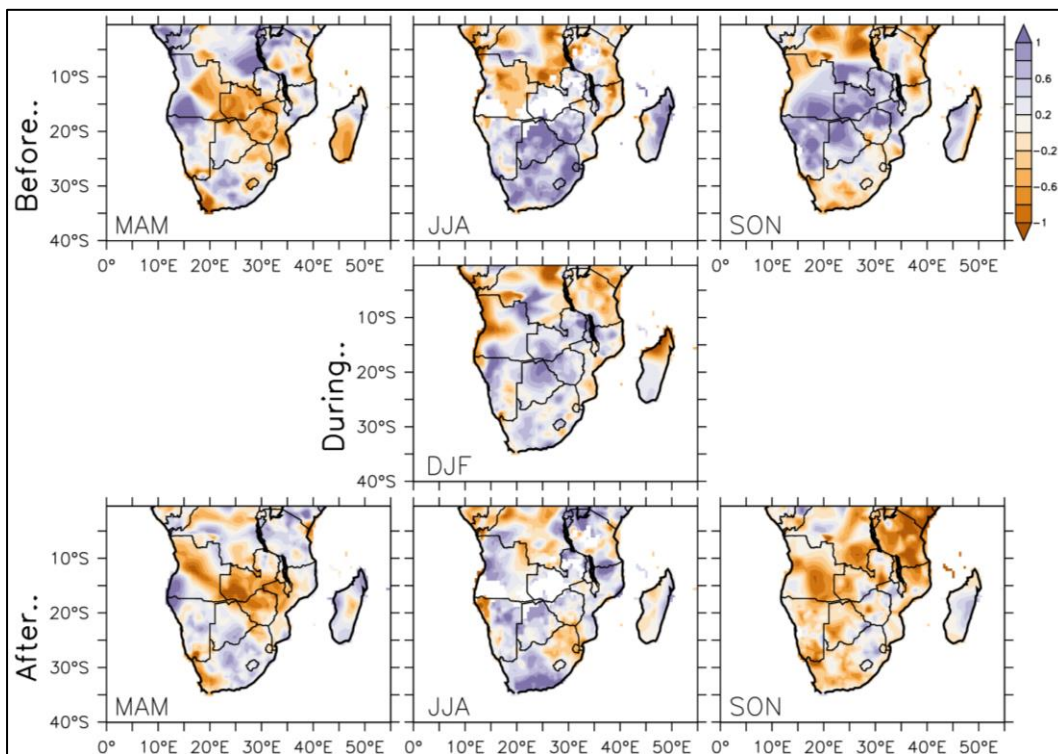
Figure 120: Composite of seasonal droughts (three-month SPI) over southern Africa before (top panels), during (middle panel), and after (lower panels) the summer of strong negative IOD and La Niña years (1964, 1971, 1974, and 1975)
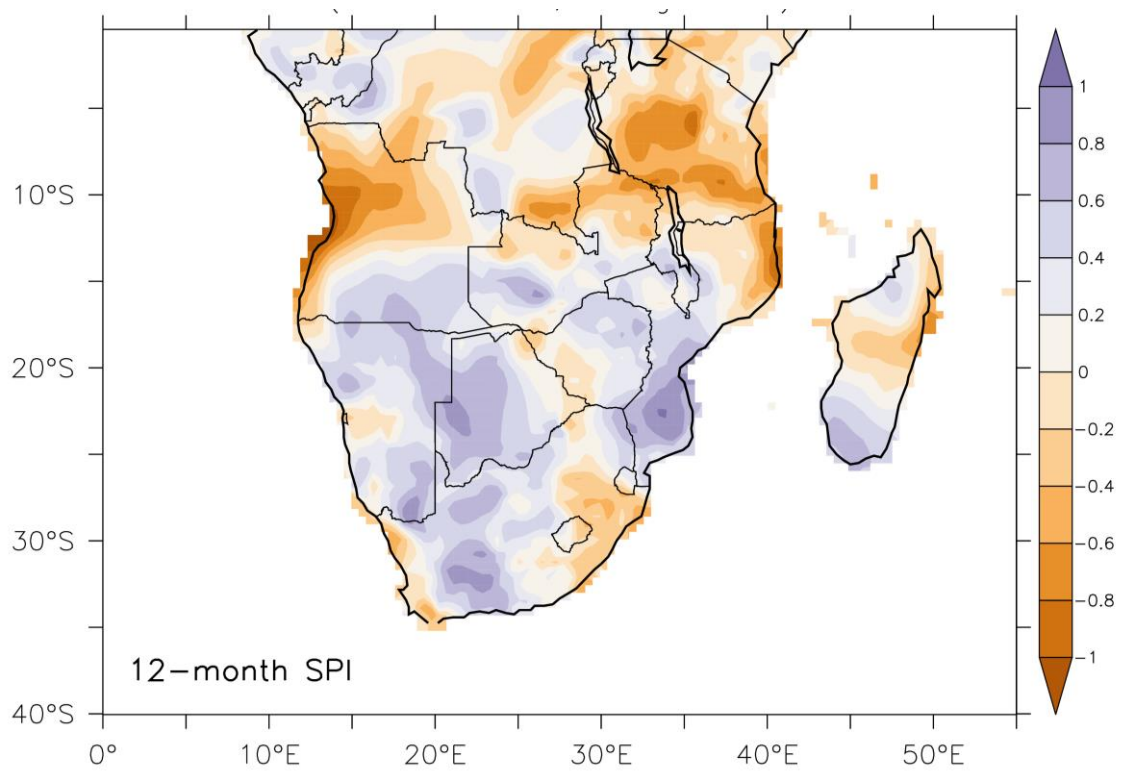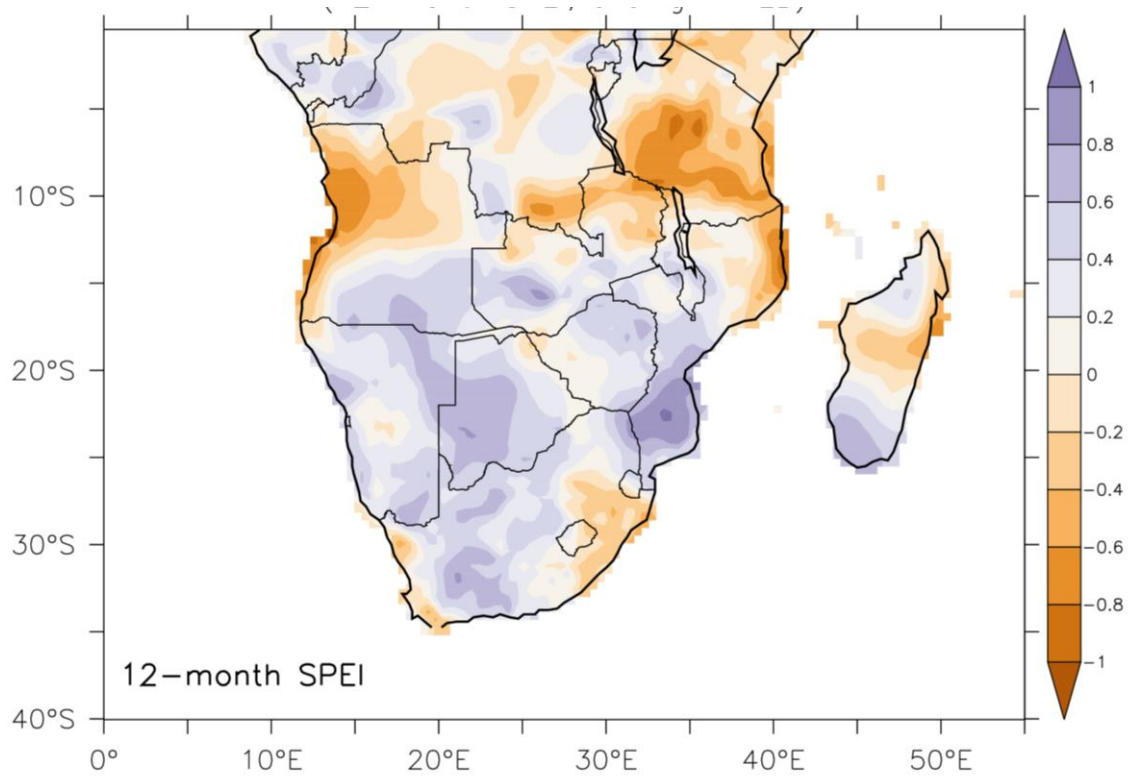
Figure 121: Composite of annual droughts (12-month SPEI and SPI, ending in February) over southern Africa during strong positive SIOD years (1969, 1974, 1976, 1981, 1982, and 1999)
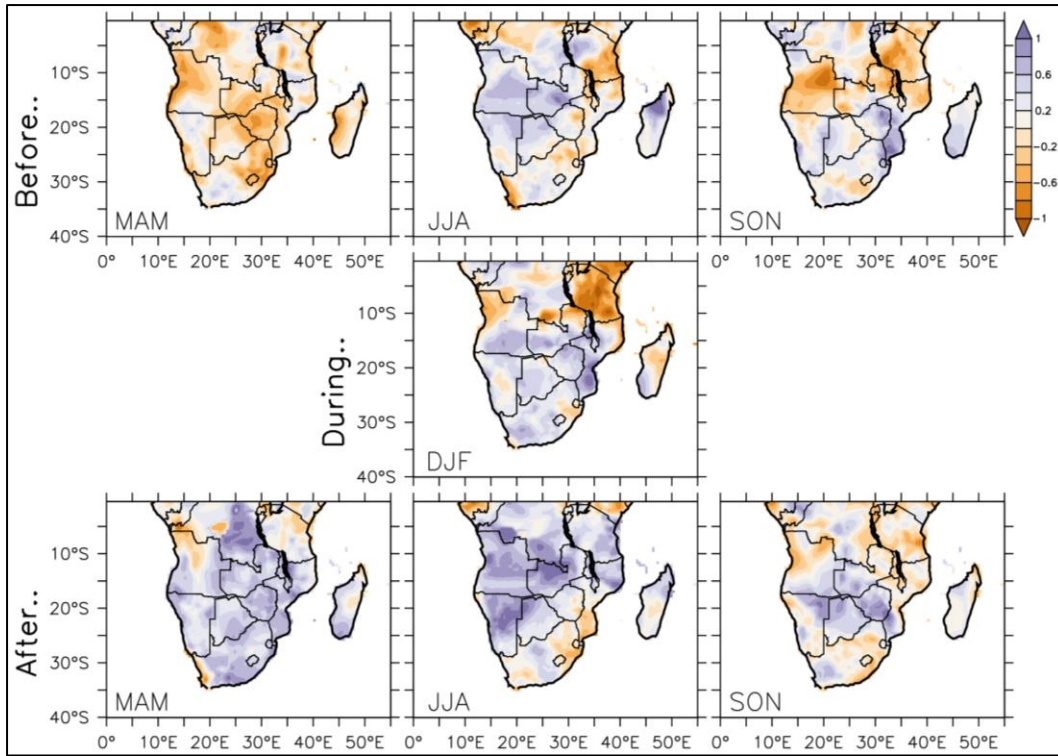
Figure 122: Composite of seasonal droughts (three-month SPEI) over southern Africa before (top panels), during (middle panel), and after (lower panels) the summer of strong positive SIOD years (1969, 1974, 1976, 1981, 1982, and 1999)
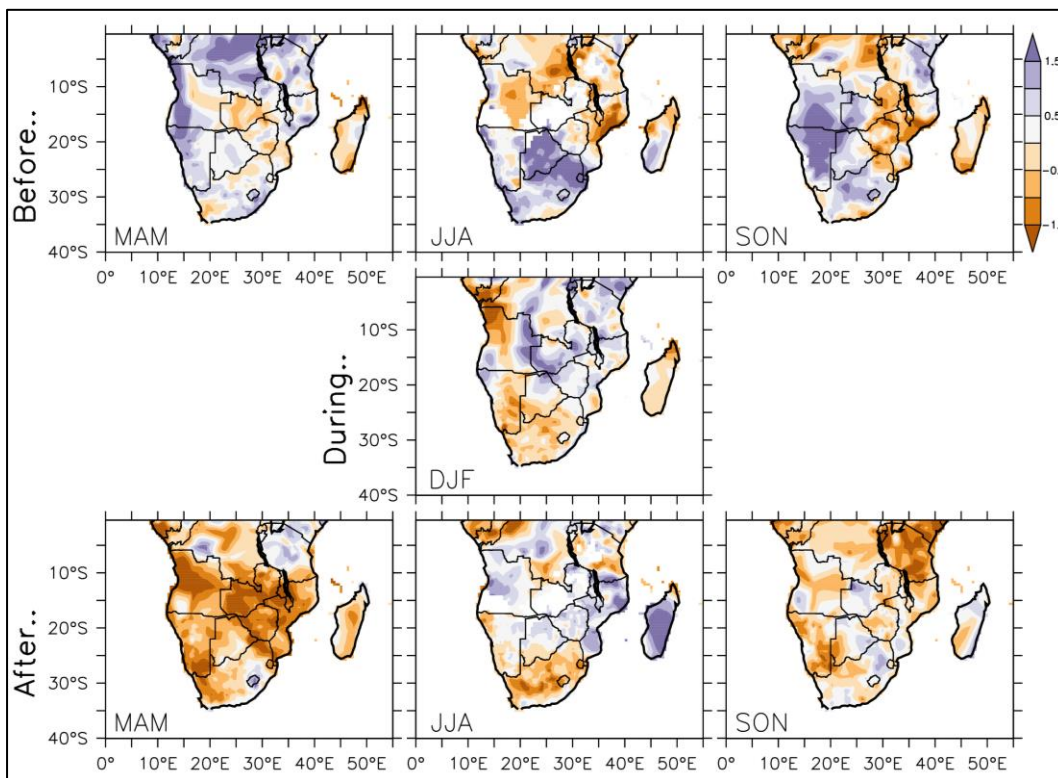
Figure 123: Composite of seasonal droughts (three-month SPEI) over southern Africa before (top panels), during (middle panel), and after (lower panels) the summer of strong positive SIOD years (1969, 1974, 1976, 1981, 1982, and 1999)
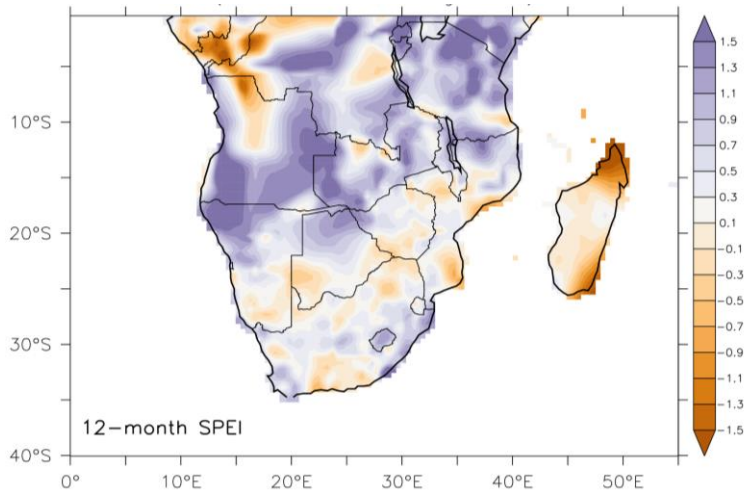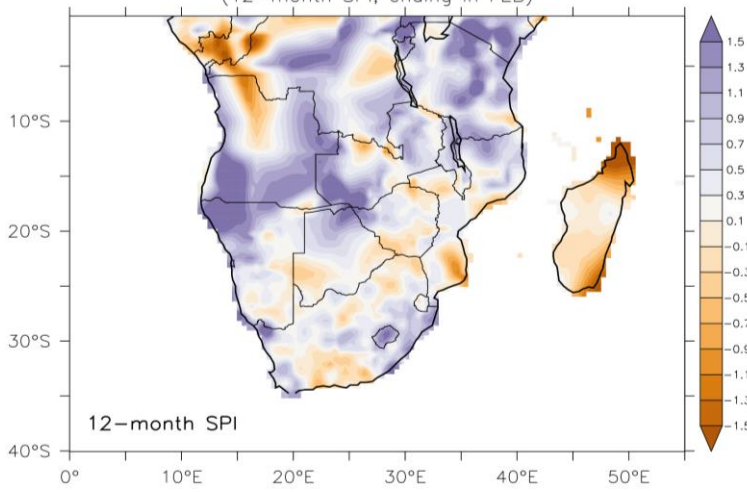
Figure 124: Composite of annual droughts (12-month SPEI and SPI, ending in February) over southern Africa during strong negative SIOD years (1958 and 1964)
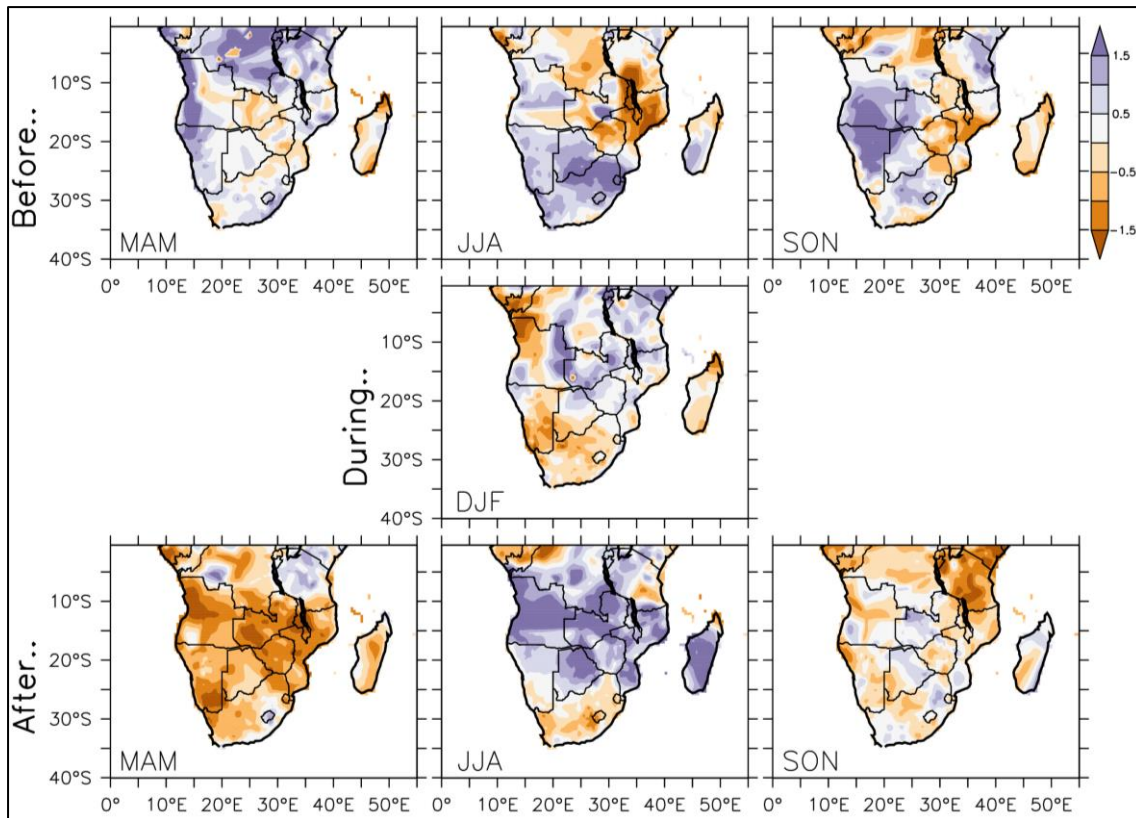
Figure 125: Composite of seasonal droughts (three-month SPEI) over southern Africa before (top panels), during (middle panel), and after (lower panels) the summer of strong negative SIOD years (1958, and 1964)
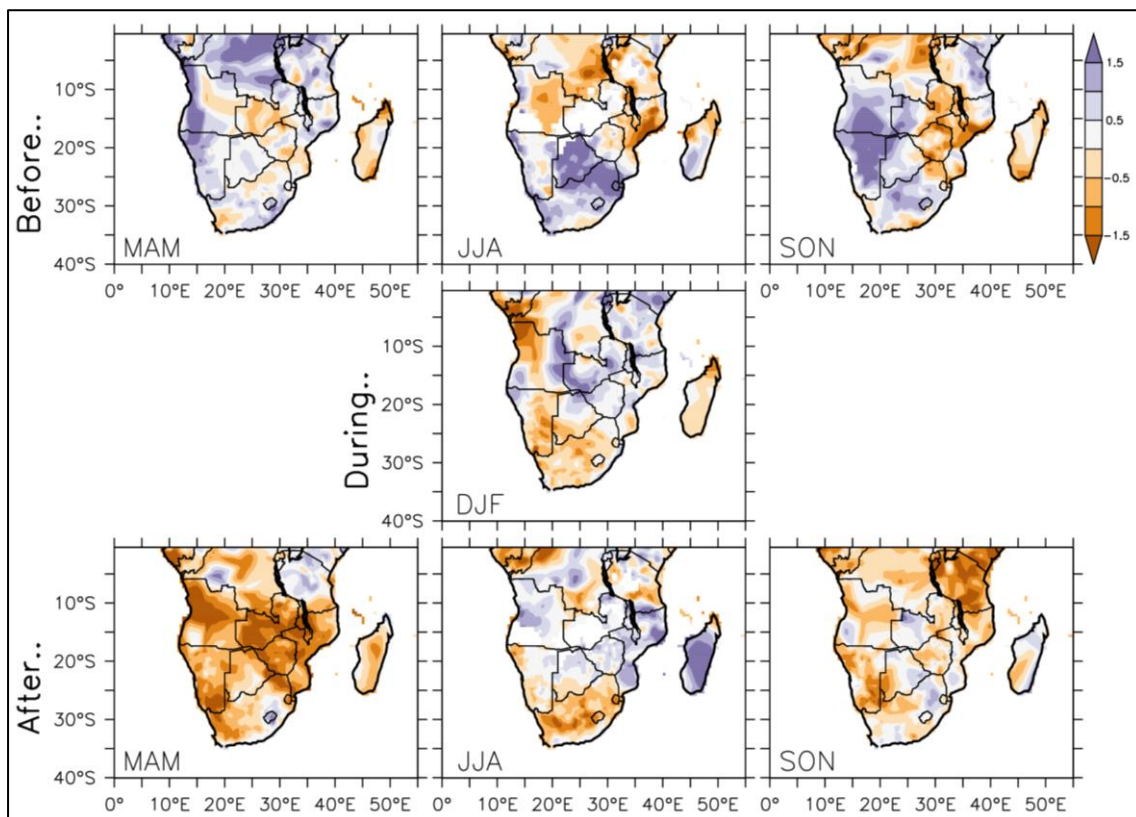
Figure 126: Composite of seasonal droughts (three-month SPI) over southern Africa before (top panels), during (middle panel), and after (lower panels) the summer of strong negative SIOD years (1958, and 1964)
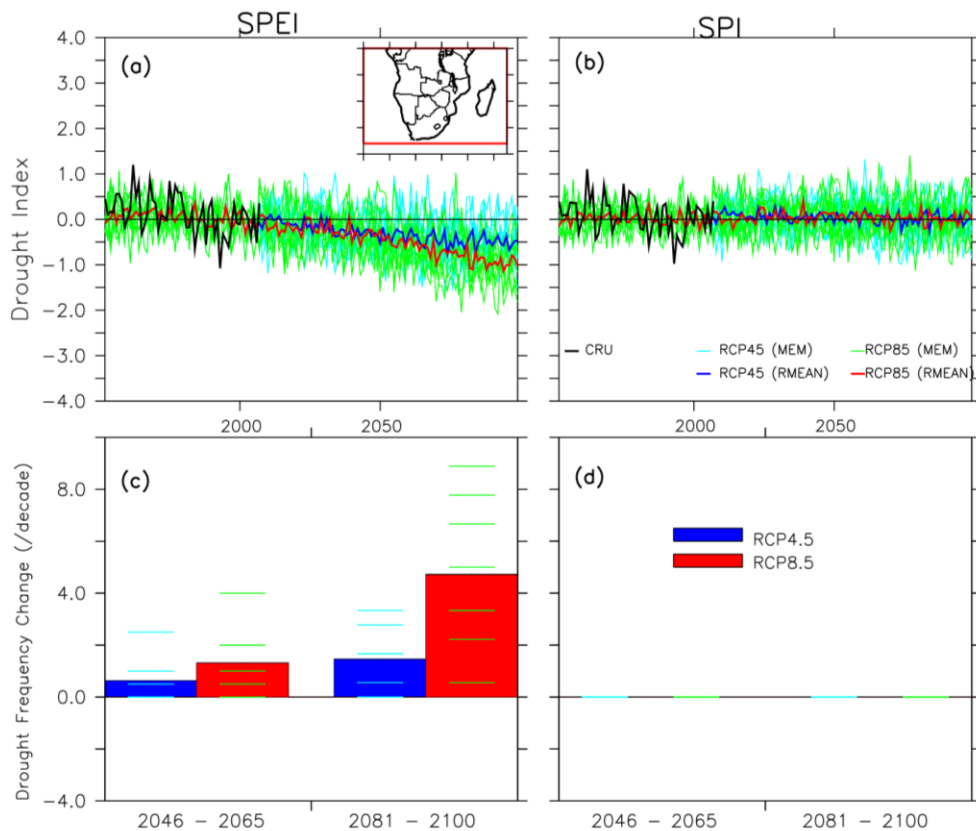
Figure 127: Future projections of annual drought intensity and frequency (12-month SPE and SPI, ending in February) over southern Africa
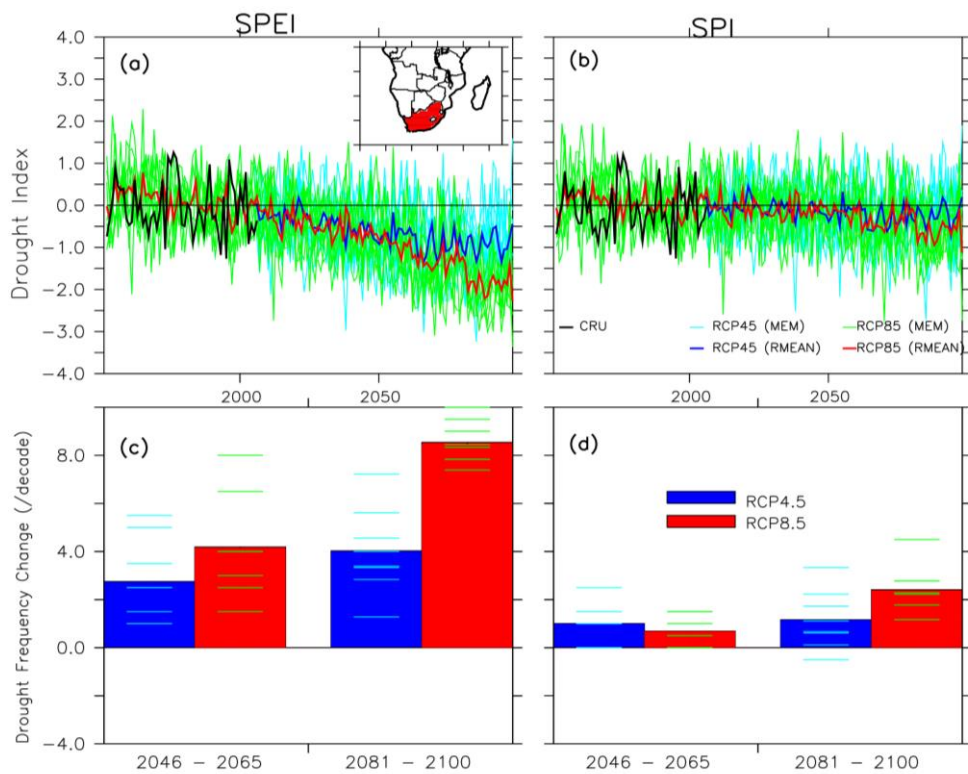
Figure 128: Future projections of annual drought intensity and frequency (12-month SPE and SPI, ending in February) over South Africa

141
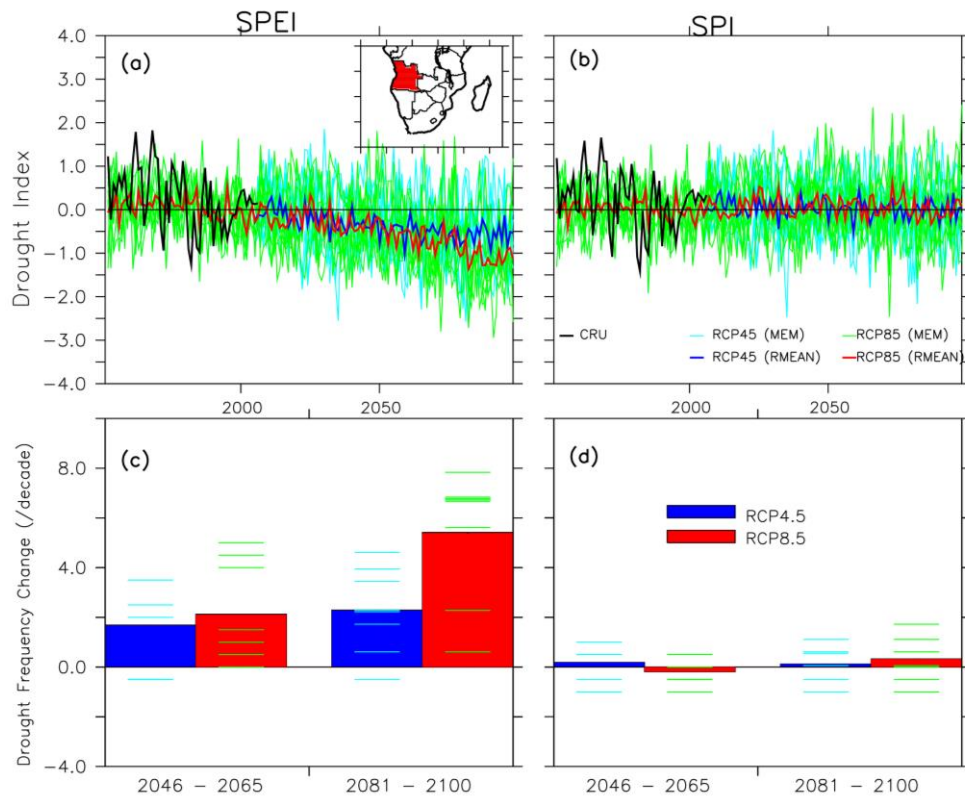
Figure 129: Future projections of annual drought intensity and frequency (12-month SPE and SPI, ending in February) over Angola
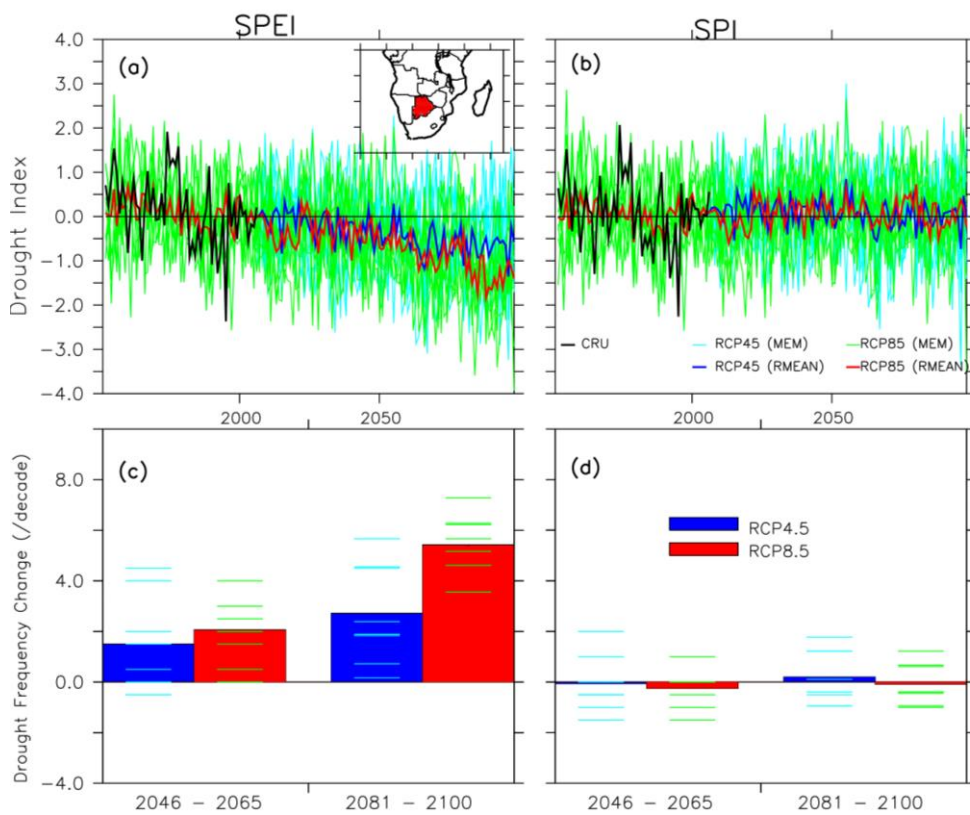
Figure 130: Future projections of annual drought intensity and frequency (12-month SPE and SPI, ending in February) over Botswana

142
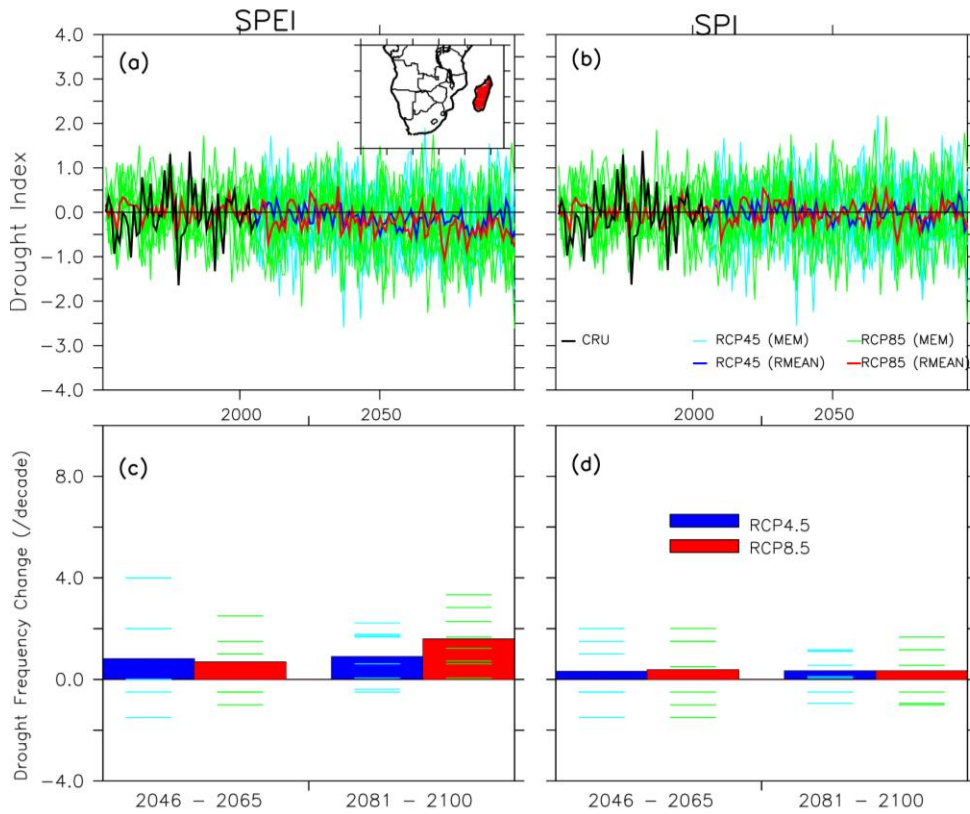
Figure 131: Future projections of annual drought intensity and frequency (12-month SPE and SPI, ending in February) over Madagascar
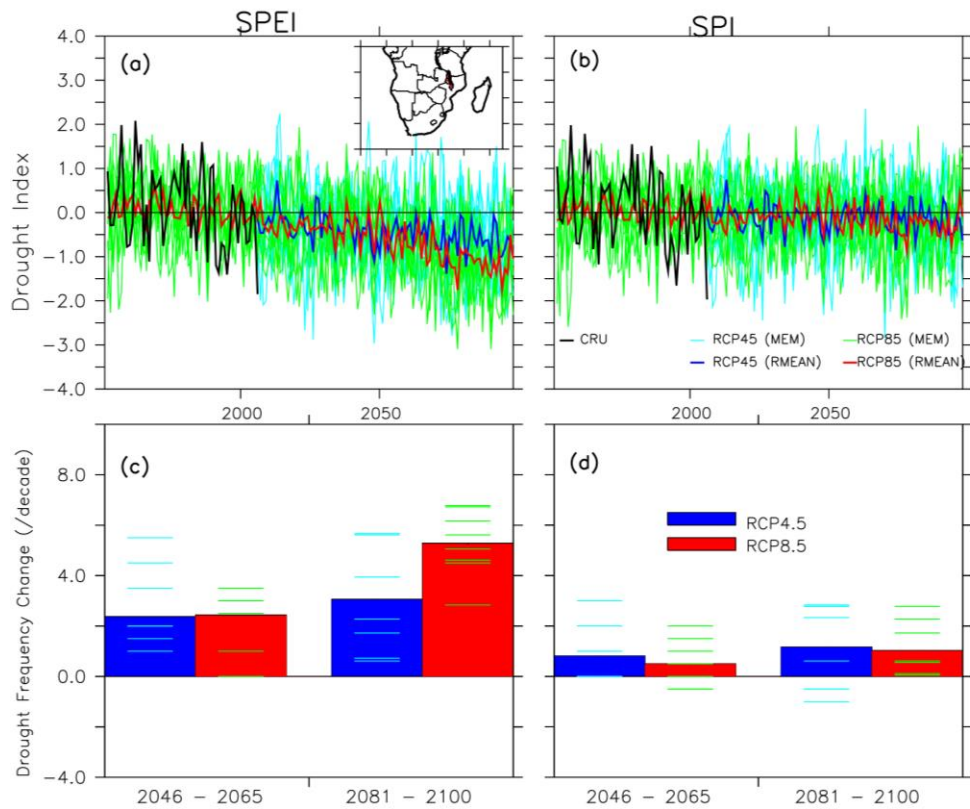
Figure 132: Future projections of annual drought intensity and frequency (12-month SPE and SPI, ending in February) over Malawi

143
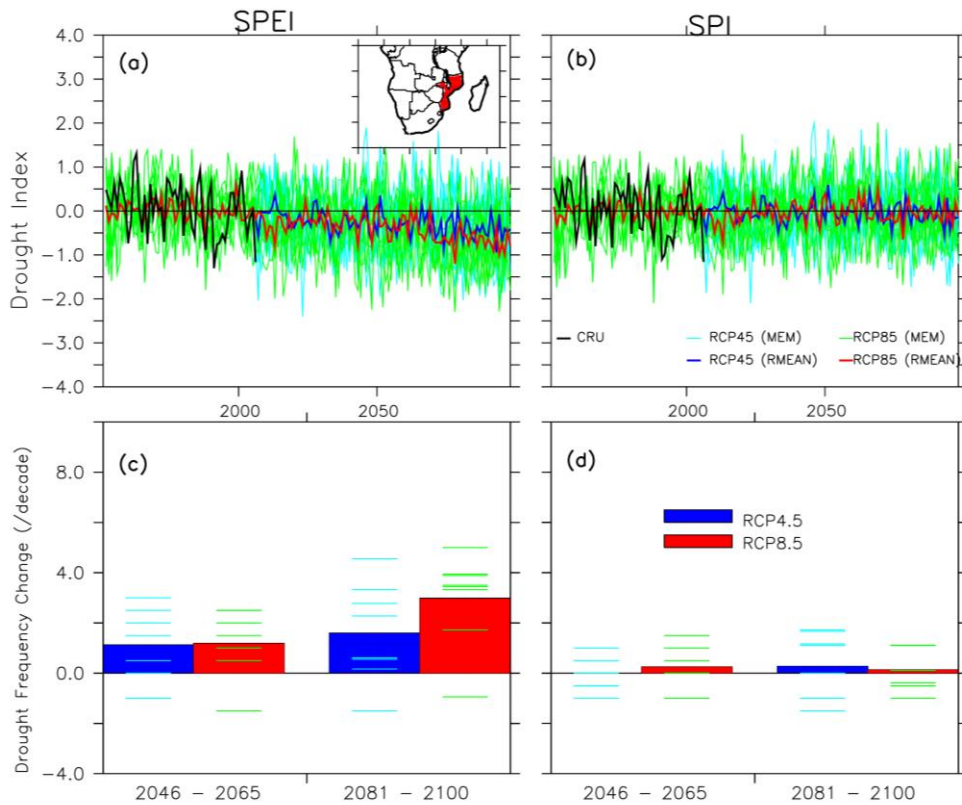
Figure 133: Future projections of annual drought intensity and frequency (12-month SPE and SPI, ending in February) over Mozambique
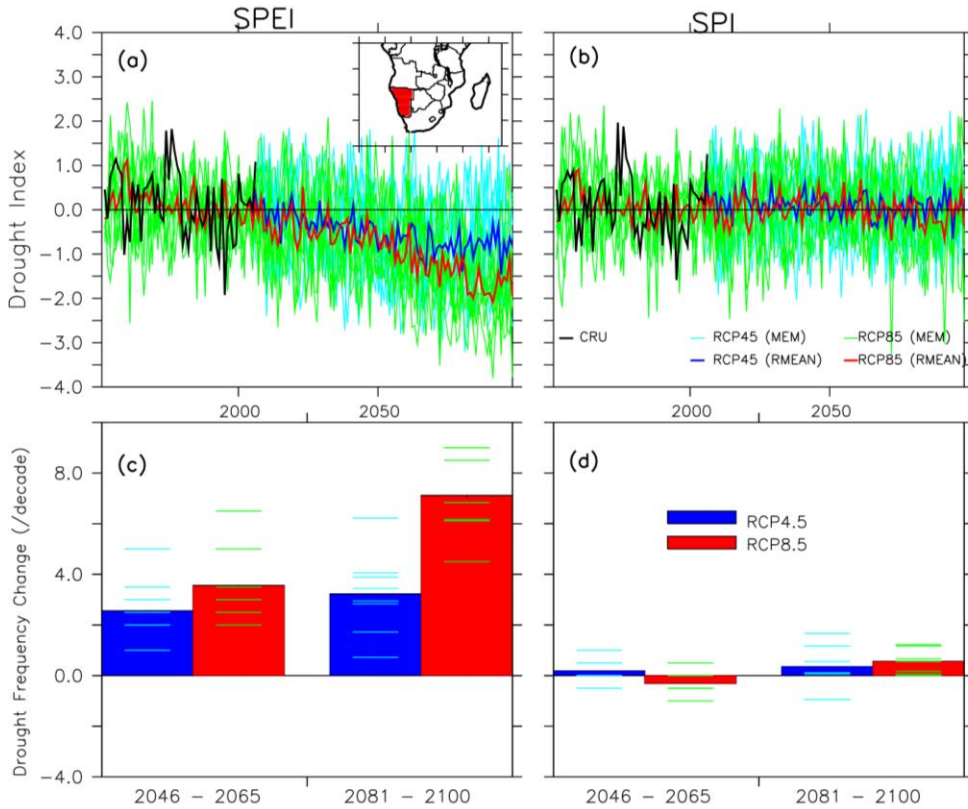
Figure 134: Future projections of annual drought intensity and frequency (12-month SPE and SPI, ending in February) over Namibia

144
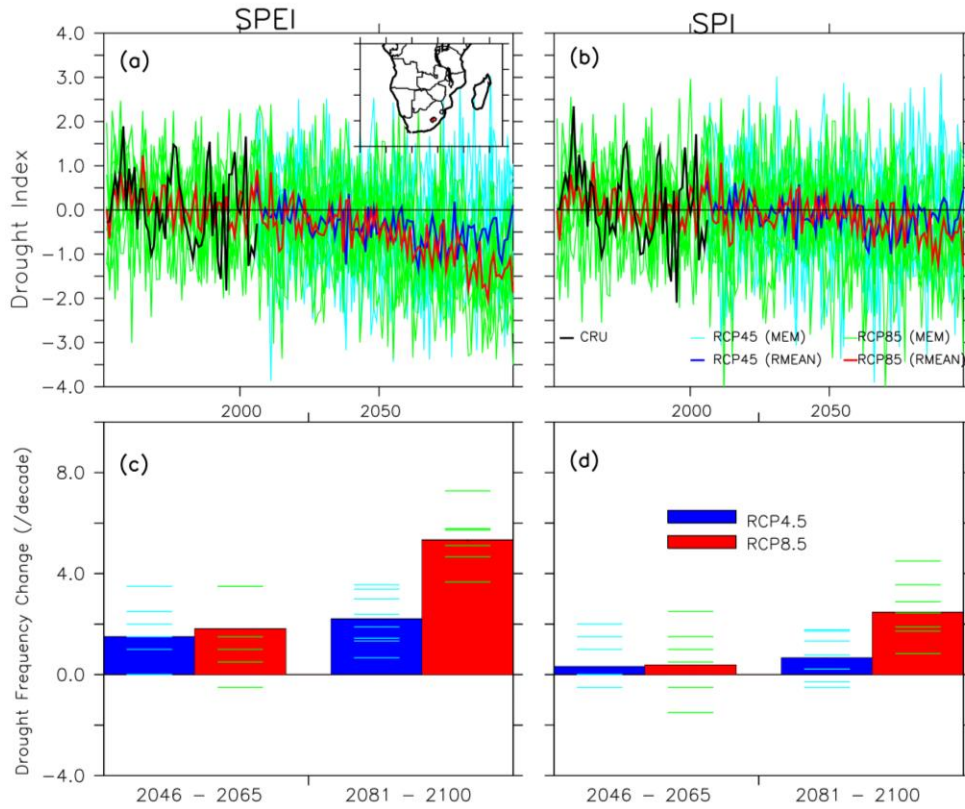
Figure 135: Future projections of annual drought intensity and frequency (12-month SPE and SPI, ending in February) over Lesotho
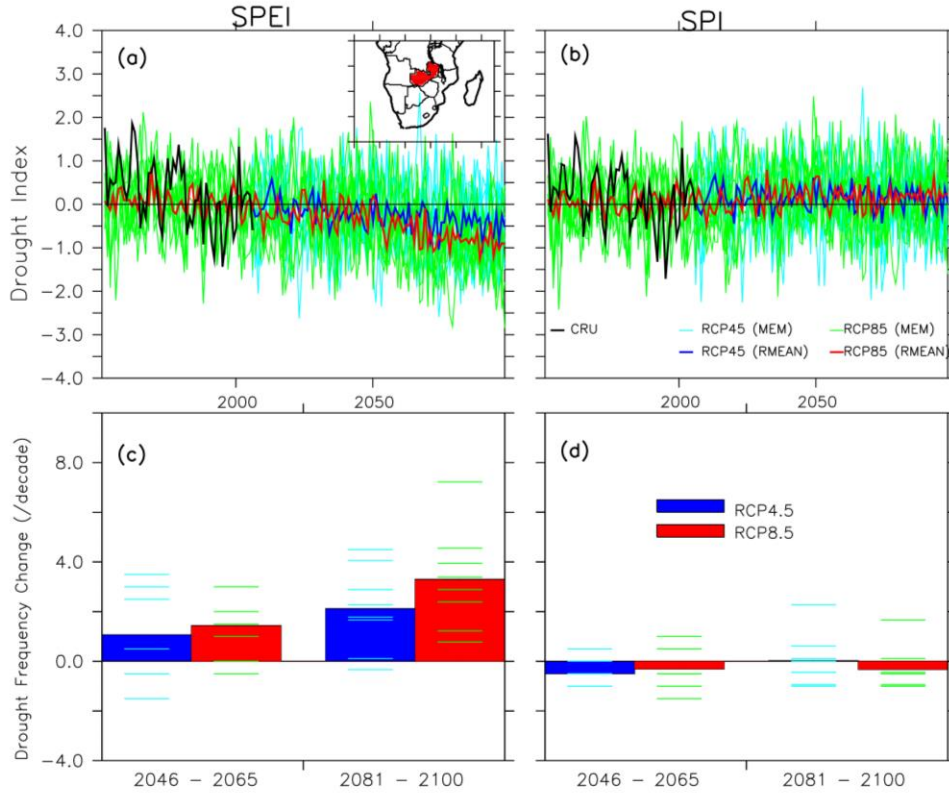
Figure 136: Future projections of annual drought intensity and frequency (12-month SPE and SPI, ending in February) over Zambia

145
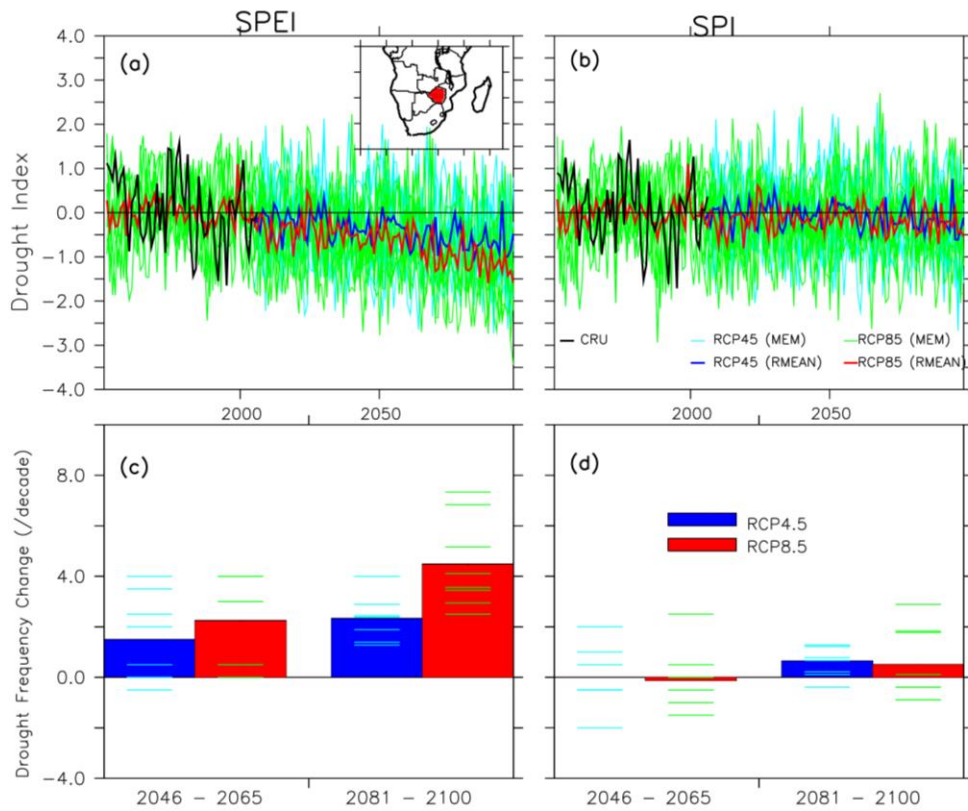
Figure 137: Future projections of annual drought intensity and frequency (12-month SPE and SPI, ending in February) over Zimbabwe